Accretion onto black holes across the mass scale

Riccardo Arcodia

München 2021

Accretion onto black holes across the mass scale

Riccardo Arcodia

Dissertation
an der Fakultät der Physik
der Ludwig–Maximilians–Universität
München

vorgelegt von
Riccardo Arcodia
aus Vasto (CH, Italy)

München, den 02/07/2021

Erstgutachter: Prof. Dr. Kirpal Nandra
Zweitgutachter: Prof. Dr. Andreas Burkert
Tag der mündlichen Prüfung: 30/09/2021

Contents

List of Figures

List of Tables

Zusammenfassung

Schwarze Löcher gehören zu den faszinierendsten Konzepten, sowohl für (Astro-)Physiker als auch für die Öffentlichkeit. Sie sind jedoch viel mehr als nur faszinierende Objekte, die im Schatten des Universums lauern. Viele der hellsten, lang- sowie kurzlebigen, Phänomene die wir im Universum beobachten, hängen mit der Akkretion von Materie auf schwarze Löcher zusammen. Man geht heutzutage davon aus, dass Schwarze Löcher in verschiedenen Massenbereichen existieren. Dabei gibt es zwei Hauptpopulationen: stellare und supermassereiche Schwarze Löcher (SMBHs - super-massive black holes). Erstere sind das Endprodukt der massereichen Sternentwicklung und wir beobachten sie meist bei hellen Ausbrüchen im Röntgenbereich, in sogenannten Röntgendoppelsternen (XRB - X-ray binary). Supermassereiche Schwarze Löcher bilden eine Population von Objekten mit Massen zwischen dem Bruchteil einer Million bis zu mehreren Milliarden Sonnenmassen. Ein Teil der SMBHs ist dank reicher Gasreservoirs, die für die Akkretion zur Verfügung stehen, leuchtkräftig und wird als aktive Galaxienkerne (AGN - active galactic nuclei) bezeichnet. Diese sind aber nur eine kleine Gruppe der SMBH-Population. Alle anderen SMBH sind im Allgemeinen dunkel, können aber beobachtet werden, wenn sie Materie aus ihrer Umgebung akkretieren. Die Akkretionsprozesse, die diese Systeme erleuchten lassen, können bei allen Wellenlängen beobachtet werden und überstrahlen leicht die Galaxien, die die schwarzen Löcher beherbergen. Dieser Kontrast ist besonders auffällig im Röntgenlicht, welches für uns extrem wichtig ist, da es uns erlaubt die innersten Regionen um Schwarze Löcher zu beobachten.

Seit der Entdeckung der Quasare in den 1960er Jahren wurde viel Arbeit in die Beobachtung und das Verständnis der Objekte investiert, zusammen mit der Entwicklung der Akkretionstheorie, um sie zu verstehen. Ein wichtiges beobachtetes Merkmal ist der Zusammenhang zwischen der Helligkeit im optischer/UV- sowie im Röntgenlicht, die in hellen AGN zu beobachten ist. Dieser repräsentiert das energetische Zusammenspiel zwischen den inneren Teilen der Akkretionsströme, speziell der Akkretionsscheibe im optischen/UV, und der Korona im Röntgenbereich. Während die beobachtete Korrelation gut etabliert und quantifiziert ist, fehlt jedoch noch eine solide und schlüssige theoretische Erklärung. In dieser Arbeit verwende ich ein selbstkonsistent gekoppeltes Scheiben-Korona-Modell, welches aus der Literatur angepasst und verbessert wurde, um diese offene Frage anzugehen. Ich identifiziere eine mögliche physikalische Ursache für das wichtigste Merkmal der beobachteten Beziehung, nämlich, dass die Röntgenemission relativ zur Scheibenemission weniger stark zunimmt, wenn man von schwächeren zu helleren Quellen geht. Dies wird durch unser Modell reproduziert, in dem der innere Akkretionsfluss hellerer Quellen in einer viel größeren Region als bei schwächere Quellen durch den

Strahlungsdruck dominiert wird. Dieses Regime dämpft den ansonsten effizienten Energietransfer zur Röntgenkorona, die daher einen geringeren Anteil der Akkretionsleistung abgibt, als die Scheibe. Ich präsentiere auch einen quantitativen Test des Modells mit der Beobachtung einer Referenzstichprobe von typischen, hellen AGN. Wenn ich die beobachteten schwarzen Löcher als nicht-rotierend modelliere, stellt ich fest, dass die Akkretionsmodelle, die in der Lage sind, die Steigung der beobachteten Beziehung zu erfüllen, nicht deren Normalisierung vorhersagen, da die erzeugte Röntgenemission zu schwach ist. Die Annahme einer schnell rotierenden Population von schwarzen Löchern reduziert die Diskrepanz zwischen Modell und Beobachtungen erheblich. Obwohl dieser Test nicht alle Facetten der AGN-Phänomenologie abdeckt, ist er einer der gründlichsten, die dem Verständnis der UV-Röntgen-Beziehung von AGN gewidmet wurden.

Eine weitere faszinierende und seit langem bestehende Frage ist, ob der Akkretionsfluss um Schwarze Löcher über die mehrere Größenordnungen umfassende Massenskala von XRBs bis zu AGN vergleichbar ist. Sowohl die Variabilität als auch die Spektralanalyse deuten darauf hin, dass die Art und Weise, wie Schwarze Löcher Materie akkretieren, zwischen AGN und XRBs in gewisser Weise vergleichbar ist. Was jedoch noch ungeklärt ist, ist wie ähnlich die Prozesse sind und wie sich unterschiedlichen physikalischen Bedingungen im Materiereservoir (d.h. Dichte, Temperatur, Ionisation und die daraus resultierende Druckunterstützung der Akkretionsscheibe) und der Umgebung (d.h. ein einzelner Stern im Vergleich zu dem Zentrum einer Galaxie) auf die physikalischen Prozesse hinter den beobachteten Phänomenen auswirken. In dieser Arbeit untersuche ich diesen Zusammenhang, indem ich die beobachteten Eigenschaften von Scheiben-Korona-Systemen in XRBs und in AGNs in ihren strahlungs-effizienten Phasen vergleiche. Ich kann zeigen, dass XRBs und AGN unterschiedliche beobachtete Akkretionsraten und Verteilungen des spektralen Index im Röntgenbereich aufweisen. Sobald man diesen Unterschied jedoch berücksichtigt, sind die Scheiben-Korona-Systeme in den beiden Klassen schwarzer Löcher recht gut vergleichbar. Dies deutet darauf hin, dass es tatsächlich eine Massenskalierung der Eigenschaften geben könnte. Dabei sind meine Ergebnisse mit Scheiben-Korona-Systemen konsistent, die die gleichen physikalischen Prozesse in AGN und XRBs zeigen, wenn auch unter unterschiedlichen Bedingungen. Diese unterschiedlichen Bedingungen sind zum Beispiel die Temperatur, optische Tiefe und/oder Elektronenenergieverteilung in der Korona, Heiz-Kühl-Gleichgewicht, Geometrie der Korona und/oder Spin des Schwarzen Lochs.

Zusätzlich zu den bisher diskutierten kontinuierlich akkretierenden Schwarzen Löchern kann die Akkretion von Schwarzen Löchern auch ein vorübergehendes und variables Phänomen sein. Sogenannte quasi-periodische Eruptionen (QPEs) sind extreme, hochamplitudige Ausbrüche von Röntgenstrahlung, derzeit unbekannter Natur, die alle paar Stunden wiederkehren und ihren Ursprung in der Nähe der zentralen supermassiven Schwarzen Löcher in galaktischen Kernen haben. Vor dieser Arbeit war diese Phänomenologie nur in zwei Quellen beobachtet worden, die entweder zufälligerweise oder in Archivdaten gefunden wurden. Ein weiterer wichtiger neuer Beitrag in dieser Arbeit ist die Entdeckung von QPEs in zwei weiteren Galaxien, die mit einer blinden und systematischen Suche über die Hälfte des Röntgenhimmels mit dem eROSITA-Röntgenteleskop gefunden wurden. Die wichtigste Neuerung ist, dass im Gegensatz zu den beiden vorherigen Beispielen, die optischen Spektren der hier gesehenen Galaxien, die die QPEs umgeben, keine Signatur von Aktivität von schwarzen Löchern zeigen. Dies könnte darauf hindeuten, dass ein existenter Akkretionsfluss, wie er für AGN typisch ist, nicht erforderlich ist,

um QPEs auszulösen. In der Tat sind die Perioden, Amplituden und Profile der neu entdeckten QPEs unvereinbar mit bisher vorgeschlagenen Modellen, die auf Strahlungsdruck getriebene Instabilitäten in der Akkretionsscheibe zurückgehen. Stattdessen könnten die QPEs von einem umkreisenden kompakten Objekt angetrieben werden. Ihre beobachteten Eigenschaften setzen voraus, dass die Masse des zweiten Objekts viel kleiner ist als die des primären Objektes und zukünftige Röntgenbeobachtungen könnten mögliche Änderungen der Periode aufgrund der Entwicklung der Umlaufbahn bestimmen. Mit diesen Beobachtungen wurde eine neue, exotische Erscheinungsform der Akkretion auf Schwarze Löcher gefunden, die mit eROSITA und zukünftigen Generationen von Röntgenmissionen weiter untersucht werden wird.

Abstract

Black holes are amongst the most fascinating concepts both for (astro-) physicists and the public. However, they are not only intriguing objects lurking in the cosmic shadows. Many of the most luminous phenomena, both persistent and transient, that we know in the Universe are somehow related to accretion of matter onto them. Black holes are predicted and inferred to exist in different mass ranges, with two main populations consisting of stellar-mass and super-massive black holes (SMBHs). The former originate from the endpoint of massive star evolution and are brought to our attention mostly when they undergo X-ray bright outbursts in X-ray binary (XRB) systems. The latter constitute a population of objects with masses between fractions of a million to several billion times that of our Sun. Some fraction of SMBHs are observed to be luminous thanks to rich gaseous reservoirs available for accretion, and are called active galactic nuclei (AGN). These are in fact a minority of the SMBH population. The others are generally quiescent, but can be revealed if they receive a sudden donation of matter in their vicinity. The accretion processes powering these systems can make them bright at all wavelengths, and may easily outshine the galaxies that host them. This contrast is particularly striking in the X-rays, which are particularly important because they trace the innermost regions around black holes.

Since the discovery of quasars in the 1960s, much observational effort has been devoted to their study, along with the development of accretion theory to understand them. An important observed feature is the correlation between optical/UV and X-ray luminosities seen in bright AGN. This represents the energetic interplay between the inner parts of accretion flows, namely the accretion disk in the optical/UV and the X-ray corona. While the observed correlation is well established and quantified, a solid and conclusive theoretical explanation is still lacking. In this Thesis, I use a self-consistently coupled disk-corona model, adapted and improved from the literature, to tackle this open question. I identify a possible physical driver for the most crucial characteristic of the observed relation, namely that the X-ray emission increases less, relative to the disk emission, going from fainter to brighter sources. This is reproduced by my model, in which the inner accretion flows of brighter sources are dominated by radiation pressure through a much larger region compared to fainter sources. This pressure regime notoriously damps the otherwise efficient energy transfer to the X-ray corona, which therefore dissipates a lower fraction of accretion power, relative to the disk. I also present a quantitative observational test of the model using a reference sample of typical bright AGN. Modelling the observed black hole population as non-spinning, I find that the accretion prescriptions that are able to match the slope of the observed relation are unable to match its normalization, in the sense that the X-ray emission produced is too weak. Considering a highly-spinning black hole population

significantly relaxes the tension between the model and observations. Despite being incomplete in addressing all the many faces of AGN phenomenology, this test is among the most thorough so far devoted to the understanding of UV-X-ray relation.

A further intriguing and long-standing question exists as to whether the accretion flow around black holes is similar over the several order-of-magnitude masses scale from XRBs to AGN. There is evidence from both variability and spectral analysis that the way black holes accrete matter is indeed somewhat analogous between AGN and XRBs. What is yet to be established is the extent of this analogy and the impact of different physical conditions in the matter reservoir (i.e. density, temperature, ionisation, and consequently pressure support of the accretion disk) and the surrounding environment (i.e. a single star with respect to the centre of a galaxy) on the physical processes behind the observed phenomenology. In this Thesis, I explore this connection by comparing the observational properties of disk-corona systems in both XRBs and AGN in their radiatively-efficient phases. I find that XRBs and AGN show different observed accretion rate and X-ray spectral index distributions. Once this difference is controlled for, however, the disk-corona systems in the two black holes classes compare quite nicely. This indicates that a mass-scaling of properties might indeed hold, with my results being consistent with disk-corona systems exhibiting the same physical processes in AGN and XRBs, albeit under different conditions for instance in terms of temperature, optical depth and/or electron energy distribution in the corona, heating-cooling balance, coronal geometry and/or black hole spin.

In addition to the continuously accreting black holes discussed so far, black hole accretion can also be a transient and variable phenomenon. So-called quasi-periodic eruptions (QPEs) are extreme high-amplitude bursts of X-ray radiation of currently unknown nature, recurring every few hours and originating near the central supermassive black holes in galactic nuclei. Before this thesis, this phenomenology had been seen in only two sources, found either serendipitously or in archival data. Another important new contribution in this Thesis is the discovery of QPEs in two further galaxies, obtained with a blind and systematic search over half of the X-ray sky with the eROSITA X-ray telescope. The main novelty is that, contrary to the two previous examples, the optical spectra of the QPE host galaxies seen here show no signature of black hole activity. This might indicate that a pre-existing accretion flow typical of AGN is not required to trigger these events. Indeed, the periods, amplitudes and profiles of the newly discovered QPEs are inconsistent with models that invoke radiation-pressure driven accretion disk instabilities, which were previously suggested. Instead, QPEs might be driven by an orbiting compact object. Their observed properties require the mass of the secondary object to be much smaller than the main body and future X-ray observations may constrain possible changes in the period due to orbital evolution. With these observations a new, exotic manifestation of accretion onto black holes has found and this will continue to be studied with eROSITA and future generations of X-ray missions.

Chapter 1

Introduction

1.1 Accretion onto black holes across the mass scale

The concept of black holes (BHs) entered into scientific discourse in the eighteenth century (as 'dark stars'[1]), well before any quantitative theory, let alone any space mission, was put forward. Since then, it has been among the most fascinating concepts both for (astro-) physicists and the public. No surprise then, that the 2017 Nobel Prize laureate in Physics Kip Thorne was also producer and scientific consultant of one of the most acclaimed sci-fi movies 'Interstellar', which won the Academy Award for Best Visual Effects thanks to its realistic representation of the black hole 'Gargantua' (top panel of Fig. 1.1). By analogy with the novels written by F. Rabelais from which the name is borrowed, the fictional black hole Gargantua is a giant, with a mass of 100 million Suns. This giant, if it existed, would be among the so-called supermassive black holes, a category which spans from about tenths of a million to tens of billions of solar masses.

We now know of more than one million black holes, for which however we rather observe radiation coming from their immediate vicinity and assume their presence. Particularly strong evidence for the existence of black holes was obtained when the teams led by R. Genzel and A. Ghez pointed telescopes at the centre of our Galaxy and observed single stars moving around something they could not see, which needed to be very compact and as massive as 4 million Suns (Genzel et al. 1997; Ghez et al. 1998; Schödel et al. 2002), a discovery that led to the 2020 Nobel Prize in Physics. Another break-through was the first 'visual' evidence of the silhouette of the black hole at the centre of M87 (bottom panel of Fig. 1.1) by the Event Horizon Telescope (EHT) Collaboration (Event Horizon Telescope Collaboration et al. 2019).

The three publicly renowned black holes of the twenty-first century mentioned above (artificial or real) are all supermassive (SMBHs), but black holes are predicted and inferred to exist over a wide mass range. Observationally, however, a distinction is often drawn between stellar-mass (Section 1.2) and SMBHs (Section 1.3). The former population is the result of the evolution

[1]From 'On the means of discovering the distance, magnitude, &c. of the fixed stars, in consequence of the diminution of the velocity of their light, in case such a diminution should be found to take place in any of them, and such other data should be procured from observations, as would be farther necessary for that purpose' by the Rev. John Michell, in a letter to Henry Cavendish, http://doi.org/10.1098/rstl.1784.0008

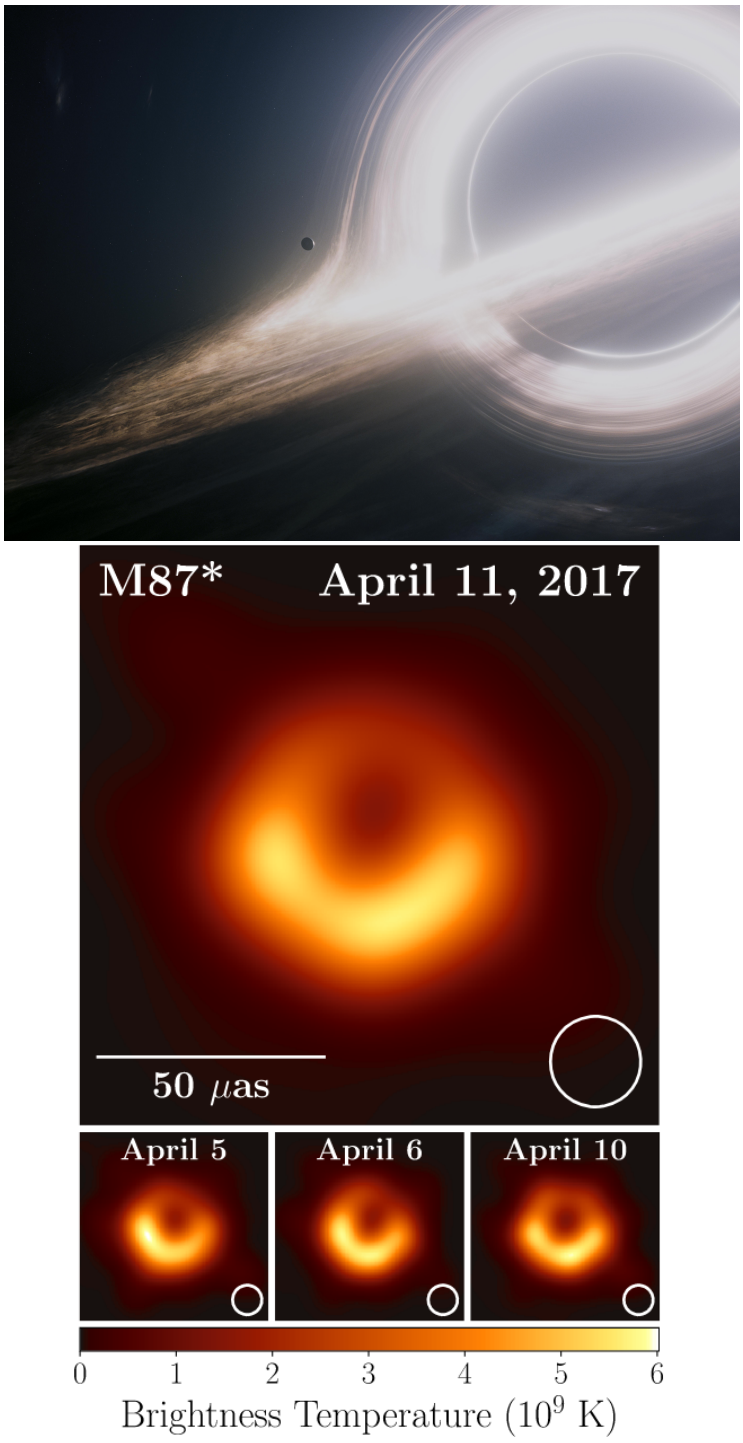

Figure 1.1: *Top:* the artificial image of the supermassive black hole Gargantua appeared in the movie 'Interstellar' (credits: Paramount Pictures). *Bottom:* the reconstructed image of the black hole at the centre of M87 (Event Horizon Telescope Collaboration et al. 2019).

of massive stars and the typical black hole mass (M_{BH}) in our Galaxy tend to fall in a quite narrow range around $M_{BH} = 7.8 \pm 1.2 M_{\odot}$ (Özel et al. 2010). SMBH, on the other hand, are found in the centres of galaxies and have acquired most of their mass via accretion. They span at least four order of magnitudes in mass in the range $M_{BH} \sim 10^6 - 10^{10} M_{\odot}$ and evolve with cosmic time (e.g., Merloni & Heinz 2008; Shankar et al. 2009). Black holes with masses in between these two categories are thought to exist as well, but they have been so far more elusive (Section 1.4).

Black holes are not only a fascinating and exotic type of celestial body. Some of the most luminous transient and persisting phenomena we observe are related to matter accreting onto them, which can happen in many different ways. For instance, a semi-continuos flow of gaseous matter (Section 2) is implied in Active Galactic Nuclei (AGN) with accreting SMBHs (Section 1.3.1), fed by the galaxy's interstellar medium. Stellar-mass BHs in X-ray binaries (XRBs) are by contrast fed by a single companion star (Section 1.2). Alternatively, black holes can entirely or partially swallow objects such as stars passing nearby (Section 1.3.2). More generally, accretion is an extremely common and important astrophysical process, present in a wide range of objects, and responsible for the growth and evolution of many astrophysical systems, from galaxies to planets. Examples usually involve a centre of mass M, be it a star or a compact object onto which matter accretes. We will focus here specifically on accretion onto black holes, which are also the simplest type of accretors since they lack a surface or 'hair' (Ruffini & Wheeler 1971), meaning any distinctive feature which is not their mass, spin or electric charge (assumed to be zero for astrophysical black holes).

It is commonly inferred that accreting systems involve the formation of astrophysical disks. If material in gravitational acceleration ($\propto R^{-2}$) infalls with some angular momentum, it will be rotationally supported by centripetal acceleration ($l^2 R^{-3}$, where l is the specific angular momentum). Therefore material would soon circularise but would not reach the central mass unless angular momentum is lost. How this happens is one of the key questions that accretion theories try to answer, another being how the gravitational binding energy is converted into observable forms (Section 2). Black holes must be very efficient overall in converting part of what they accrete into radiation, since we often observe them outshining the whole galaxy at the centre of which they reside. Indeed, in terms of efficiency ϵ_0, black holes convert $\approx 10\%$ of the available rest mass energy mc^2 in the process of accretion (Thorne 1974). This can be shown to zeroth order by considering the gravitational potential energy released to accrete a particle m from infinity to R around M_{BH} (which is $GM_{BH}m/R$), as the fraction ϵ_0 of the rest mass energy mc^2 of the particle. This yields $\epsilon_0 \sim r_g/R$, where r_g is the gravitational radius GM_{BH}/c^2, therefore the higher the compactness of the accretor ($\sim M/R$) the higher the efficiency. For a non-rotating black hole, accreting down to its innermost stable circular orbit (ISCO) at $6r_g$ results in $\epsilon_0 \sim 0.17$, which is the same order of magnitude as what is obtained with proper general relativity (0.057; Thorne 1974) and accretion (Section 2) calculations. In the most general terms, the luminosity generated by this process is then:

$$L = \epsilon_0 \dot{M} c^2 \tag{1.1}$$

where $\dot{M} = dM/dt$ is the mass accretion rate, usually expressed in solar masses per year.

The fuel available to a giant black hole at the center of a galaxy is obviously not the same as the one donated by a star to a stellar-mass black hole, therefore L is several orders of magnitudes

apart for the two source classes. Usually, L is conveniently scaled by a mass-dependent *rough* accretion limit, which is the Eddington luminosity $L_{edd} = 1.3 \times 10^{38} M_{BH}/M_{\odot}$ erg s^{-1}. It is computed by balancing radiation pressure through Thomson scattering (cross section σ_T) on unbound electrons of a spherically symmetric plasma around M_{BH}, which is $\sigma_T L/4\pi R^2 c$, with the gravitational pull of M_{BH}, which acts mostly on protons (mass m_p) and therefore is $\sim GM_{BH}m_p/R^2$. The so-called 'Eddington limit' however, should not be seen as an insuperable barrier, but rather as an approximate mass-dependent value to reasonably normalize the accretion process, which also eases comparisons across the mass scale. It is in fact only a 'rough' accretion limit because of the assumptions of a steady flow, of fully ionised matter with Thomson cross-section on the unbound electrons, and spherical geometry, all of which are probably violated in a realistic accretion flow (Frank et al. 2002).

Once L and $\dot{M}$ are scaled by the respective Eddington values (i.e. here $\lambda_{edd} = L/L_{edd} = \dot{m} = \dot{M}/\dot{M}_{edd}$, called the Eddington ratio), and since radial scales can also be normalized by M_{BH} via r_g, it is easier to compare accretion flows around black holes across the mass scale (Section 1.5). Simple arguments can also be introduced to estimate the energy range where most of the radiation is coming from for different values of M_{BH}. If accretion is via a disk with each annulus radiating locally as a black-body (flux $\propto T_{bb}^4$ where T_{bb} is the black body temperature), the radiated energy can be equated to the gravitational energy the matter loses as it is accreted. Assuming that most of the radiation comes from around $10r_g$, the maximum temperature $T_{bb,max}$ is $\propto (L/R^2)^{1/4} \propto L^{1/4} M_{BH}^{-1/2}$, which for sources of different masses accreting at a fixed fraction of Eddington ($\propto M_{BH}$) becomes $\propto M_{BH}^{-1/4}$. This corresponds to energies around soft X-rays for stellar-mass BHs ($M_{BH} \sim 10 M_{\odot}$) and UV for super-massive BHs ($M_{BH} \sim 10^8 M_{\odot}$).

In this Thesis we will focus on multi-wavelength observations of black holes of different sizes, on how they compare with each other and with predictions from accretion theories.

1.2 Stellar-mass black holes

Stellar-mass black holes form at the end of the evolution of massive stars (Woosley & Weaver 1995; Heger et al. 2003). Many massive stars, perhaps even the majority, evolve and interact with a companion (Sana et al. 2012). Consequently, it is typical for stellar-mass black holes to have a stellar companion which can transfer mass via Roche-lobe overflow or via stellar winds, depending on the mass of the companion. The existence of these black hole binary systems is inferred via multi-wavelength observations ($M_{BH} \sim 5 - 15\, M_{\odot}$; Casares et al. 2017, and references therein) or via gravitational wave (GW) signals ($M_{BH} \sim 7 - 50\, M_{\odot}$; Abbott et al. 2016a,b; Abbott et al. 2017; Abbott et al. 2017a,b, 2019).

X-ray observations play a particularly important role, and X-ray astronomy blossomed after the first X-ray observations of stellar-mass BHs (Pounds 2014, for a review), in particular of Cygnus X-1, the first observed Galactic black hole. More than half a decade later, there is a compilation of a couple dozens of similar objects in our Galaxy (Remillard & McClintock 2006; Casares et al. 2017), but they are also observed in other nearby galaxies as an X-ray emitting population (e.g., Grimm et al. 2003). If they are not persistent (e.g. Cygnus X-1), these sources are discovered when they undergo an X-ray bright outburst, hence their name X-ray Binaries

(XRBs). Outbursts usually last from days to months and repeat after some (much longer) periods of quiescence (Remillard & McClintock 2006). The strongest evidence of the presence of a black hole is however measured during quiescence, from the radial velocity curve of the companion star, if the minimum mass allowed for the compact object is above the maximum stable mass of a neutron star (e.g., Kalogera & Baym 1996).

An X-ray outburst in XRBs is thought to be triggered when the mass transfer rate from the companion is such that hydrogen becomes ionized in a given region of the quiescent accretion flow (e.g., Lasota 2001; Done et al. 2007, for a review). When this happens, the opacity rises quite steeply with temperature between $\approx 10^4 - 10^5$ K (e.g., Seaton et al. 1994), thus the flow in that region can not efficiently cool and heats up. This might then trigger a heating wave propagating through neighbouring regions. X-ray irradiation from the now radiatively efficient inner accretion disk keeps the outer regions hotter than the Hydrogen recombination temperature for a while until matter is depleted and the outburst fades on viscous timescales, hence much more slowly than when it started (Dubus et al. 2001; Lasota 2001). This simple scenario was shown to be remarkably consistent with the observed properties (e.g. luminosities, light curves and spectra) of both persistent and transient black hole XRBs (van Paradijs 1996; Coriat et al. 2012).

Even though outbursts from different systems and different outbursts from the same source can be diverse in terms of, for instance, duration or amplitude in luminosity, most of them are shown to follow a clear pattern in the so-called 'turtle-head plot' or 'q-plot' (e.g. Dunn et al. 2010) (top panel of Figure 1.2). This plot can indicate how these sources change their X-ray spectral shape as a function of time and luminosity (both in X-rays and radio), hence the name hardness–luminosity diagram (HLD; Fender et al. 2004). Typically (see Belloni & Motta 2016, for a recent review), a source starts an outbursts in the bottom right of the q-plot, namely with a very hard X-ray spectrum and overall low X-ray luminosity, then it brightens whilst keeping an hard spectrum (the so-called 'low/hard state'), which slightly softens with increasing brightness (e.g., Motta et al. 2009) and shows accompanying steady and collimated radio emission (e.g., Mirabel & Rodríguez 1999; Fender 2001); then, the same observed X-ray luminosity is maintained whilst the spectrum softens (hard and soft intermediate states) and bright radio flares occur (Fender & Gallo 2014); the source then enters a state in which most of the X-ray counts are below ~ 10 keV and the X-ray luminosity decreases over time (the so-called high/soft state), with weak or absent radio emission (e.g., Fender et al. 1999); the outburst ends with the source going back to the low/hard state through the intermediate ones, albeit at the lowest X-ray luminosities (top panel of Figure 1.2).

Despite the fact that different phases, or 'states', can be clearly distinguished in the HLD, there is no unique association between hardness-ratio or luminosity and a spectral state, as it was soon clear that sources typically undergo an hysteresis cycle in that diagram (Miyamoto et al. 1995). Instead, it was found that a given spectral hardness corresponds, regardless from its flux/luminosity, to a given value of fractional rms of the observed variability (bottom panel of Figure 1.2). This quantity is normally computed integrating the power density spectra of the X-ray light curve between two frequencies (actually the square root of this area, hence 'root mean square', rms) and normalising with the average count rate observed (e.g., Belloni 2010). The low/hard state is the most variable, with values of fractional rms as high as 40%, down to the

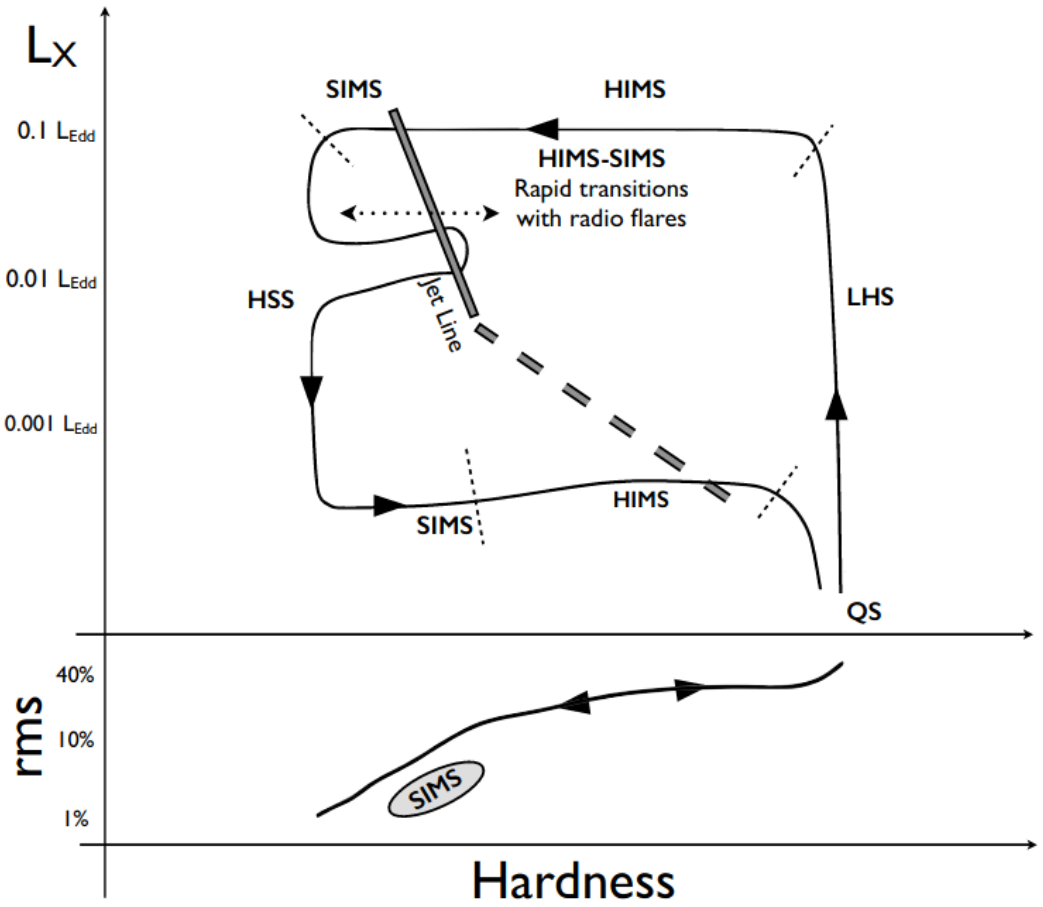

Figure 1.2: Schematic representation of hardness-intensity and rms-intensity diagrams. The short dotted lines in the top panel show the transitions between states: LHS for low/hard state, HIMS and SIMS for hard and soft intermediate state, HSS for high/soft state and QS for quiescence (Section 1.2 for a description). Arrows give the direction along the diagram. The 'jet line' separates radio luminous (rightwards) from radio quiet or weak regions (leftwards). Adapted from Kylafis & Belloni (2015).

high/soft state during which only a few percent is normally observed (Belloni & Motta 2016). Given this univocal relation with spectral hardness, it is therefore easier to discern different XRB states via timing properties.

Furthermore, there seems to be an interplay between two components along the q-plot which shape the overall spectral energy distribution (SED): a soft component, commonly identified as thermal emission from an accretion disk (e.g., Makishima et al. 1986), and a hard component looking like a power-law at zeroth-order which is usually interpreted as inverse-Compton (up-) scattering of the accretion disk photons (Zdziarski & Gierliński 2004), or as emission from the jet base if in the hard state (Markoff et al. 2005). The simplified but widely accepted interpretation consists of an evolving truncated disk (Esin et al. 1997; Done et al. 2007), which we briefly

summarize here. Within this scenario, in the hard state the truncation radius is large and effectively most of the inner accretion flow consists of hot optically thin plasma, with the innermost regions responsible for launching the jet observed in radio (e.g., Mirabel & Rodríguez 1999); since the luminosity of the outer optically-thick geometrically-thin disk, which provides the seed photons for inverse-Compton in the hot thin plasma, is low, cooling is inefficient and electrons in the thin plasma can reach very high temperatures, which for a given optical depth makes the convoluted thermal-Comptonisation power-law hard ($\Gamma < 2$ as slope of the photons spectrum $\propto E^{-\Gamma}$, therefore slope of the $F_\nu \propto \nu^\alpha$ energy spectrum > -1, hence a slope in the νF_ν SED which is > 0 and peaking at $\approx 100\,\mathrm{keV}$). As the mass accretion rate increases during the first part of the outburst and up to the intermediate states, more and more annuli of the flow collapse into a more geometrically-thin optically-thick disk. In the high/soft state the truncation radius extends close to ISCO, the seed photons luminosity is dominant and inverse-Compton cooling is more efficient, the electrons population (likely hybrid rather than only thermally distributed, Coppi 1999) in what remains of the hot thin plasma therefore cannot reach high temperature and the Comptonisation spectrum is much softer ($\Gamma \gtrsim 2$); the overall X-ray spectrum is instead dominated by the thermal emission of the accretion disk, which is shown to follow $L \propto T^4$ with an almost constant inner radius (Dunn et al. 2011) modulo some correction factors (Merloni et al. 2000; Done et al. 2007); in this state the jet likely switched off, given the weak or absent radio emission (Fender & Gallo 2014), while the presence of equatorial disk winds is inferred from absorption lines in X-ray spectra (Ponti et al. 2012).

In summary, XRBs are very important for the study of accretion onto black holes for quite a few reasons. First, they evolve (even several times) over 'human' timescales (Remillard & McClintock 2006), therefore we can study a more or less complete accretion cycle spanning different states. Moreover, we can be almost sure that these outbursts are mostly regulated by changes in accretion rate because we can observe them in single objects, namely with one given mass, spin and inclination. It is true that normally these are not parameters well constrained in an absolute sense (Remillard & McClintock 2006; Casares et al. 2017), but they do not change within the same outburst(s). Furthermore, matter around stellar-mass black holes is hotter and denser with respect to their super-massive relatives, therefore spectroscopy studies and accretion disk modelling suffer from less complications (e.g., Done et al. 2012). We will benefit from these advantages in Chapter 4.

1.3 Supermassive black holes

Contrary to XRBs, the formation of super-massive black holes is very much an open and lively topic of discussion to date (Volonteri 2010, for a review), challenged by the observation of AGN up to, currently, $z \sim 7.5$ (Bañados et al. 2018). In the case of SMBHs the complexity of their formation, of their co-evolution with the surrounding galaxy and galaxies which results in a mixed bag of masses, growth phases, spins, environments, all hinder a systematic and comprehensive characterisation. Very recently SMBHs were proved to exist (Genzel et al. 1997; Ghez et al. 1998; Event Horizon Telescope Collaboration et al. 2019). In hindsight, these giants were not trying to stay hidden at all and were spotted, unrecognised, since more than a hundred years

ago (e.g., Curtis 1918; Seyfert 1943; Baade & Minkowski 1954) up to the early sixties when several bright point-like sources were observed in optical images (e.g., Schmidt 1962; Matthews & Sandage 1963), albeit still considered as peculiar stellar sources, hence the name quasi-stellar radio sources (or objects) or quasars (QSOs). It was not however until M. Schmidt published evidence that the QSO 3C273 had an 'appreciable redshift' ($z = 0.138$; Schmidt 1963) that the pieces of the puzzle started to be put together (Greenstein 1963; Oke 1963; Greenstein & Matthews 1963; Hazard et al. 1963; Sandage 1965; Schmidt 1968).

After more than half a century later, we now know of more than one million QSOs (e.g., Ahumada et al. 2020). Even before reaching conclusive evidence, good arguments in favour of the existence of black holes in the nuclei of (almost all) galaxies (e.g., Schmidt 1978; Soltan 1982) were built during the previous decades. To name just a couple, the high luminosity excluding most of the emission mechanisms but accretion of matter onto 'massive objects of relatively small size' (Salpeter 1964; Zel'dovich 1964); fast (hours or less) X-ray variability observed in some galaxies (e.g., Lawrence et al. 1985; McHardy 1989), or the dynamics of stars and gas in galaxy cores (e.g., Kormendy & Richstone 1995, and references therein), both indicating high compactness of the central mass.

Observations of SMBHs find them in different phases of their evolution as a function of redshift (Schmidt 1968; Soltan 1982; Ueda et al. 2003; Aird et al. 2015; Miyaji et al. 2015), which traces quite faithfully (Merloni & Heinz 2008; Delvecchio et al. 2014; Aird et al. 2015) the evolution of star formation rate (SFR) in galaxies (Madau & Dickinson 2014). SMBHs which are observed to be active are luminous and radiatively efficient thanks to their rich gaseous reservoir (Section 1.3.1), but they are in fact a minority of the SMBH population (Bongiorno et al. 2012, 2016; Georgakakis et al. 2017; Aird et al. 2017). The others are quiescent, either in absolute sense or simply faint enough to be hidden behind the emission of the surrounding galaxy (e.g., Gilfanov & Merloni 2014). Few of these are spotted when they receive a sudden donation of mass (Section 1.3.2), usually from a stellar-mass companion which got close enough to the SMBH to be partially stripped by its tidal forces (hence the name Tidal Disruption Events, TDEs; Komossa 2015, for a review), but not too close to be swiftly and silently swallowed.

1.3.1 Accreting supermassive black holes: active galactic nuclei

A SMBH is considered an AGN when it accretes from the orbiting gaseous reservoir within its sphere of gravitational influence (Bondi 1952), which is regulated by the interstellar medium of the galactic nuclei they reside in, and efficiently radiates. Contrary to XRBs, which are mostly regulated by the interaction with one companion and the mutual orbital evolution, accretion onto AGN eventually involves all scales from the ISCO to the host galaxy's outskirts, $\sim$ 9 orders of magnitudes in distance apart (Figure 1.4 for the inner regions). To put this into context, the equivalent would be studying every ant in a colony and the effect they have on something which is located at the opposite side of the Earth's surface. Furthermore, if XRBs can be almost entirely described by the accretion-ejection paradigm as inferred from X-rays and radio data (Section 1.2), the spectral energy distribution of AGN is far more complex and can span from radio to gamma (Figure 1.3). This multi-scale multi-waveband problem inevitably resulted in a plethora of names and classification schemes through the last decades (Padovani et al. 2017, for

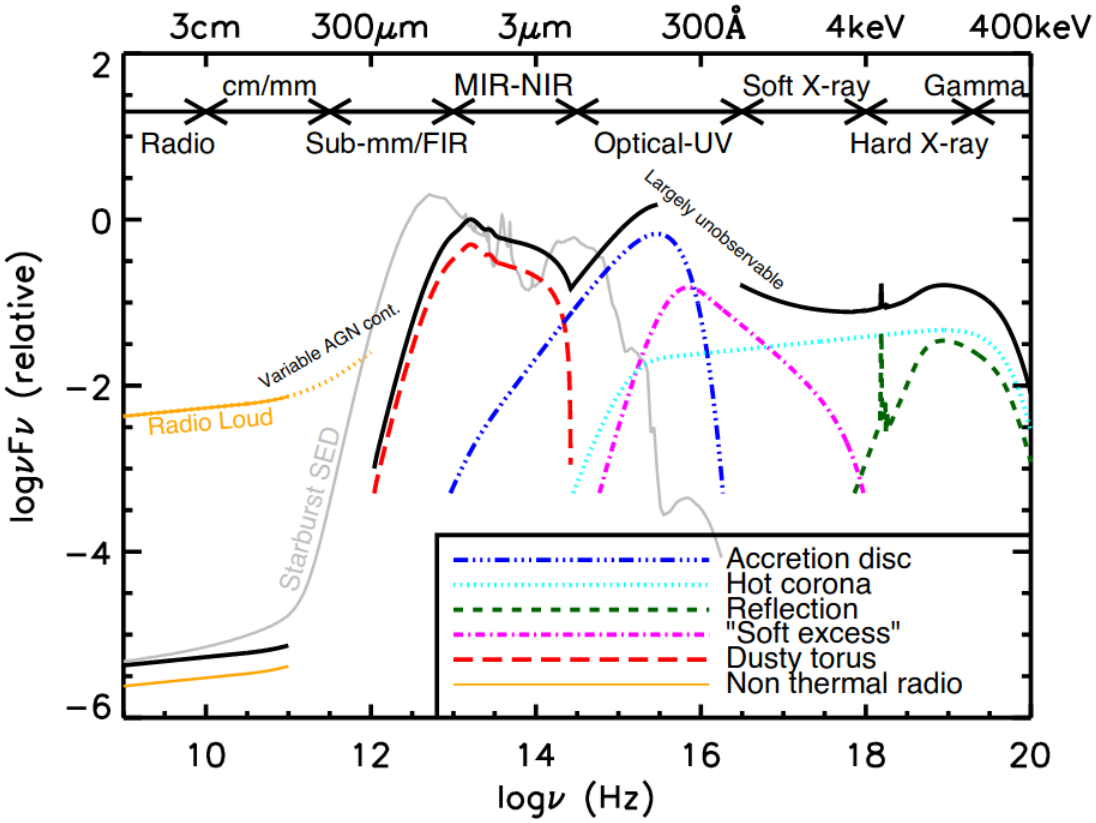

Figure 1.3: Schematic representation of an AGN SED, with the various coloured curves showing the different components (Section 1.3.1), as described in the legend. From Harrison (2014).

a review).

The first QSOs were considered stellar objects for their bright point-like emission in the optical-UV band (Schmidt 1968). Despite being primarily motivated by the discovery of Galactic accreting stellar-mass black holes (Section 1.2), since the early days of accretion theory (Shakura & Sunyaev 1973, Section 2) it was predicted that disks' emission would peak indeed in the optical-UV for super-massive black holes. This so-called 'big blue bump' (blue line in Figure 1.3) is broadly reproduced by such models with fair success (Kishimoto et al. 2008; Capellupo et al. 2015, 2016), albeit there are quite a few complications arising when every aspect is quantitatively compared (e.g., Koratkar & Blaes 1999; Blaes 2007; Lawrence 2012; Antonucci 2015). Some problems affect accretion theories at a fundamental level, for instance a break in the optical-UV spectra is commonly observed, but it does not scale with mass in the predicted way (e.g., Shang et al. 2005). However, it should not be a particular surprise that a theory involving a static flow and relying on many simplifying assumptions (Section 2) is not able to fully grasp all the observational properties of what is almost certainly a very dynamic and chaotic system. We will discuss this issue in more details in Chapter 3, see in particular Discussion in Section 3.5.

Some other complications are merely observational, the first barrier being that space observatories are needed to observe UV and X-ray radiation, which is where the inner radii of

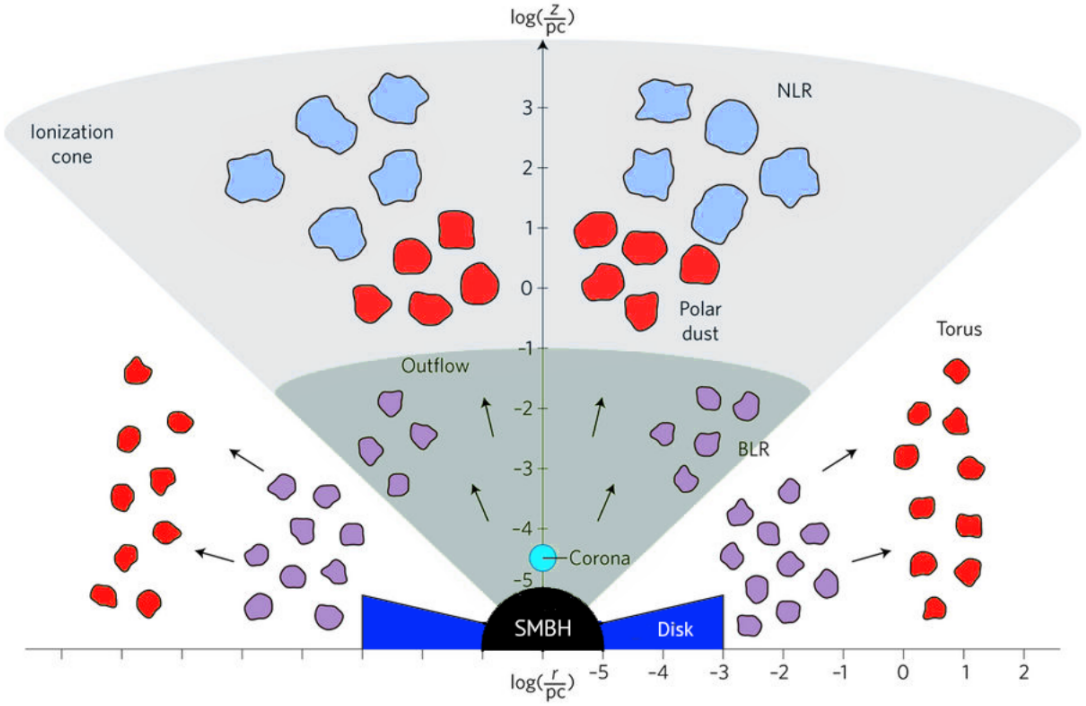

Figure 1.4: Schematic and simplistic representation of an AGN model and its different components (Section 1.3.1). The disk, X-ray corona, and nuclear obscurer are coloured with the same coding of Figure 1.3. Reported from Ramos Almeida & Ricci (2017); Hickox & Alexander (2018).

the accretion flow emit. Moreover, the continuum emission of the accretion disk is contaminated by narrow and broad emission lines (Seyfert 1943; Schmidt 1963) or severely absorbed (Hickox & Alexander 2018) by circum-disk material (Ramos Almeida & Ricci 2017) and/or the host galaxy itself (e.g., Buchner & Bauer 2017). The presence of broadened atomic emission lines, attributed to high-velocity motion of gas near the SMBH, was inferred since the discovery of QSOs (Schmidt 1963). It was soon realised that the disk emission photo-ionises this gas (Davidson 1972; Davidson & Netzer 1979), the so-called 'broad-line region' (BLR), which also responds after some delay to the continuum variability (Cherepashchuk & Lyutyi 1973; Eilek et al. 1973; Osterbrock et al. 1976; Tohline & Osterbrock 1976; Boksenberg & Netzer 1977). By monitoring how fast the BLR responds after the continuum (in a few days, e.g., Grier et al. 2012) we infer that it must be relatively small and close to the SMBH, namely around scales of hundreds to thousands r_g (e.g. Figure 1.4); and that this gas is dense, so that the recombination time is shorter than the light travel time from the nucleus (e.g., Osterbrock et al. 1976; Tohline & Osterbrock 1976; Boksenberg & Netzer 1977; Antonucci & Cohen 1983). Results from this technique, called 'Reverberation Mapping' (Blandford & McKee 1982), suggest the BLR dynamics is dominated by the central mass and it is a viable way to infer it, albeit with some complications (Davidson & Netzer 1979; Marconi et al. 2008; Shen et al. 2008; Shen 2013). However, the exact details of the BLR structure, kinematics and formation are still to be

fully grasped (Czerny 2019). Regarding the structure, a rotating disk-like geometry for the BLR was soon suggested (e.g., Wills & Browne 1986; Eracleous & Halpern 1994; Vestergaard et al. 2000; Jarvis & McLure 2006). The strongest evidence was eventually brought by the Gravity Collaboration (Gravity Collaboration et al. 2017), which observed a BLR consistent with a thick disk perpendicular to the jet axis of QSO 3C 273 (Gravity Collaboration et al. 2018), once again first of the QSO class, and confirmed these results with two other sources shortly after (Gravity Collaboration et al. 2020a; GRAVITY Collaboration et al. 2021).

Furthermore, the obscuration of the emission of the disk (e.g., Kishimoto et al. 2008) and X-ray corona (Ramos Almeida & Ricci 2017; Buchner et al. 2019), as well as the almost ubiquitous infrared emission (Barvainis 1987; Netzer 2015) argue for the existence of additional obscuring material, which is usually referred to as infrared or dusty 'torus' for historical reasons (Antonucci 1993; Netzer 2015). This material is still within the gravitational influence of the SMBH and could be considered as a smooth continuation of the outer region of the BLR and the disk (Baskin & Laor 2018; Naddaf et al. 2021), where dust grains can form and are not sublimated (e.g. Figure 1.4). This clumpy and dusty material with a large and luminosity-dependent covering fraction (Barvainis 1987; Ramos Almeida & Ricci 2017) is responsible for obscuring the disk continuum and reprocessing it into IR emission with a peak around $\approx 10 - 50\,\mu$m (Pier & Krolik 1992; Nenkova et al. 2008; Schartmann et al. 2008; García-Burillo et al. 2016). More insights on the spatial structure and kinematics of this dusty obscurer have been recently obtained with ALMA (e.g., García-Burillo et al. 2016) and Gravity (Gravity Collaboration et al. 2020b,c). Narrow emission lines (hence the name narrow-line region, NLR) in the optical spectra of AGN are more ubiquitous than broad ones (Seyfert 1943), they are not obscured by the nuclear obscurer (e.g., Antonucci & Miller 1985; Ramos Almeida & Ricci 2017) and do not respond to the continuum variability (Antonucci & Cohen 1983). Hence it is believed that they are farther away (e.g. Figure 1.4) and less dense (Boksenberg & Netzer 1977), also due to the presence of 'forbidden' lines. The NLR dynamics is influenced by the galaxy bulge rather then the central mass (e.g., Ho 2009), although their spatial distribution ($\approx 10 - 10^4$ pc from the BH; Chen et al. 2019) is also shaped by the behaviour of the inner nuclear system (e.g., Capetti et al. 1996).

Since the first AGN X-ray surveys were performed (e.g. Elvis et al. 1978; Turner & Pounds 1989), the need for an additional spectral component to extend the cold-disk's $\lesssim$keV temperatures was evident. This so-called X-ray corona (e.g. Liang & Price 1977; Galeev et al. 1979) is considered as a hot ($\sim 10^9$ K), optically thin ($\tau \lesssim 1$) plasma up-scattering the disk photons via thermal Comptonisation (Haardt & Maraschi 1991, 1993; Haardt et al. 1994; Stern et al. 1995). The proximity of the corona to the central black hole was immediately suggested by its strong and fast variability (e.g. McHardy 1989) and by the presence of reflection signatures (Lightman & White 1988; Pounds et al. 1990; Nandra et al. 1991; Williams et al. 1992; Tanaka et al. 1995), but in-depth information regarding its geometry and formation mechanism is still lacking. The geometry can be constrained via the observation of X-ray reverberation lags (Fabian et al. 2009; De Marco et al. 2013; Uttley et al. 2014; Fabian et al. 2017), that seem to show a, possibly non-static, corona extending vertically and radially over the underlying disk for a few and a few tens of gravitational radii, respectively (Wilkins et al. 2016). The compactness of the corona and the origin of the X-rays close to the black hole ($\lesssim$ tens of r_g) also appear to be confirmed by micro-lensing results (e.g. Mosquera et al. 2013; Reis & Miller 2013). Even if in AGN an

additional warm component is sometimes needed to fit the softest X-rays (i.e. the 'soft-excess'; Petrucci et al. 2018; Kubota & Done 2018, and references therein), the X-ray corona is considered analogous to the one in XRBs (Section 1.2). As a matter of fact, X-ray emission from the corona is ubiquitous in accreting compact objects and does not depend obviously on M_{BH}. Despite this remains unexplained at a fundamental level, the inferred coronal temperatures are within the range defined by virial values ($k_B T \sim GM_{BH}m/R$) for electrons ($m = m_e$) and protons ($m = m_p$) around a BH (Gilfanov & Merloni 2014), which are independent from the black hole mass M_{BH} at a given distance (which is $\propto M_{BH}$).

A minority of AGN ($\lessapprox 1 - 10\%$; Kellermann et al. 1989; Padovani 2011) also emit strong radio emission (e.g. Figure 1.3) with a variety of spectral slopes and morphology (e.g., Padovani et al. 2017, for a review). The main game-changer is the presence in these sources of a relativistic jet, with the dominant emission process in the radio band being synchrotron. In the most (energetically) extreme cases in which the jet is pointing along the line of sight (merely a geometric effect), AGN are called blazars. Their SED is completely altered due to relativistic beaming (Fossati et al. 1998; Abdo et al. 2010; Ghisellini et al. 2010, 2017; Padovani et al. 2017) with respect to non-jetted AGN or even jetted AGN for which however the angle between jet axis and observer is larger than $\approx 10^\circ - 15^\circ$ and beaming effects become negligible (Dermer 1995; Sbarrato et al. 2015).

1.3.1.1 X-ray to optical-UV diagnostics in AGN

In Chapter 3 we will focus on X-ray and optical-UV observations of AGN rather than on the full SED (e.g. Figure 1.3) and here we expand more on the topic. As a matter of fact, X-ray to optical-UV energetics were soon understood to be key to study the disk-corona accretion flow in AGN (e.g., Tananbaum et al. 1979). After half a century, much effort is still being put into trying to shed light on the physics of the disk-corona system (see Blaes 2014) and this will continue with global 3D radiation-MHD simulations (e.g. Jiang et al. 2019b), that are now approaching sub-Eddington flows as well (Jiang et al. 2019a). However, the gap between simulations and observations in AGN needs to be bridged and simplified but physically-motivated analytic prescriptions still represent a powerful tool to explain the observed multi-wavelength scaling relations, and this will be our approach in Chapter 3.

Observationally, the increase in quality and quantity of available AGN X-ray-to-UV data from large samples can provide insightful diagnostics, more easily approachable than simulations. The smoking gun of the disk-corona interplay in radiatively efficient AGN is given by the non linear correlation observed between the 2 keV and 2500Å monochromatic luminosities (e.g., Vignali et al. 2003; Strateva et al. 2005; Steffen et al. 2006; Young et al. 2009; Lusso et al. 2010; Lusso & Risaliti 2016, and references therein), that persists throughout the common observed X-ray and optical-UV bands (Jin et al. 2012). Despite the possible differences arising from different sample selections and linear regression techniques, most observations point towards a $\log L_X - \log L_{UV}$ correlation with a slope ≈ 0.6, a dispersion that can be as small as $\sigma \approx 0.2$ dex (Lusso & Risaliti 2016; Chiaraluce et al. 2018). Since such a tight correlation has no apparent redshift dependency, some cosmographic studies paved the way for quasars as standard candles (Risaliti & Lusso 2015, 2019), in what has recently become a rejuvenated research

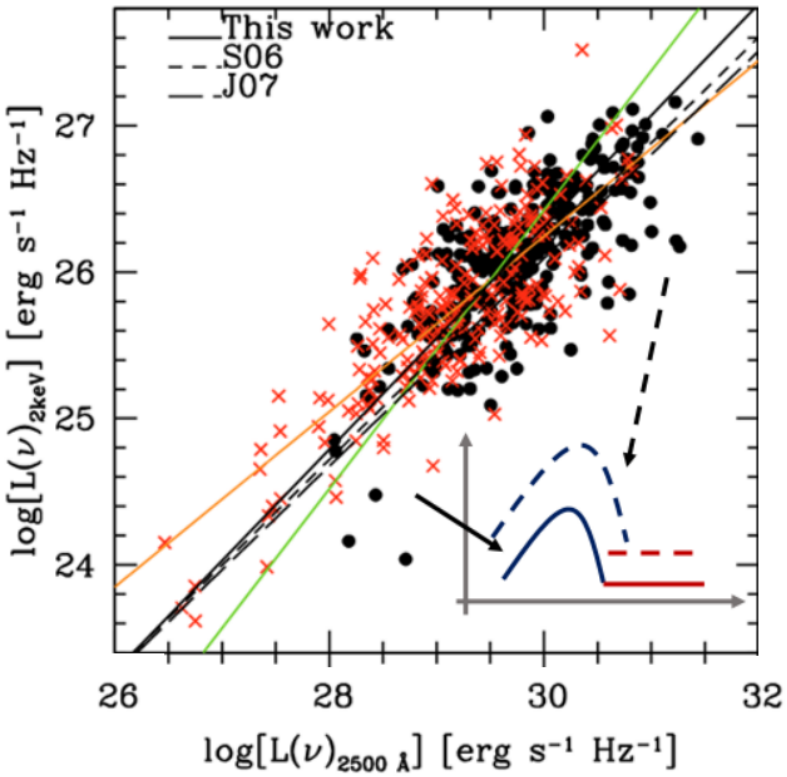

Figure 1.5: Observed relation between the 2 keV and 2500Å monochromatic luminosities in X-ray selected AGN, adapted from Lusso et al. (2010). An inset graphic was added to highlight that moving from the bottom left (SED with solid lines) to the top right (SED with dashed lines) of the relation, since the slope is smaller than one in log space, the disk emission increases more relative to the corona emission.

field (Risaliti & Lusso 2019; Melia 2019; Khadka & Ratra 2020; Lusso et al. 2019; Yang et al. 2020; Velten & Gomes 2020; Zheng et al. 2020). Furthermore, the slope of the $\log L_X - \log L_{UV}$, being smaller than unity, indicates that from lowly to highly accreting AGN, the disk emission increases more than the corona emission (e.g., Kelly et al. 2008) with crucial implications for the physics governing the coupled disk-corona system. We show an example of this in Fig. 1.5, where the inset shows a sketch of the AGN disk-corona SED changing with overall luminosity of the system. However, a solid and conclusive theoretical explanation, for what is one of the most studied multi-wavelength observables in AGN, is still lacking and we will tackle this in Chapter 3.

1.3.2 Spoon-feeding of supermassive black holes

Most of SMBHs do not actively accrete from a rich gaseous reservoir (Bongiorno et al. 2012, 2016; Georgakakis et al. 2017; Aird et al. 2017) and are in fact overall inactive or hidden behind the host galaxy's curtains. Some of them are brought to our attention when they suddenly

brighten up when a stellar object ventures too close, as in the case of TDEs (Hills 1975; Rees 1988). TDEs are stars or stellar objects which are ripped apart by the tidal forces of the SMBH and spoon-feed it. They are usually observed[2] in X-rays, UV and optical (e.g., Komossa 2015; van Velzen et al. 2020; Saxton et al. 2020), as well as in radio, occasionally (Alexander et al. 2020). Radiation is produced by a new-born compact accretion flow fed by a good fraction of the stellar material and TDE flares fade on the timescale of months to years (Komossa 2015; van Velzen et al. 2021). The inferred rate is of the order of $\sim 2-3\times10^{-5}$ yr^{-1} per galaxy (van Velzen & Farrar 2014; Khabibullin & Sazonov 2014), but some of them might be hidden among AGN populations (Merloni et al. 2015). Moreover, during these events also the emission of GW is expected (Kobayashi et al. 2004; Guillochon et al. 2009; Toscani et al. 2020), which is of particular interest for the planned or proposed next generation of GW detectors: the Laser Interferometer Space Antenna (LISA; Amaro-Seoane et al. 2017), TianQin (Luo et al. 2016), the DECI-hertz inteferometer GW Observatory (Sato et al. 2009) and the Big bang observatory (Harry et al. 2006). However, for LISA only a handful of events is predicted (e.g., Pfister et al. 2021). A related class of events would be the so-called extreme mass ratio inspirals (EMRI; Amaro-Seoane et al. 2007; Babak et al. 2017; Wang et al. 2019b), broadly defined as a stellar-mass compact object in-spiralling into a SMBH, for which however an electromagnetic counterpart was not yet observed (but see Chapter 5 for a possibility).

1.4 Intermediate-mass black holes

Objects in the mass range in between stellar-mass and super-massive black holes ($M_{BH} \sim 100$ – few$\times10^5\ M_\odot$) constitute what we call intermediate mass black holes (IMBHs; Greene et al. 2020, for a recent review). This mass regime is poorly probed and constrained, with some concrete evidence of black holes existing around $M_{BH} \approx 10^5\ M_\odot$ and some hints around $M_{BH} \approx 10^4\ M_\odot$ (Greene et al. 2020), while GWs are starting to scratch the low-mass end of IMBHs ($M_{BH} \sim 80-160\ M_\odot$ Abbott et al. 2019, 2020; Abbott et al. 2020). We focus here on a subset of IMBHs search methods which are relevant for this Thesis work, namely on those based on accretion signatures from galactic nuclei. IMBH candidates can be searched for via optical spectroscopy of low-mass galaxies (e.g., Filippenko & Ho 2003; Barth et al. 2004; Greene & Ho 2007; Liu et al. 2018a), a method which however unveils only the brightest end (close to L_{edd}) of the putative population and relies on the presence of broad-lines, which for fainter sources might be absent (Elitzur & Ho 2009), or hidden. Instead, in X-rays the contrast between nuclear and non-nuclear emission at a given luminosity is larger with respect to the optical (e.g., Gilfanov & Merloni 2014), allowing us to dig deeper into the low accretion rate/luminosity range. Hence, some other IMBH candidates were searched for in X-ray nuclei of low-mass galaxies (e.g., Desroches & Ho 2009; She et al. 2017a,b; Gallo & Sesana 2019) or via X-ray variability (e.g., Kamizasa et al. 2012; Ho & Kim 2016). IMBHs can be also revealed when they suddenly become accreting via TDEs (e.g., Wevers et al. 2017; van Velzen 2018), but, again, there is likely strong observational overlap with the low-mass faint end of the AGN population (e.g., Merloni et al. 2015).

[2]Refer to https://tde.space/ for a lively updated list.

1.5 Mass-invariant scaling relations

An intriguing and long-standing (e.g., White et al. 1984) question exists as to whether the accretion flow around BHs is similar among masses ($m = M_{BH}/M_{\odot}$) that are orders of magnitude apart, ranging from XRBs (Section 1.2) to AGN (Section 1.3.1). There is evidence that the phenomenology of how BHs accrete matter is indeed somewhat analogous (e.g. Ruan et al. 2019a) between AGN and XRBs, suggesting that they lack not only 'hair' (Ruffini & Wheeler 1971) but also diversity in dining habits. What is yet to be established is the extent of this analogy between supermassive and stellar BHs and the impact of a different matter reservoir (i.e. density, temperature, ionisation, and consequently pressure support) and surrounding environment (i.e. a single star with respect to the centre of a galaxy) on the physical processes behind the observed phenomenology.

The description of the accretion flow structure around BHs is typically simplified (more details in Section 2) with a more (e.g. Shakura & Sunyaev 1973; Pringle 1981) or less (e.g. Narayan & Yi 1994) radiatively efficient disk with an X-ray corona (Galeev et al. 1979; Haardt & Maraschi 1991; Svensson & Zdziarski 1994) and, possibly, a relativistic jet (Mirabel & Rodríguez 1994; Fender 2001; Blandford et al. 2019). Similarities or scale-invariant relations between XRBs and AGN have always been sought after, and they were found, for example, in the break of the power spectrum and hence in the X-ray variability amplitudes (e.g. Uttley et al. 2002; McHardy et al. 2004; Uttley & McHardy 2005; McHardy et al. 2006), or by exploring possible correlations among observational proxies of these different spectral components (Heinz & Sunyaev 2003).

In particular, evidence of a common accretion–ejection paradigm emerged from the so-called 'fundamental plane' (Merloni et al. 2003), which connects radio and X-ray luminosity with the BH mass (Fig. 1.6): low-luminosity AGN (which are found to be more radio loud[3], e.g. Ho 2002; Sikora et al. 2007) were shown to be scaled-up hard-state XRBs (e.g. Belloni & Motta 2016) with a prominent jet component and a radiatively inefficient accretion flow (Merloni et al. 2003; Falcke et al. 2004) while moderately and high-accreting AGN (both combined spanning $\lambda_{edd} \simeq 0.02-1$; e.g. Noda & Done 2018; Vahdat Motlagh et al. 2019) were connected to XRBs in the soft states (SS; Maccarone et al. 2003) and soft-intermediate states (SIMS; Sobolewska et al. 2009). This picture has been confirmed and expanded by Körding et al. (2006) to include the analogy between hard-intermediate states in XRBs, where there is some disk contribution but the radio jet is present as well, and radiatively efficient radio-loud quasars; and by analysing AGN caught in the (very slow) act of transitioning between these states (e.g. Marchesini et al. 2004; Marecki & Swoboda 2011). Further, this scale-invariant accretion-ejection scenario has been proven to hold using simultaneous UV and X-ray observations of AGN (Svoboda et al. 2017).

Moreover, the disk–corona connection has been studied for decades in AGN (Section 1.3.1.1) and it was also tested in XRBs with an analogous proxy (Sobolewska et al. 2009) and more recently even in TDEs (Wevers 2020; Wevers et al. 2021). A comparison between XRBs and AGN was then performed using the observable disk/corona ratio (see Fig. 1.7), which is now more generically referred to as 'corona loudness' because in XRBs both components emit in X-

[3]See (Hao et al. 2014) for a few definitions of radio loudness, usually defined as a flux or luminosity ratio between the radio with respect to another band.

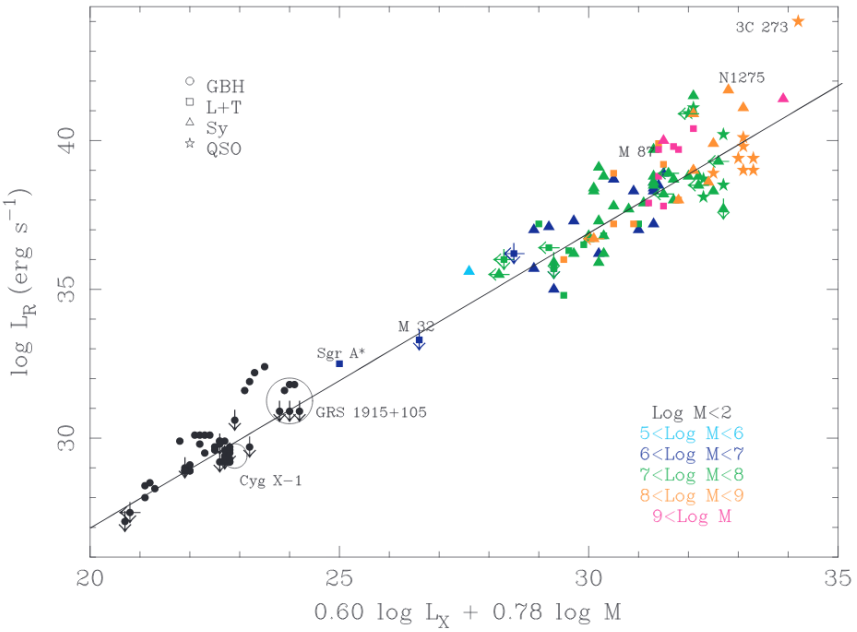

Figure 1.6: Fundamental plane of black hole activity from Merloni et al. (2003). It shows the connection between the inner accretion flow (via X-rays) and the jet emission (via radio) in stellar mass and supermassive black holes in their radiatively inefficient accretion regimes.

rays. This was shown by Sobolewska et al. (2011), who produced a set of simulated AGN spectral states scaling the luminosity ($\propto M_{BH}$) and the disk temperature ($\propto M_{BH}^{-1/4}$) from a selection of the XRB GROJ1655-40 spectral fits. These latter authors predicted an inversion of the corona loudness trend with λ_{edd} to occur at low luminosity ($\lambda_{edd} \lessapprox 0.01$), approximately where the accretion flow is thought to become radiatively inefficient (e.g. Maccarone 2003; Noda & Done 2018). This transition was recently confirmed by Ruan et al. (2019a) using changing-look (or state) AGN (or quasars, here referred to as CLAGN; e.g., LaMassa et al. 2015; MacLeod et al. 2016; Trakhtenbrot et al. 2019) in their shut-down phase. However, with respect to the better-studied radio-to-X-ray correlations (e.g., Merloni et al. 2003; Falcke et al. 2004), one should be careful in testing the inefficient mode of accretion with UV-to-X-ray proxies in AGN, particularly if the sources become radiatively inefficient and faint, reducing the contrast with respect to the host galaxy's emission (e.g., Gilfanov & Merloni 2014). Moreover, despite the supposedly more secure observational proxies, there are still puzzling differences between the two source classes when they are bright and radiatively efficient: for instance, there is much more scatter in corona loudness, for a given disk emission, for XRBs compared to AGN (see Fig. 1.7), which is contrary to the expectations since AGN are contaminated by different masses, inclinations, spins to name a few. The study of these differences will be indeed the aim of Chapter 4.

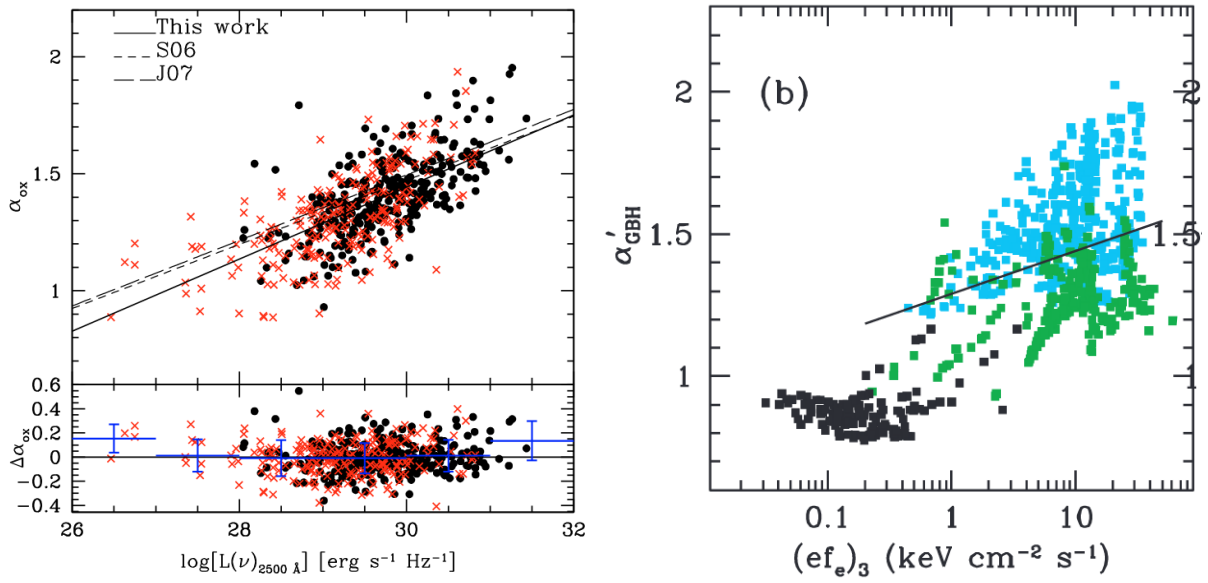

Figure 1.7: Both panels show the X-ray corona loudness as a function of a proxy for the accretion disk luminosity. On the *left*, it is parametrised as α_{OX} versus rest-frame 2500Å monochromatic luminosity for a sample of X-ray selected AGN, from Lusso et al. (2010). On the *right*, it is parametrised for XRBs with an analogous flux ratio named α_{GBH} versus the 3 keV monochromatic luminosity, from Sobolewska et al. (2009). Here hard states are shown in black, soft-intermediate and soft states in green and cyan. A qualitative comparison should be made between AGN data and XRB in the soft and soft-intermediate state.

1.6 Outline of this Thesis

The most luminous persistent or transient phenomena in the Universe are related to accretion onto black holes. This is a multi-scale issue that goes from the BH event horizon to much larger distances, up to galaxies outskirts for super-massive black holes sitting at their centres. In this Thesis we focus on multi-wavelength observations of black holes of different sizes. Particular attention is given to X-ray observations, starting from the most typical manifestations of accreting super-massive and stellar-mass BHs, and going to newly discovered X-ray phenomena which are yet to be understood.

We compare observational properties of black holes across the mass scale as well as with the predictions from accretion theories. Therefore we start in Chapter 2 with the basics of accretion disk models with X-ray coronae.

In Chapter 3 we test our disk-corona model against one of the most studied multi-wavelength observed relation in AGN, which highlights the presence of a mechanism regulating the energetic interaction between the accretion disk and the X-ray corona. The aim is to infer a theoretical explanation for this observed connection, which is still missing despite its large use.

In Chapter 4 we compare observed disk-coronae properties of XRBs and AGN to test whether the two source classes behave similarly in their radiatively-efficient phases. The aim is to provide

additional insights on whether accretion properties scale with the black hole mass and how.

In Chapter 5 we report the discovery of yet another interesting manifestation of accretion onto black holes, discovered with the recently launched eROSITA X-ray telescope. Our work unveils the sudden awakening of two super-massive black holes in previously quiescent galaxy nuclei, providing a new feasible way to study these new phenomena.

Chapter 2

Brief overview of accretion disk-corona models

Motivated by the discovery of QSOs (Schmidt 1963) and by the first results of the newborn discipline of X-ray astronomy (Pounds 2014, for a review), the importance of laying the fundamentals of an accretion theory started to be highlighted (Salpeter 1964; Zel'dovich 1964). Accretion of matter onto SMBHs was soon proposed as the efficient mechanism needed to power QSOs and Seyfert galaxies, via a 'flat disk' differentially rotating and liberating energy via 'friction' (Lynden-Bell 1969). Within a few years the basis of accretion disk theory was laid down (Pringle & Rees 1972; Shakura & Sunyaev 1973; Pringle et al. 1973; Novikov & Thorne 1973). Perhaps the most crucial (and still debated) problem is our understanding of the nature of viscosity and hence angular momentum transport in accretion disks (e.g., Papaloizou & Lin 1995; Blaes 2014). In Shakura & Sunyaev (1973) our ignorance was cleverly parametrized with the so-called $\alpha-$prescription, a proportionality constant which locally connects the stress between annuli with the disk's thermal pressure. On the one hand, this allowed us to compare theory with observations (e.g. see Chapter 3). On the other hand, the prescription lacks physical motivation, and hence raises important issues for accretion theorists (e.g., Blaes 2014). A viable option for the origin of angular momentum transport in accretion disks was provided in the nineties by Balbus & Hawley in the form of the so-called magneto-rotational instability (MRI; Balbus & Hawley 1991, 1992; Hawley & Balbus 1991, 1992). This series of papers showed that a weak vertical magnetic field is unstable in a rotating fluid with angular velocity increasing inward (see also, e.g., Velikhov, 1959; Chandrasekhar 1960). The usual example employed to simplify this magnetic instability is to picture two masses (m_1 and m_2) in such a flow and connected by a spring (which here mimics the magnetic force): a small inward displacement for, e.g., m_1, would bring it in a slightly closer orbit with slightly higher angular velocity; the pull of the spring would induce a retarding torque on m_1, angular momentum is lost and m_1 moves further in; conversely m_2, in a slightly slower outer orbit, would perceive a positive torque, gain angular momentum and move further out leading to a runaway instability (e.g., Balbus & Hawley 1991).

In this Chapter we outline the basics of accretion disk prescriptions for black holes accreting via a geometrically-thin and optically-thick disk, which makes them radiatively-efficient and luminous, as argued above from the observational point of view. This is the putative mode of

accretion in a small, well-defined range of mass accretion rates, from about a few percent to about Eddington. Despite this regime being probably where most of the known luminous sources lie (e.g., the SDSS AGN and QSOs; Ahumada et al. 2020), it may not be representative of how fainter (e.g., Narayan & Yi 1994) and brighter (e.g., Abramowicz et al. 1988) sources would accrete. In the former case, matter in a optically-thin geometrically-thick accretion flow cools much more slowly than viscous timescales and it is dominated by radial advection of matter onto the central black hole, due to the overall low accretion rate and gas density (Ichimaru 1977; Narayan & Yi 1994, 1995; Narayan & McClintock 2008). In the latter case advection is still important, albeit because the accretion rate, gas density and opacity are so high that radiation is trapped (Abramowicz et al. 1988; Sądowski 2009). We refer the reader to the above mentioned papers for more details on radiatively-inefficient accretion models. The focus of this Thesis, and therefore of this Chapter, is instead on the radiatively-efficient end of accretion across the black hole mass scale.

2.1 Basics of thin accretion disk models

Here, we present the basics of geometrically-thin optically-thick accretion disk models, based on standard prescriptions from seminal papers and reviews (e.g., Shakura & Sunyaev 1973; Pringle 1981; Frank et al. 2002). We define the central black hole mas to be M_{BH} with ISCO at $R_0 = 3R_S$, where $R_S = 2r_g = 2GM_{BH}/c^2$. An annulus between R and $R + \Delta R$ has the following mass and angular momentum:

$$\begin{cases} M_{ann} = 2\pi R \Delta R \Sigma \\ L_{ann} = 2\pi R \Delta R \Sigma R^2 \Omega \end{cases} \tag{2.1}$$

Here $\Sigma(R,t) = \int_{-\infty}^{+\infty} \rho dz = 2H\rho$ is the surface density, where H is half of the vertical scale-height of the disk. In the steady-disk approximation there is no time variation of the disk properties (e.g. density), as the inflow rate of gas from the outer edge of the flow is assumed equal to that of the gas lost into the black hole. The angular velocity is assumed Keplerian, $\Omega = \Omega_K = \left(GM_{BH}/R^3\right)^{1/2}$.

The inward net flow (with a radial velocity v_r) of the mass through the annulus is:

$$\frac{\partial}{\partial t} M_{ann} = 2\pi R\Sigma(R) v_r(R) - 2\pi(R+\Delta R)\Sigma(R+\Delta R) v_r(R+\Delta R) \tag{2.2}$$

$$\simeq -2\pi \Delta R \frac{\partial}{\partial R}(R\Sigma v_r)$$

leading to the conservation equation:

$$R\frac{\partial \Sigma}{\partial t} = \frac{\partial}{\partial R}(R\Sigma v_r) \tag{2.3}$$

For a steady disk $\partial\Sigma/\partial t = 0$ then $R\Sigma v_r =$ constant, resulting in the well-known relation for the constant inward mass accretion rate:

$$\dot{M} = 2\pi R\Sigma v_r = 4\pi R H \rho v_r \tag{2.4}$$

The same balance can be computed for the angular momentum, in which also the viscous torque $\mathcal{T}$ has to be included:

$$\begin{aligned}\frac{\partial}{\partial t}L_{ann} &= 2\pi R\Sigma(R)v_r(R)R^2\Omega \\ -2\pi(R+\Delta R)\Sigma(R+\Delta R)v_r(R+\Delta R)(R+\Delta R)^2\Omega(R+\Delta R) &\\ +\mathcal{T}(R+\Delta R)-\mathcal{T}(R) &\\ \simeq -2\pi\Delta R\frac{\partial}{\partial R}(R\Sigma v_r R^2\Omega)+\frac{\partial\mathcal{T}}{\partial R}\Delta R &\end{aligned} \tag{2.5}$$

leading to the conservation equation:

$$R\frac{\partial(\Sigma l)}{\partial t}+\frac{\partial}{\partial R}(R\Sigma v_r l)=\frac{1}{2\pi}\frac{\partial\mathcal{T}}{\partial R} \tag{2.6}$$

where $l = R^2\Omega$ is the specific angular momentum.

For a steady disk, this reduces to:

$$2\pi R\Sigma v_r l = \mathcal{T} + C \tag{2.7}$$

where C is given by the initial condition, i.e. the by angular momentum transfer at the inner radius $C = \dot{M}R_0^2\Omega_0 = \dot{M}(GMR_0)^{1/2}$, when we assume that no shear occurs.

Equations 2.4 and 2.7 together determine the first important relation for the disk model:

$$\dot{M}(GM_{BH}R)^{1/2}J(R) = \mathcal{T} \tag{2.8}$$

where $J(R) = 1 - \sqrt{R_0/R}$ describes the no-torque boundary condition at $R = R_0$, for which Eq. 2.8 reduces to $\mathcal{T} = 0$.

The viscous torque is:

$$\mathcal{T} = R\mathcal{F}_{visc} = R\tau_{r\phi}2\pi R2H = 4\pi R^2 H\tau_{r\phi} \tag{2.9}$$

where the viscous force is expressed in terms of $\tau_{r\phi}$, i.e. the vertically averaged stress acting as a pressure on the vertical surface that separates two consecutive annuli at R.

From energy conservation, neglecting any inward advection in a steady disk, the local internal dissipation is balanced by the local vertical cooling ($Q_+ = Q_-$), for the whole disk. We can compute the dissipation rate per unit area of gravitational energy due to viscosity (e.g. for the upper half of the disk):

$$Q_+ = \frac{1}{2}R2H\tau_{r\phi}\frac{d\Omega}{dR} \tag{2.10}$$

Using Eq. 2.8 and 2.9, this leads to the famous equation:

$$Q_+ = \frac{3GM_{BH}\dot{M}}{8\pi R^3}J(R) \tag{2.11}$$

Moreover, hydrostatic equilibrium in the z direction gives:

$$\frac{\partial P}{\partial z} = -\frac{GM_{BH}\rho z}{R^3} \tag{2.12}$$

Then, setting $\partial P/\partial z \sim P/H$ and $z \sim H$, we obtain a relation for the disk scaleheight:

$$H = \frac{c_s}{\Omega} \tag{2.13}$$

where $c_s = \sqrt{P/\rho}$ is the isothermal sound speed. Using this last relation in Eq. 2.10, an alternative form for Q_+ is obtained:

$$Q_+ = \frac{3}{2} c_s \tau_{r\phi} \tag{2.14}$$

Then, from the total energy balance we obtain a second key equation for the thin disk model:

$$\frac{3}{2} c_s \tau_{r\phi} = \frac{3GM_{BH}\dot{M}}{8\pi R^3} J(R) \tag{2.15}$$

These are the key ingredients of a steady geometrically-thin and optically-thick accretion disk with no advection of mass, for which the assumption of efficient cooling of the viscous heating at each annulus (i.e., $Q_+ = Q_-$) is valid. They were simply obtained from the conservation equations of the mass, angular momentum and energy. Now we add another energetic component, an X-ray emitting corona, which was not present in the original prescriptions (e.g., Shakura & Sunyaev 1973; Pringle 1981). The presence of this component was first considered in detail in the nineties (Haardt & Maraschi 1991; Svensson & Zdziarski 1994, e.g.,), by postulating that a constant fraction of the heating power which is not dissipated within the disk but instead into a hot corona. This fractional power f dissipated in the corona (e.g., Stella & Rosner 1984; Di Matteo 1998), modifies the vertical radiative diffusion balance. The radiative flux emerging from the disk surface is accordingly reduced by a factor $(1 - f)$:

$$Q_- = F_d = (1 - f) Q_+ = (1 - f) \frac{3GM_{BH}\dot{M}}{8\pi R^3} J(R) \tag{2.16}$$

where F_d can be computed from the vertical radiative transfer:

$$F_d = c \frac{dP_{rad}}{d\tau} = \frac{c}{k\rho} \frac{dP_{rad}}{dz} = \frac{acT^4}{3k\rho H} \tag{2.17}$$

2.2 A self-consistently coupled disk-corona model

We now outline a modified version of the disk-corona model introduced in the previous Section, which maintains some of the same prescriptions while adding some more complexities. This model, presented in Arcodia et al. (2019) is largely based on that put forward by Merloni (2003) (see also Merloni & Fabian 2002, 2003), in which the standard conservation equations of a geometrically-thin and optically-thick accretion disk are self-consistently coupled with the X-ray corona, parametrised as:

$$f = \frac{Q_{cor}}{Q_+} \tag{2.18}$$

with $Q_{cor} = v_D P_{mag}$, where v_D is the vertical drift velocity (taken proportional to the Alfvén speed via an order-unity constant b), $P_{mag} = B^2/8\pi$ is the magnetic pressure and Q_+ is given by Eq. 2.14.

This is based on the simplifying assumption that the corona is magnetically-dominated with an efficient saturation of the magnetic field that is amplified via the magneto-rotational instability (Chandrasekhar 1960; Balbus & Hawley 1991, 1992; Hawley & Balbus 1991, 1992) and extending buoyantly upward (and downward) from the denser parts of the disk (Galeev et al. 1979; Stella & Rosner 1984; Di Matteo 1998; Merloni & Fabian 2002; Blackman & Pessah 2009). Magnetic reconnection can then keep the corona hot (e.g., Liu et al. 2002; Uzdensky & Goodman 2008; Uzdensky 2016; Beloborodov 2017; Werner et al. 2019; Ripperda et al. 2019). This scenario seems to be supported by magneto-hydrodynamic (MHD) simulations (Miller & Stone 2000; Uzdensky 2013; Bai & Stone 2013; Jiang et al. 2014; Salvesen et al. 2016; Kadowaki et al. 2018), although only qualitative comparisons with observations have been made so far (however, see Schnittman et al. 2013). We will assume here that f indeed represents a simplified but motivated representation of this complex MHD problem.

The stress tensor $\tau_{r\phi}$ in Eq. 2.14 can be assumed to be dominated by Maxwell stresses (e.g., Hawley et al. 1995; Sano et al. 2004; Minoshima et al. 2015), from which we can write $\tau_{r\phi} = k_0 P_{mag}$, with k_0 being a constant of order unity (Hawley et al. 1995). To build a self-consistent solution to the accretion problem, we need to relate the stress tensor (via the magnetic pressure) with local quantities that are familiar in standard analytical models. This is where the standard Shakura & Sunyaev $\alpha-$prescription comes into play. It assumes a stress proportional to the total (gas plus radiation) pressure P_{tot} (Shakura & Sunyaev 1973) via α. It is not, however, the only possibility. Within the same basic framework modifications to the viscosity law can be introduced depending on whether the viscous stress is assumed to scale with the above standard prescription (Shakura & Sunyaev 1973), with the gas pressure alone (Lightman & Eardley 1974; Sakimoto & Coroniti 1981; Meyer & Meyer-Hofmeister 1982; Stella & Rosner 1984) or with the geometric mean of the two (Ichimaru 1977; Taam & Lin 1984; Burm 1985; Merloni 2003). It was soon found that the first prescription leads to thermally and viscously unstable disks in the radiation-pressure dominated regions (see Section 2.2.2), with the first instability acting on shorter timescales (Lightman & Eardley 1974; Shakura & Sunyaev 1976; Pringle 1976). This encouraged many authors (Hoshi 1985; Szuszkiewicz 1990; Merloni & Nayakshin 2006; Grzędzielski et al. 2017b) to generalize the viscosity law. Recent simulations (albeit of gas-pressure dominated disks only) indeed seem to show a power-law stress-pressure relation (Sano et al. 2004; Minoshima et al. 2015; Ross et al. 2016; Shadmehri et al. 2018), with an index varying from zero to one according to the different assumptions.

Here, we address this issue generalising the model reported in Merloni (2003) with:

$$P_{mag} = \alpha_0 P_{gas}^{\mu} P_{tot}^{1-\mu} \tag{2.19}$$

where α_0 is a constant, generally not equal to $\alpha_{SS73} = P_{mag}/P_{tot}$. This behavior is physically motivated by the MRI prescriptions, as its growth rate was shown to depend on the P_{rad}-to-P_{gas} ratio (Blaes & Socrates 2001; Turner et al. 2002) influencing the level of the magnetic field saturation. Equations 2.18 and 2.19 provide the closure equation of the disk-corona system:

$$f = \sqrt{\frac{2\alpha_0}{k_1^2}} \left(1 + \frac{P_{rad}}{P_{gas}}\right)^{-\mu/2} \tag{2.20}$$

where $k_1 = 3k_0/2b$ gathers the model's uncertainties in an order unity factor (Merloni 2003). Its exact value only affects f at its maximum $\left(f_{max} = \sqrt{2\alpha_0/k_1^2}\right)$ and not the nature of what is described throughout this Thesis work.

The model is then completed with the equation of state:

$$P_{tot} = P_{gas} + P_{rad} = \frac{2\rho k_B T}{m_p} + \frac{aT^4}{3} \tag{2.21}$$

using molecular weight 1/2 for ionized hydrogen, and with a density- and temperature-dependent opacity $\kappa = \kappa(\rho, T)$. We compute the opacity value self-consistently with the density and temperature at each radius with an iterative process, using as reference stellar opacity tables (at solar metallicity) from the Opacity Project (Seaton et al. 1994; Seaton 1995). This is important since the density and temperature regimes relevant for AGN disks imply opacities that can be significantly different from the electron scattering value (e.g., see Jiang et al. 2016; Czerny et al. 2016; Grzędzielski et al. 2017a).

Further, we assume a downward component of the X-ray emission (η) and a disk albedo (a_{disk}), which modifies the disk equations from the usual $(1 - f)$ factor (Svensson & Zdziarski 1994; Merloni 2003) to:

$$1 - \tilde{f} = 1 - f\left[1 - \eta(1 - a_{disk})\right] \tag{2.22}$$

We here adopt $\eta = 0.55$ and $a_{disk} = 0.1$, respectively (e.g., Haardt & Maraschi 1993). These are typical values for anisotropic Comptonization in a plane-parallel geometry, although more generally the product $\eta(1 - a_{disk})$ can be a function of the X-ray spectral form, e.g. as measured by the continuum photon index Γ (Beloborodov 1999; Malzac et al. 2001) and of the disk's vertical structure.

For simplicity, we adopt dimensionless units for the black hole mass, the accretion rate, the radial distance and the vertical scale-height:

$$\begin{cases} m = M_{BH}/M_\odot \\ \dot{m} = \frac{\dot{M}}{L_{edd}/\epsilon_0 c^2} = m^{-1} \frac{\dot{M}\epsilon_0 c^2}{1.3\times10^{38}} \\ r = R/R_s = m^{-1} Rc^2/2GM_\odot \\ h = H/R_s = m^{-1} Hc^2/2GM_\odot \end{cases} \tag{2.23}$$

We now report the model equations for h, mid-plane ρ (g cm^{-3}), P (dyn cm^{-2}) and T (K), with the closure equation for f, obtained solving the system of equations 2.8, 2.15, 2.16, 2.21, 2.19 and 2.20. Once m, $\dot{m}$, α_0, μ and f_{max} are fixed, one can numerically solve the closure equations for f at each radius (see the last rows of Eq. 2.24 and 2.26, respectively). The left-hand side is equal to P_{rad}/P_{gas} and we can infer the correct regime and compute the main physical quantities at the mid-plane (ρ, P, T, κ).

The general solutions for the radiation pressure dominated regions are:

$$\rho = \rho_{const}\, k_0^{-\frac{4}{\mu+4}} [\alpha_0 m]^{-\frac{4}{\mu+4}} [\dot{m}J(r)]^{\frac{2(3\mu-4)}{\mu+4}} r^{\frac{3(2-3\mu)}{\mu+4}} (1-\tilde{f})^{\frac{6(\mu-2)}{\mu+4}}$$

$$T = T_{const}\, k_0^{-\frac{1}{\mu+4}} [\alpha_0 m]^{-\frac{1}{\mu+4}} [\dot{m}J(r)]^{\frac{2\mu}{\mu+4}} r^{\frac{3(2\mu^2-3\mu-2)}{2(2-\mu)(\mu+4)}} (1-\tilde{f})^{\frac{2\mu-1}{\mu+4}}$$

$$h = 9.14\, \dot{m}J(r)(1-\tilde{f})$$

$$P = P_{const}\, k_0^{-\frac{4}{\mu+4}} [\alpha_0 m]^{-\frac{4}{\mu+4}} [\dot{m}J(r)]^{\frac{8\mu}{\mu+4}} r^{\frac{6(2\mu^2-3\mu-2)}{(2-\mu)(\mu+4)}} (1-\tilde{f})^{\frac{4(2\mu-1)}{\mu+4}}$$

$$\frac{P_{rad}}{P_{gas}} = \frac{(2\alpha_0)^{1/\mu} - k_1^{2/\mu} f^{2/\mu}}{k_1^{2/\mu} f^{2/\mu}} = \tilde{C}\, k_0^{\frac{1}{\mu+4}} [\alpha_0 m]^{\frac{1}{\mu+4}} [\dot{m}J(r)]^{\frac{8}{\mu+4}} r^{-\frac{21}{2(\mu+4)}} (1-\tilde{f})^{\frac{9}{\mu+4}} \tag{2.24}$$

The constant values depend on μ as follows:

$$\rho_{const} = \left(4.7\times10^{-68}\right)^{\frac{6(2-\mu)}{\mu+4}} \left(5.5\times10^{48}\right)^{\frac{2(8-3\mu)}{\mu+4}} \left(1.5\times10^{-23}\right)^{\frac{4\mu}{\mu+4}}$$

$$T_{const} = \left(4.7\times10^{-68}\right)^{\frac{1-2\mu}{\mu+4}} \left(5.5\times10^{48}\right)^{\frac{2(\mu^2-3\mu+2)}{(2-\mu)(\mu+4)}} \left(1.5\times10^{-23}\right)^{\frac{\mu}{\mu+4}}$$

$$P_{const} = \frac{a}{3} \left(4.7\times10^{-68}\right)^{\frac{4(1-2\mu)}{\mu+4}} \left(5.5\times10^{48}\right)^{\frac{8(\mu^2-3\mu+2)}{(2-\mu)(\mu+4)}} \left(1.5\times10^{-23}\right)^{\frac{4\mu}{\mu+4}}$$

$$\tilde{C} = \left(4.7\times10^{-68}\right)^{\frac{-9}{\mu+4}} \left(5.5\times10^{48}\right)^{\frac{-10}{\mu+4}} \left(1.5\times10^{-23}\right)^{\frac{4}{\mu+4}} \tag{2.25}$$

We note that in the gas pressure dominated region, we include also a numerical factor ξ in Eq. 2.16 to parametrize the possible difference in the vertical density profile in this region (Merloni 2001, PhD thesis). The solutions for gas pressure dominated regions, that are independent on the choice of μ in the viscosity law, are:

$$\rho = 14.44\; k_0^{-3/5} \xi^{3/10} [\alpha_0 m]^{-7/10} [\dot{m}J(r)]^{2/5} r^{-33/20} (1-\tilde{f})^{-3/10}$$

$$T = 8.01\times10^{8}\; k_0^{-4/15} \xi^{-1/5} [\alpha_0 m]^{-1/5} [\dot{m}J(r)]^{2/5} r^{-9/10} (1-\tilde{f})^{1/5}$$

$$h = 1.72 \times 10^{-2}\ k_0^{-7/15} \xi^{-1/10} [\alpha_0 m]^{-1/10} [\dot{m} J(r)]^{1/5} r^{21/20} (1 - \tilde{f})^{1/10}$$

$$P = 1.91 \times 10^{8}\ k_0^{-13/15} \xi^{1/10} [\alpha_0 m]^{-9/10} [\dot{m} J(r)]^{4/5} r^{-51/20} (1 - \tilde{f})^{-1/10}$$

$$\frac{P_{rad}}{P_{gas}} = \frac{4\alpha_0^2 - k_1^4 f^4}{k_1^4 f^4} = 5.41 \times 10^2\, k_0^{-1/5} \xi^{-9/10} [\alpha_0 m]^{1/10} [\dot{m} J(r)]^{4/5} r^{-21/20} (1 - \tilde{f})^{9/10} \tag{2.26}$$

The value of ξ can be obtained by studying the continuity of all the above quantities at the boundary between the radiation pressure- to the gas pressure-dominated regions. It corresponds to $\xi \simeq 1.00 k_0^{-1/3}$.

These equations are reported in the Newtonian approximation (however, see Merloni & Fabian 2003, for a relativistic derivation of the $\mu = 0.5$ case). A constant efficiency of $\epsilon_0 = 0.057$, typical of non-rotating black holes, and a no-torque inner boundary condition ($J(r) = 1 - \sqrt{r_0/r}$, with $r_0 = 3$ and $r_{out} = 2000$) are here adopted.

To compute the effective temperature at the surface from the mid-plane profile we assume:

$$T_{eff}(r) \propto \frac{T(r)}{\tau(r)^{1/4}} \tag{2.27}$$

where we take $\tau(r) = h(r)\,\rho(r)\,\kappa(r)$. From this, monochromatic optical-UV luminosities for the disk can be then easily computed in the multi-color blackbody approximation:

$$L_\nu(r) = 2\pi r \Delta r\, \pi\, B_\nu(T_{eff}) \tag{2.28}$$

where $\pi\, B_\nu(T_{eff})$ is the black-body flux at the frequency ν and temperature $T_{eff}(r)$.

In this framework, the energy per unit area dissipated in the corona at each radius is $Q_{cor}(r) = f(r) Q_+(r)$, although only a fraction $(1 - \eta)$ will contribute to what is observed as X-ray emission:

$$L_{X,tot}(r) = 2\pi r \Delta r\, (1 - \eta)\, f(r) Q_+(r) \tag{2.29}$$

Here, we did not include the component reflected by the disk (given by the fraction $f\,\eta\,a_{disk}$), so that we could easily extrapolate at each radius a monochromatic value, for instance L_{2keV}, assuming a simple power-law spectrum within $\nu_i = 0.1\,\mathrm{keV}$ and $\nu_f = 100\,\mathrm{keV}$:

$$L_{X,tot} = K \int_{\nu_i}^{\nu_f} \nu^{-(\Gamma-1)}\, d\nu$$

$$L_{2keV} = K\, {\nu_{2\,keV}}^{-(\Gamma-1)} = L_{X,tot}\, (2 - \Gamma)\, \frac{{\nu_{2\,keV}}^{1-\Gamma}}{{\nu_f}^{2-\Gamma} - {\nu_i}^{2-\Gamma}} \tag{2.30}$$

The model relies on the assumption that a plane-parallel geometry holds for bright radiatively-efficient sources, lying in a sweet spot of accretion rate ($\dot{m}$ approximately from a few percent to Eddington). Hence, the accretion disk extends down to the ISCO and no advection is included.

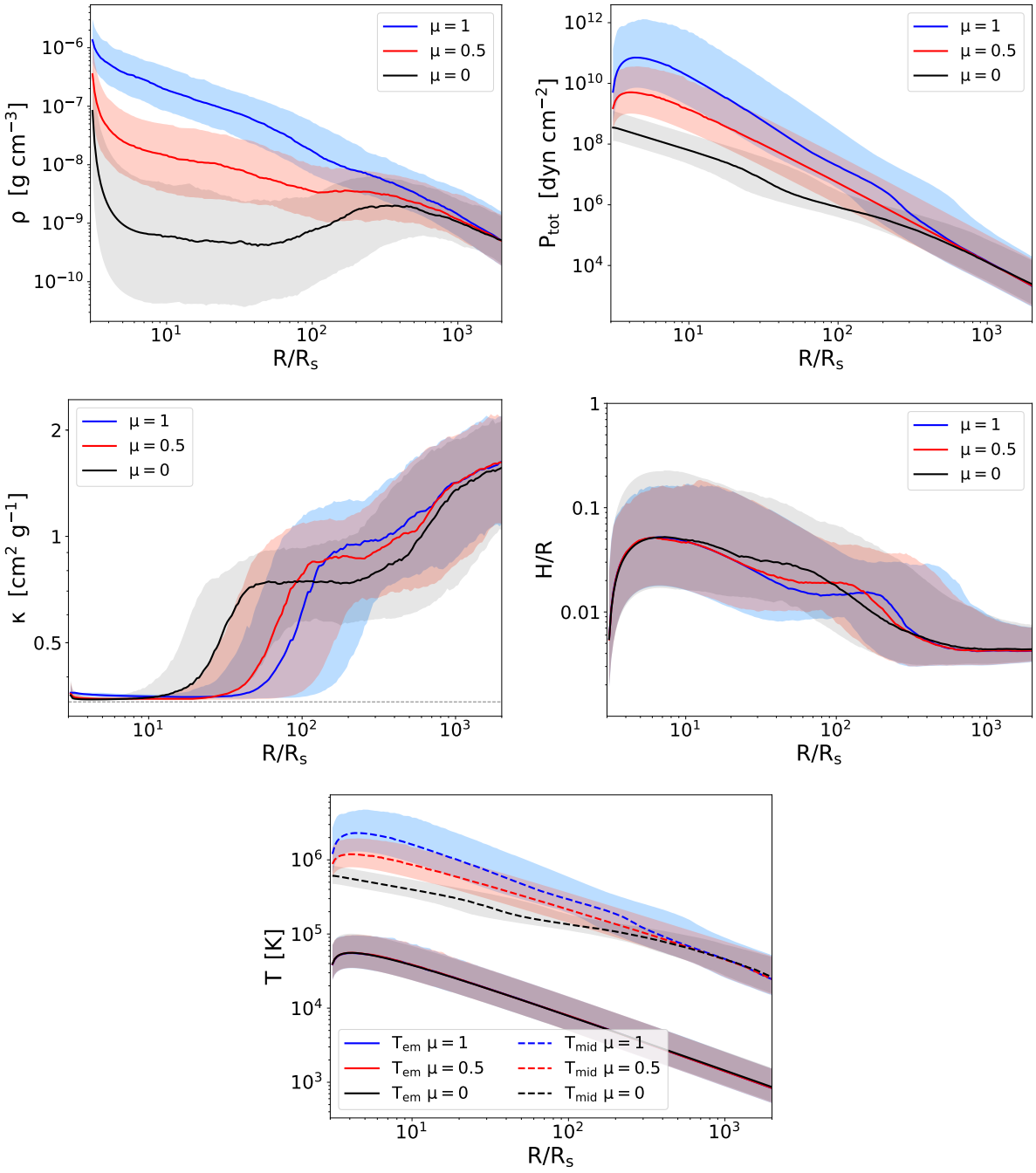

Figure 2.1: Radial profiles for the mid-plane ρ (top left), P_{tot} (gas plus radiation, top right), κ (middle left), h/r (middle right) and T (both mid-plane and surface, bottom). They are obtained with fixed $\alpha_0 = 0.02$ and $f_{max} = 0.5$. Colors are coded according to the choice of the viscosity law: stress proportional to P_{tot} ($P_{gas} + P_{rad}$, $\mu = 0$, black), to P_{gas} ($\mu = 1$, blue), or the geometric mean of the two ($\mu = 0.5$, red). The continuous solid, or solid-dashed, lines represent the median profiles, with the related shaded areas showing the 16th and 84th percentiles, the scatter due to the range of sources (i.e. m and $\dot{m}$) modelled.

Table 2.1: Summary of recurring model parameters.

Parameter	Definition	Comments
μ	Regulates the scaling between the magnetic stress and the thermal pressure: $\tau_{r\phi} \propto P_{mag} = \alpha_0 P_{gas}^{\mu} P_{tot}^{1-\mu}$	$\mu = 0 \rightarrow P_{mag} \propto P_{tot}$ $\mu = 0.5 \rightarrow P_{mag} \propto \sqrt{P_{gas} P_{tot}}$ $\mu = 1 \rightarrow P_{mag} \propto P_{gas}$
α_0	Proportionality constant of the viscosity law (see above)	Small influence on $L_X - L_{UV}$
$f(r)$	Fraction of accretion power dissipated in the corona	$f(r)$ for $\mu \neq 0$
f_{max}	Maximum value of $f(r)$	Impacts the normalization of the $L_X - L_{UV}$
$<f>$	Mean value of a $f(r)$ profile	Real fraction of bolometric power emitted by the corona
η	Fraction of f emitted downward back to the disk	Exact value impacts the normalization of the $L_X - L_{UV}$

A scripted version of the model outlined in this Section is publicly available online[1]. A summary of the recurring model parameters is shown in Table 2.1. In Fig. 2.1 we report examples of radial profiles for ρ, P_{tot}, κ, h/r, T_{mid} and T_{eff}. Similar examples for f and L_{2keV} are shown in Fig. 2.2 (see Section 2.2.1 for more details). A range of m, $\dot{m}$ and Γ was chosen, representative of the typical observed distributions (see Section 3.3), specifically with median values (and related 16th and 84th percentiles) of $\log m = 8.7^{+0.4}_{-0.5}$, $\dot{m} = 0.2^{+0.5}_{-0.1}$ and $\Gamma = 2.1 \pm 0.1$. Once f_{max} is fixed, the dominant variance within the models is given by the choice of the viscosity law (μ), while α_0 plays a minor role. This is shown in Fig. 2.3, where profiles for f and L_{2keV} show little difference in varying α_0 from 0.02 to 0.2.

2.2.1 Radial profiles for f and L_{2keV}

In Fig. 2.2 we show as an example radial profiles of f and L_{2keV}, obtained by solving Eq. 2.24, 2.26, 2.29 and 2.30. For simplicity, we fixed $\alpha_0 = 0.02$ and $f_{max} = 0.5$ and used the three values of μ corresponding to the most-used viscosity laws, namely $\mu = 0$, 0.5 and 1, for P_{mag} proportional to P_{tot}, $\sqrt{P_{gas} P_{tot}}$ and P_{gas}, respectively. Other values of μ would support the same picture with analogous intermediate profiles.

The solid (or solid-dashed) lines represent the median profiles, with the corresponding shaded areas showing the 16th and 84th percentiles of the distribution. The top panel of Fig. 2.2 shows how the standard $\mu = 0$ law (Shakura & Sunyaev 1973) results in $f = f_{max}$ at all radii (Svensson & Zdziarski 1994), whereas alternative viscosity laws (e.g., $\mu = 0.5$ and $\mu = 1$) show non-constant

[1] https://github.com/rarcodia/DiskCoronasim

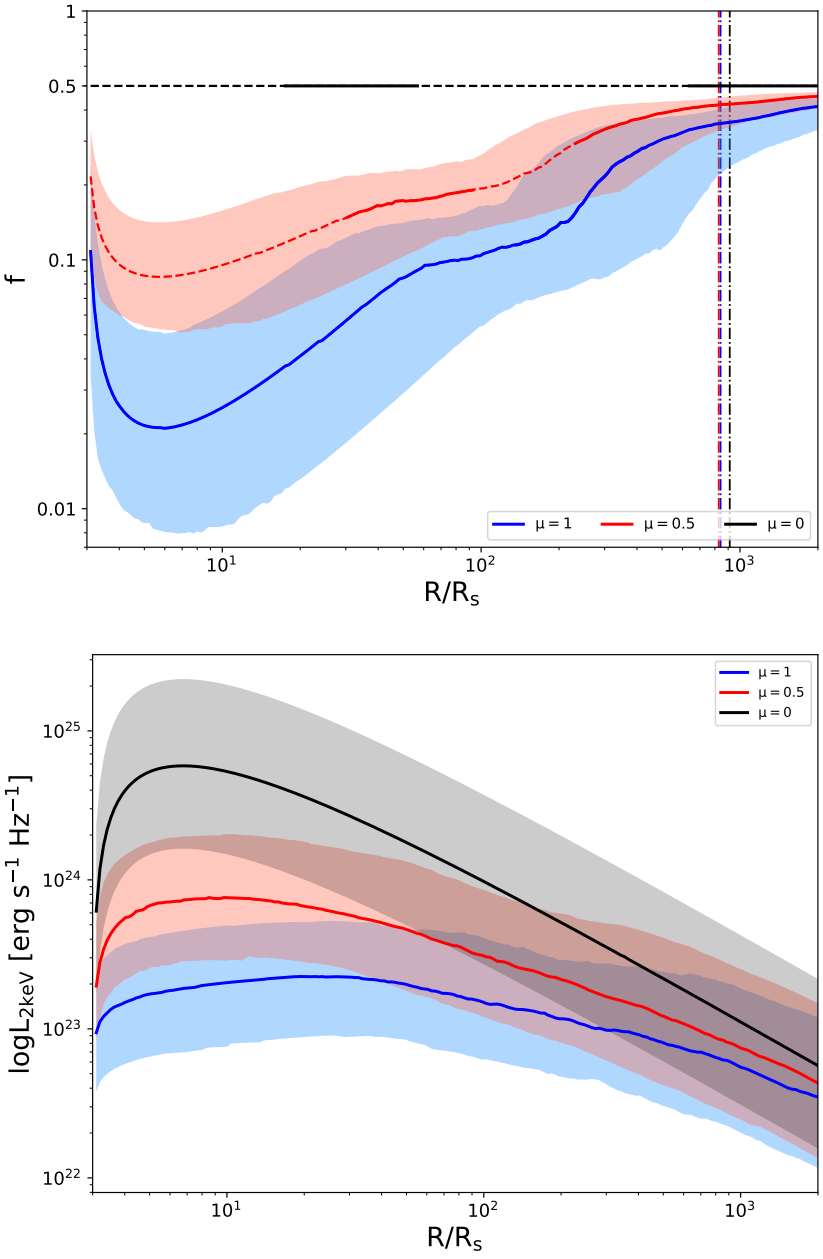

Figure 2.2: Same as Fig. 2.1, but with radial profiles for the fraction f of power dissipated in the corona (top panel) and L_{2keV} (bottom panel). L_{2keV} is proportional to the product of f and Q_+ (the accretion power per unit area). As Q_+ has very similar profiles across all models, those systems for which f is smaller produce weaker coronae in the central part. In the top panel, a solid line for the median f-profile represents (thermally) stable regions of the median test source, whereas a dashed line highlights the instability regions. The vertical dot-dashed lines show instead where the median transition radius, from P_{rad}- to P_{gas}-dominated regions, lies. Refer to Section 2.2.1 for details.

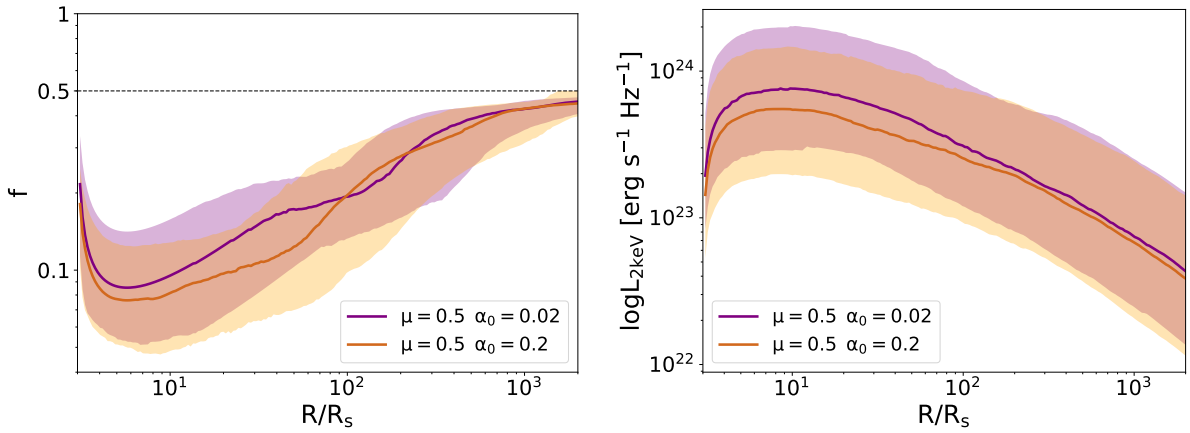

Figure 2.3: Same as in Fig. 2.1 and 2.2. Here, we highlight the (minor) influence on varying α_0 from 0.02 (purple) to 0.2 (orange) in f- and L_{2keV}-profiles.

radial profiles for f: in the latter cases, the fraction of power dissipated in the corona is smaller in the regions strongly dominated by P_{rad}. As was shown in Merloni (2003) in particular for the $\mu = 0.5$ scaling, the higher suppression of the growth rate in P_{rad}-dominated regions of the disk leads to such damped f-profiles. This directly influences the strength of the coronal emission, as L_{2keV} is proportional (through $L_{X,tot}$) to the product of f and Q_+: Q_+ peaks at small radii in a very similar way across all models, therefore the ones with deeper f-profiles show flatter L_{2keV} radial profiles and, hence, weaker coronae (bottom panel of Fig. 2.2). The exact shape of $f(r)$ also affects the strength of the disk emission since the two are self-consistently coupled (see Eq. 2.22).

We can also define the mean value of each $f(r)$ profile (i.e. for each combination of m, $\dot{m}$ and Γ):

$$<f>_i = \frac{\int f_i(r)\, Q_{+,i}(r)\, 2\pi r\, dr}{\int Q_{+,i}(r)\, 2\pi r\, dr} \tag{2.31}$$

that is also a function of μ, α_0 and f_{max}. Then, the mean value can be computed for the median f profiles in the examples in the top panel of Fig. 2.2: $<f>_{median} = 0.5$, 0.13 or 0.05, for $\mu = 0$, 0.5 and 1, respectively. Of course, within such a model the exact value of $<f>_{median}$ depends on its normalization f_{max}, that is a free parameter in the model only bound to be < 1. Nonetheless, simply from looking at $<f>_{median}$ as a function of μ (and from Fig. 2.2) we can see how, for the same set of inputs (e.g., m, $\dot{m}$), the different accretion prescriptions relate to the output corona luminosities: in a nutshell, going from $\mu = 0$ to $\mu = 1$ produces lower $<f>_{median}$, thus weaker coronae.

Changing μ also affects the scatter in the radial profiles, from being absent in $\mu = 0$ to increase with μ for $\mu \neq 0$ (see Fig. 2.2). The spread on a given $f(r)$ curve is due to the scatter in m, $\dot{m}$ and Γ, with the major factor being the accretion rate (e.g., see Fig. 1 in Merloni 2003). Crucially, $<f>$ decreases with increasing $\dot{m}$ for all $\mu \neq 0$ models. This points in the same direction as the evidence for the X-ray bolometric correction (that is proportional to the inverse of f) increasing

with the accretion rate (e.g. Wang et al. 2004; Vasudevan & Fabian 2007, 2009; Lusso et al. 2010; Young et al. 2010). This relation between $<f>$ and $\dot{m}$ also has important implications for our model predictions about the physical mechanisms behind the observed $L_X - L_{UV}$ relationship, which will be the focus of Chapter 3.

2.2.2 Local thermal stability

The type of thermal-viscous instability in accertion flows introduced for quiescent XRBs (Section 1.2) is thought to happen only at low luminosities, where the temperatures are such that there can be a large jump in opacity due to Hydrogen ionization. They are therefore not usually thought to be relevant for AGN (Hameury et al. 2009). However, since the early days of accretion theories other scenarios in which thermal (Pringle 1976) and viscous (Lightman & Eardley 1974) instabilities might occur were considered, in particular in regions where the radiation pressure, P_{rad}, dominates the pressure support ($P \approx P_{rad}$).

Thermal instability in such a regime can occur since a small increase in temperature leads to a large increase in pressure ($P \propto T^4$) hence stress ($\propto P$ for $\mu = 0$, i.e. as in the standard prescription). Therefore a large increase in heating (Q_+) is not balanced by an equal increase in cooling (Q_-) since there is no consistent decrease in opacity with increasing temperature ($k \approx k_{es}$, and hence is not a function of temperature). Viscous instability instead is thought to occur when there is an increase in mass accretion (also for instance due to thermal instability itself in a given annulus) which depletes a region of the disk faster than it can be viscously replenished by outer annuli, leading to fragmentation (e.g., Lightman & Eardley 1974). Since in a thin disk ($H/R << 1$, e.g. Fig. 2.1) the thermal timescale ($\tau_{\rm th} \sim \alpha^{-1}(GM_{\rm BH}/R^3)^{-1/2}$) is much shorter than the viscous one ($\tau_{\rm visc} \sim (H/R)^{-2}\tau_{\rm th}$), the former is usually studied. Observations, on the other hand, argue against this type of instability being common, since XRBs in their soft state are stable throughout their evolution despite accreting at levels which the theory considers unstable (e.g., Done et al. 2007). Hence the standard stress prescription ($\mu = 0$ in this work) is likely to be incorrect or incomplete, and indeed alternatives were suggested already in the seventies (e.g., Lightman & Eardley 1974, here $\mu = 1$).

Here, we briefly discuss the stability issue for the various adopted viscosity laws. Jiang et al. (2016) showed that the presence of the iron bump in the opacity at $\sim 2 \times 10^5$ K stabilizes the flow in the disk regions around that temperature, where the cooling term has a different dependency and thermal runaway is avoided (Grzędzielski et al. 2017a). In the top panel of Fig. 2.2, a solid median line for the f-profile represents (thermally) stable regions of the median test source, whereas a dashed line highlights the instability regions. The vertical dot-dashed lines show instead where the median transition radius, from P_{rad}- to P_{gas}-dominated regions, lies. This highlights that, for the median test source, the stability region extends also well within P_{rad}-dominated regions of the disk, confirming previous results (Jiang et al. 2016; Grzędzielski et al. 2017a). More quantitatively, we computed the thermal stability balance (e.g. Pringle 1976) for each test source (m, $\dot{m}$) at all radii with varying viscosity laws. The new stability regions in the inner P_{rad}-dominated portions of $\mu = 0$ and $\mu = 0.5$ disks are ubiquitous, but they appear at different radii according to where the disk reaches the temperatures around the iron bump in κ (see also Fig. 2.1). The $\mu = 1$ case, as it is well known (e.g. Lightman & Eardley 1974), is stable

throughout.

2.2.3 Model usage

The disk-corona model described above is publicly available[2]. It is able to compute the luminosity of the accretion disk and the X-ray corona given the observed, or assumed, BH mass, accretion rate, spin and X-ray spectral index of the source. It was extensively used throughout this Thesis work, particularly in Chapter 3 where it was tested against multi-wavelength AGN data.

[2]https://github.com/rarcodia/DiskCoronasim

Chapter 3

The disk-corona interplay in radiatively efficient broad line AGN

The correlation observed between monochromatic X-ray and UV luminosities in radiatively-efficient AGN still lacks a clear theoretical explanation, despite being used for many applications (see Section 1.3.1.1). Such a correlation, with its small intrinsic scatter and its slope that is smaller than unity in log space, represents the compelling evidence that a mechanism regulating the energetic interaction between the accretion disk and the X-ray corona must be in place (Fig. 1.5). In this Chapter, we discuss the use of a self-consistently coupled disk-corona model (Section 2.2) that can identify this regulating mechanism in terms of modified viscosity prescriptions in the accretion disk. We discuss how the model predicts a lower fraction of accretion power dissipated in the corona for higher accretion states. We also present a quantitative observational test of the model using a reference sample of broad-line AGN and modelling the disk-corona emission for each source in the $L_X - L_{UV}$ plane. We used the slope, normalization, and scatter of the observed relation to constrain the parameters of the theoretical model. For non-spinning black holes and static coronae, we find that the accretion prescriptions that match the observed slope of the $L_X - L_{UV}$ relation produce X-rays that are too weak with respect to the normalization of the observed relation. Instead, considering moderately-outflowing Comptonising coronae and/or a more realistic high-spinning black hole population significantly relax the tension between the strength of the observed and modeled X-ray emission, while also predicting very low intrinsic scatter in the $L_X - L_{UV}$ relation. In particular, this latter scenario traces a known selection effect of flux-limited samples that preferentially select high-spinning, hence brighter, sources.

This work was published as Arcodia et al. (2019) in Astronomy & Astrophysics, Volume 628, A135.

3.1 The open question: origin of the $L_X - L_{UV}$

The goal of this work is indeed to test a self-consistently coupled disk-corona model (Section 2.2) against the observed $L_X - L_{UV}$ (see Section 1.3.1.1). Given the existing gap between simulations and observations, we argue that the use of simplified (but motivated) prescriptions still represents

a powerful tool to explain observed disk-corona scaling relations, as it was done with the X-ray photon index (or the X-ray bolometric correction) correlation with the Eddington ratio (Wang et al. 2004; Cao 2009; Liu & Liu 2009; You et al. 2012; Liu et al. 2012, 2016a; Wang et al. 2019a), or with the $\log L_X - \log L_{UV}$ itself (Lusso & Risaliti 2017; Kubota & Done 2018). We here rely uniquely on the $\log L_X - \log L_{UV}$ relation, since monochromatic L_X and L_{UV} values can be directly obtained from spectral fits. Forward modelling monochromatic luminosities circumvents difficulties and issues typical of model comparisons with accretion rate, Eddington ratio or bolometric luminosity estimates (e.g., Richards et al. 2006; Davis & Laor 2011; Slone & Netzer 2012; Krawczyk et al. 2013; Capellupo et al. 2015, 2016; Kilerci Eser & Vestergaard 2018).

We described our disk-corona model in the first Chapter of this Thesis (Section 2.2) and we briefly show its qualitative predictions in Section 3.2. Then, we outline the observational test that we put forward to thoroughly understand the disk-corona interplay in Section 3.3 and we show the results in Section 3.4. Throughout this work, we quote median values with 16th and 84th percentiles unless otherwise stated. As outlined in Section 2.2, we adopt dimensionless units for the black hole mass, the accretion rate, the radial distance and the vertical scale-height.

3.2 Predictions of the disk-corona model on the $L_X - L_{UV}$ relation

Before performing a more quantitative observational test (Section 3.3), we here outline the predictions of our model concerning the disk-corona energetics and the expected impact of our accretion prescription on the $L_X - L_{UV}$.

The schematic illustration in Fig. 3.1 summarizes the qualitative take-home messages of this work. The observed $L_X - L_{UV}$ states that going from a lower to a higher accretion regime, the luminosity of the corona increases less than the disk luminosity, resulting in a slope smaller than one in the log-space. In our model for the disk-corona system, the luminosity outputs are directly modified by the viscosity prescription in the flow, determined by the parameter μ, and by the fraction of accretion power going into the corona, f (see Table 2.1 for a summary on the model parameters). Among all scenarios spanned by these two main unknowns, the qualitative behavior of the accretion disk-corona system, along its radial extent, is similar: higher accretion states have a more powerful disks and coronae, but wider P_{rad}-dominated inner region and, only for modified viscosity prescriptions (i.e. $\mu \neq 0$), lower relative contribution of the corona to the total luminosity (see the upper diagram in Fig. 3.1).

Thus, our model can provide a simple explanation for the observed slope of the L_X-L_{UV} relation, bridging in a simple but effective way the gap between the observed X-to-UV energetics and some aspects of MRI simulations. Changing μ not only affects the disk thermodynamics, but also changes the amount of power carried away by the corona (see Fig. 2.2). A constant radial profile for f (e.g., Svensson & Zdziarski 1994; here $\mu = 0$) would naturally result in a $L_X - L_{UV}$ close to a one-to-one relation. On the contrary, the alternative viscosity prescriptions, that we identify with $\mu \neq 0$, inherently result in a different disk-corona energetic coupling for varying accretion rates: in particular, higher $\dot{m}$ yield more damped $f-$profiles (see also Merloni 2003).

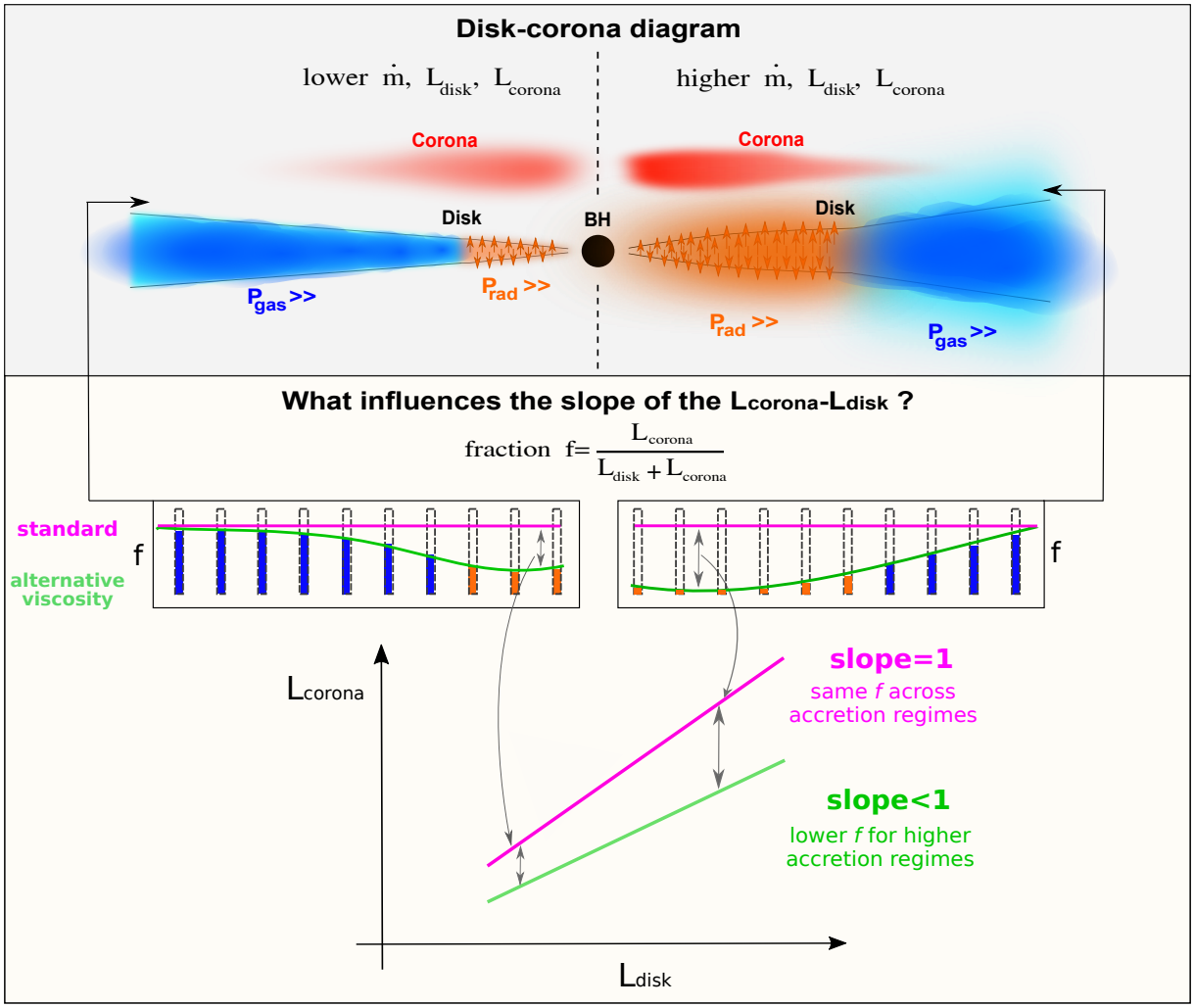

Figure 3.1: Schematic illustration of our model and how it relates to the observed $L_X - L_{UV}$ (see Section 3.2 for an interpretative guide).

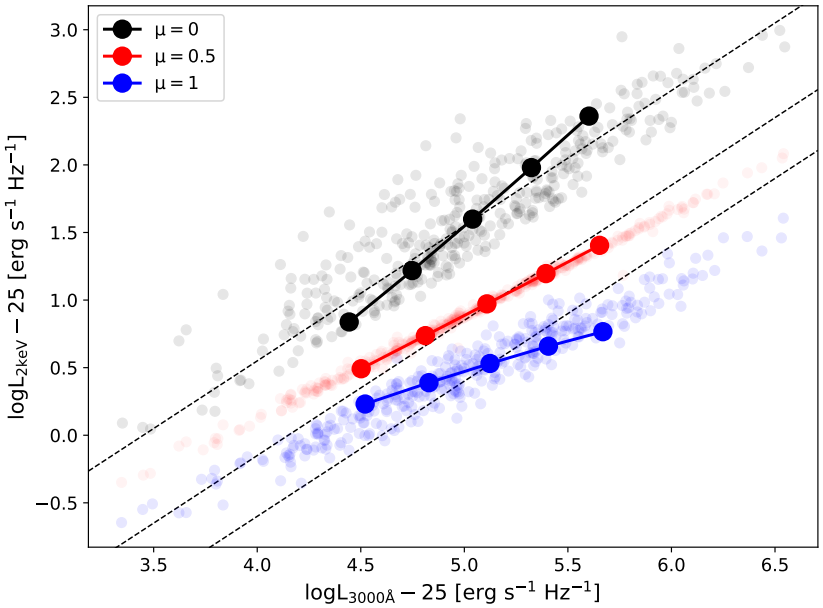

Figure 3.2: Mock $L_X - L_{UV}$ with fixed $f_{max} = 0.5$ and different μ color coded, as in Fig. 2.2. The connected solid points show the trend of a single typical mass ($\log m = 8.7$) with $\dot{m} = 0.03$, 0.07, 0.17, 0.42, 1 (increasing from left to right in L_{UV}). The dashed lines indicate a slope of one. The distributions of transparent points show the mock $L_X - L_{UV}$ for a range of $\log m = 8.7^{+0.4}_{-0.5}$, $\dot{m} = 0.2^{+0.5}_{-0.1}$ and $\Gamma = 2.1 \pm 0.1$, that follows the typically observed objects (see Section 3.3).

In this scenario, the outcome would be a slope of the $L_X - L_{UV}$ that is smaller than one (see the lower diagram in Fig. 3.1).

It is worth stressing that it is only the relative fraction f that is more suppressed in the inner regions of systems with a modified viscosity and not the X-ray emission per se. Regardless the underlying assumption of a plane-parallel geometry for the disk-corona system (see Eq. 2.22), the X-ray emission peaks in the innermost radii (e.g., see the $\mu = 0.5$ case in Fig. 2.2). This will be addressed in details in Section 3.4.1.

Fig. 3.2 shows an example of a mock $L_X - L_{UV}$ from the model realizations, with $f_{max} = 0.5$ and different values of μ as in Fig. 2.2, with the same color coding. For the connected solid points, a single typical mass ($\log m = 8.7$) is adopted, with increasing $\dot{m} = 0.03$, 0.07, 0.17, 0.42, 1 (from left to right in L_{UV}). The relation is linear for a given mass, with the dashed lines indicating a slope of one to guide the eye. As qualitatively shown in the illustrative Fig. 3.1, models where f is constant in radius and in accretion state (black points) yield a slope close to one (even higher for the single mass); instead, alternative viscosity prescriptions (red and blue), that change the disk-corona energetic interplay via $f(r)$, show a flatter slope. The underlying transparent points show the mock $L_X - L_{UV}$ for a distribution of $\log m = 8.7^{+0.4}_{-0.5}$, $\dot{m} = 0.2^{+0.5}_{-0.1}$ and $\Gamma = 2.1 \pm 0.1$, that follows the typically observed objects (see Section 3.3).

3.3 Observational test: modeling the $L_X - L_{UV}$

In the previous section we qualitatively outlined the physical mechanisms identified as the origin of the observed slope smaller than one. A more quantitative test is needed to thoroughly investigate all aspects of the observed $L_X - L_{UV}$, including its normalization and intrinsic scatter. The exact value of the slope given by the models not only depends on the unknowns μ, f_{max} and α_0, but also on the details of the distributions of m, $\dot{m}$, Γ that are adopted for the calculations. Nonetheless, not all combinations of these three parameters are observed, because they do not exist in nature or we are biased against their detection. That is why we select a reference sample of radiatively-efficient broad-line AGN (Section 3.3.1) and model the most likely values for m, $\dot{m}$, Γ for each source individually, based on the available data.

3.3.1 The reference sample of broad-line AGN

We built our reference sample starting from the 1787 AGN within the XMM-XXL north survey (Pierre et al. 2016) identified as broad-line AGN (BLAGN) by the Baryon Oscillation Spectroscopic Survey (BOSS) follow-up (Menzel et al. 2016; Liu et al. 2016b). The X-ray spectral analysis on these sources was performed in Liu et al. (2016b) with the Bayesian X-ray Analysis software (BXA, Buchner et al. 2014), providing N_H values, photon indexes (Γ) and the rest-frame $2-10$ keV intrinsic luminosities ($L_{2-10\,keV}$). Furthermore, single-epoch virial black hole masses (M_{BH}, e.g. Shen et al. 2008) and continuum luminosities (at 1350, 1700, 3000 and 5100 Å) were obtained on the BOSS spectroscopy with a fitting pipeline (Shen & Liu 2012; Liu et al. 2016b). Luminosities were computed in Liu et al. (2016b) assuming $H_0 = 70\,\mathrm{km\ s^{-1}\ Mpc^{-1}}$, $\Omega_m = 0.27$ and $\Omega_\Lambda = 0.73$[1].

Then, we applied some cleaning criteria to avoid, as much as possible, imprecise estimates for the intrinsic (accretion-powered) L_X and L_{UV} and to remain consistent with what is computed by the model. Firstly, among the monochromatic luminosity values available in the optical-UV from Liu et al. (2016b) we adopted $L_{3000\text{Å}}$, obviously inducing a redshift cut in the sample (see Fig. 3.4 in Section 3.3.1). There is no difference in computing $L_{3000\text{Å}}$ or the more standard $L_{2500\text{Å}}$, and Jin et al. (2012) showed compatible correlations between the X-ray luminosity and each wavelength of the optical spectrum, although their coverage starts from 3700Å. We verified a posteriori that this choice does not affect significantly the slope of the $L_X - L_{UV}$ or the conclusions of our work.

Secondly, despite being defined as BLAGN, Liu et al. (2018b) found that a fraction of these sources shows continuum reddening probably due to intervening dust along the line of sight, not accounted for by our model. Liu et al. (2018b) defined a slope parameter α' for the optical-UV continuum, to discern between the reddened sources and the bulk of blue BLAGN at each redshift. The contamination from extinction at $L_{3000\text{Å}}$ was minimized by conservatively selecting sources with $\alpha' < -0.5$ (see Liu et al. 2018b, their Fig. 2).

[1]We will refer to other data throughout the paper and possible discrepancies in luminosities due to different cosmological parameters may occur. Nonetheless, we verified that the biggest difference in luminosity values ($\sim$ 0.01 dex) is obtained assuming a Planck with respect to a WMAP release, while using different releases of the same instrument will have a negligible impact ($\lesssim$ 0.005 dex).

Moreover, the XMM-XXL survey has a typical exposure time of ~ 10 ks per pointing (Pierre et al. 2016; Liu et al. 2016b). Here, the analysis was restricted to sources with at least 10 counts in the EPIC-pn (Strüder et al. 2001) and EPIC-MOS (Turner et al. 2001) cameras on board XMM-Newton (Jansen et al. 2001), to exclude sources with extremely low-quality X-ray spectra.

Then, to exclude data contaminated by X-ray absorption, not accounted for in our modeling, we conservatively selected only sources in which the 84th percentile of the N_H posterior distribution was smaller than $10^{21.5}$ cm^{-2}, a value typically adopted to distinguish X-ray obscured and un-obscured sources (Merloni et al. 2014; see also Della Ceca et al. 2008).

Finally, we take L_{2keV} as reference for the corona emission in the $L_X - L_{UV}$. In the model, we computed mock $L_{X,tot}$ with no reflection, so that we could easily extrapolate L_{2keV} assuming a simple power-law spectrum. However, in Liu et al. (2016b) the reflection component was also included in the calculation of $L_{2-10keV}$, as it is usually observed both in low-z (e.g. Nandra et al. 2007) and high-z (e.g. Baronchelli et al. 2018) spectra (see the average-AGN model in Buchner et al. 2014). Therefore, we consistently excluded from the analysis all the sources with a significant reflection component: given the high errors of the typical $\log R$ fit in Liu et al. (2016b)[2], we included only sources in which the 16th percentile was < -0.2 and the 84th was < 0.5. We note that Liu et al. (2016b) included in the fit also a scattering contribution from ionized material inside the angle of the torus (see Buchner et al. 2014), although the fit normalizations are on the order of 10^{-4} with respect to the main power-law component.

The final cleaned subsample, to which we will refer as XMM-XXL, consists of 379 sources with observed m (with median $\log m = 8.7^{+0.4}_{-0.5}$), $L_{3000\text{Å}}$, Γ (with median $\Gamma = 2.1 \pm 0.1$) and L_{2keV}. In Fig. 3.3 we show the $\log L_X = \widehat{\alpha} + \widehat{\beta} \log L_{UV}$ relation, with the best-fit linear regression given by:

$$\log L_{2keV} - 25 = (-1.25 \pm 0.12) + (0.54 \pm 0.02)\,(\log L_{3000\text{Å}} - 25) \tag{3.1}$$

with intrinsic scatter $\sigma_{intr} = 0.27 \pm 0.01$. Linear regressions in two (or more) dimensions were performed with emcee (Foreman-Mackey et al. 2013), accounting for uncertainties on all variables and an intrinsic scatter using the likelihood provided in D'Agostini (2005). The uncertainty in the independent variable(s) is propagated with the derivative $\partial Y/\partial X$ calculated in X (X_i), equal to the slope coefficient(s) in the linear case (D'Agostini 2003). The slope we measure is slightly flatter than what is quoted in the recent literature (e.g., Lusso & Risaliti 2016), although we did not consider all the possible biases of flux-limited samples. For the main scope of the work presented in this Chapter, it is sufficient to have a reference sample cleaned in accord with the physics described within the model. Therefore the sample described above will be used throughout this Chapter.

We now briefly check the possible impact of the XMM-XXL flux limit on our reference sample. In Fig. 3.4 we show the distribution of L_{2keV} (left panel) and $L_{3000\text{Å}}$ (right panel) in the luminosity-redshift plane of the 379 sources (red and blue respectively), with respect to the parent sample of BLAGN from Liu et al. (2016b), shown in black. The $L_X - L_{UV}$ slope of this reference sample is 0.54 ± 0.02, from Eq. 3.1. This is incompatibly flatter than the values quoted in the recent literature, namely 0.64 ± 0.02 (Lusso & Risaliti 2016) or 0.63 ± 0.02 (Lusso & Risaliti 2017). The cleaning criteria applied above were aimed to exclude low-quality data and to be

[2] R is the ratio of the normalization of the reflection component with respect to the power-law component.

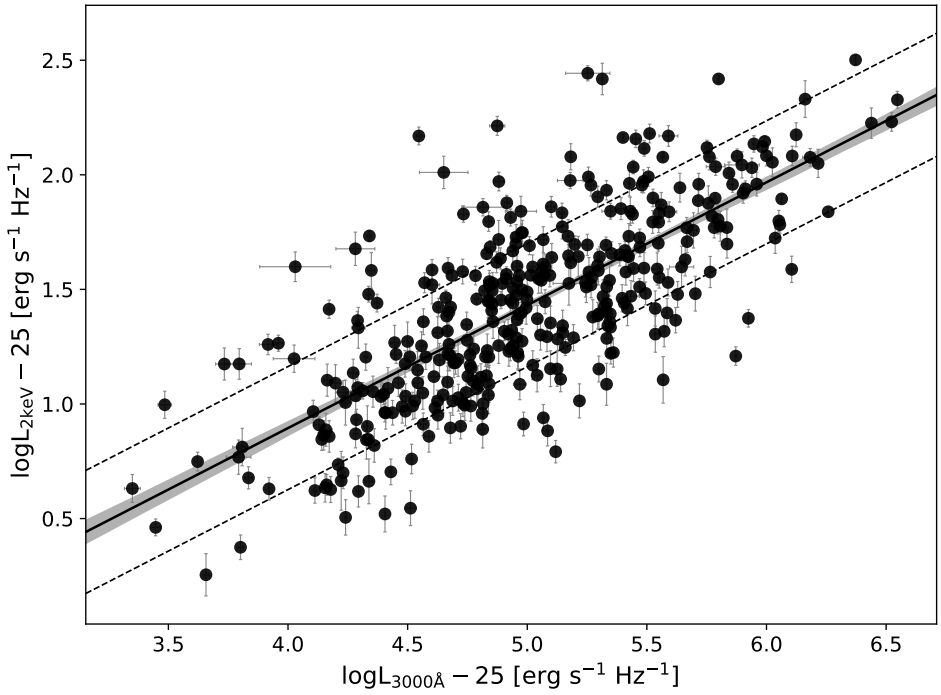

Figure 3.3: $L_X - L_{UV}$ relation of the 379 bright BLAGN of XMM-XXL. Monochromatic luminosity values are here scaled by 25 dex, to ease the comparison with recent works. The solid black line is the median regression line obtained with emcee, with the corresponding 16th and 84th percentiles represented with the shaded gray area. The dashed black lines show the intrinsic scatter around the median relation.

consistent with the model, while in the above-mentioned literature the possible biases of flux-limited samples were treated carefully in order to reliably use quasars for cosmology (Risaliti & Lusso 2019).

We investigated whether this inconsistency in the slope would be bridged restricting the analysis to the brightest objects at all redshifts with a very crude and conservative selection. From the sensitivity curve of the XXL-N survey in the $0.5 - 10$ keV band at half of the survey area (Liu et al. 2016b, their Fig. 3) we obtained the flux limit in that energy band. Then, we interpolated the flux limit at 2 keV using the mean photon index of the sample, obtaining the sensitivity curve shown in red in the left panel of Fig. 3.4. In Menzel et al. (2016) a cut at $r < 22.5$ mag was applied. We converted this magnitude limit in a luminosity sensitivity only within $0.80 \lesssim z \lesssim 1.27$, for which 3000Å was actually detected in the r band. For different redshifts, we first computed a redshift dependent color correction for the other bands (u,g,i and z) performing a linear regression on the difference with the r-band magnitude. This provided a magnitude limit for $L_{3000\text{Å}}$ at all redshifts, consistently with the band in which that wavelength was actually detected, from which we obtained the related sensitivity line in the right panel of Fig. 3.4. We then divided XMM-XXL in six redshift bins, making sure to have at least 30 counts per bin. For each bin, we

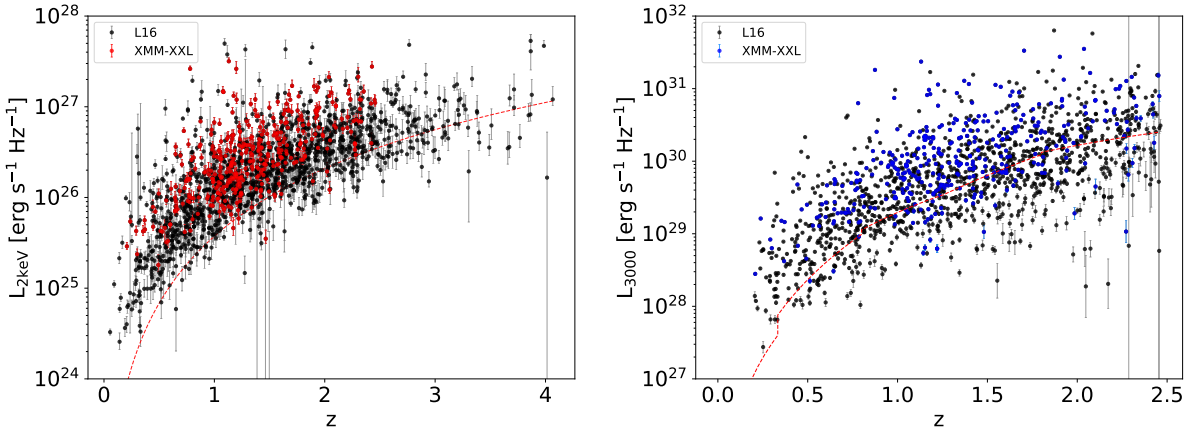

Figure 3.4: Distribution of L_{2keV} (left panel) and $L_{3000\text{Å}}$ (right panel) in the luminosity-redshift plane of the 379 sources of our XMM-XXL sample (red and blue respectively), with respect to the parent sample of BLAGN from Liu et al. (2016b) (black). The dashed red lines broadly represent the sensitivity of the survey at the related frequency (see the text for a description).

excluded all the sources below the limits given by the sensitivity curves on both axis, evaluated at the maximum z of the bin to be conservative (Fig. 3.5). The resulting cleanest subsample reaches accordance with the recent literature of the $L_X - L_{UV}$, with a slope of 0.59 ± 0.03. This value will be the one used (e.g. see Fig. 3.9) as reference for normalization and slope in the data-model comparison.

3.3.2 Methodology of the observational test

In our model $\dot{m} = \lambda_{edd} = L_{bol}/L_{edd}$, although we do not take as reference also $\dot{M}$ or λ_{edd} from Liu et al. (2016b): the former is interpolated from the mass and a monochromatic optical luminosity (Davis & Laor 2011), while the latter depends on a disk-luminosity estimate via L_{bol}. Both approaches are based on standard-disk assumptions or calculations and using those values within our non-standard disk models would be an inconsistency. One can also estimate L_{bol} applying bolometric corrections (BC) to the observed monochromatic optical-UV luminosities (Richards et al. 2006; Runnoe et al. 2012), although the many uncertainties in play (Krawczyk et al. 2013; Kilerci Eser & Vestergaard 2018) and the high scatter in the BCs (Richards et al. 2006; Lusso et al. 2012) discouraged us from relying on this approach. Then, for every source we iteratively obtain the $\dot{m}$ value yielding a model $L_{3000\text{Å}}$ consistent with the observed one within its errors (typically ~ 0.01 dex). This approach is similar to the interpolation method put forward by Davis & Laor (2011), although we do it consistently for each different model, which is given by a choice of μ, α_0 and f_{max}.

The methodology then consists in fixing μ, α_0 and f_{max} (see Table 2.1 for a summary on the model's parameters), which will be referred to as the model choice, within a discrete 3D grid in $\mu = [0, 0.2, 0.4, 0.5, 0.6, 0.8, 1]$, $\alpha_0 = [0.02, 0.2]$ and $f_{max} = [0.1, 0.2, 0.3, 0.5, 0.7, 0.9, 0.99]$. Then, we take as input m, Γ and $L_{3000\text{Å}}$ from the observed data, allowing us to solve the equa-

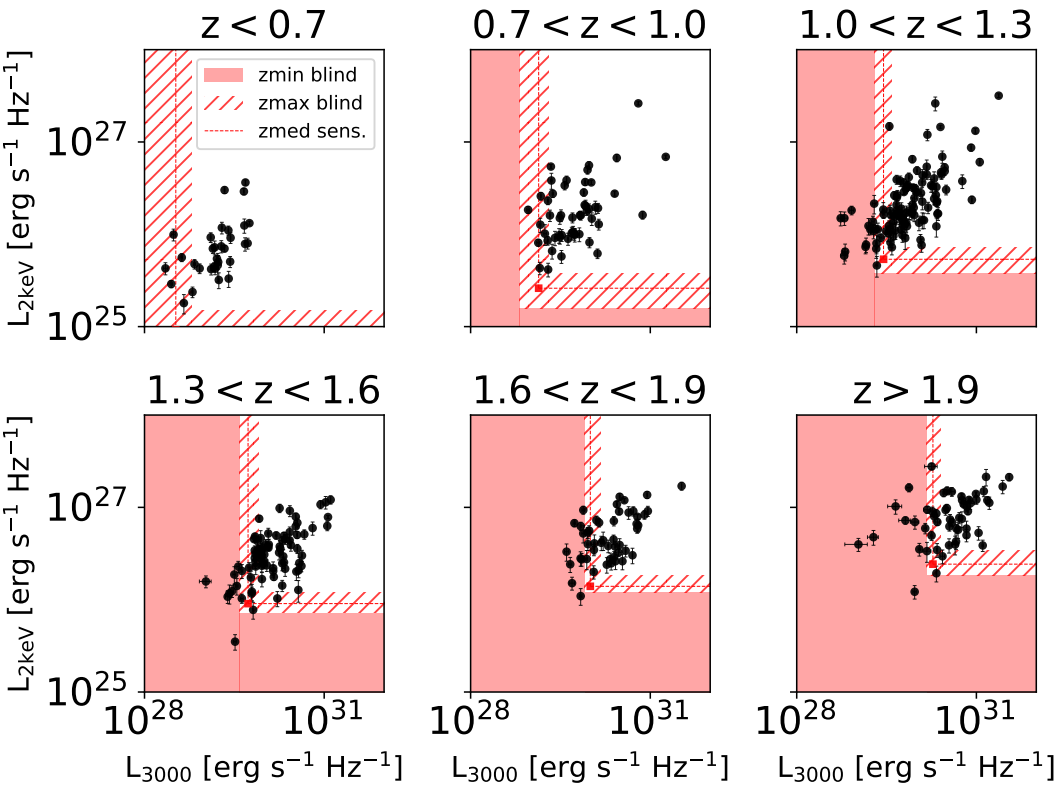

Figure 3.5: $L_X - L_{UV}$ relation in the redshift bins reported in the sub-titles. The sensitivity surfaces at the minimum, median and maximum redshift of the bin are represented in red with a full area, a dashed line and a shaded area respectively. These surfaces are obtained from the sensitivity lines in Fig. 3.4 at the above-mentioned redshifts. The sources above the shaded sensitivity area in each z-bin give the cleanest XMM-XXL sample.

tions of the model for each source and compute $\dot{m}$ and L_{2keV} values (see Section 2.2). For each observed source of the reference sample, every model in the 3D grid can provide a mock entry for the $L_X - L_{UV}$. A proper comparison requires uncertainties to be assigned on the mocks, as the observed m, Γ and $L_{3000\text{Å}}$ come with their own measurement and systematic errors, where obviously the $\sim 0.4 - 0.5$ dex systematics in the mass estimates (e.g. Shen 2013, and references therein) play the dominant role. As it is mentioned above, mock $L_{3000\text{Å}}$ values converge to the related observed quantities within their errors, hence we conservatively fixed the mock $\delta L_{3000\text{Å}}$ at the 90th percentile of the uncertainty distribution in the observed $L_{3000\text{Å}}$ (i.e. ~ 0.03 dex). In order to compute uncertainties for $\dot{m}$ and L_{2keV}, we ran each model 200 times on the same source, extracting the input values (m, Γ and $L_{3000\text{Å}}$) from a normal distribution with mean and standard deviation taken from the observed quantities and their errors. Then, the uncertainty on $\dot{m}$ and L_{2keV} is taken from the dispersion of the 200 runs.

3.4 Results of the observational test

For all the models on the discrete 3D grid in the μ, α_0 and f_{max} parameter space (see Section 3.3.2 and Table 2.1), we fit the L_X-L_{UV} distribution with a log-linear relation $\log L_X = \widehat{\alpha} + \widehat{\beta} \log L_{UV}$. Three examples are shown in Fig. 3.6 for μ corresponding to the known analytic viscosity prescriptions (see Section 2.2). Ideally, a model should reproduce the observed $L_X - L_{UV}$ in both normalization and slope. However, we can start decomposing the problem in two parts: a good match in the normalization ($\widehat{\alpha}$) would state that globally, for a given optical-UV luminosity distribution, the modeled corona emission was strong enough (see Section 3.4.1); instead, if the slope ($\widehat{\beta}$) is matched, then the model accurately describes how the coronal strength varies from lowly- to highly-accreting sources (see Section 3.4.2). Moreover, as it can be seen from the examples in Fig. 3.6, our models come with their one intrinsic scatter, given by different m and Γ at a fixed $\dot{m}$. This provides precious insights on the nature of the total observed scatter (see Section 3.4.3).

3.4.1 The normalization of the $L_X - L_{UV}$

First, we investigate how well the mocks reproduce the data normalization along the vertical axis of the $L_X - L_{UV}$. To do so, we define a score for the goodness of match:

$$r_i^2 = 1 - \frac{\sum_i \left(y_{data,i} - y_{mock_i}\right)^2}{\sum_i \left(y_{data,i} - < y_{data} >\right)^2} \tag{3.2}$$

The r^2 score is computed drawing 1000 random samples from the observed $\log L_{2keV}$ within their errors (i.e. $y_{data,i}$), and 1000 random regression lines from emcee's chains on the mock (i.e. y_{mock_i}). Then, the median and the 84th-16th inter-quantile range are quoted from the resulting distribution of 1000 r_i^2 scores. Negative scores indicate the data are poorly reproduced by the model; an $r^2 = 0$ would be obtained by a constant value corresponding to the mean of the observed $\log L_{2keV}$ distribution. We can put a quality threshold and keep all the models that yield a positive score.

The r^2 score as a function of f_{max} is shown in Fig. 3.7, where the choice of μ is color coded and the additional dependency on α_0 is represented with varying line-types (it is minor or absent, as in $\mu = 0$). We show for simplicity only values of μ corresponding to the known analytic viscosity prescriptions (see Section 2.2). The other values used would accordingly show intermediate results. For each viscosity law there is a preferred f_{max}, that fixes the maximum coronal strength in a model.

Models with higher μ need higher normalization f_{max}, since they have a comparably weaker X-ray emission, in accord with their lower $<f>_{median}$ (see Fig. 2.2 and Section 2.2.1). Nonetheless, the law correspondent to $\mu = 1$ does not produce adequately strong coronae even with $f_{max} = 0.99$ and can be ruled out (see Fig. 3.6). Furthermore, $\mu = 1$ produces a radially flatter X-ray emission profile (see bottom panel of Fig. 2.2), in contrast with observations that hint for coronae peaking in the inner radii (e.g. Mosquera et al. 2013; Reis & Miller 2013; Wilkins et al. 2016). We explore this behavior more quantitatively in the top panel of Fig. 3.8 showing how

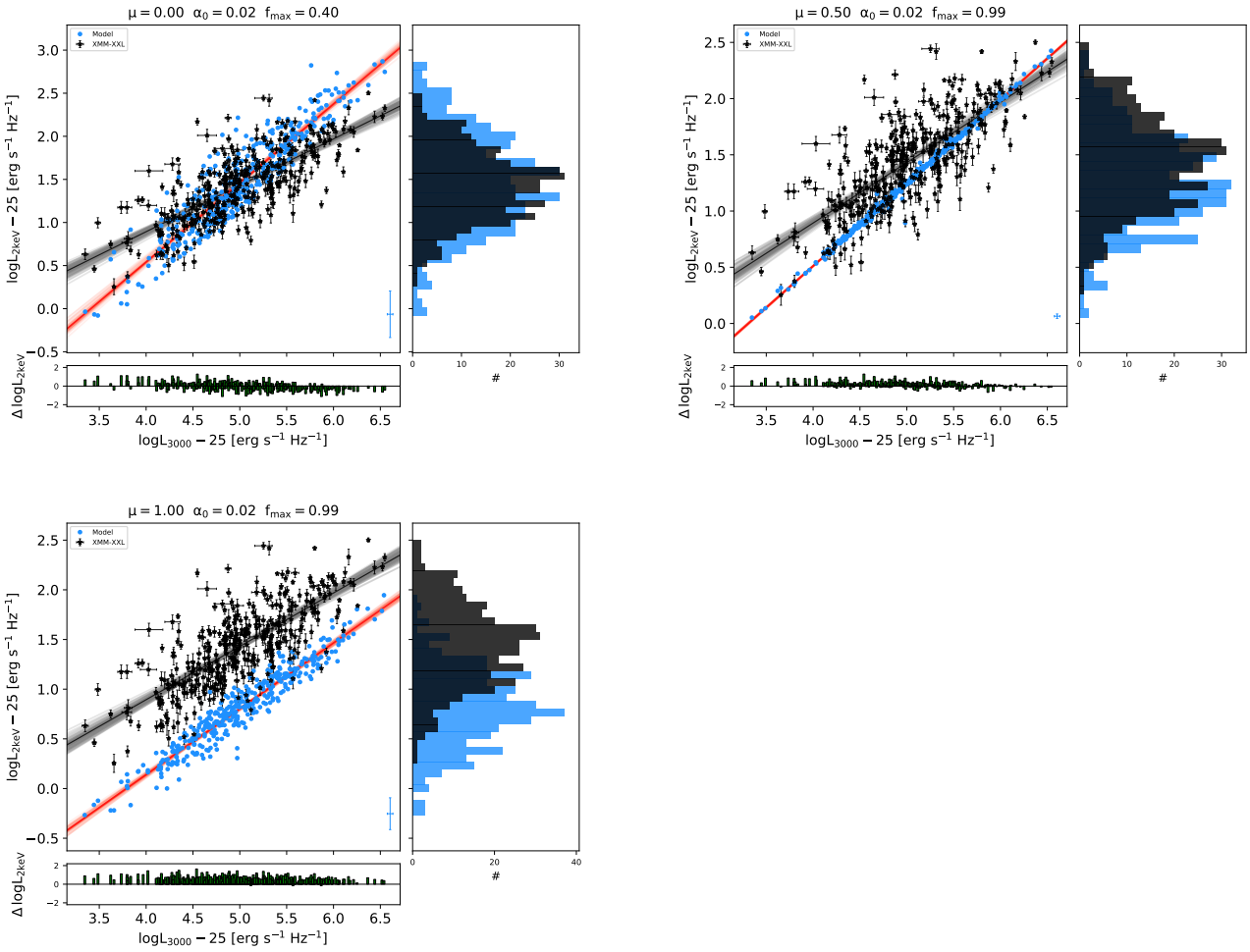

Figure 3.6: The central panel of each image shows an example of the $L_X - L_{UV}$ relation for both XMM-XXL (black stars) and the model (blue dots), in which the choice of μ, α_0 and f_{max} is shown in the titles. The black and red solid lines are randomly drawn from the posterior distributions of normalization and slope for XMM-XXL and the model, respectively, with the median regression line thickened. The bottom panels show the residuals given by the difference of observed and mock log L_{2keV} and the right panels show the related distributions. The errors on the model are show in the bottom right corner of the central panels.

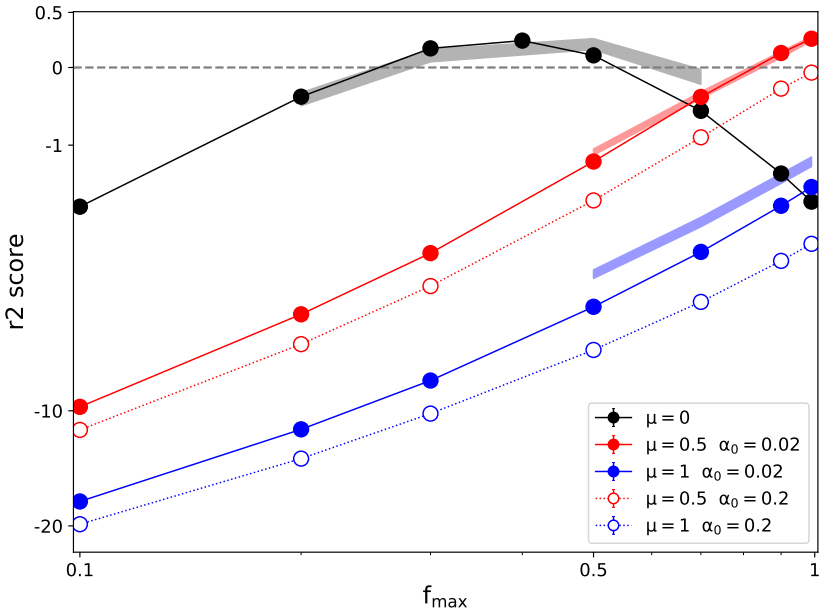

Figure 3.7: r^2 score, representing the goodness of match between XMM-XXL and mocks (see text), as a function of f_{max}. Models with $\mu = 0$, 0.5, 1 are color coded in black, red and blue, respectively. The additional dependency on α_0 is represented with varying line-types as shown in the legend, when present (it is absent for $\mu = 0$). A good match is represented with a score greater than zero. The points include the uncertainties in the score values. The shaded areas represent the results obtained applying the same methodology on a different sample (RM-QSO, Liu et al. in prep), fixing $\alpha_0 = 0.02$ and using the same colors. There is general agreement with XXM-XXL, suggesting that our results are independent from the sample used.

the radius of the annulus at which the 2 keV emission peaks (r_{peak}, or at which it is 90% of the total, r_{90}) varies with μ: as μ increases, most of the corona emission comes from annuli placed at larger and larger radii.

We also verified that our results do not depend on the sample adopted as reference. We performed the same analysis with the RM-QSO sources (Liu et al. in prep; Shen et al. 2019), on which a similar analysis was performed and on which we applied compatible cleaning criteria and methodology, as described in Sections 3.3.1 and 3.3.2. The results are shown in the r^2 score plot (Fig. 3.7) with shaded areas, color coded for μ in the same way and using only $\alpha_0 = 0.02$. There is generally a good agreement between the two samples, suggesting that our results are not dependent from the different data used.

It is worth stressing that the f_{max} value at which each μ (possibly) matches the observed normalization is degenerate with the assumptions on the accretion efficiency and on the product $\eta(1-a_{disk})$. Namely, higher accretion efficiencies and/or a higher fraction of the coronal emission beamed away from the disk would increase the normalization of the L_X-L_{UV} relation, and shift all curves of Fig. 3.7 to the left. This will be further examined in Sections 3.4.6 and 3.4.7.

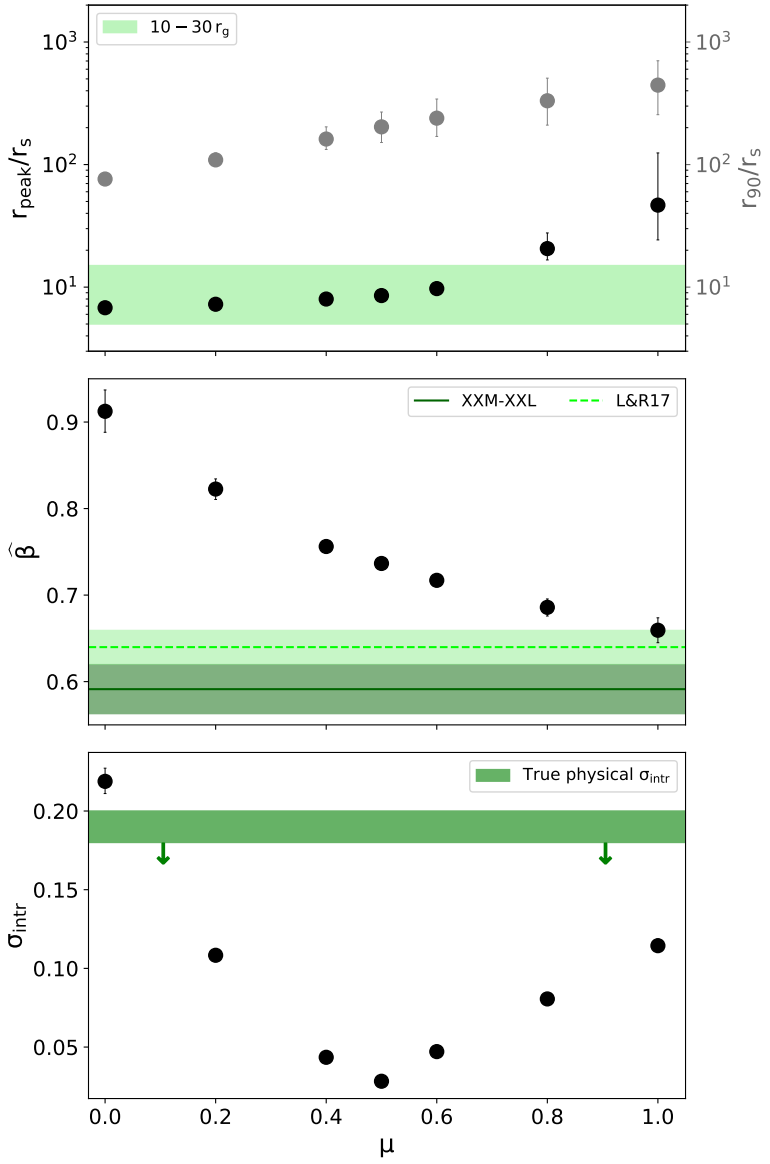

Figure 3.8: *Top panel*: the 2 keV-emission r_{peak} (r_{90}) as a function of μ is represented in black (gray). The green shaded area qualitatively shows the inner radii, where the bulk of X-ray emission is supposed to come from according to X-ray reverberation and micro-lensing. For increasing μ, the X-ray emission profile peaks at larger radii. *Middle panel*: for increasing μ the models obtain a slope of the $L_X - L_{UV}$ closer to the observed one. The dark-green area represents the reference slope of the cleanest XXM-XXL (Section 3.3.1), while the light-green refers to the slope quoted in Lusso & Risaliti (2017). *Bottom panel*: intrinsic scatter of the mock $L_X - L_{UV}$ relations as a function of μ. The green area represents a tentative upper limit of the true scatter (Lusso & Risaliti 2016; Chiaraluce et al. 2018), that is only due to the physical properties of AGN. For simplicity, all panels show only the results obtained with a single f_{max}, corresponding to the highest r^2-score (e.g., Fig. 3.7), and fixed $\alpha_0 = 0.02$.

3.4.2 The slope of the $L_X - L_{UV}$

Figure 3.7 allows us to track the models (i.e. combinations μ, α_0 and f_{max}, see Table 2.1) that broadly reproduce the normalization $\widehat{\alpha}$ of the observed $L_X - L_{UV}$. Nonetheless, obtaining the correct normalization is simply a weighting exercise of the energetic outputs of the disk and the corona. It is the slope that carries the exact information on how the disk-corona interplay changes across the different accretion regimes of bright radiatively-efficient AGN (see Section 3.2). This would require a precise knowledge of the true slope of the the $L_X - L_{UV}$. The observations suggest a value around ≈ 0.6 (Lusso & Risaliti 2016, 2017, our Section 3.3.1) and we can acknowledge this value as reference. Our methodology, however, can be regarded as data-independent, and it would applicable even if future works will update the current knowledge on the exact value of the slope.

In the middle panel of Fig. 3.8 we show how the modeled slope of the of the $L_X - L_{UV}$ gets closer to the observed one for increasing μ (i.e. for more damped radial f-profiles), for a fixed $\alpha_0 = 0.02$ and using only the f_{max} corresponding to the highest r^2-score. This is because models with increasing μ have higher logarithmic scatter in $f(r)$, meaning that going from lowly- to highly-accreting sources the span in $<f>_i$ is larger, with high-$\dot{m}$ objects having comparably weaker X-ray emission with respect to low-$\dot{m}$ companions (see Section 3.2). We show this for $\mu = 0$, 0.5 and 1, respectively[3]:

$$\begin{aligned}
\log <f> &= \log f_{max} \\
\log <f> &= (-1.12 \pm 0.24) - (0.15 \pm 0.02) \log \dot{m} \\
&\quad + (0.05 \pm 0.03) \log m \\
\log <f> &= (-1.82 \pm 0.36) - (0.27 \pm 0.03) \log \dot{m} \\
&\quad + (0.07 \pm 0.04) \log m
\end{aligned} \tag{3.3}$$

where the steepest dependency from $\dot{m}$ is obtained for larger μ.

This test points in the same direction as the evidence of an X-ray bolometric correction increasing with the accretion rate (e.g. Wang et al. 2004; Vasudevan & Fabian 2007, 2009; Lusso et al. 2010; Young et al. 2010), although we refrain to compare this observable with our regressions (e.g. Wang et al. 2004; Cao 2009; Liu & Liu 2009; You et al. 2012; Liu et al. 2012, 2016a), due to the many more uncertainties in play when deriving bolometric luminosities in comparison to the quantities entering in the $L_X - L_{UV}$ (see the discussion in Section 3.3.2).

3.4.3 The scatter of the $L_X - L_{UV}$

The observed scatter of the $L_X - L_{UV}$ for the sample used in this work is $\sigma_{intr} = 0.27 \pm 0.01$ (Section 3.3.1). As a matter of fact, this value represents an upper limit to the intrinsic dispersion inherent to the physics of the system, as the observed scatter is affected by a combination of

[3]The distributions of mock $\dot{m}$ are very similar across the models, with median values (and related 16th and 84th percentiles) of $0.16^{0.69}_{0.04}$, $0.15^{0.65}_{0.05}$ and $0.14^{0.59}_{0.04}$ for $\mu = 0$, 0.5 and 1, respectively. The tails include Eddington or even super-Eddington sources. We note that the uncertainty on the modeled $\dot{m}$, propagated through the ones in the observations, is as large as ≈ 0.65 dex.

instrumental and calibration issues, UV and X-ray variability, non-simultaneity of the multi-wavelength observations. A lot of effort has been put into trying to quantify as accurately as possible all these contaminants (e.g. Vagnetti et al. 2013; Lusso 2019a, and references therein), with claims that the intrinsic scatter in the L_X-L_{UV} relation is smaller than $\lesssim 0.18 - 0.20$ (Lusso & Risaliti 2016; Chiaraluce et al. 2018). Any successful model should be able to reproduce such a low scatter.

From the examples of mock $L_X - L_{UV}$ relations plotted in Fig. 3.6, it can already be seen that our models come with their intrinsic scatter. In our methodology (Section 3.3.2), the modeled $\dot{m}$ was tuned to the observed $L_{3000\text{Å}}$, hence the intrinsic scatter of the mock $L_X - L_{UV}$ relations is simply the dispersion of the modeled L_{2keV}, at a given $\dot{m}$, due to different m and Γ. We show this more quantitatively in the bottom panel of Fig. 3.8. The models dispersion varies with μ because changing the viscosity law induces a different logarithmic scatter in $f(r)$ (see Fig. 2.2) and it also affects the distance (in gravitational radii) from which the bulk of the L_{2keV} is coming (see top panel of Fig. 3.8). The resulting σ_{intr} of the models is likely a complex combination of these (and possible more) factors. All the models, with the exception of $\mu = 0$, lie below the available observational constraints (Lusso & Risaliti 2016; Chiaraluce et al. 2018) of $\lesssim 0.18 - 0.20$. This is another successful prediction of our model (see Section 3.2).

3.4.4 A complete picture: the slope-normalization plane of the $L_X - L_{UV}$

In the previous Sections, we decomposed the match in either normalization or slope to have a better understanding on how our disk-corona models can relate to the observed $L_X - L_{UV}$. However, the goal would be to have a model that can fully encompass these observables. Hence, in Fig. 3.9 we display 1-, 2- and 3-sigma contours in the slope-normalization plane $(\widehat{\beta} - \widehat{\alpha})$ of the $L_X - L_{UV}$ for both data and models. All regressions were performed with emcee normalizing both L_X and L_{UV} to the median value of XMM-XXL. The data contours are related to the cleanest XMM-XXL version (Section 3.3.1) and to the RM-QSO sources[4]. Model contours are shown for $\mu = [0, 0.2, 0.4, 0.5, 0.6, 0.8, 1]$ using a single f_{max}, corresponding to the highest r^2-score (e.g., Fig. 3.7) for each μ, and a fixed $\alpha_0 = 0.02$, for simplicity.

Fig. 3.9 shows that models reproducing the observed slope, namely the ones with higher μ (as in middle panel of Fig. 3.8), are also the ones that show weaker coronae (lower normalization $\widehat{\alpha}$) and overly extended L_{2keV}-emission (i.e. higher r_{peak} and r_{90}, top panel of Fig. 3.8).

3.4.5 The 3D plane: L_X vs L_{UV} vs m

As shown by Lusso & Risaliti (2017), the $L_X - L_{UV}$ relation for AGN is rather a three-dimensional problem, with the mass (or its proxy given by the full-width half-maximum of broad emission lines) playing a significant role as well. The observed $L_X - L_{UV} - m$ plane from XMM-XXL can

[4]XMM-XXL luminosities were obtained in Liu et al. (2016b) including a Balmer continuum component in the fit (refer to Shen & Liu 2012), although for the RM-QSO this component was switched off (Shen et al. 2019). For consistency, a rigid shift of -0.12 dex was applied to the RM-QSO $L_{3000\text{Å}}$ (Shen & Liu 2012) for obtaining the contours displayed in Fig. 3.9.

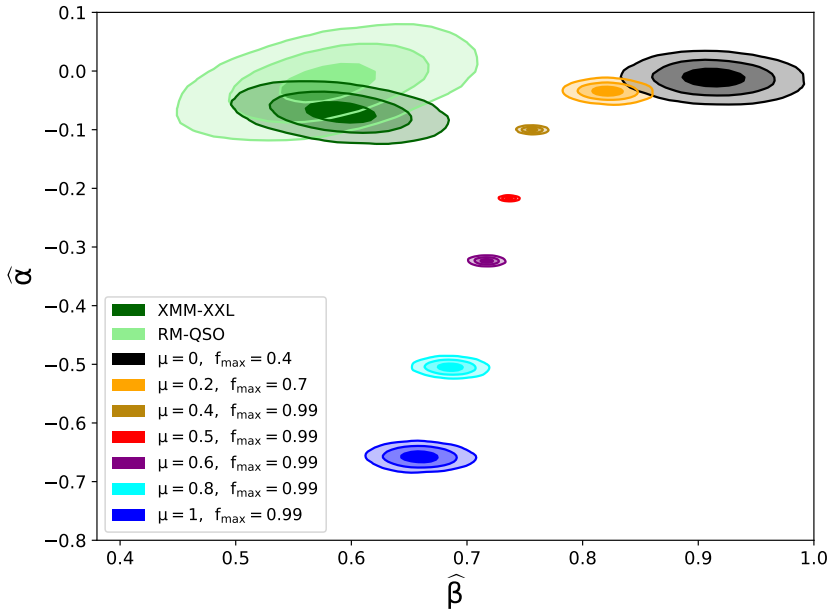

Figure 3.9: 1-, 2- and 3-sigma contours of the emcee regressions in the slope-normalization $(\widehat{\beta} - \widehat{\alpha})$ plane of the $L_X - L_{UV}$ for both data and models, normalizing all L_X and L_{UV} to the corresponding median values of XMM-XXL. Dark green contours are related to the cleanest XMM-XXL sample (Section 3.3.1) and the light green ones to the RM-QSO sources. The contour of the models are color coded for $\mu = [0, 0.2, 0.4, 0.5, 0.6, 0.8, 1]$, as shown in the legend. For simplicity, we report for each μ only results obtained with a single f_{max}, corresponding to the highest r^2-score, and fixed $\alpha_0 = 0.02$. Models that reproduce the observed slope $\widehat{\alpha}$ are also the ones that show weaker coronae (lower normalization $\widehat{\alpha}$).

be fit by:

$$\begin{aligned}\log L_{2keV} - 25 = (-0.91 \pm 0.13) &+ (0.39 \pm 0.03)\,(\log L_{3000\text{Å}} - 25) \\ &+ (0.23 \pm 0.04)\,(\log m - 7)\end{aligned} \tag{3.4}$$

and the mock $L_X - L_{UV} - m$ from models with $\mu = 0$, 0.5 and 1, respectively:

$$\begin{aligned}\log L_{2keV} - 25 = (-3.49 \pm 0.15) &+ (1.08 \pm 0.03)\,(\log L_{3000\text{Å}} - 25) \\ &- (0.27 \pm 0.03)\,(\log m - 7)\end{aligned}$$

$$\begin{aligned}\log L_{2keV} - 25 = (-2.41 \pm 0.15) &+ (0.73 \pm 0.01)\,(\log L_{3000\text{Å}} - 25) \\ &+ (0.013 \pm 0.004)\,(\log m - 7)\end{aligned} \tag{3.5}$$

$$\begin{aligned}\log L_{2keV} - 25 = (-2.28 \pm 0.08) &+ (0.57 \pm 0.02)\,(\log L_{3000\text{Å}} - 25) \\ &+ (0.14 \pm 0.02)\,(\log m - 7)\end{aligned}$$

The comparison in the 3D plane states that the exact dependency is not obtained by any of the models, with $\mu = 1$ being the closest in qualitatively retrieving the coefficients for $L_{3000\text{Å}}$ and m. We note that the mass is taken from the observations, thus this mismatch states that the luminosities in the model do not depend on the mass in the correct way.

3.4.6 The impact of the accretion efficiency

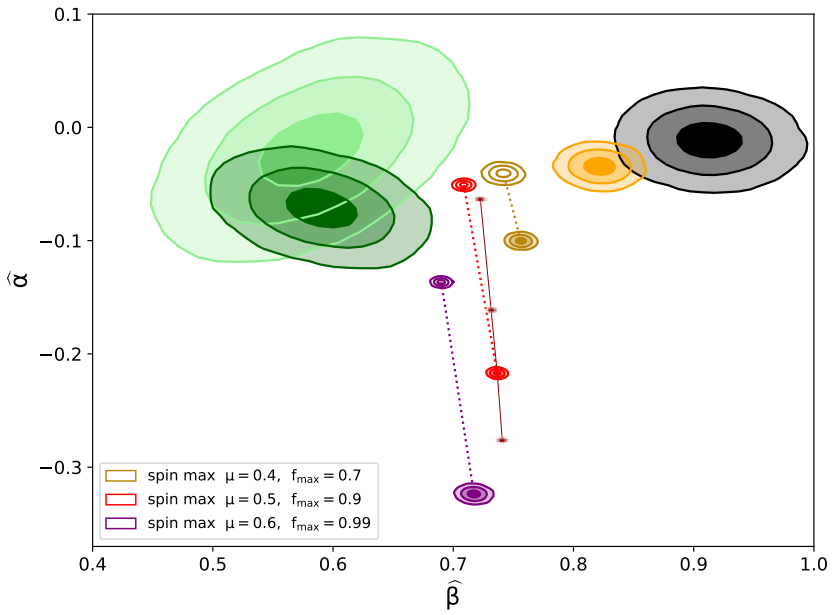

Figure 3.10: Same as Fig. 3.9, with the addition of empty contours for $\mu = 0.4$, 0.5 and 0.6 (color coded in the legend) obtained with maximally spinning black holes (i.e. with $\epsilon_0 = 0.3$ and $r_0 = 1.24r_g$). The dashed lines connect them to the non-spinning analogous realizations. Dark-red density spots represent the location of the center of different contours of the standard $\mu = 0.5$ case, in which the only difference is the adoption of η (downward scattering component) varying among 0.4, 0.5 and 0.6, going from higher to lower $\widehat{\alpha}$, respectively.

Throughout this work we adopted an efficiency $\epsilon_0 = 0.057$, typical of non-rotating black holes (e.g. Shapiro 2005), for simplicity. Nonetheless, a high spin seems to be preferred to model the blurred relativistic iron line, detected both in the local Universe (Nandra et al. 2007; Reynolds 2013) and up to $z \sim 4$ (e.g. Baronchelli et al. 2018). Moreover, flux-limited samples are known to be biased in preferentially detecting high-spinning black holes (Brenneman et al. 2011; Vasudevan et al. 2016), simply because they are brighter than their non-rotating analogous (see Reynolds 2019).

Then, we tested the model using maximally-spinning black holes, with radiative efficiency 0.3 and ISCO down to $r_0 = 1.24r_g$ (Thorne 1974). This has a major impact on the normalization axis of the $L_X - L_{UV}$. Everything else in the source being equal, in a spinning black hole matter can be accreted down to smaller distances with respect to their non-rotating companions, thus

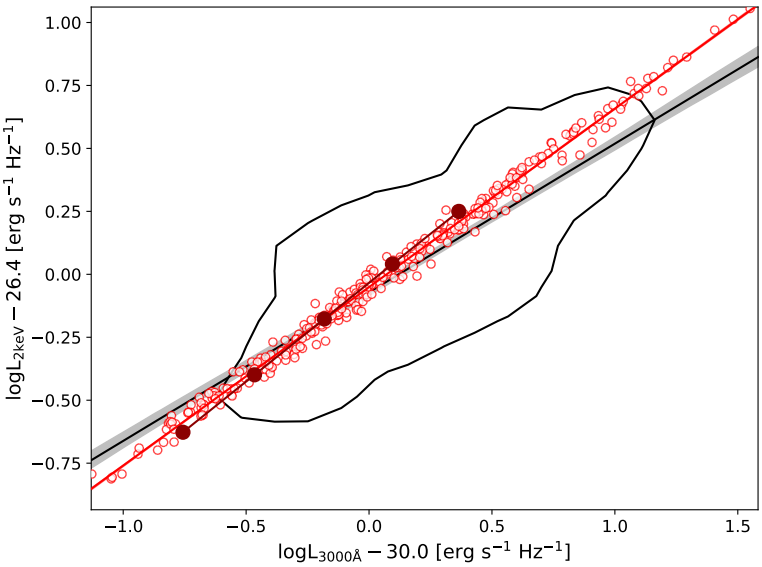

Figure 3.11: $L_X - L_{UV}$ relation for the high-spin model with $\mu = 0.5$, $\alpha_0 = 0.02$ and $f_{max} = 0.9$ (empty red points, corresponding to the empty red contour in Fig. 3.10), with the red line showing best fit slope from emcee. The connected filled points (dark red) show the single-mass trend ($\log m = 8.7$) for varying accretion rate $(0.03, 0.07, 0.17, 0.42, 1)$. For a comparison, the black contour shows where the data lie in the plane, with the related best-fit slope (black line).

the accretion power in the system is much higher. As a matter of fact, changing the radiative efficiency has an impact on the numerical equation that regulates f(r): for the same m and $\dot{m}$ and $r > 3$ the values of f is higher, and the transition radius between P_{rad}- and P_{gas}-dominated regions moves at lower radii. This self-consistently affects the disk equations via the $(1 - \tilde{f})$ factor (see Section 2.2), hence the surface temperature is decreased at higher radii, where most of the disk emission at 3000Å comes from. Then, the modeled $\dot{m}$ value needed to match the observed $L_{3000\text{Å}}$ is higher (see Section 3.3.2) and, consequently, $L_{2keV} \propto f Q_+$ is higher.

In Fig. 3.10 we show the model contours in the correlation slope-normalization plane computed for both low and high radiative efficiency, for $\mu = 0.4$, 0.5 and 0.6 only.

Interestingly, maximally-spinning sources yield a better match with the data contours, in particular for the viscosity law $\mu = 0.5$, with $f_{max} = 0.9$. For instance, Fig. 3.11 shows how the data and this high-spin model compare in the $L_X - L_{UV}$ plane. We want to stress that using only a maximum spin for all sources is an extreme measure, but since the (unknown) observed spin distribution is likely dominated by high-spin values (Reynolds 2019), model contours of a more realistic diverse population of high-spinning sources would be closer to the high-efficiency ones in Fig. 3.10 rather than to the spin-zero case. We also note that, even if the modeled coronae would be somewhat weaker using a realistic spin distribution, with respect to the maximum-spin case, the model with $\mu = 0.5$ can still be realized with a higher $f_{max} = 0.99$. Thus, we speculate that the new empty red contours in Fig. 3.10 consist in a fair approximation of a realistic high-spin population model. The tension with the observed $L_X - L_{UV}$ would be significantly relaxed.

3.4.7 The impact of the downward scattering component

The results shown in Fig. 3.7 are also degenerate with the assumptions on the value of the product $\eta(1 - a_{disk})$, that is on the assumed downward component of the X-ray emission (η) and on the disk albedo. The adopted value of $\eta = 0.55$ is typical for anisotropic Comptonization in a plane-parallel corona (Haardt & Maraschi 1993), although it is unclear how much it would change in different geometries or prescriptions. In a patchy corona (Haardt et al. 1994) η would unlikely part significantly from the one in the slab case. The only major difference would rather involve the transmission or absorption by the corona of the radiation reflected by the disk. However, we conservatively excluded from the reference sample adopted in the observational test all the sources with a non-negligible reflection component detected (see Section 3.3.1), allowing us to avoid its complicated modeling. In an outflowing corona (e.g. Beloborodov 1999; Malzac et al. 2001), the ratio between the downward and the upward flux decreases with the bulk velocity of the corona (e.g. Janiuk et al. 2000). We tried to quantify possible offsets in the $\widehat{\beta}$-$\widehat{\alpha}$ plane due to different values of η, ranging from 0.6 (slightly enhanced downward scattering) to 0.4 (reduced downward scattering, roughly approximating an outflowing corona with $\beta_{bulk} \approx 0.1 - 0.2$, e.g. Janiuk et al. 2000). We show this in Fig. 3.10 for the $\mu = 0.5$ case, with dark-red density spots ($\eta = 0.4$, 0.5 and 0.6 from higher to lower $\widehat{\alpha}$, respectively). Changing the downward component by $\Delta\eta \sim 0.1$ induces a significant offset of ≈ 0.1 dex in $\widehat{\alpha}$ and a minor change in $\widehat{\beta}$.

3.5 Discussion

The $L_X - L_{UV}$ relation has been studied for decades (starting with the better-known α_{OX} parameter, Tananbaum et al. 1979), its robustness used for bolometric estimates (e.g. Marconi et al. 2004; Hopkins et al. 2007; Lusso et al. 2010) and recently even for cosmology (Risaliti & Lusso 2015, 2019). Nonetheless, there is currently no solid and exhaustive physical explanation for it. In Section 3.2 we outlined the qualitative predictions of our model and in Section 3.4 we obtained that concordance with current data can be obtained with a modified viscosity prescription in the accretion flow ($\mu = 0.5$), provided the spin of the sources is high. Here, we briefly discuss whether other competing analytic disk-corona models succeed or not and then we try to investigate the impact of the assumptions in our model on the results.

3.5.1 Comparison with other models

Lusso & Risaliti (2017) tried to explain this relation with a very simplified, but effective, toy-model. Most of their assumptions are in common with our work (see Section 3.5.2), although our treatment is more complete and physically motivated. The assumption of the MRI amplifying the magnetic field to a lesser extent in P_{rad}-dominated regions (Blaes & Socrates 2001; Turner et al. 2002; Merloni 2003) is taken to the extreme with a step function for the f-profile: all the accretion power is emitted by the disk in P_{rad}-dominated regions (i.e. $f(r_{rad}) = 0$), whereas it is equally distributed between disk and corona in P_{gas}-dominated regions (i.e. $f(r_{gas}) = 0.5$). The resulting predicted slope and normalization of the $L_X - L_{UV}$ are claimed to be consistent with the

observations. The former can be confirmed by our analysis, as their $f(r)$ step-function is nothing but an extremely damped $f(r)$ beyond $\mu = 1$, whose mock slope of the $L_X - L_{UV}$ was the closest to the observed one. In the latter case, their match in normalization might be an involuntary artifact: with respect to the power transferred to the corona f, the observed luminosity is roughly halved if a downward scattering component is included (i.e. $f(1-\eta)$, with $\eta \approx 0.5$).

We verified this running our model with $\mu = 0$ and $\alpha_0 = 0.02$, forcing $f = 0$ in the P_{rad}-dominated region and fixing both $f = 0.50$ and $f = 0.99$ in P_{gas}-dominated radii. In Fig. 3.12 we show the related contours in the $\widehat{\beta} - \widehat{\alpha}$ plane along with our results of Fig. 3.9. This confirms that their step f-profile results in a slope consistent with the observed value, albeit producing overly weak coronae (too low normalization in the $\widehat{\beta} - \widehat{\alpha}$). Hence, their toy-model does not reproduce the $L_X - L_{UV}$. Moreover, the X-ray emission from their toy-model inevitably peaks at the transition radius between P_{rad}- and P_{gas}-dominated regions. Indeed, their model with $f_{gas} = 0.99$ yields $r_{peak} = 142^{438}_{51}$ and $r_{90} = 790^{1490}_{445}$ (i.e. produces extremely extended coronae).

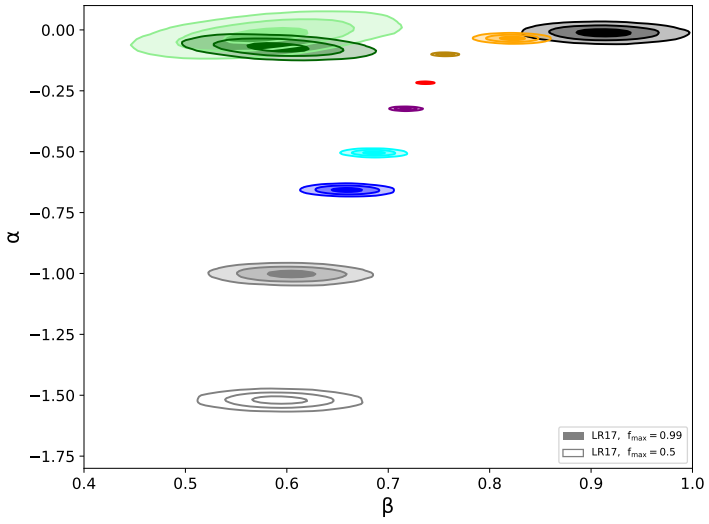

Figure 3.12: Same as Fig. 3.9 with the addition of a reproduction of Lusso & Risaliti (2017)'s toy-model as gray contours.

Kubota & Done (2018) coupled an outer standard disk with an inner warm Componising region, that produces the soft X-ray excess, and an innermost hot corona for the hard X-ray continuum. Their model fits remarkably well the broadband continua of three sources spanning a wide range of accretion rates. They also claim to reproduce the observed $L_X - L_{UV}$, using both the regression line and data points from Lusso & Risaliti (2017), although only displaying all the possible sources modelled within a grid of $m = 10^6 - 10^{10}$ and $\dot{m} = 0.03 - 1$ (their Fig. 7 and 8). Nonetheless, first-order normalization matches, even with m and $\dot{m}$ spanning within typical values, can be misleading. A more conclusive test would be, as we do, to match mock and data sources one by one.

3.5.2 Further assumptions and theoretical uncertainties

Only models with $\mu \lesssim 0.4$ are able to reproduce the observed normalization within the range of possible f_{max} values, whereas for $\mu \gtrsim 0.5$ they are off by $\gtrsim 0.1 - 0.2$ dex along the normalization. In Sections 3.4.6 and 3.4.7 we showed how a higher accretion efficiency and/or a different downward scattering component may affect our results in the slope-normalization plane. Their impact would be significant and can possibly ease the tension between data and models: high-spin black holes and/or moderately outflowing coronae would be consistent with the observations. We now try to investigate some other simplifications of our model, likely to have a minor or less quantifiable effect on our conclusions.

3.5.2.1 Soft X-ray excess and thermal instability

The XMM-XXL L_{2keV} value was interpolated from the $L_{2-10\,keV}$ fit in Liu et al. (2016b) after excluding sources with high reflection fraction (Section 3.3.1). The impact of the soft X-ray excess component can be considered negligible in that energy range, thus data points in the $L_X - L_{UV}$ are likely not contaminated. However, our models do not include a soft X-ray excess generation mechanism, the monochromatic L_{2keV} being extracted from a power-law spectrum within $0.1 - 100$ keV. If a significant fraction of the power dissipated in the corona is actually used by a different mechanism producing the observed soft-excess, namely from a warm corona (e.g. Petrucci et al. 2018; Kubota & Done 2018; Middei et al. 2019), the mock L_{2keV} would be overestimated to an unclear extent. Nonetheless, if the soft X-ray excess is produced by blurred relativistic reflection (e.g. Crummy et al. 2006; García et al. 2019), the influence of this component on our analysis would have been excluded with our selection criteria (Section 3.3.1).

In Section 2.2, we briefly addressed the disk-instability problem (see Fig. 2.2, top panel) and despite the local stabilizing effect of the iron bump in the opacities, disks with $\mu = 0$ (Shakura & Sunyaev 1973) and 0.5 (Merloni 2003) are globally unstable in P_{rad}-dominated regions. An intriguing question may be whether the unstable regions in the disk are responsible for generating the soft-excess, possibly within inhomogeneous flows (e.g. Merloni et al. 2006). As a matter of fact, the higher $\dot{m}$ the wider the region where P_{rad} dominates and the higher the soft-excess strength (e.g. Boissay et al. 2016). Nonetheless, a more thorough investigation of this scenario is beyond the reach of this paper.

3.5.2.2 Magnetically-dominated disks

In our model the stress tensor is dominated by Maxwell stresses as confirmed by simulations (e.g., Hawley et al. 1995; Sano et al. 2004; Minoshima et al. 2015), although the magnetic pressure is bound to be only a fraction of the product $P_{gas}^{\mu} P_{tot}^{1-\mu}$ via α_0 at the mid-plane. However, there are theories postulating disks that are P_{mag}-dominated also in the denser regions (e.g. Begelman & Silk 2017, and references therein) and not only in the upper layers (e.g. Miller & Stone 2000), possibly solving a few long-standing issues of the standard accretions disk theory (Dexter & Begelman 2019). Simulations indeed showed that P_{mag} can become an important competitor in supporting the disk vertically (Bai & Stone 2013; Salvesen et al. 2016), although heavily depending on the strength of the net vertical magnetic field, the origin of which is not fully understood,

yet. If this imposed net vertical field is small (if $\beta_0 = P_{tot}/P_{mag} >> 1$), the buoyant escape of the toroidal component, amplified by MRI, is faster than its creation and a disk-corona system consistent with our model is formed. However, the evidence of disks that are magnetically-dominated even at the mid-plane is supported by Jiang et al. (2019a), that recently performed a global 3D radiation-MHD simulation of two sub-Eddington flows. The structure of their simulated disks is significantly different from the standard Shakura & Sunyaev (1973) model and reaches a complexity that our simplified prescriptions are not able to grasp. On the other hand, these simulations could not produce spectra and luminosities, yet. We here rely on the assumption that the energetics of P_{mag}-dominated disks are not significantly different from standard thin disks at radii larger than $\sim 10r_g$ (e.g., see Sądowski 2016).

3.5.2.3 Winds and outflows

In order to see if any known broad absorption line (BAL) quasars were present in our sample, we cross-matched the XMM-XXL catalog (Menzel et al. 2016; Liu et al. 2016b) with SDSS-DR12 (Pâris et al. 2017), that flagged 29580 BAL QSO after visual inspection. Only two sources among the 379 used in our analysis were flagged, although they were both assigned zero indexes in the common metrics used for a more quantitative measurement of the BAL properties (Pâris et al. 2017). Hence, our sample has no contaminations from known BALs, although we can investigate the possible impact of un-modeled wind-dominated objects on our work. For instance, Nomura et al. (2020) recently developed a disk model compensating for the mass-loss rates of UV-driven winds, while consistently adjusting the temperature and emission of the underlying disk. They referred to a future work for a more complete modeling of the inner radii and the hard X-ray emission, but the influence on $L_{3000\text{Å}}$ values seems already significant, provided $\dot{m} \gtrsim 0.5$. Since winds appear to act only from moderate to Eddington $\dot{m}$, neglecting their presence would have an impact on the modeled $L_X - L_{UV}$ slope. The wind carries away kinetic energy reducing the disk emission accordingly, thus for a given observed high $L_{3000\text{Å}}$, our no-wind model would underestimate $\dot{m}$ for the possible outflowing sources contaminating our sample.

3.5.2.4 The larger-than-predicted disk argument

One of the most studied issues of the standard disk model (Shakura & Sunyaev 1973) is that observed sizes appear to be larger than expected at optical-UV wavelengths, using both microlensing effects (e.g. Morgan et al. 2010; Blackburne et al. 2011; Jiménez-Vicente et al. 2012) and flux variability lags across multiple bands in the so-called reprocessing scenario (e.g. Edelson et al. 2015; Fausnaugh et al. 2016, 2018; Jiang et al. 2017; Cackett et al. 2018; McHardy et al. 2018), in which often a compact X-ray emitting region (e.g., a lamppost corona) irradiates the disk inducing light-travel lags in the UV-optical bands. However, even combining all these results discordant with the theoretical predictions is not trivial (Kokubo 2018), particularly if different techniques are used (see Moreno et al. 2019; Vio & Andreani 2018). What is more, there are also numerous studies finding consistency with the sizes predicted by the standard theory (e.g. McHardy et al. 2016; Mudd et al. 2018; Yu et al. 2020; Edelson et al. 2019; Homayouni et al. 2019), thus we do not consider necessary to use the larger-than-predicted argument to abandon

all the standard prescriptions, yet.

3.5.2.5 No-torque inner boundary

For convenience, we adopted the no-torque condition with the stress vanishing at the inner edge. However, the presence of magnetic torques (Gammie 1999; Agol & Krolik 2000) would increase the disk effective temperature and the Q_+ emissivity in the innermost radii (Agol & Krolik 2000; Dezen & Flores 2018) and, if applied to the disk only, it would cause instead a drop in the fraction f (Merloni & Fabian 2003). Without a proper MHD treatment, it is unclear how the modeled $L_{2keV} \propto fQ_+$ would be affected, and consequently the $L_X - L_{UV}$ slope.

3.5.2.6 The vertical structure

Our model does not properly treat the vertical structure of the disk. The effective temperature is obtained from $T_{eff} \propto T_{mid}/\tau^{1/4}$, where $\tau = h\rho\kappa$ assumes constant ρ and κ along the scale-height. Even keeping the approximation of a constant ρ, κ should change self-consistently with the decrease in temperature. A more thorough modeling of the disk vertical structure in supermassive black holes was presented by Hubeny and collaborators, taking into account both scattering processes and free-free and bound-free opacities (Hubeny et al. 2000, 2001). Their model also shares some of our limits (e.g., stationary disk, α-prescription, no-torque boundary, vertical support from thermal pressure only), validating the comparison. The overall SED has lower (higher) fluxes at low (high) frequencies with respect to standard calculations, with the most significant impact on the modeling of the soft-excess (Done et al. 2012). The computation of $L_{3000\text{Å}}$ should be affected in a minor way, with a small overestimation on the order of a color correction (e.g. Done et al. 2012), that is either roughly constant or weakly depending on m and $\dot{m}$ (e.g. Davis & El-Abd 2019). Our conclusions should not be significantly affected, although this would need to be improved for a proper SED modeling and time-lags predictions.

3.6 Conclusions

The gap between simulations and observations in AGN needs to be bridged and simplified, but motivated, analytic prescriptions still represent a powerful tool to explain the observed multi-wavelength scaling relations. For instance, the clear correlation observed between monochromatic logarithmic L_X and L_{UV} luminosities has been used for decades (in the shape of the more-known α_{OX} parameter, Tananbaum et al. 1979) in many applications (even for cosmology, e.g. Risaliti & Lusso 2015, 2019). Despite this, a conclusive theoretical explanation for the observed correlation is still lacking. Being smaller than one, the observed slope indicates that, going from low- to high-accretion rate AGN, the X-ray emission increases less than the optical-UV emission. Any viable disk-corona model must be able to explain this.

In this work, we tested a self-consistent disk-corona model (Section 2.2) against the $L_X - L_{UV}$ relation. We were able to identify the possible mechanism regulating the disk-corona energetic interplay, in terms of viscosity prescriptions (e.g., $\mu = 0.5$) that naturally lead to an X-ray emission increasing less than the disk emission going to higher accretion rates (see Section 3.2).

We also put forward a quantitative observational test (Section 3.3), using a reference sample of AGN (Section 3.3.1) observed both in the (rest-frame) UV and in X-rays: taking from each source the observationally determined m, $\dot{m}$ and Γ we were able to model an analogous mock object (Section 3.3.2) producing a set of mock $L_X - L_{UV}$. This allowed us to reach a deep understanding of the physics driving the slope, normalization and scatter of the $L_X - L_{UV}$ (see Section 3.4).

We find that if the black-hole population is assumed to be non-spinning, results from this test are inconclusive: the viscosity prescriptions reproducing the slope of the observed $L_X - L_{UV}$ relation, also produce overly weak coronae. Interestingly enough, the tension between the strength of the observed and modeled X-ray emission (i.e. in the normalization of the $L_X - L_{UV}$) can be significantly relaxed adopting a more realistic high-spinning black-hole population and/or with moderately-outflowing coronae. We tested the former case adopting the efficiency (and the inner orbit) of maximally-spinning black holes, in which matter is able to accrete further into the potential well, resulting in a much higher accretion power and, consequently, in much stronger coronae (Section 3.4.6). Moreover, if the spin is high the X-ray emission profile peaks closer to the black hole, in even better agreement with X-ray reverberation and microlensing studies (Mosquera et al. 2013; Reis & Miller 2013; Wilkins et al. 2016). In particular, the disk-corona model testing maximally-spinning black holes with $\mu = 0.5$ (i.e. magnetic stress proportional to the geometric mean of P_{gas} and P_{tot}, e.g. see Merloni 2003), $f_{max} = 0.9$, $\alpha_0 = 0.02$ (see Table 2.1) provides the best match with the observations (Fig. 3.11), although the modeled slope is still somewhat larger than the observed one (Fig. 3.10). Going beyond this type of exercises, only 3D global radiation-MHD simulations will be able to better disclose the disk-corona physics (e.g. Jiang et al. 2019b,a), provided a clearer way of approaching the observations will be reached.

Chapter 4

Do stellar-mass and super-massive black holes have similar dining habits?

Over the years, numerous attempts have been made to connect the phenomenology and physics of mass accretion onto stellar-mass and super-massive black holes in a scale-invariant fashion (see Section 1.5). In this Chapter, we explore this connection at the radiatively efficient (and non-jetted) end of accretion modes by comparing the relationship between the luminosity of the accretion disk and corona in the two source classes. Motivated by the apparently tight relationship between these two quantities in AGN (see Chapter 3), we analyse 458 RXTE-PCA archival observations of the XRB GX 339-4, using this object as an exemplar for the properties of XRBs in general. We focus on the soft and soft-intermediate states, which have been suggested to be analogous to radiatively efficient AGNs (see Section 1.5). The observed scatter in the $\log L_{disk} - \log L_{corona}$ relationship of GX 339-4 is high (~ 0.43 dex) and significantly larger than in a representative sample of radiatively efficient, non- or weakly jetted AGN (~ 0.30 dex). At first glance, this would appear contrary to the hypothesis that the disk-corona systems simply scale with mass. On the other hand, we also find that GX 339-4 and our AGN sample show different accretion rate and power-law index distributions, with the latter in particular being broader in GX 339-4 (dispersion of ~ 0.16 cf. ~ 0.08 for AGN). GX 339-4 also shows an overall softer slope, with a mean value of ~ 2.20 as opposed to ~ 2.07 for the AGN sample. Remarkably, once similarly broad Γ and $\dot{m}$ distributions are selected, the AGN sample overlaps nicely with GX 339-4 observations in the mass-normalised $\log L_{disk} - \log L_{corona}$ plane, with a scatter of $\sim 0.30 - 0.33$ dex in both cases. This indicates that a mass-scaling of properties might hold after all, with our results being consistent with the disk-corona systems in AGN and XRBs exhibiting the same physical processes, albeit under different conditions for instance in terms of temperature, optical depth and/or electron energy distribution in the corona, heating-cooling balance, coronal geometry and/or black hole spin.

This work was published as Arcodia et al. (2020) in Astronomy & Astrophysics, Volume 638, A100.

4.1 The open question: the presence of a mass-scaling of radiatively efficient disk-coronae

In Section 1.5 we outlined the current picture of accretion across the BH mass scale, which compares observational properties of XRBs and AGN. Here, we aim to improve on this connection in the radiatively efficient (and non-jetted) end of accretion modes, comparing AGN and XRBs in such regime and test whether they share the same phenomenology and physics based on their disk–corona energetic output. Regarding the phenomenology, the disk–corona connection has been studied in AGN for decades (e.g. Arcodia et al. 2019, and references therein; see Chapter 3 of this Thesis) via the X-ray loudness parameter α_{OX} (Tananbaum et al. 1979) and was also tested in XRBs with an analogous proxy (e.g. Sobolewska et al. 2009). For the case of AGN, there are many indications that the physical scatter in X-ray coronae for a given disk luminosity (once excluding variability and non-simultaneous observations) is very small ($\lessapprox 0.19-0.20$ dex; Lusso & Risaliti 2016; Chiaraluce et al. 2018). However, in soft states (SSs) and soft-intermediate states (SIMSs) of XRBs, namely supposedly scaled-down radiatively efficient AGN, the relative strength of the X-ray corona with respect to the disk shows large scatter in a relatively narrow range of soft X-ray monochromatic (i.e. disk) flux (Sobolewska et al. 2009, see Figure 1.7). Furthermore, one should keep in mind that when a single XRB is used, any possible issue arising from non-simultaneity of the data probing the two components is circumvented and there is no additional scatter coming from a mixed bag of masses, distances, and inclinations (see Section 1.2). Then, under the assumption of a scale-invariant accretion paradigm, one would rather expect the scatter in XRBs to be smaller (but see Figure 1.7).

Therefore, a more thorough study of the source of the scatter in the XRBs disk–corona plane may help to shed light on the putative analogy between accretion flows around stellar-mass and supermassive BHs. This highlights the importance of our work, since the $\alpha_{OX} - L_{disk}$ relation in AGN revealed itself to be a powerful tool for studying the physics of accretion (Lusso & Risaliti 2017; Kubota & Done 2018; Arcodia et al. 2019) up to high redshift (Nanni et al. 2017; Vito et al. 2019; Salvestrini et al. 2019) and its scatter represents an important factor in the now rejuvenated role of quasars as cosmology probes (Risaliti & Lusso 2015, 2019; Melia 2019; Khadka & Ratra 2020; Lusso et al. 2019; Yang et al. 2020; Velten & Gomes 2020; Zheng et al. 2020).

4.2 Our sandbox: GX 339-4

GX 339-4 was discovered almost five decades ago (Markert et al. 1973) and is one of the most studied Galactic BH candidates (Zdziarski et al. 1998; Hynes et al. 2003). It has since undergone several X-ray outbursts, which were also simultaneously detected and monitored at almost all wavebands (e.g. Homan et al. 2005; Coriat et al. 2009; Cadolle Bel et al. 2011; Dinçer et al. 2012; Buxton et al. 2012; Corbel et al. 2013; Vincentelli et al. 2018), with particularly good coverage during the Rossi X-ray Timing Explorer (RXTE) era.

We are interested in comparing XRBs in regions of the q-plot (e.g. Fender et al. 2004, see also Section 1.2) where the analogy with bright radiatively efficient quasars might hold (e.g. Maccarone et al. 2003; Körding et al. 2006; Sobolewska et al. 2009). We conservatively selected

both SS and SIMS states, including spectra in which the hard component can be almost as strong as the soft component. This selection criterion was then confirmed a posteriori with our control AGN sample (Section 4.5 and 4.6.3.1).

We selected the 2002-2003, 2004-2005, 2006-2007, and 2010-2011 outbursts, which are the ones with the highest coverage in the RXTE archive for GX 339-4. We referred to the extensive literature on GX 339-4 to select SSs and SIMSs in the above-mentioned outbursts (hereafter SS02, SS04, SS07, and SS10, respectively), from both spectral (i.e. low hardness-ratio) and timing analysis (i.e. low fractional rms) constraints: in SS02 we included all RXTE observations between MJD=52411.60 and 52694 (Belloni et al. 2005), 116 in total; SS04 started at MJD∼53235 (Belloni et al. 2006) and ended at MJD∼53456 (using colour constraints from Dunn et al. 2008), with 78 observations in total; our SS07 selection started in MJD=54147 and ended around MJD=54230, including only observations marked as high-SSs or SIMSs from timing analysis constraints (Motta et al. 2009), 69 in total[1]; SS10 contains observations within MJD= 55331 – 55565 (Debnath et al. 2010; Nandi et al. 2012), 195 in total. This adds up to 458 observations, covering almost 10 years of RXTE data.

4.3 Data analysis

RXTE observations during SS02, SS04, SS07, and SS10 include data from the Proportional Counter Array (PCA, Jahoda et al. 1996). Data from the High-Energy X-ray Timing Experiment (HEXTE, Rothschild et al. 1998) were not included in the analysis, since the background of the instrument dominates over the (faint) hard spectral component in the SSs and SIMSs. In the PCA, we analysed only energies in the range 3 – 25 keV, where the effective area of the instrument is at its best. We reduced the selected observations following the standard procedure outlined in the RXTE cookbook[2]. PCA spectra were extracted from the top layer of the Proportional Counter Unit (PCU) 2, which is reported to be the best calibrated. A systematic uncertainty of 0.5% was added to all channels to account for calibration uncertainties.

In this work, the spectral analysis on each individual observation was performed using v2.8 of BXA (Buchner et al. 2014)[3], which connects a nested sampling algorithm (Feroz et al. 2009) with a fitting environment. For the latter, we used `Sherpa` v4.11.0 (Freeman et al. 2001; Doe et al. 2007) for the spectral fits and `XSPEC` v12.10.1 (Arnaud 1996), with its Python oriented interface[4], for the flux calculations and spectral simulations (see Section 4.3.2.1).

Our approach was to first model the PCA background spectrum empirically in the 3 – 25 keV band with a mixture of broken power-law and Gaussian components for each observation. Once satisfactory residuals were obtained, this background model was included as a model component in the spectral fit of source plus background spectra, leaving the power-law normalisation as the single free background parameter. This ensured a more robust statistical treatment of the

[1](Motta et al. 2009) performed the timing analysis up to MJD=54208. We included all observations up to MJD=54230 with a cut in HR corresponding to the value at the start of the SIMS as reported by (Motta et al. 2009).

[2]RXTE cookbook

[3]https://github.com/JohannesBuchner/BXA/

[4]pyXSPEC

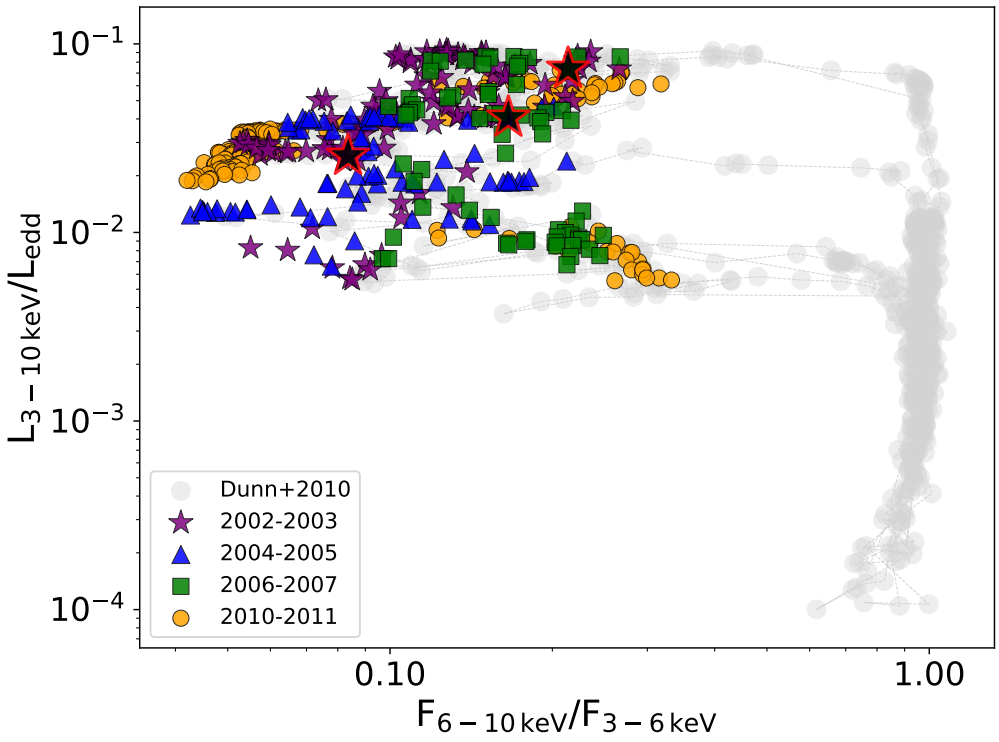

Figure 4.1: Hardness-luminosity diagram (HLD) of GX 339-4 in its four outbursts used in this analysis (i.e. 2002-2003, 2004-2005, 2006-2007 and 2010-2011). *Grey* circles are archival data taken from Dunn et al. (2010), over which our own data points for SS02, SS04, SS07, and SS10 are superimposed; these are colour coded following the legend in the figure. Black symbols with red contours refer to the examples in Fig. 4.2.

counts (e.g. Loredo 1992; van Dyk et al. 2001), since all the background-subtracted spectra would have had several bins with negative counts close to the high-energy end of the adopted $3 - 25$ keV range. Moreover, the free background normalisation was allowed to span along the 3σ errors of the value obtained in the background fit alone, which excludes an overestimation of our knowledge of the PCA background. Unless stated otherwise, we quote and plot median values with 16th and 84th percentiles of the BXA posterior distributions.

4.3.1 The spectral model

Each X-ray spectrum was fit with a source model consisting of an accretion disk (`DISKBB`; Mitsuda et al. 1984) plus a Comptonisation component (`NTHCOMP`; Zdziarski et al. 1996; Życki et al. 1999)[5], with the complex features of the reflection spectrum approximated with a

[5]The model `compps` (Poutanen & Svensson 1996) is reported to be more accurate for Comptonisation (e.g. see comparison figures in Niedźwiecki et al. 2019), although the major problems of `NTHCOMP` lie in the estimate of the high-energy cutoff. First, our analysis is restricted in the $3 - 25$ keV band; moreover, we leave the cutoff energy

Gaussian component[6]. The source model was then absorbed by a Galactic column density free to vary in a ±15% uncertainty interval (see Arcodia et al. 2018, Sec. 5.7.2) around the tabulated value including the molecular component ($N_H = 5.18 \times 10^{21}$ cm^{-2}; Willingale et al. 2013). This source model corresponds to `xstbabs*(xsdiskbb+xsnthcomp+xsGaussian)` in `Sherpa` and `tbabs*(diskbb+nthcomp+Gaussian)` in `XSPEC`, to which a complex background spectral model was added, with only a free normalisation parameter.

`DISKBB` free parameters are the temperature at the inner disk radius T_{in} and the normalisation, which is a function of the inner radius R_{in}, the distance d of the source and the inclination i of the disk. The `NTHCOMP` free parameters were the asymptotic photon index Γ, the normalisation, and the electron temperature kT_e (see footnote 5), while we tied the temperature of the seed photons (i.e. the low-energy rollover) to the typical disk temperature as fit by `DISKBB`. The multi-colour black-body approximation in the `DISKBB` model was chosen over more rigorous accretion disk models, such as for example `BHSPEC` (Davis & Hubeny 2006), due to its simplicity and easier coupling with the Comptonisation emission of `NTHCOMP`. In Section 4.4.1.2 we further discussed our choice and we presented our tests with `BHSPEC` performed in order to verify the impact of a different disk model on our results. All the parameters in the Gaussian line model were left free to vary within the following intervals: a line with $E_{line} = 6.4 - 6.966$ keV, width $\sigma_{line} = 0 - 1.5$ keV, and free normalisation.

In BXA, we adopted uninformative priors for all ten free parameters[7]. The Bayesian methodology allowed us to use this complex model for all spectra, even for the few ones in which the Gaussian component might not have been needed. In this cases, the procedure would yield a flat posterior distribution for (i.e. a correct marginalisation over) the free parameters of that component.

4.3.2 Results of the spectral fits

The overall behaviour of GX 339-4 in its SSs and SIMSs is studied with 458 observations. We show in Fig. 4.1 the HLD, in which the four complete outbursts are shown in grey (data from Dunn et al. 2010) and our data from SS02, SS04, SS07, and SS10 are represented with purple stars, blue triangles, green squares, and yellow circles, respectively. Three examples of source plus background spectra are reported in Fig. 4.2, selected taking the 84th percentile, median, and 16th percentile of the total $3 - 25$ keV flux distribution of the total XRB sample used in Section 4.5.

In Fig. 4.3 we show the evolution of spectral quantities with time along the four outbursts, namely the source plus background count rate in the $3 - 25$ keV, the X-ray photon index Γ, the

parameter free to vary and we are not interested in using the (likely unconstrained) fit values. We are confident that the impact on our analysis would be minor and we use `NTHCOMP` for its simplicity.

[6]We also explored the `laor` model (Laor 1991) to exclude that this simplified treatment of the reflection features had a significant impact on our results (see Section 4.6.3.3).

[7]In a few rare cases we observed a bimodality in some of the Photon Index posterior distributions, or a posterior pegged at one of the extremes ($\Gamma = 1 - 4$). For those, a broad Gaussian prior centered at the peak of the observed distribution with a sigma of $0.3 - 0.5$ was adopted. This avoids unphysical posterior distributions without strongly affecting the spectral fit, the prior being very broad.

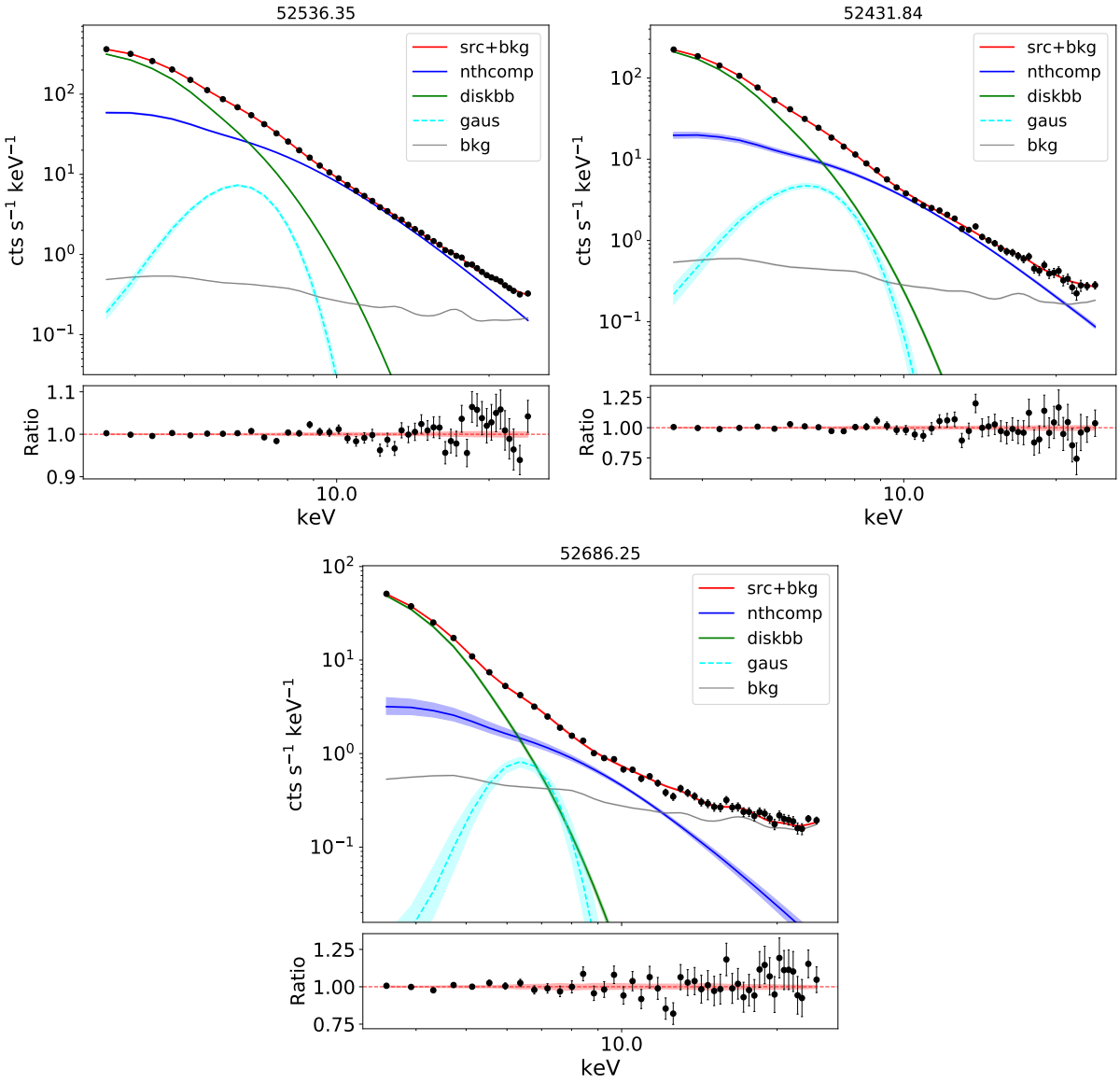

Figure 4.2: Three examples of source plus background spectra (black dots, error bars included), with related data–model ratios in the lower panels. The three observations were selected taking the 84th percentile, median, and 16th percentile of the total 3 – 25 keV flux distribution of the full XRB sample used in Section 4.5, shown from top left to bottom respectively. These correspond to the three larger black symbols in Fig. 4.1, going downwards in the q-plot. All additive model components are shown and defined in the legend, with the total source plus background model shown in red. For each component, the solid lines represent the median of the model distribution computed from the posteriors of the fit parameters (with 16th-84th percentile coloured contours around them, in some cases smaller than the thickness of the line).

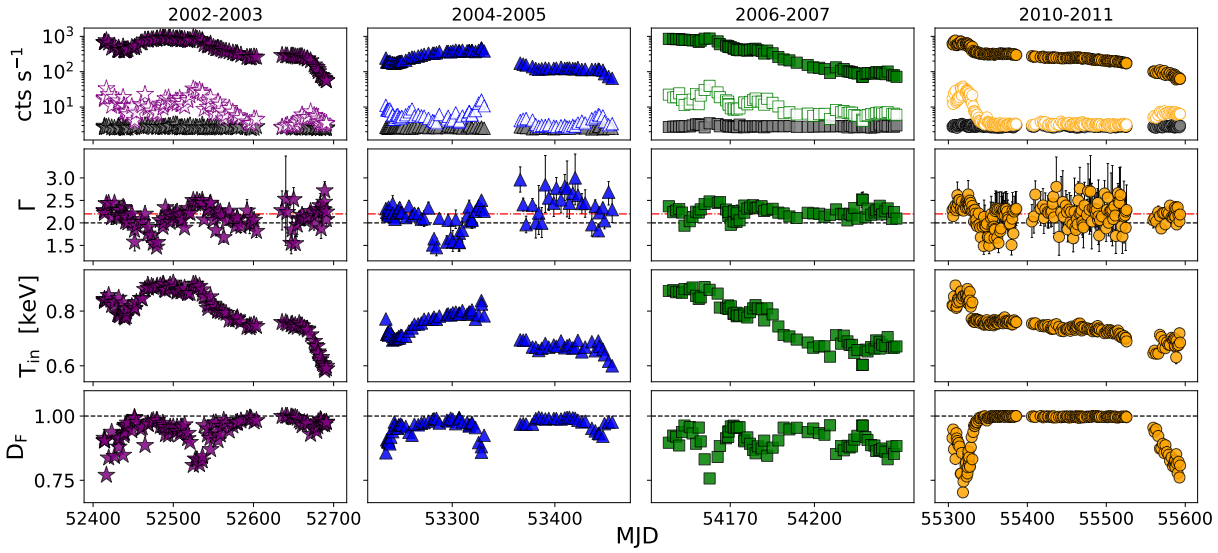

Figure 4.3: Evolution of the 3 − 25 keV count rate, of the fit photon index and disk temperature, and of the disk fraction D_F (see Eq. 4.1) is shown along the four different outbursts (same colour coding and symbols as in Fig. 4.1). In the top panels, filled coloured symbols represent the total (source plus background) 3−25 keV count rates, the coloured empty symbols the total count rates in the 10−25 keV band, and the grey symbols the background count rates in the 10−25 keV band. In the middle-top panel, a black dashed line at $\Gamma = 2$ is shown to guide the eye, whereas the red dot-dashed line highlights the median $\Gamma = 2.20$ of the whole XRB sample used in Section 4.5.

disk temperature T_{in} (i.e. a proxy of the mass accretion rate), and the disk fraction D_F. The latter is defined as in Dunn et al. (2010):

$$D_F = \frac{F_{0.001-100\,keV,\,disk}}{F_{0.001-100\,keV,\,disk} + F_{1-100\,keV,\,cor}}. \tag{4.1}$$

The `NTHCOMP` parameter kT_e was completely unconstrained as expected given the RXTE-PCA bandpass (see also footnote 5). It was left free to vary to avoid, as much as possible, systematic errors on the estimate of Γ, which, with the used nested sampling algorithm, is marginalised over the unconstrained kT_e. Thus, the uncertainties on Γ should include our lack of knowledge on the corona temperature. We refer to Section 4.3.2.1 for our spectral simulations and posterior predictive checks that were made to investigate the robustness of our fit results.

4.3.2.1 The robustness of spectral analysis results

In X-ray spectral analysis, the outcome of a fit should not be blindly trusted without simulations, particularly in low-count regime or when the background is at a level compatible with (part of) the source emission. Since in our science case the putative physics of the source is such that the hard component can be comparable to the RXTE background at energies above ≈ 10 keV, a more thorough investigation is needed to validate our spectral fit results. One should bear in mind

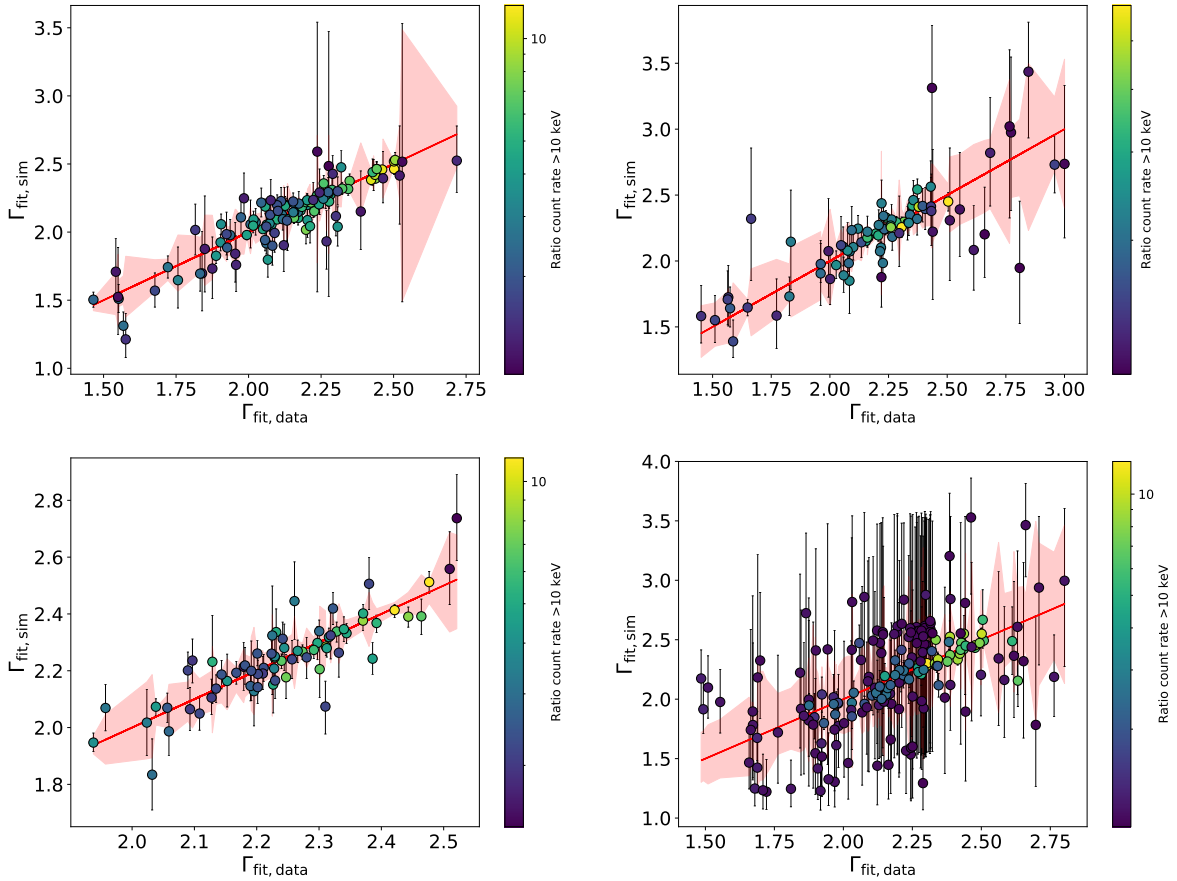

Figure 4.4: Comparison between the photon index obtained in the spectral fit (see Section 4.3.2; $\Gamma_{fit,data}$), which was then simulated and fit again ($\Gamma_{fit,simul}$). From top left to bottom right, results for SS02, SS04, SS07, and SS10 are shown. Error bars for $\Gamma_{fit,simul}$ are shown (16th-84th percentiles), whereas we show uncertainties (16th-84th percentiles) in $\Gamma_{fit,data}$ around the 1:1 relation. We colour coded data with the ratio between the total (source plus background) and background-only 10−25 keV count rates (see white and grey symbols in the top panel of Fig. 4.3).

that this does not happen necessarily only when the total flux is low, as in spectra with a strong soft component and a weak hard component the total 3 – 25 keV emission is actually around the average value of the outburst.

Two types of problems can arise in fitting the hard component that make a specific fit of a state questionable. Firstly, one may not be able to robustly fit a specific region of the source parameter space (e.g. the intrinsic photon index or hard flux) for instrumental or observational biases, for instance due to the background or to possible covariances; the fit parameters could be scattered in another region of the parameters space, physically reasonable, and the observer would have no way of knowing this from the fit alone, which can in principle appear robust. At first order, this can be tested simulating a synthetic spectrum from the best-fit parameters and fitting it again with the same model: if the input and output agree, that region of the parameters

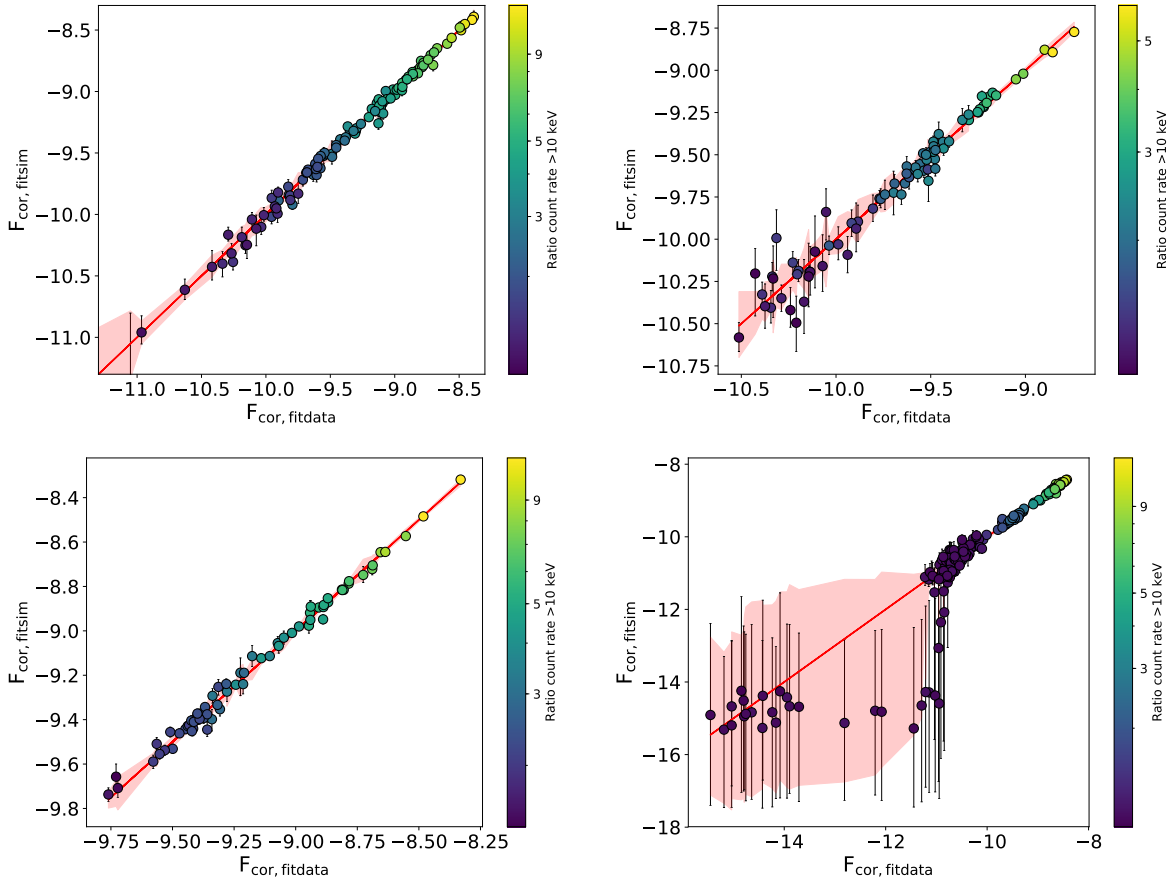

Figure 4.5: Same as in Fig. 4.4 but with the $2-10$ keV flux under the NTHCOMP model of the hard component. In the top left panel, the figure is cut around $\log F_{cor} \sim -11$ for visualisation purposes and at lower fluxes simulations and fits are compatible within their very large errors.

space is recoverable; if not, that spectral fit cannot be considered robust. Secondly, even if one is able to fit a specific parameters space region, one cannot be sure that biases have scattered a source, originally with other parameters, in the location of the parameter space where one has fit it. This is more subtle and would require a set of multidimensional spectral simulations, beyond the scope of this paper.

We try to address here the first problem with spectral simulations. We simulated each XRB state from the best-fit model with the pyXSPEC command `fake it` adding also statistical fluctuations. Then, we fit each simulated spectrum with the same model (see Section 4.3) and checked if the retrieved parameters were compatible, within errors, with the simulated spectrum (See Fig. 4.4 and 4.5). Simulations clearly show that for SS02, SS04 and SS07 all the spectral fits can be considered to be in reliable places of the explored parameters space. Instead, simulations of SS10 state that results from several observations are to be taken with caution (see bottom panels of Fig. 4.4 and 4.5): in particular, observations with relatively low count rates above ~ 10 keV, namely with a factor $\lessapprox 1.5$ in ratio between the total (source plus background)

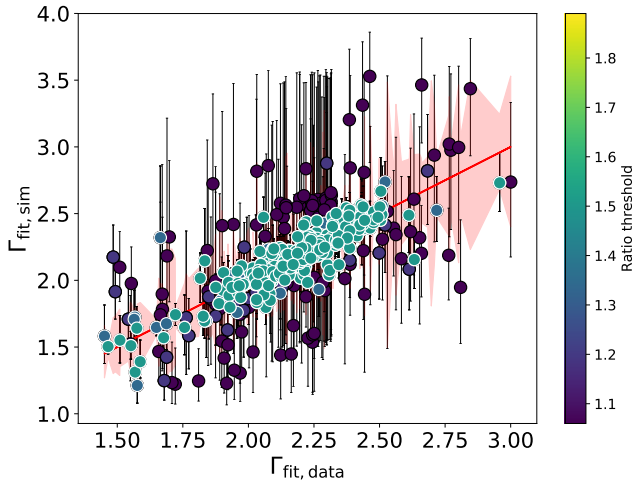

Figure 4.6: Same as Fig. 4.4, but colour coded with the threshold on the ratio between the total (source plus background) and background-only $10-25$ keV count rates. The one we adopted (i.e. ~ 1.3) is shown with white contours on data points.

and background-only $10-25$ keV count rates (see white and grey symbols in the top panel of Fig. 4.3 and Fig. 4.7). In most of these background-contaminated spectral states, the input and output values are compatible within their (very large) 1st-99th interquantile range, and therefore we are not overestimating our knowledge of the hard component even in these extreme cases. Nonetheless, it is evident that the median of the posterior distribution for Γ strongly departs from the simulated value. In Fig. 4.6 we show all the outbursts combined, colour coding the threshold of the ratio between total (source plus background) and background-only $10-25$ keV count rates, highlighting with white contours the sources above ~ 1.3. This threshold ensures that $\lessapprox 4\%$ of the input-output parameters are not compatible within their 16th-84th interquantile range. This represents the sub-sample selected for the comparison with AGN in Section 4.5. It is worth noting that in these background-contaminated states the presence of a disk only indirectly hampers the detectability of the hard component, as they do not host the brightest disks (see colour coding in Fig. 4.7).

Moreover, we show in Fig. 4.7 how this count rate ratio is related to the fit Γ in our spectral analysis. As it can be noted, our cut in ratio around 1.3 also consequently narrows the Photon Index distribution, although above it one can still note the softer-when-brighter behaviour of our SSs and SIMSs. It is a typical habit to exclude extremes Γ values from AGN samples before testing for correlations and physical interpretations, with the underlying assumption that they come from low-quality spectra. This can be true in most cases, although one can see that applying a vertical selection in Fig. 4.7 one could end up excluding not only the low-quality (or background-contaminated) states, but also the brightest-softest spectra and a few hard-faint (but still sufficiently-well constrained) spectra. Furthermore, excluding extremes X-ray slopes is a physical selection and applying it before looking for physical correlation and interpretations is a circular process. Conversely, a selection in count rate ratio is purely observational and for most

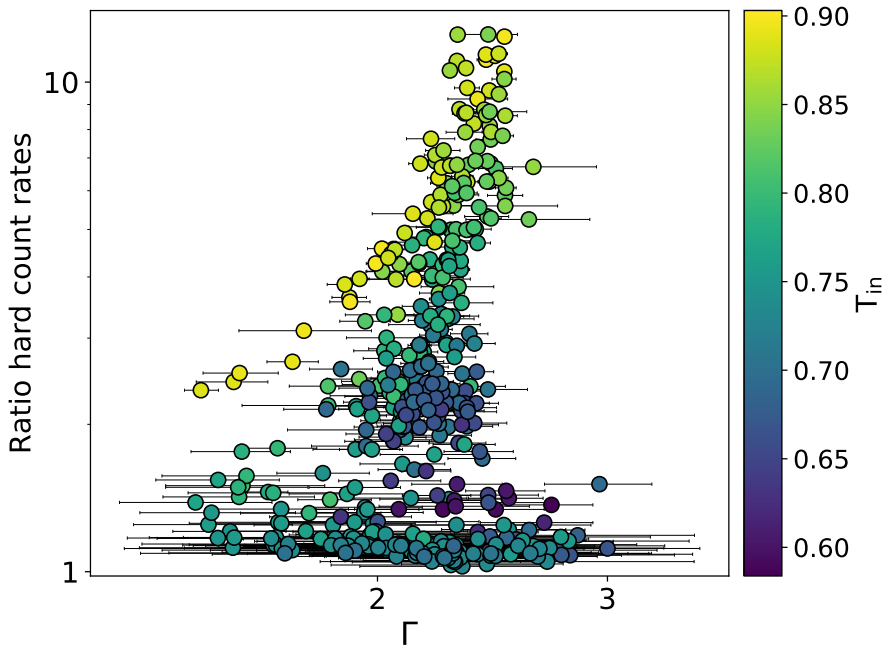

Figure 4.7: Ratio between the total (source plus background) and background-only 10 – 25 keV count rates (see white and grey symbols in the top panel of Fig. 4.3) as a function of the fit Γ, colour coded with the fit disk temperature.

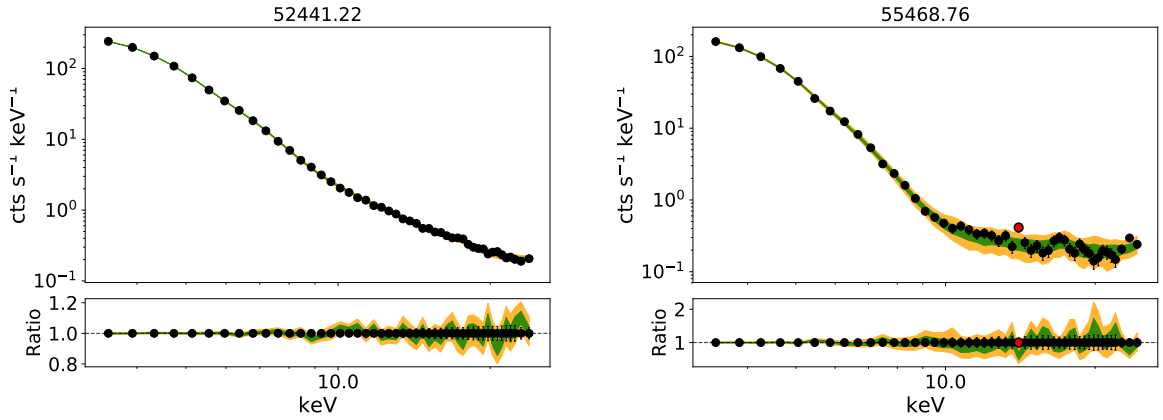

Figure 4.8: Two examples of the posterior predictive check performed simulating 300 count rate spectra starting from the best-fit parameters posterior distributions. Data points are the actual spectrum, with green and orange contours as 16th-84th and 1st-99th interquantile ranges representing the predictive power of the spectral model. Energy bins in which the observed data point was not compatible within the 1st-99th interquantile range of the predicted spectra from the best-fit models are shown in red.

of the sources results in an equivalent selection.

Finally, we also performed a posterior predictive check simulating 300 count rate spectra starting from the posterior distributions of the best-fit parameters. This is then visually compared with the original spectrum (examples in Fig. 4.8), flagging possible energy bins in which the observed data point was not compatible within the 1st-99th interquantile range of the predicted spectra from the best-fit models. This test highlights regions of the spectrum where our model predictions of future datasets significantly depart from the observed data. In general, we observe very few of these features, meaning that the uncertainties on our model are large enough not to overestimate the information drawn from the data. In particular, this check confirmed that results for most of the SSs in SS10 can be considered reliable only within the very large uncertainties and must be taken with caution. For instance, refrain from using only median values for Γ from our SS10 results instead of considering the hard component as largely unconstrained. Alternatively, the more conservative option is to adopt the sub-sample of sources above a ratio between the total (source plus background) and background-only $10-25$ keV count rates of ~ 1.3.

4.4 The disk–corona relationship in GX339-04

In radiatively efficient AGN, we observe a tight correlation between monochromatic X-ray and UV luminosities (see Chapter 3). Its small physical intrinsic scatter ($\sigma_{phys} \lessapprox 0.19-0.20$ dex; e.g. Vagnetti et al. 2013; Lusso & Risaliti 2016; Chiaraluce et al. 2018) defines the diversity in coronae emission for a given disk. Its slope, which is smaller than unity in log space, represents instead the evidence that the coronal emission increases less than the disk emission when going from fainter to brighter sources (see, e.g., Kubota & Done 2018; Arcodia et al. 2019).

A similar disk-corona regulating mechanism might also be in place in SSs and SIMSs of XRBs, although previous comparisons have only been qualitative. For example, the XRB equivalent of the AGN α_{OX} parameter has been reported with large scatter in a relatively narrow range of soft X-ray monochromatic (i.e. disk) flux (Sobolewska et al. 2009, 2011). However, one would expect the scatter in XRBs to be smaller, since they are free from any non-simultaneity biases and the single source obviously comes with the same mass, distance, and inclination.

In this work we want to populate the $\log F_{disk} - \log F_{cor}$ plane (hereafter also simply referred to as $F_{disk} - F_{cor}$), which is the XRB equivalent of the $L_X - L_{UV}$ (or $\alpha_{OX} - L_{UV}$) relation in AGN (see Arcodia et al. 2019, and references therein). With respect to earlier literature, we refined the choice of the observables going in the $F_{disk} - F_{cor}$. For instance, we refrained from using a monochromatic flux in the soft band obtained with the full (soft plus hard component) model (e.g. as in Sobolewska et al. 2009) as a disk emission proxy, as this would bias the estimate in a relatively unpredictable way moving along the HLD. In the bottom panels of Fig. 4.3 one can see the D_F distribution: even conservatively selecting states above $D_F \sim 0.8$ (e.g., Dunn et al. 2010), there is still up to $\sim 20\%$ of the total flux coming from the Comptonisation component. Instead, we computed our disk and corona emission proxies with fluxes under the single `DISKBB` and `NTHCOMP` model, respectively. Moreover, the hard component in SSs and SIMSs can fluctuate down to the background level (e.g. see white symbols with respect to the grey in the top panel of Fig. 4.3), and therefore we consider our approach of modelling the background emission crucial

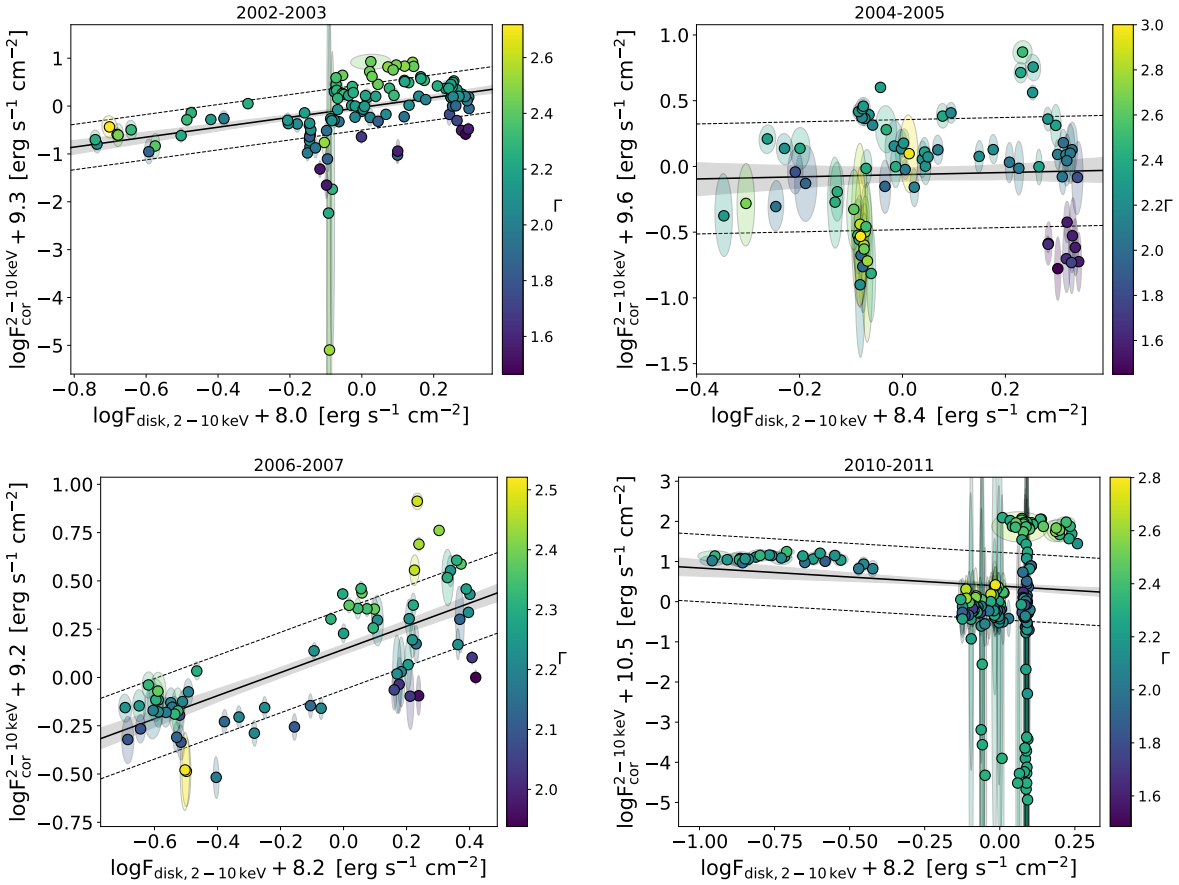

Figure 4.9: $F_{disk} - F_{cor}$ plane for SS02, SS04, SS07, and SS10 (from top left to bottom right), with fluxes scaled with their median value. As uncertainties, we report 3σ contours of the 2D distribution of fluxes from the posterior chains, shown with ellipsoids. The solid black line is the median regression line obtained with emcee, with the corresponding 16th and 84th percentiles represented with the shaded grey area. The dashed black lines show the fit scatter around the median relation.

to disentangle the hard component and the background, minimising statistical problems related to the counts-subtraction process (e.g. Loredo 1992; van Dyk et al. 2001).

In the following sections, unless otherwise stated, we use the $2 - 10$ keV flux under the single `DISKBB` and `NTHCOMP` model as proxy for the disk and corona components, respectively. We adopted a non-monochromatic proxy because the corona emission estimate was found to be more stable against the variations of the putative disk–corona relation due to the Γ distribution, and the $2 - 10$ keV band because it is more easily comparable with AGN (see Section 4.4.1.1 for differences in the $F_{disk} - F_{cor}$ among the different proxies).

Table 4.1: Summary of slope and scatter of the $\log F_{disk} - \log F_{cor}$ plane computed in the 2 – 10 keV energy band across the four outbursts. The second-to-last row refers to results with a joint analysis on the combined 458 states, the last is obtained on a subset of the total sample described in Section 4.4.3.

Outburst	Slope	Scatter
SS02	1.04 ± 0.18	0.47 ± 0.03
SS04	0.08 ± 0.25	$0.42^{+0.04}_{-0.03}$
SS07	0.60 ± 0.07	0.21 ± 0.02
SS10	-0.45 ± 0.22	0.84 ± 0.05
All	0.34 ± 0.12	$0.71^{+0.03}_{-0.02}$
All_r1.3	0.47 ± 0.07	0.41 ± 0.02

4.4.1 The robustness of the observed relationship

4.4.1.1 Testing different proxies for the disk and corona emission

Throughout this study, we use the 2−10 keV flux under the single `DISKBB` and `NTHCOMP` model as proxy for the disk and corona component, respectively. Here, we investigate whether our results change with a different proxy. For what concerns the $F_{disk} - F_{cor}$ in XRBs only, we tested the adoption of fluxes in the range 3 – 25 keV (the full energy range used in our spectral analysis) or a broader band: $F_{0.001-100\,keV,\,disk} - F_{1-100\,keV,\,cor}$ (e.g. Dunn et al. 2010). As shown in Table 4.2, the scatter values and slopes are compatible within errors.

Moreover, in Section 4.5 we changed the disk proxy using a monochromatic flux for the disk emission at 0.2 keV, which is the rough low-mass equivalent of what is 3000Å for AGN. We then tested if in the XRBs dataset the change in disk proxy affects what is described in Section 4.3.2 and 4.4. As shown in Table 4.2, all the scatter and most of the slope values are compatible within errors. The fact that some slopes are not validates our choice of using the scatter of the $F_{disk} - F_{cor}$ to test the disk-corona relation in XRBs. It also argues that uncertainties in extrapolation of the RXTE response down to 0.2 kev and in N_H (which we leave free to vary within a ±15% of the tabulated value) are minimal or affect mostly the slope, if anything.

4.4.1.2 Testing a different accretion disk model

Throughout the work, we used `DISKBB` as disk model for its simplicity and better coupling with the Comptonisation model `NTHCOMP`, with respect to more accurate disk models (e.g. `BHSPEC`, Davis & Hubeny 2006). `DISKBB` simply fits for the temperature at the inner disk radius T_{in} and for the normalisation, which is a function of the inner radius R_{in}, the distance d of the source and inclination i of the disk. Knowing R_{in} and its evolution is not the purpose of this work, and therefore the large uncertainties on d and i (see, e.g., Heida et al. 2017; Zdziarski et al. 2019) are

not of great concern. Instead, the BHSPEC parameters are $\log L/L_{Edd}$, which is the luminosity of the accretion disk as a fraction of the Eddington luminosity, d, i, m and the spin a_*. This model would in principle provide a more physical description of the accretion disk emission in terms of more useful source parameters with respect to DISKBB, although all these are very uncertain and extremely debated parameters (e.g. Hynes et al. 2003, 2004; Zdziarski et al. 2004; Muñoz-Darias et al. 2008; Kolehmainen & Done 2010; Parker et al. 2016; Ludlam et al. 2015; García et al. 2015; Heida et al. 2017; Zdziarski et al. 2019). Fixing them, despite the large uncertainties, would be a much greater approximation than using DISKBB, with much less control on the many degeneracies and large dimensions involved in the problem; and the more proper approach of jointly fitting for d, i, m and a_* across all the 458 states would be prohibitive.

Here, we explore the use of BHSPEC and test whether or not our data are good enough to try and directly constrain the disk parameters. We first separately fit 44 states which show a ratio between the total (source plus background) and background-only $10-25$ keV count rates below ~ 1.1, ensuring minimum contamination from non-disk components. We leave m, d, i and a_* free to vary (within $m = 3-10$, $d = 7-12$ kpc, $i = 5^\circ - 77^\circ$ and $a_* = 0-0.9$) in addition of $\log(L/L_{edd})$ and the other source parameters of NTHCOMP and the Gaussian model (see Section 4.3.1). Despite the good fits, the distribution of fit BHSPEC parameters is quite diverse and unconstrained and their errors quite large. Secondly, we simultaneously fit the three states with the lowest ratio between the total (source plus background) and background-only $10-25$ keV count rates, keeping m, d, i and a_* tied together and the other source parameters free to vary. This yields a good fit with median values of $m \sim 5.8$, $d \sim 7.8$ kpc, $i \sim 25^\circ$ and $a_* \sim 0.47$. However, adding one or two more states to the simultaneous fit does not reach convergence, with the sampling far from the minima found with three sources. For this reason and the fact that among the 44 states separately fit there was generally poor agreement, we refrain from using any estimate of m, d, i and a_* coming from the simultaneous fit for more than just Eddington-ratio related calculations.

Now, we fit all the states in SS02 with the same configuration as in Section 4.3.1 (fixing the seed photons temperature to the value obtained with DISKBB) but with BHSPEC fixed at $m \sim 5.8$, $d \sim 7.8$ kpc, $i \sim 25^\circ$ and $a_* \sim 0.47$ and free accretion rate. This allows us to estimate whether, despite the non-robust source parameters for the disk model, the impact of a different accretion disk model on our results is significant. The slope and scatter of the $F_{disk} - F_{cor}$ plane are 0.88 ± 0.13 and 0.34 ± 0.03 respectively, to be compared with the DISKBB run[8] which yields 0.88 ± 0.17 and 0.40 ± 0.03. Both values are compatible within errors. Instead, BHSPEC yields a mean $\Gamma \sim 2.46$ with respect to $\Gamma \sim 2.14$ obtained with DISKBB.

Finally, we use this BHSPEC run on SS02 to compute a correction on the monochromatic F_{disk} at 0.2 keV, since DISKBB is known to underestimate the very soft emission in an RXTE-like instrument, even if above ~ 3 keV the two models produced the same flux (see Done & Davis 2008). DISKBB has reportedly a narrower band-pass with respect to more physical models including radiative transfer in each disk annulus, of the order of a colour correction which is however not constant in radius, and relativistic effects (e.g. Davis & Hubeny 2006). This narrower band-

[8]Both results refer to a SS02 subsample of 105 states above the threshold of ~ 1.3 of counts ratio between source plus background and background only; see Section 4.3.2.1.

Table 4.2: Same as Table 4.1, but with additional columns: marked with _3-25 and _full, obtained within $3 - 25$ keV and $F_{0.001-100\,keV,\,disk} - F_{1-100\,keV,\,cor}$, and with _0.2, obtained with $F_{0.2\,keV}$ as a disk proxy.

Outburst	Slope_3-25	Scatter_3-25	Slope_full	Scatter_full	Slope_0.2	Scatter_0.2
SS02	$1.21\pm^{+0.17}_{-0.16}$	0.40 ± 0.03	1.44 ± 0.21	0.41 ± 0.03	1.49 ± 0.39	$0.51^{+0.04}_{-0.03}$
SS04	$0.45^{+0.25}_{-0.27}$	$0.39^{+0.04}_{-0.03}$	$0.30^{+0.30}_{-0.31}$	$0.38^{+0.04}_{-0.03}$	$-0.73^{+0.42}_{-0.44}$	$0.41^{+0.04}_{-0.03}$
SS07	0.64 ± 0.07	0.19 ± 0.02	$0.69^{+0.08}_{-0.09}$	0.20 ± 0.02	0.74 ± 0.12	0.24 ± 0.02
SS10	$-0.48^{+0.21}_{-0.22}$	$0.78^{+0.05}_{-0.04}$	$-0.74^{+0.24}_{-0.23}$	0.76 ± 0.04	-1.28 ± 0.27	$0.80^{+0.05}_{-0.04}$

pass results in underestimation of soft fluxes in RXTE-like instrument or the hard-flux end of the disk emission in CCD-like instruments (see Done & Davis 2008). The offset was quantified to be a fairly narrow distribution with a median of ~ 0.26 dex, for RXTE-PCA at 0.2 keV.

4.4.2 The $F_{disk} - F_{cor}$ plane across the outbursts

In this section we focus on the $\log F_{disk} - \log F_{cor}$ plane across the four outbursts of GX 339-4 separately in order to see if and how they compare. We show the relations in Fig. 4.9 and report the related results of the linear regression performed with `emcee` (Foreman-Mackey et al. 2013) in Table 4.1. The full relation used is $\log F_{cor} - c_1 = a + b\,(\log F_{disk} - c_2)$, where c_1 and c_2 are the median value of $\log F_{cor}$ and $\log F_{disk}$, respectively (i.e. a different scaling for each regression). Uncertainties on all variables and an additional scatter term (hereafter also referred to as observed scatter) were accounted for using the likelihood provided in D'Agostini (2005).

The main conclusion from Fig. 4.9 is that, at first glance, the four separate $\log F_{disk} - \log F_{cor}$ planes do not appear the same. First, the linear correlations do not show evidence of a common slope, which instead spans positive to negative values. A possible reason for this might be that the dynamic range covered by F_{disk} (i.e. the horizontal axis) of one order of magnitude and even less is too small for a solid estimate of the slope. Such a range is in fact not even close to the three to four orders of magnitude spanned by UV luminosities in bright AGN (e.g. Lusso & Risaliti 2016). This is discussed further in Section 4.5, nevertheless here we conclude that the slope in the $F_{disk} - F_{cor}$ plane does not appear to be a good proxy for the disk–corona physics in XRBs.

Furthermore, the path of an outburst in the HLD also somewhat reverberates on the $\log F_{disk} - \log F_{cor}$. It is particularly evident in SS10, where both the HLD and the $\log F_{disk} - \log F_{cor}$ are populated by three clumps (e.g. see the bottom panel of Fig. 4.9 and the yellow points in Fig. 4.1). Moreover, in Fig. 4.9 data points seem to oscillate around the putative relation rather than sitting on it; these abrupt changes in F_{cor} for a narrow range of F_{disk} reflect the horizontal paths in the HLD commonly observed during SSs and SIMSs, in which a source can significantly change its hardness ratio while maintaining the same total (disk-dominated) luminosity (e.g. see Fig. 4.1). This could be either a peculiarity of XRBs or a trend that we would observe in more massive sources if the coverage was of comparably high cadence. However, a crude mass-scaling of these relatively short timescales (i.e. days) would be around hundreds of thousands of years for

AGN.

Finally, the observed scatter, which is in general very high (between $\sim 0.2 - 0.8$ dex), also seems to be inconsistently different across the outbursts, although it appears to be clearly proportional to the range spanned by Γ during the outburst (see colour coding in Fig. 4.9). Before comparing XRBs to AGN, the data for the former need to be homogenised across the outbursts and the differences among them understood and addressed. In particular, the observed scatter seems a more promising and understandable proxy of the disk–corona relation in XRBs and will be the focus of the following section.

4.4.3 The observed scatter of the disk–corona relation

The scatter of the $F_{disk} - F_{cor}$ relation is likely due to a combination of factors and, before a comparison with AGN is performed, a more thorough test on our whole GX 339-4 dataset is necessary since it spans rather different values across the outbursts. For instance, the scatter does not depend on the luminosity range covered by an outburst in the HLD or by the dynamic range in F_{disk} (i.e. accretion rate). This is indicated by the scatter in SS04 being compatible with that in SS02, despite the former having a much lower spread in F_{disk} (see Fig. 4.9) and in $L_{3-10\,keV}/L_{edd}$ (see Fig. 4.1); and by the fact that SS02 and SS07 span roughly the same range in luminosity and disk temperature, somewhat related to accretion rate, despite the latter showing an incompatibly smaller scatter. Conversely, the scatter appears to be lower for outbursts with a narrower Γ distribution and particularly high in SS10, for which several states had hard count rates ($\gtrsim 10$ keV) at background level (see top panel in Fig. 4.3).

The two quantities seem to be somewhat correlated, as Γ seems to reach the extremes of its distribution mostly in these background-contaminated states (see Fig. 4.7). Nonetheless, since a simple cut in Γ is rather arbitrary and there is no physical reason to remove the flat or steep end of the corona emission a priori, it is experimentally meaningful to test the impact of the background influence on the scatter of the $F_{disk} - F_{cor}$. Moreover, this test is particularly relevant for the comparison with AGN (Section 4.5), for which the disk is observed in a different energy band, and background-dominated coronae would be either undetected, or poorly constrained and therefore excluded from any quality selection.

We show in the top panel of Fig. 4.10 how the scatter of the $F_{disk} - F_{cor}$ changes as a function of a cut performed on the ratio between the total (source plus background) and background-only $10 - 25$ keV count rates (see, e.g. white and grey symbols in the top panel of Fig. 4.3). In Fig. 4.10, grey symbols show results obtained excluding SS10, stating that the enormous scatter is mostly due to some SS10 states in which the hard component is background-contaminated. From spectral simulations (see Section 4.3.2.1), we conservatively obtained a value of ~ 1.3 for this count-rate ratio above which all spectral fits can be considered robust. Above this threshold, the fraction of states that did not retrieve the input Γ within the 16th-84th interquantile range in the simulations is below $\sim 4\%$ and remains roughly constant. Moreover, this value is also approximately where the scatter with and without SS10 share the same trend (top panel of Fig. 4.10), namely where the critical states seem to be excluded.

Furthermore, an accurate comparison between XRBs and AGN should take their different sampling and evolution timescales into account. Building the $F_{disk} - F_{cor}$ plane with multi-epoch

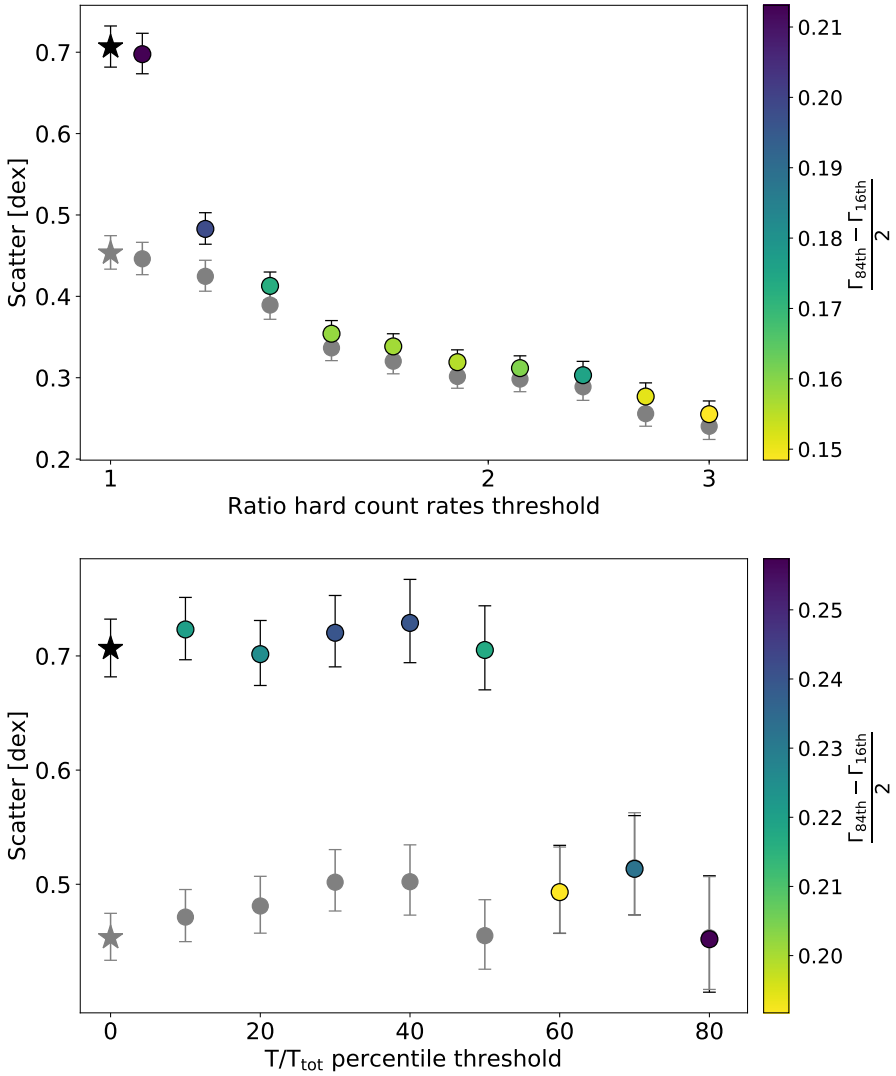

Figure 4.10: *Top panel*: Scatter of the $F_{disk} - F_{cor}$ relation as a function of a cut in the ratio between the total (source plus background) and background-only 10−25 keV count rates. Coloured points are relative to the full sample and coded with the 16th-84th interquantile range in the related Γ distributions, whereas grey points are obtained excluding SS10. Stars correspond to the starting sample with no filters. *Bottom panel*: Scatter as a function of a cut in the fraction of time spent by GX 339-4 in a region of the outburst, including SSs and SIMSs only (see Section 4.4.3 for a detailed description). Colour coding and symbols are the same as in the top panel.

observations of a single super-massive AGN requires too greater an effort, although the first test cases at the low-mass end are now being explored (e.g. Ruan et al. 2019b). Therefore, large AGN samples are typically used to trace the evolution of one (or a few) XRB(s), assuming a putative scaling between the two classes. AGN would be preferentially found in periods of their evolution that broadly correspond to regions of the HLD where XRBs spend most of their time. Therefore,

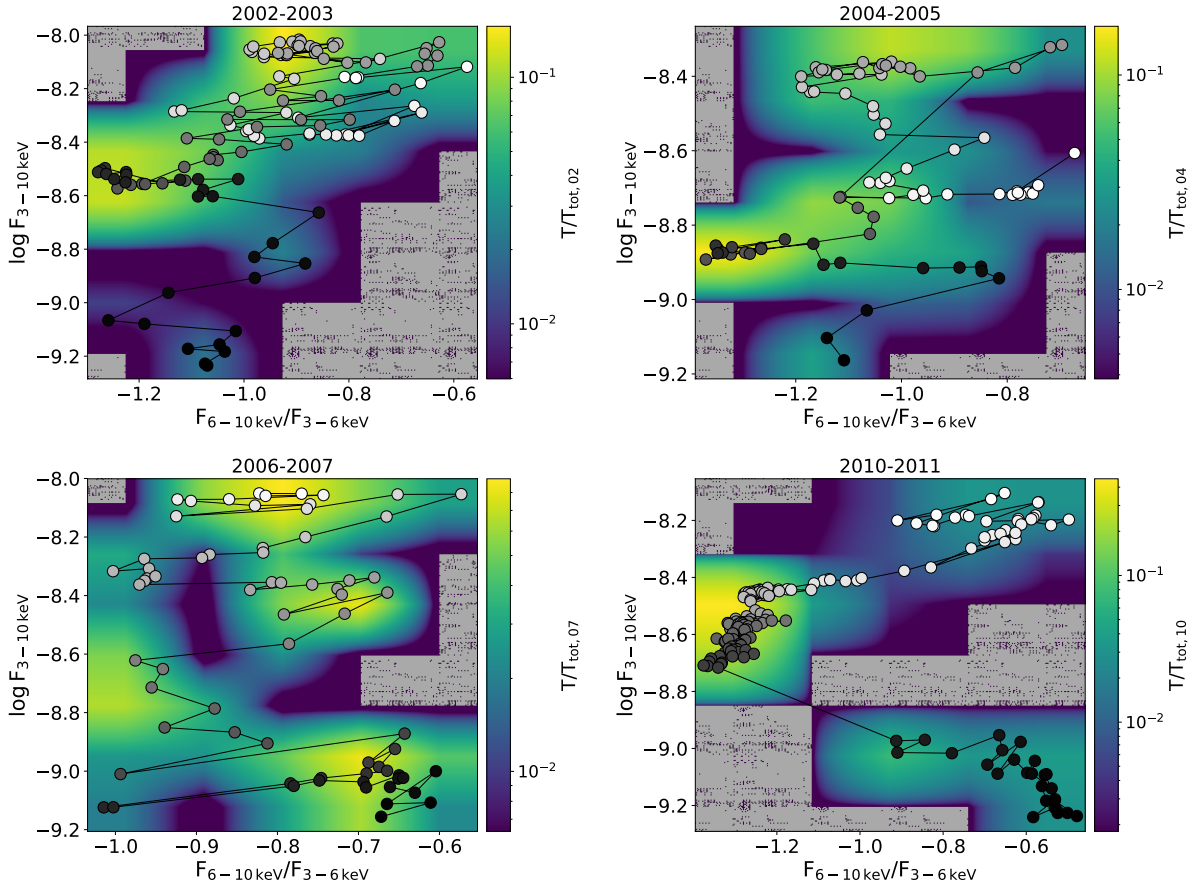

Figure 4.11: Hardness-intensity diagram of the four outbursts, colour coded from white to black, with MJD values, superimposed to a smoothed map showing the fraction of time spent in each region, including only SSs and SIMSs.

we tried to compute a rough but motivated estimate of the fraction of time spent by GX 339-4 in each portion of its SS and SIMS phases combined, for each outburst separately. We first verified that the duration and cadence of observations were fairly uniform, which is often the case with monitoring instruments like RXTE. We then computed a modified duration adding half of the unobserved time fraction, both before and after, to each observation exposure in order to sample the whole SS and SIMS duration. We then built a grid in HR (six bins) and luminosity (eight bins) in the HLD and summed this extended duration in each bin. The resulting smoothed maps obtained by normalising for the total time spent in the SS and SIMS for each outburst separately, are shown in Fig. 4.11.

The bottom panel of Fig. 4.10 shows how the scatter of the $F_{disk} - F_{cor}$ changes as a function of a cut performed on this fraction of time T/T_{tot} (which colour codes Fig. 4.11). Because each SS-SIMS outburst did not last the same amount of time, we cut the data subsets selecting above a given percentile (e.g. from the 10th to the 80th) of T/T_{tot}, with the actual value then changing among the outbursts accordingly. As can be seen in Fig. 4.10, the scatter changes as a function

of the cut in the time fraction only if SS10 is included and this is a spurious effect driven by the background contamination described above: the scatter jumps to lower values around the cut with the 50th percentile of T/T_{tot} simply because the low F_{cor} data points in SS10 are cut out of the data set; as a matter of fact, there is no evolution if SS10 is left out from the exercise (grey points in the bottom panel of Fig. 4.10). Hence, the scatter in XRBs is not high because of the frequent sampling and the shorter variability timescales.

Summarising, the overall conclusion to be taken from this section is that the scatter in the $F_{disk} - F_{cor}$ plane for XRBs is very high mostly because of a subset of spectra in which the hard band count rate ($\gtrsim$ 10 keV) is comparable to the background level (see also Section 4.3.2.1). Nonetheless, even excluding the most critical states (e.g. a ratio of $\gtrsim 1.3 - 1.5$ in the top panel of Fig. 4.10) the scatter of the relation is between ~ 0.30 and 0.45 dex, still higher than what is claimed to be the physical scatter of the $L_{disk} - L_{cor}$ in AGN ($\lessapprox 0.19 - 0.20$ dex; Lusso & Risaliti 2016; Chiaraluce et al. 2018). Furthermore, we stress that in XRBs, all disk–corona data come simultaneously and from the same source, namely from constant mass, distance, and inclination, even if the estimates are uncertain in an absolute sense. Therefore, the source of this scatter cannot be due to these factors, which makes the high observed scatter even more puzzling. This result is important because a higher scatter for XRBs would either disfavour a common scale-invariant accretion paradigm, or would mean that the physical scatter in AGN is not necessarily as low as we think.

Here, we showed that different outbursts are not intrinsically homogeneous, the main differences being both observational (a different background contamination of the hard component) and physical (different Γ distribution spanned during the outbursts). Based on the above arguments and on spectral simulations (see Section 4.3.2.1), we solved the former selecting a subset of XRB states that are above a ratio between the total (source plus background) and background-only 10−25 keV count rates of ~ 1.3. The top and bottom panels of Fig. 4.12 show the $F_{disk} - F_{cor}$ relation of the full XRB sample and the one of this subset, respectively. The related slope and scatter in the last two rows of Table 4.1.

In Fig. 4.13 we show count spectra and the related spectral energy distributions (SEDs) of three states, selected by taking the 10th, 50th, and 90th percentile of $\log F_{cor}$ in a narrow range of F_{disk} (namely around a ± 0.05 dex of the median $\log F_{disk}$). This allows us to more clearly illustrate the scatter in the $F_{disk} - F_{cor}$ as a variety of observed spectra and modelled SEDs. Data and models are colour coded by the fit Γ to highlight the softer-when-brighter trend (where both softer and brighter here refer to $\log L_{cor}$ alone in this context) also visible from the colour coding of Fig. 4.9. These three states are represented by red-contour data points in the bottom panel of Fig. 4.12.

4.5 Comparisons between XRBs and AGN

For the rest of the AGN–XRB comparison, we adopt an Eddington-normalised (i.e. mass-normalised) monochromatic luminosity (i.e. $\nu L_{disk,\nu}/L_{edd}$) as disk proxy, which is computed at 0.2 keV and 3000Å for XRBs and AGN, respectively. The physical reason for adopting 0.2 keV is that this energy is roughly the XRB equivalent of what is 3000Å for AGN, assuming $\nu \propto m^{-1/4}$

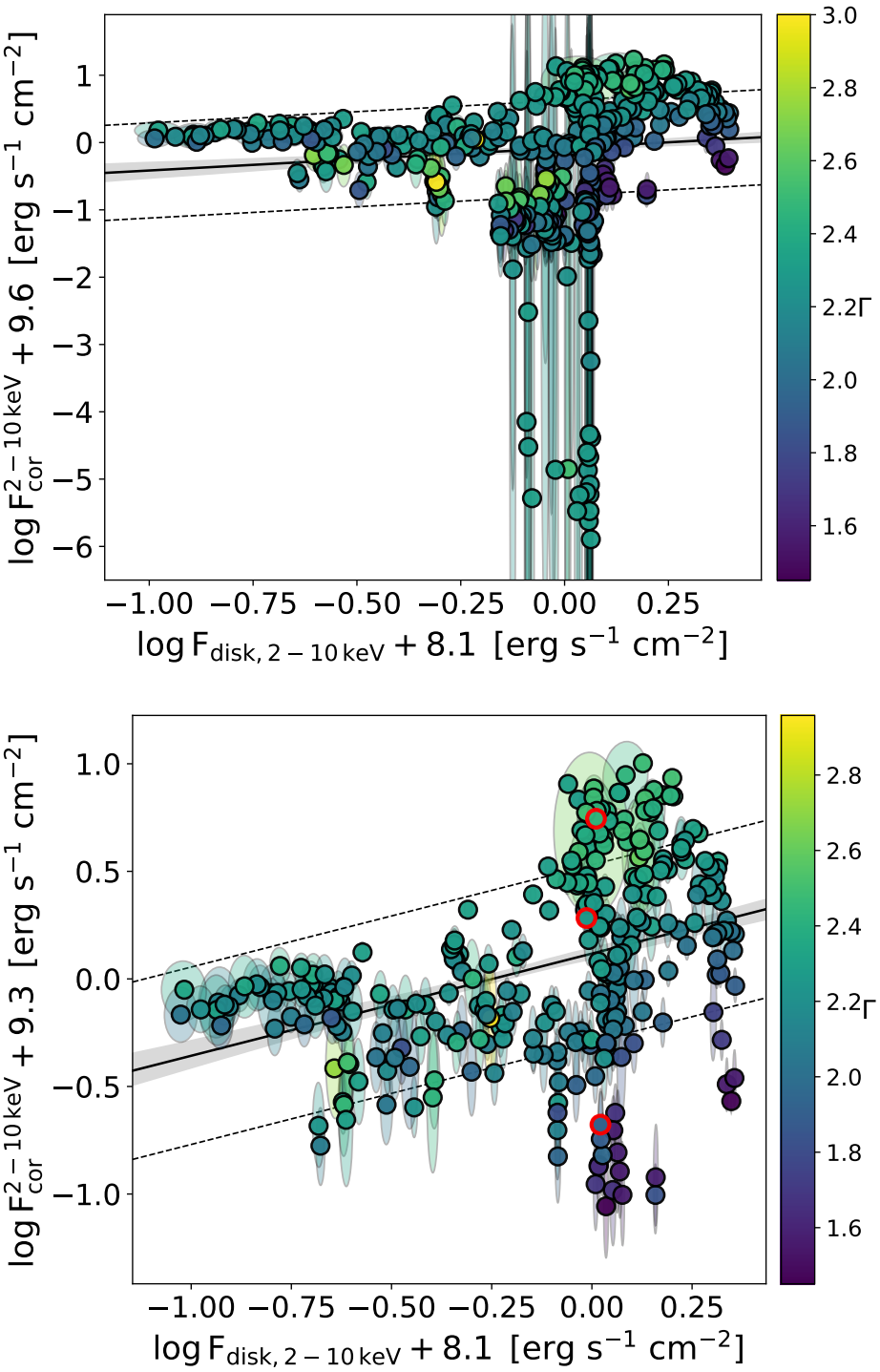

Figure 4.12: $F_{disk} - F_{cor}$ plane as described in Fig. 4.9, but shown here for all outbursts combined (*top panel*) and for the subset used for the comparison with AGN (*bottom panel*), as described and motivated in Section 4.4.3. In the bottom panel, points with a red contour highlight three states taken as examples for Fig. 4.13.

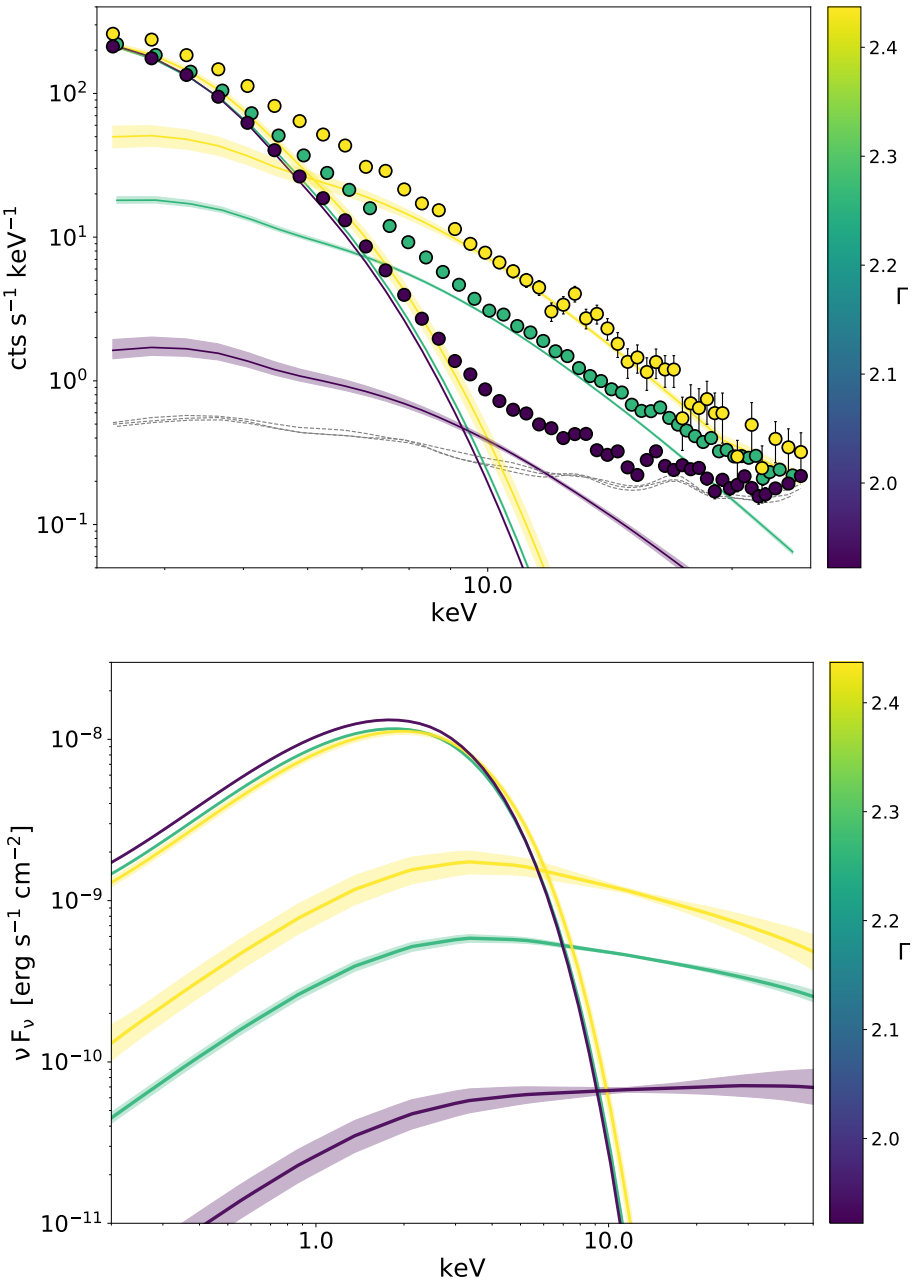

Figure 4.13: Examples of observed spectra with best-fit models (*top*, including background, shown with a grey-dashed line) and modelled spectral energy distributions (*bottom*, without background) of three states, selected taking the 10th, 50th, and 90th percentile of $\log F_{cor}$ in a narrow range of F_{disk} (namely around a ±0.05 dex of the median $\log F_{disk}$). Both data and models are colour-coded with the fit Γ, highlighting a softer-when-brighter trend in $\log F_{cor}$. These three states are represented by red-contour data points in the bottom panel of Fig. 4.12.

for a given Eddington ratio (e.g. Calderone et al. 2013). We note that, from an experimental point of view, at such a soft energy the required extrapolation of the RXTE response is large and there are covariances with the Galactic column density value. For the latter, we note that we left N_H free to vary within a ±15% of the tabulated value (e.g. Arcodia et al. 2018) in the spectral fits; thus this effect can be considered under control as we are marginalising over this uncertainty interval in Galactic N_H. We also tested in Section 4.4.1.1 the impact of this change of disk emission proxy on the results discussed in the previous sections. All the scatter values remain compatible within their 16th-84th interquantile range (see Table 4.2), stating that uncertainties in N_H and in the RXTE response extrapolation are not significant. In addition, we added an offset to the 0.2 keV fluxes in order to correct for the known underestimation of soft fluxes in RXTE-like instruments by `DISKBB` (refer to the end Section 4.4.1.2 for a more detailed description).

Instead, the proxy for the corona is the Eddington-normalised broadband luminosity (L_{cor}/L_{edd}, also in erg cm^{-2} s^{-1}) computed in the $2-10$ keV energy band, which is easily available for both XRBs and AGN. We adopted a black hole mass $m = 5.8$ and a distance $d = 7.8$ kpc to estimate these luminosities for GX 339-4 (see Section 4.4.1.2). The estimates of mass and distance for GX 339-4 are very uncertain and are debated, although the value is obviously the same for all data points and the resulting systematic error would be imprinted in the same way on both axes for all the points.

We show this mass-normalised $\log L_{disk} - \log L_{cor}$ plane in the top left panel of Fig. 4.15 and we report regression results in the top section of Table 4.3. Data for AGN consist of a subset of 651 XMM-XXL broad-line AGN (BLAGN; Liu et al. 2016b; Menzel et al. 2016), which were obtained excluding some objects to minimise the contamination from extinction in the UV (selecting optical-UV continuum $\alpha' < -0.5$; see Liu et al. 2018b) and obscuration in X-rays (selecting sources for which the 84th percentile of the $\log N_H$ posterior is < 21.5; e.g. Merloni et al. 2014). Moreover, 44 radio-loud sources were excluded[9], which are thought to be scaled-up HIMSs (Körding et al. 2006), in order to validate our comparison with SSs and SIMSs only (see also Section 4.6.1). Hereafter, when referring to our AGN sample we refer to radiatively efficient radio-quiet AGN.

The observed scatter for the AGN sample is ~ 0.31 dex. This is higher than the putative upper-limit on the real physical scatter of the relation, tentatively estimated at $\lessapprox 0.19 - 0.20$ by controlling for non-simultaneity, variability (e.g. Vagnetti et al. 2013; Lusso & Risaliti 2016; Chiaraluce et al. 2018), and potential instrumental calibration uncertainties (Lusso 2019b). This is partially because no further selections (i.e. on Γ or X-ray counts) were performed in this work. Nevertheless, the observed scatter in AGN is incompatibly lower than in the XRB data-set (~ 0.43 dex). Furthermore, the dynamic range in disk luminosity is obviously larger for AGN (top left panel of Fig. 4.15) and this is related to the wider $\dot{m}$ distribution (top right panel of Fig. 4.15). The accretion rate for GX 339-4 is shown with a red dashed line distribution and was estimated from the fit T_{in} using the standard formulae of the multi-colour black body used in `DISKBB` (Mitsuda et al. 1984) with the modifications of Kubota et al. (1998), taking the radiative efficiency and innermost stable circular orbit (ISCO) given a spin of 0.5 and assuming $m = 5.8$

[9]Selected cross-matching the XMM-XXL sample with the FIRST survey (Becker et al. 1995) using both R_X and R_{uv}, as defined in (Hao et al. 2014), as radio-loudness parameter.

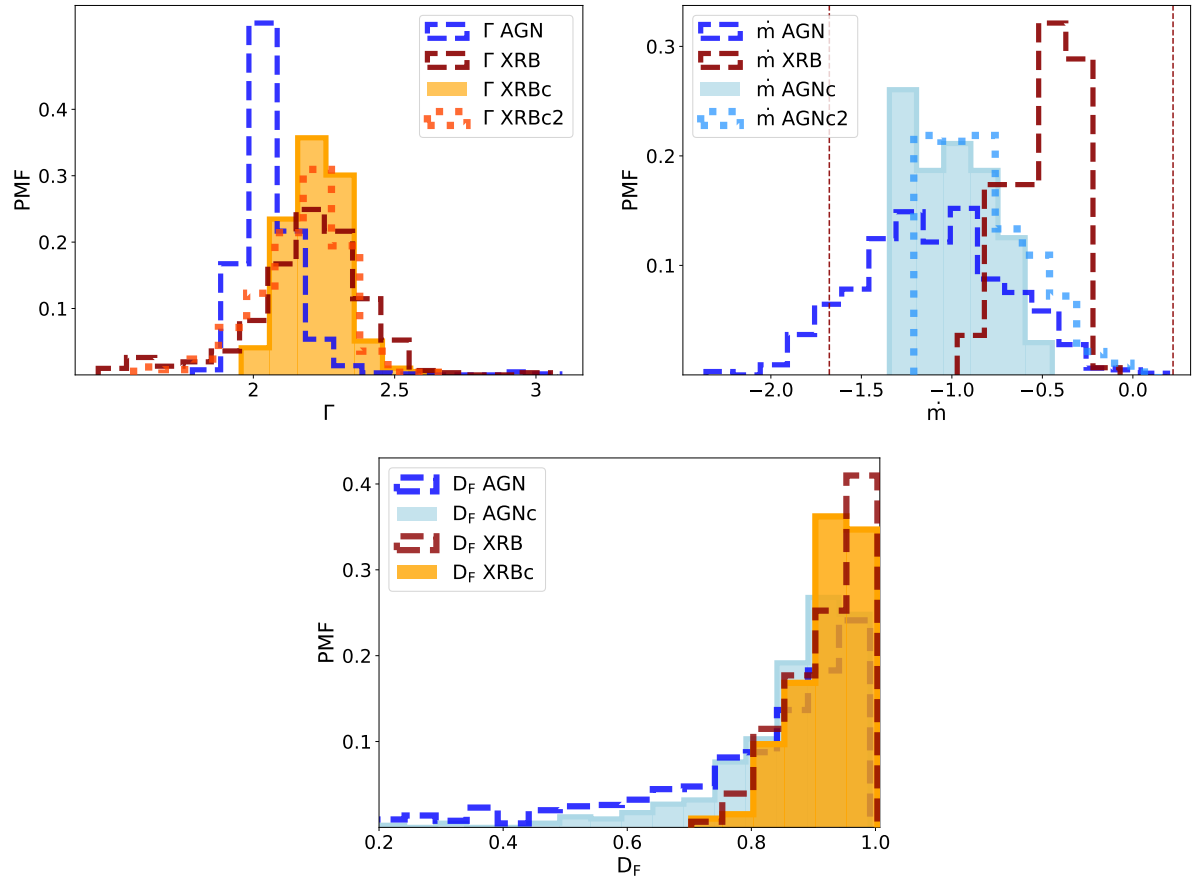

Figure 4.14: Γ, $\dot{m}$ and D_F histograms of the full AGN and XRB samples (blue and red-dashed lines) with additional subsamples: 'AGNc' (light blue) is obtained reshaping the original $\dot{m}$ distribution to be as narrow as the one in XRBs (using its 16th and 84th percentiles), albeit keeping the same median as in the full 'AGN' sample; the same reasoning is applied with the Γ distributions to select 'XRBc' (orange) from 'XRB'; instead, 'AGNc2' (dark azure) is obtained by selecting sources with $\dot{m}$ compatible within 0.4 dex with the 5th-95th interquantile of 'XRB', whereas 'XRBc2' (dark orange) follows the same reasoning, selecting Γ compatible within errors with the 'AGN' Γ distribution. The vertical dashed lines in the top-right panel represent the location of the 1st and 99th percentile of multiple XRB $\dot{m}$ distributions, obtained by converting the fit T_{in} spanning $a_* = 0-0.98$ and $m = 5-10$, while we highlight with a red-dashed histogram the one obtained with $a_* = 0.5$ and $m = 5.8$ (see text).

(see Section 4.4.1.2 for these estimates). The vertical dashed lines in the top-right panel of Fig. 4.14 represent the location of the 1st and 99th percentiles of the same distribution spanning from spin 0 to 0.98 and m from 5 to 10.

Also, the Γ distribution appears significantly different and is narrower and peaked to harder values in AGN compared to XRBs (top-left panel in Fig. 4.14). Before thoroughly addressing the possible causes for the differences between these distributions (see Section 4.6), it is intriguing

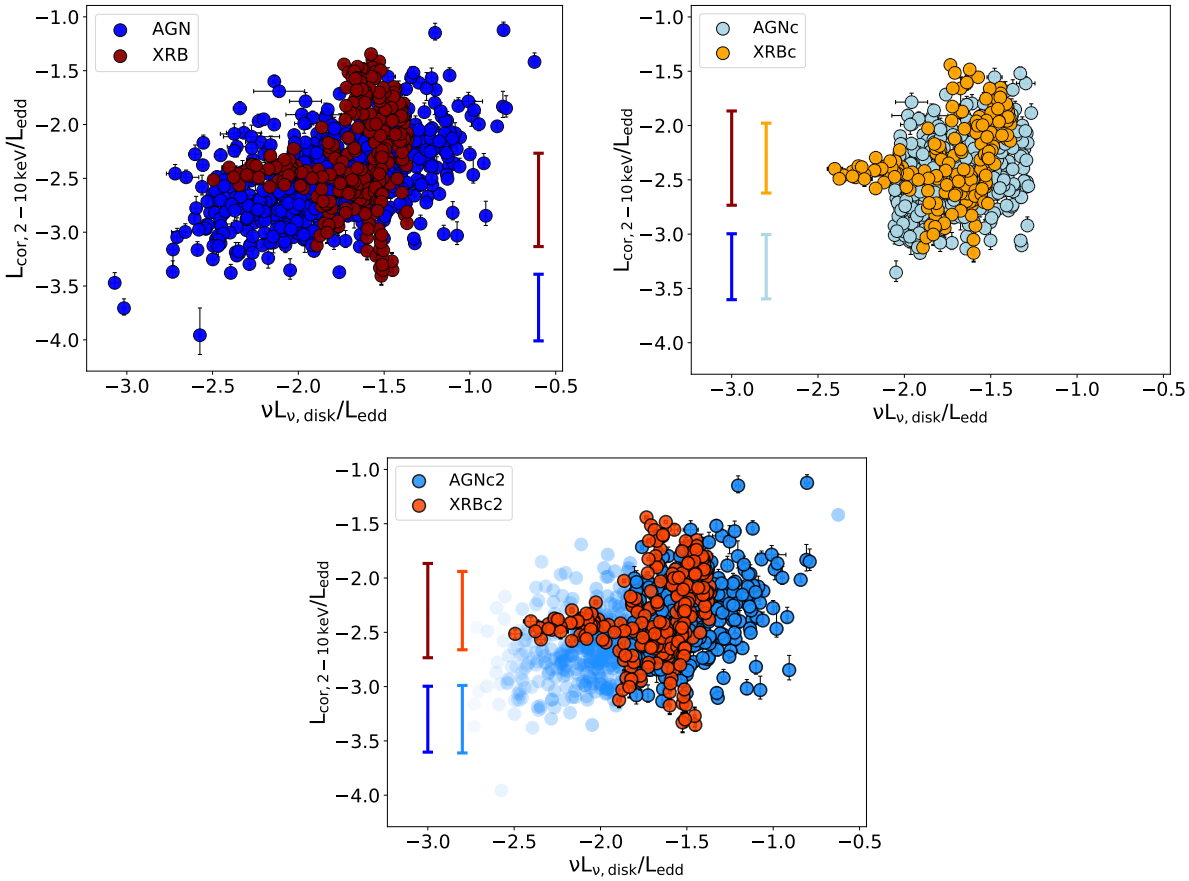

Figure 4.15: Mass-normalised log L_{disk} − log L_{cor} plane for the full AGN and XRB samples (top-left) and the 'c' (top-right) and 'c2' (bottom) subsamples (see Fig. 4.14). In the latter case, the uncertainty in determining $\dot{m}$ for XRBs (vertical dashed lines in the top right panel of Fig. 4.14) reverberated in the dark-azure points spreading in the log L_{disk} − log L_{cor} plane, covering the same dynamic range of the full AGN sample. The computed observed scatter of each relation is shown on the side, with the same colour coding as the data: 0.30 ± 0.01 dex and 0.43 ± 0.02 dex for the full samples of AGN and XRBs, respectively; 0.30 ± 0.01 and 0.33 ± 0.02 in the respective 'c' subsamples, 0.31 ± 0.01 and 0.36 ± 0.02 for the 'c2'.

that once these distributions are made equally narrow the overlap in the log L_{disk} − log L_{cor} plane becomes remarkable. For example, in the top-right panel of Fig. 4.15, light blue points are a subset (named 'AGNc') of the parent AGN sample obtained by selecting all sources with $\dot{m}$ values (taken conservatively with a ∼ 0.4 dex systematic uncertainty, coming from the mass measurement) compatible with an interquantile range as wide as the 16th-84th range of the $\dot{m}$ distribution of the XRB sample; orange points are instead a subset (named 'XRBc') of the XRB parent sample obtained by selecting all sources with Γ values compatible with an interquantile range as wide as the 16th-84th range of the Γ distribution of the AGN sample (see also Fig. 4.14). In this case, the distributions were kept at the same median values and simply narrowed according

Table 4.3: Summary of slope and scatter of the mass-normalised $\log L_{disk} - \log L_{cor}$, with a monochromatic disk proxy at 0.2 keV energy band, on the full AGN and XRB samples and their subsets, as shown in Fig. 4.14 and 4.15 and described in Section 4.5.

Sample	Slope	Scatter
AGN	0.49 ± 0.03	0.30 ± 0.01
XRB	0.39 ± 0.11	0.43 ± 0.02
AGNc	0.51 ± 0.07	0.30 ± 0.01
XRBc	0.55 ± 0.10	0.33 ± 0.02
AGNc2	0.49 ± 0.06	0.31 ± 0.01
XRBc2	0.36 ± 0.09	0.36 ± 0.02

to the other source class. However, we note that a very similar result for the observed scatter is obtained if the AGN and XRB Γ and $\dot{m}$ distributions are aligned in a different way (defined with 'c2', see Fig. 4.15), namely taking values of Γ ($\dot{m}$) for XRBs (AGN) that are compatible within errors with the 5th-95th interquantile ranges of the analogous distribution for AGN (XRBs). Regression results on both sets of AGN and XRB subsamples are shown in Table 4.3, all showing a compatible scatter within errors around ~ 0.33 dex. This is the reference value we attribute to the observed scatter in the $\log L_{disk} - \log L_{cor}$ plane for XRBs, using GX 339-4 as a test case.

4.6 Discussion

Results from Section 4.5 show that AGN and XRBs overlap considerably in the $L_{disk} - L_{cor}$ plane, in terms of a compatible observed scatter ($\sim 0.30 - 0.33$ dex) and dynamic range on the x-axis, but only after similarly broad Γ and $\dot{m}$ distributions were selected, which represent the diversity in coronae and disks, respectively. This was merely a sanity check on the putative AGN–XRB analogy and it is indeed interesting to understand why the two distributions appear different.

4.6.1 Our selection of AGN and XRB accretion states

Our comparison performed in Section 4.5 relied on the key assumption that radiatively efficient AGN not dominated by the jet emission resemble scaled up XRBs in their SS and SIMS. This association is based on the fact that for both source classes the radio emission appears to be quenched with respect to their radio-loud phases, looking both at the fundamental plane of accretion (Maccarone et al. 2003) and at the disk-fraction–luminosity diagram (Körding et al. 2006); and on the fact that the corona-loudness was already found to be broadly compatible (Sobolewska et al. 2009). It is true that the definition of XRB accretion states based on both spectral (via D_F)

or timing (via fractional rms) analysis is rather a continuum and the same should also be true for AGN. However, one can obtain a fairly reliable understanding of the HIMS-SIMS and SIMS-SS transitions from timing analysis constraints (e.g. Belloni & Motta 2016, and references therein) and this is indeed the criterion on which we mostly relied to select our SS-SIMS sample (see Section 4.2).

In this section, our aim is to further elaborate on the choice of including SSs and SIMSs and excluding HIMS from our XRB sample. We note that a comparably clear accretion state separation, which is nicely obtained in XRBs with fractional rms constraints, is more elusive for AGN where we can only more crudely rely on radio-loudness or spectral estimates. Therefore, we first tested whether the inclusion of SIMSs could also be motivated a posteriori comparing D_F estimates for both our XRB and AGN samples (see the bottom panel of Fig. 4.14). For AGN, D_F was computed extrapolating the $2-10$ keV catalogue value to the bandwidth used in Eq. 4.1 for the corona emission and with the disk luminosity defined in the XMM-XXL AGN catalogue (Liu et al. 2016b) that was approximated with standard thin-disk formulae from an optical monochromatic luminosity. The two distributions in the bottom panel of Fig. 4.14 do appear quite similar, with the only significant difference being a longer tail at low D_F for AGN, although one must bear in mind that the full-band L_{disk} estimate for AGN suffers from a much more uncertain extrapolation of the peak in the UV. From this comparison, there is no apparent reason to exclude SIMSs, which by definition sit at the lower end of the reported D_F distribution of our XRBs sample (red dashed and dot-dashed histograms in Fig. 4.16; see also Section 4.6.3.1).

We also tested the exclusion of HIMS from our analysis by fitting with the same disk–corona model the HIMS states of the 2002-2003 outburst (see Section 4.3.1), as defined by Belloni et al. (2005) with timing analysis constraints, which we note are independent of D_F-based classifications. The top panel of Fig. 4.16 shows the mass-normalised $L_{disk} - L_{cor}$ plane (as in the top-left panel of Fig.4.15) with the SS02 states (i.e. SSs plus SIMSs; dark red) plus the newly fitted HIMSs (grey squares). Soft-intermediate states are highlighted with a thicker black contour and we also show lines of approximately constant D_F with related values annotated in the figure. Hard-intermediate states indeed appear as different branches in the disk–corona emission plane, similarly to HLD diagrams, perhaps confirming that they are dominated by the jet emission processes while the SS-SIMS are not. In the bottom panel of Fig.4.16 we display instead the related D_F distributions for SS-SIMSs (dashed red) and HIMSs (grey), which show again different properties with a small expected overlap, also visible in the top panel via the drawn D_F lines. We also report the radio-loud (but radiatively efficient) AGN distribution (black-dotted line) of the 44 such sources in XMM-XXL that were excluded from our analysis, which is remarkably similar to the HIMS confirming the analogy between the two source classes (Körding et al. 2006). We therefore verified that our analysis included a relatively pure sample of radiatively efficient accreting systems which are not jet-dominated, selected among SS-SIMS in XRBs and (optical and X-ray) bright radio-weak AGN.

4.6.2 The different $\dot{m}$ distribution in AGN and XRBs

The different $\dot{m}$ distribution and dynamic range in $\log L_{disk}$ covered by the two samples (see Fig. 4.14) might indicate that the two systems do not follow the same accretion regimes. How-

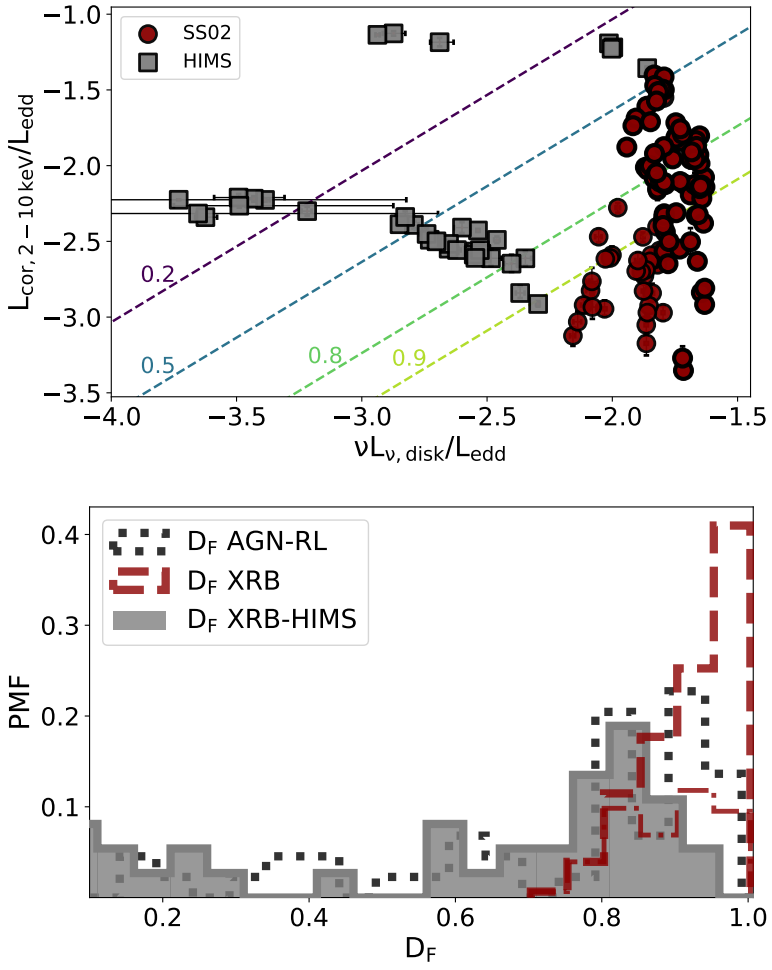

Figure 4.16: *Top panel*: Same as the top-left panel of Fig.4.15, with only the SSs and SIMSs of the 2002-2003 outburst (dark red circles, with SIMS highlighted by a thicker black contour) and its HIMSs (grey squares). Lines of approximately constant D_F are shown with dashed lines, and the related values are shown in the figure. *Bottom panel*: Same as the bottom panel of Fig.4.14, but with again the SS-SIMS (dark red dashed, with SIMS only highlighted by the dot-dashed line) and HIMS (grey) of the 2002-2003 outburst, plus the 44 radio-loud AGN excluded from our AGN sample (black dotted line).

ever, the almost four orders of magnitude span in AGN mass can play a role in enhancing this difference. Indeed, predictions from disk–corona models do indicate that for the single mass the $L_{disk} - L_{cor}$ in AGN is in place but with a much lower dynamic range in $\log L_{disk}$ (slightly more than one order of magnitude for the typical $m \sim 10^8 - 10^9$ spanning $\dot{m} \sim 0.03 - 1$; e.g. Kubota & Done 2018; Arcodia et al. 2019) , similarly to our XRB results (see Fig. 4.9 and 4.12). Moreover, $\dot{m}$ values for both AGN and XRBs are not a secure measurement, particularly if compared to a quantity such as Γ: $\dot{m}$ values for the AGN sample were computed with a single bolometric correction (5.15; Shen et al. 2008) on the monochromatic luminosity at 3000Å divided by

a notoriously uncertain mass estimate (Shen et al. 2008) which also hampers the selection of AGN within a narrow mass range; and $\dot{m}$ for XRBs was converted from the fit T_{in} distributions assuming a $m = 5.8$ and $d = 7.8$ kpc and changing these values, even within some reasonable intervals around spin and mass (e.g. $a_* = 0 - 0.98$ and $m = 5 - 10$), would significantly shift the $\dot{m}$ distribution (see top-right panel in Fig. 4.14). However, the width of this distribution would remain approximately the same and this validates our exercise in Section 4.5, where we relied on the width rather than the location of the XRB $\dot{m}$ distribution (i.e. relying on the 'c' subsamples; see top-right panel of Fig. 4.15). We conclude that AGN and XRBs do appear to have different $\dot{m}$ distributions and dynamic range in $\log L_{disk}$, although a significant role is played by the uncertainties and systematic errors on the m and $\dot{m}$ estimates. Therefore, we cannot rule out that the intrinsic $\dot{m}$ distributions are instead broadly compatible.

4.6.3 The different Γ distribution in AGN and XRBs

In principle, Γ is a quantity that can be more securely estimated (see Section 4.3.2.1). In our work, we found evidence that XRBs have a distribution that is broader and shifted to softer values with respect to AGN (see Fig. 4.14). This result is puzzling and deserves a more in-depth analysis.

The AGN sample used in this work has a Γ distribution with mean and standard deviation of $\Gamma = 2.06 \pm 0.11$. This is in line with diverse large samples of bright AGN (with either no jet or a non-jet-dominated emission) which show a fairly narrow distribution of Γ, typically centred in the range $\Gamma = 1.9 - 2.1$ up to high redshift (e.g. Vito et al. 2019, and references therein), with a dispersion spanning $\approx 0.10 - 0.40$ which is not always corrected for uncertainties and depends on the sample selection (e.g. Zdziarski et al. 2000; Caccianiga et al. 2004; Piconcelli et al. 2005; Beckmann et al. 2009; Young et al. 2009; Mateos et al. 2010; Corral et al. 2011; De Rosa et al. 2012; Liu et al. 2016b; Ricci et al. 2017; Zappacosta et al. 2018; Ananna et al. 2020). Instead, from our analysis of GX 339-4, the fitted Γ values compile a distribution that is broader and shifted to softer values, with a mean and standard deviation of $\Gamma = 2.19 \pm 0.21$. This is consistent with previous results for GX 339-4 in its SSs and SIMSs obtained with RXTE alone (Zdziarski et al. 2004; Dunn et al. 2008), with XMM-Newton and INTEGRAL data (Caballero-García et al. 2009), and with simultaneous XMM-Newton and RXTE data (Aneesha et al. 2019). For instance, cross-matching our MJD with Dunn et al. (2010) we computed $\Gamma = 2.26 \pm 0.47$ for 213 states, and from the SSs and SIMSs in Motta et al. (2009) we computed $\Gamma = 2.31 \pm 0.15$. These distributions are peaked at even softer energies, which is also in line with what is generally observed in disk-dominated states for all XRBs (e.g. Remillard & McClintock 2006). We note that this difference persists also after accounting for uncertainties in the Γ values: we sampled for the mean and intrinsic deviation with `emcee` values using the likelihood defined in Maccacaro et al. (1988), obtaining 2.07 ± 0.08 (2.20 ± 0.16) for the AGN (XRB) sample. Therefore, at least for our samples, uncertainties do not play a significant role in the difference between the two source classes.

In Section 4.5 we showed that a compatible scatter ($\sim 0.30-0.33$ dex) of the $\log L_{disk} - \log L_{cor}$ between AGN and XRBs is reached when both Γ distributions were taken with the same 16th-84th interquantile width, leaving the median values unchanged (2.04 and 2.21, respectively).

This suggests that no matter where the preferred Comptonisation slope lies, a similar scatter in Γ leads to a similar diversity in X-ray coronae for a given disk (see the top-right panel of Fig. 4.15). Indeed, in the above-mentioned literature of AGN samples there is relatively good agreement on where most of the observed Γ values lie, although there is a variety of dispersion estimates according to the varying sample selections (i.e. soft or hard X-rays), instruments, analysis techniques, and model degeneracies. Interestingly, in order to match the cosmic X-ray background shape, a diversity in photon indexes is needed (e.g. with a dispersion of ~ 0.2; Gilli et al. 2007) with an impact also on the complex parameters space involved, part of which includes Γ, the reflection fraction, and the high-energy cutoff (e.g. Ananna et al. 2020). In particular, Ananna et al. (2020) explored the allowed regions of this very complex parameters space and showed that, independently from the luminosity function assumed, even a broad Γ distribution with a dispersion of $\sim 0.2 - 0.3$ can reproduce the CXB. If the true intrinsic Γ distribution of AGN followed this scenario, it would be somewhat closer to the one observed for XRBs.

However, combining several AGN samples with very different selections and characteristics to form a homogeneous picture is beyond the scope of this work. Here we focus on addressing the role of possible contaminants shaping the observed Γ distributions (Sections 4.6.3.1, 4.6.3.2 and 4.6.3.3) and, if these are understood, explore possible similarities and differences in the physical process producing the observed distribution (Sections 4.6.3.4 and 4.6.3.5).

4.6.3.1 Possible biases: the soft-excess component

We note that only BLAGN were included in our AGN sample, although the parent XMM-XXL sample also contains narrow-line AGN (NLAGN). However, the exclusion of NLAGN does not have an impact, as their Γ distribution completely overlaps with the BLAGN one (Liu et al. 2016b). An obvious objection is that we included SIMSs for XRBs, namely the brightest spectra with almost equally strong soft and hard components, although we did not include narrow-line Seyfert1 galaxies (NLS1), which might be the AGN equivalent of SIMSs (e.g. Pounds et al. 1995; Gierliński et al. 2008). This could indeed contribute to broadening the AGN Γ distribution, as the X-ray emission in NLS1s is observed to be very soft (Boller et al. 1996). However, the overall emission is softer because an additional spectral component, broadly referred to as 'soft-excess', is present (e.g. Done et al. 2012). If this extra-component is taken into account, the emission from the hard component only would be compatible with the X-ray slopes from hot Comptonizing coronae in BLAGN: for instance, in NLS1 values around $\Gamma \sim 1.8 - 2.1$ are obtained by analysing spectra only above 2 keV (e.g. Ai et al. 2011) or looking only at the hard photon-index when a broken power law is used (e.g. Grupe et al. 2010). Hence, the Γ distribution in BLAGN can be considered representative of the observed (i.e. not necessarily the intrinsic) properties of hot coronae in AGN. However, since the hard X-ray emission in soft NLS1s is only matched to the one in BLAGN when an extra-component is added to account for the soft-excess, this begs the question of whether the same should also be expected to happen in XRB SIMSs. As a matter of fact, if the different spectral states of Mrk 1018 (Noda & Done 2018) are compared to XRBs on a HLD, the brightest ones with a strong soft-excess component would broadly overlap with bright SIMSs and not with SSs (H. Noda, private communication). Moreover, there has been evidence of intermediate states requiring an additional spectral component to the thermal disk

and hot Comptonisation alone in XRBs (e.g. Kubota et al. 2001; Kubota & Makishima 2004; Kubota & Done 2004; Abe et al. 2005; Yamada et al. 2013; Hjalmarsdotter et al. 2016; Kawano et al. 2017; Oda et al. 2019) and in GX 339-4 itself (e.g. Kubota & Done 2016).

In order to test the impact of these states on our results, we excluded SIMSs as defined in the earlier literature (see Section 4.2) and the mean and standard deviation values change from $\Gamma = 2.19 \pm 0.21$ to 2.16 ± 0.21. Thus, even including only previously defined SSs the XRB Γ distribution is still broader and peaked at softer slopes with respect to our AGN sample. Instead, the scatter in the $F_{disk} - F_{cor}$ plane would go from 0.43 ± 0.02 to $0.38^{+0.03}_{-0.02}$ dex, thus it would be compatible within errors but slightly smaller. Moreover, we conservatively tested a different selection, excluding states below $D_F \sim 0.8$ (e.g. Dunn et al. 2010): the resulting mean with standard deviation is $\Gamma = 2.18 \pm 0.21$, thus almost identical; the scatter in the $F_{disk} - F_{cor}$ plane would be 0.40 ± 0.02 dex, thus again compatible within errors but slightly smaller. Therefore, here we simply highlight that the role of SIMSs, which possibly include a soft-excess component, is not trivial and may contribute in broadening the observed Γ distribution and slightly increasing the scatter in the $F_{disk} - F_{cor}$ plane, although not to the extent needed to conciliate XRBs to AGN samples. Moreover, we showed in Section 4.6.1 the AGN D_F distribution, for which the threshold $D_F = 0.8$ is actually the $\sim$ 35th percentile, with a significant tail of lower D_F values. This would argue against the exclusion of SIMSs from the comparison.

4.6.3.2 Possible biases: X-ray absorption and continuum models

The AGN sample used in this work was compiled from the parent XMM-XXL BLAGN sample (Liu et al. 2016b; Menzel et al. 2016), minimising the extinction in the UV (selecting optical-UV continuum $\alpha' < -0.5$; see Liu et al. 2018b) and obscuration in X-rays (selecting sources for which the 84th percentile of the $\log N_H$ posterior is < 21.5; e.g. Merloni et al. 2014). We tested the impact of the latter selection criterion on the observed Γ distribution, since obscuration in AGN plays an important role within a complicated mixture of orientation and evolution effects (e.g. Klindt et al. 2019, and references therein). Further, fitting for both absorption and continuum emission in X-ray spectra within the typical $\sim 0.5 - 10$ keV energy band leads to well-known covariances between the two parameters, which enhance or hamper a possible intrinsic correlation merely for observational and/or instrumental reasons. However, we tested this and the effect of selecting very unobscured objects is minimal and the observed Γ distribution is equally narrow: for the totality of 1659 objects in the XMM-XXL BLAGN sample the mean is $\Gamma = 2.01 \pm 0.10$, with respect to $\Gamma = 2.06 \pm 0.11$ of the adopted subsample. We also conservatively tested the impact of leaving the Galactic absorption free to vary within $\pm 15\%$ of the value tabulated in Willingale et al. (2013), since this may artificially broaden the spread in Γ . We used SS02 as representative of all outburts and kept the Galactic absorption column fixed, producing an almost identical Γ distribution.

Finally, since the continuum was modelled with a simple power law for AGN (Liu et al. 2016b) and with a Comptonisation model for XRBs in this work, we verified that adopting a simple power law as well has negligible effects: we fitted states in SS02 and SS07 and obtained a compatible distribution, even shifted even more to softer values with a slightly larger width. Hence, the use of the `NTHCOMP` model had a minor impact.

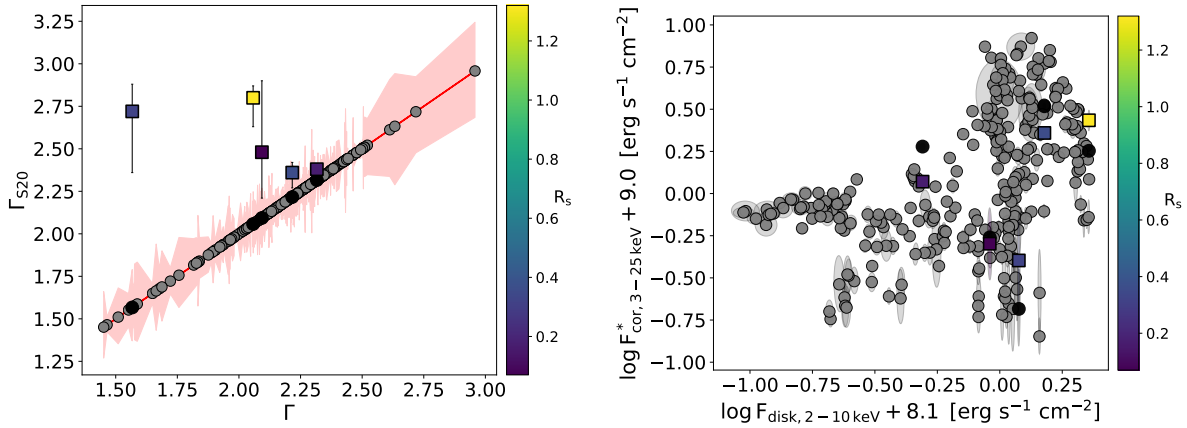

Figure 4.17: *Left panel*: Comparison between our fit Γ (black circles) and the values obtained by Sridhar et al. (2020) for the five observations in common (squares, colour coded by the reflection strength as defined by Sridhar et al.). The grey points with red contours refer to our whole sample. *Right panel*: Similar comparison in the $L_{disk} - L_{cor}$ plane where we highlight the difference between our original $F_{cor,3-25\,keV}$ (black circles) and the reflection-corrected $F^*_{cor,3-25\,keV}$ obtained with the reflection strength estimates computed by Sridhar et al. (2020).

4.6.3.3 Possible biases: X-ray reflection

Furthermore, X-ray reflection was included in the analysis of the AGN sample done by Liu et al. (2016b). We here simply empirically tested whether excluding objects with the strongest X-ray reflection (including only sources in which the 16th percentile of $\log R$ was < -0.2 and the 84th was < 0.5, where R is the ratio of the normalisation of the reflection component with respect to the power-law component) had an impact on the observed Γ distribution: the mean and standard deviation values become 2.07 ± 0.11, thus almost identical to $\Gamma = 2.06 \pm 0.11$ of the subsample adopted here.

For XRBs, we note that the reflection contribution was approximated in all spectral states with a Gaussian line bound to be centred between 6.4 and 6.97 keV, and therefore its flux did not contaminate our L_{cor} estimates. Moreover, fitting in the $3 - 25$ keV band avoided most of the contamination from the Compton hump, although the reflection spectrum can be quite complex and its contribution should be at least tentatively quantified. A thorough treatment is beyond the scope of this paper, although we performed a few tests to exclude that our simplified treatment of the reflection features had an impact on our main results. We fit SS02 (which is representative of the range of observational properties explored with the complete XRB sample) with a `laor` model (Laor 1991) and compared the newly obtained parameters (e.g. Γ, T_{in}) with the ones obtained with a simple Gaussian. The biggest effect resulted in a slight offset towards softer Γ obtained with the `laor` model, although most of the parameters are compatible within 1-sigma uncertainty intervals and almost all of them within 3σ. Hence, we consider this not to imprint a significant impact on our results and, if anything, it would enhance the difference between the observed AGN and XRB Γ distributions, strengthening our results. Moreover, Sridhar et al.

(2020) recently performed a detailed characterisation of the reflection features across the hard-to-soft transition of the 2002 and 2004 outbursts in GX 339-4. With respect to the total of 14 observations they used to sample SS02 and SS04, we only shared five, namely Obs. ID 40031-03-03-04 and 70110-01-33-00 for SS02 and Obs. ID 90704-01-03-00, 60705-01-76-00, and 90118-01-10-01 for SS04. The former two in SS02 were defined as SIMSs by Belloni et al. (2005) from timing analysis constraints and were included in our selection, while the latter in SS04 were included with our selection criterion following Belloni et al. (2006). The remaining states in Sridhar et al. (2020) were instead defined either as hard or as hard-intermediate states by Belloni et al., therefore they were not analysed in this work.

In the left panel of Fig. 4.17 we compare our fit Γ with the values from Sridhar et al. (2020), which apart from the reflection component shared the same model configuration for `DISKBB` and `NTHCOMP`. It is evident that by including the reflection, the incident Γ becomes steeper, although our median source has $\Gamma \sim 2.2$ and so the typical displacement would be small. This also appears from other works that included a reflection component in the fit of SSs and SIMSs (e.g. Plant et al. 2014) and it would increase the difference between the observed Γ distributions in AGN and XRBs even more, which is also in line with the above-mentioned `laor` model test. Furthermore, in order to check the impact on our broadband fluxes for the corona emission, we tentatively corrected them using the reflection strength defined by Sridhar et al. (2020), namely the ratio between the observed reflected component and the incident continuum component in the 20 – 40 keV band. Our original fluxes $F_{cor,\,20-40\,keV}$ were then turned into reflection-corrected $F^{*}_{cor,\,20-40\,keV}$ and then the reflection-corrected $F^{*}_{cor,\,3-25\,keV}$ was extrapolated using the asymptotic `NTHCOMP` photon index computed by Sridhar et al. (2020). We show in the right panel of Fig. 4.17 how this correction affected the five observations in common in the $L_{disk} - L_{cor}$ plane. We want to stress that this test on five sources cannot be taken as conclusive, but since the change in flux is not dramatic we can exclude a huge impact of the reflection component on our results in the $L_{disk} - L_{cor}$ plane. A proper treatment of the reflection should be done directly via spectral fitting and even then, in SSs and SIMSs it is unclear to what extent the prominent disk emission contributes to the incident radiation, both self-illuminating the outer radii from the inner ones and with returning radiation due to general relativistic effects (see, e.g. Connors et al. 2020).

4.6.3.4 Possible physical reasons for the different Γ distributions

In the previous sections we investigated some possible reasons for which the observed Γ distribution of the AGN and XRB samples might have been biased narrow or broad, respectively. Nonetheless, none of those reasons alone seems to play a major role and even a conspired combination of all is unlikely to explain all the differences. Thus, we can assume that the observed Γ distributions appear different for AGN and XRBs in their radiatively efficient phase and at least some or most of the differences is likely intrinsic to the physical mechanisms of the hard component emission. The observed differences in Γ could be due to different emission mechanisms responsible for the coronal emission in the two source classes. However, and in line with almost all past observational evidence, throughout this discussion we assume that the Γ distributions arise from hot electrons (thermally and/or non-thermally distributed; Coppi 1999; Gilfanov 2010) Compton (up)scattering the seed photons emitted by the thermal disk.

In this framework, the observational evidence we present here is that XRBs produce a preferentially softer emission than AGN. Results from MONK, a general relativistic Monte Carlo code of Comptonised spectra in the Kerr space-time (Zhang et al. 2019), indicate the opposite, namely that X-ray spectra in XRBs would appear harder if, apart from the different mass and seed photons temperature, the two source classes share the same geometry and extent of the corona, spin, inclination, and accretion rate in Eddington units (W. Zhang, private communication). Regarding the inclination, the unobscured AGN sample used here is likely composed of a mixture of objects below $\approx 30^\circ - 40^\circ$, and although the inclination in GX 339-4 is still debated, even a large difference would have a small impact on the X-ray slope above ~ 2 keV (Zhang et al. 2019). Regarding the accretion rate, we note that in Section 4.5 we test an AGN subsample (labelled 'c2') with accretion rate values compatible with the XRB distribution, for which Γ values were found to be consistent with the ones of the parent AGN sample, thus harder than in XRBs. Moreover, for both AGN and XRBs, $\dot{m}$ should not be considered a solid estimate and we cannot exclude that the two distributions are compatible within the very large uncertainties (see Section 4.6.2).

The spin is another largely unconstrained and still lively debated quantity for both AGN and XRBs (e.g. for GX 339-4, Kolehmainen & Done 2010; Parker et al. 2016; Ludlam et al. 2015; García et al. 2015), although flux-limited AGN samples are likely biased in being preferentially populated by high spin sources from several different lines of reasoning (Brenneman et al. 2011; Vasudevan et al. 2016; Baronchelli et al. 2018; Reynolds 2019), including modelling the $L_{disk} - L_{cor}$ itself (Arcodia et al. 2019). Moreover, the effect of the spin on the corona luminosity is likely degenerate with its geometry and extent and a thorough treatment of these unknowns is beyond the scope of this paper. However, we tried to qualitatively discuss their effect on our results. Using a simplified but physically motivated model which couples the disk and corona energetically (Arcodia et al. 2019)[10], we were able to infer that for a given accretion rate[11] the mass-normalised corona luminosity increases with the spin (i.e. a factor ≈ 2 between 2 and 10 keV from $a_* = 0$ to 0.998). Further, the corona luminosity also appears to increase with the radial (Zhang et al. 2019) and vertical extent of the corona (Kara et al. 2019; Alston et al. 2020). Therefore, it is remarkable that we observed a compatible normalisation in the $L_{disk} - L_{cor}$ plane for the AGN population and GX 339-4 (see Fig. 4.15). This might suggest that the spin distributions and/or the extent of the X-ray coronae, both in mass-normalised units, are not too far apart; or that obtaining a compatible normalization in the $L_{disk} - L_{cor}$ plane is just a combination of these multiple unknowns (i.e. one of the two source classes has lower spin but a wider corona or vice versa).

Finally, in case all the above quantities were found to be broadly compatible between the AGN and XRBs, a remaining possibility is that the Γ distributions are different because the typical values for temperature and/or optical depth are not the same. As a matter of fact, the Comptonisation slope depends on both (e.g. Pozdnyakov et al. 1983), and neither can be constrained in this work because we are not able to constrain the high-energy cut-off with RXTE-PCA (see footnote 5), which is in general the case for SSs (e.g. Grove et al. 1998; Gierliński et al. 1999;

[10]Code available here: https://github.com/rarcodia/DiskCoronasim

[11]Intended in units of $\mathrm{g\,s^{-1}}$, as the Eddington-normalized $\dot{m}$ is proportional to $\dot{M}$ times the radiative efficiency, which increases with the spin.

Motta et al. 2009). Alternatively, the energy distribution of the hot scattering electrons might not be the same in the two source classes. However, in both radiatively efficient AGN and XRBs we have a photon-rich environment and we are (relatively) far from the tails of the emitted spectrum, and therefore the underlying electron distribution is not necessarily a major concern (Coppi 1999).

Hence, despite the different environmental conditions (a single star versus a galactic centre) and characteristics of the matter reservoir (different density, temperature, ionisation, and pressure support), the phenomenology of the disk–corona energetic emission in radiatively efficient AGN and XRBs seems indeed very similar (see Figure 4.14 and 4.15). However, what might not be entirely understood is whether the physics of the disk–corona emission is also the same. Based on all the arguments in the discussion presented here, our results are consistent with disk–corona systems in AGN and XRBs that undergo the same physical processes under different conditions (e.g. temperature, optical depth, and electron distribution in the corona, spin regime, and/or heating-cooling balance) and/or geometry (radial and vertical extent of the corona). However, our results are also consistent with a scenario in which the physical processes are not the same and the mass-normalised disk–corona energetics are comparable by chance, although we consider this less favourable and to be in contention with decades of past results (e.g. Merloni et al. 2003; Maccarone et al. 2003; Falcke et al. 2004; Uttley & McHardy 2005; McHardy et al. 2006; Körding et al. 2006; Sobolewska et al. 2009, 2011; Svoboda et al. 2017; Ruan et al. 2019a, and references therein).

4.6.3.5 Similarities between AGN and XRBs despite the differences

In the previous section we outlined that, contrary to the observed difference in $\dot{m}$ for which we cannot securely claim that the intrinsic distributions are actually compatible, Γ values seem to be intrinsically different for (radiatively efficient and not jet-dominated) AGN and XRBs. However, we showed in Section 4.5 that when the two Γ distributions are taken with the same width, independently of where the peak lies, both AGN and XRBs show a similar scatter of $\sim 0.30 - 0.33$ dex in the $\log L_{disk} - \log L_{cor}$ plane. Thus, as far as the disk–corona relation is concerned, it seems to be more important how similarly diverse (i.e. σ_Γ) X-ray coronae are rather than how different the typical one (i.e. $<\Gamma>$) is between the two source classes. Moreover, another similarity is that in XRBs there is a clear dependence of $\log L_{cor}$ from Γ (see Fig. 4.9 and 4.12) in a softer-when-brighter pattern (where both softer and brighter refer to $\log L_{cor}$ alone in this context; see Fig. 4.13). This trend is absent in our sample of BLAGN (see also Beckmann et al. 2009; Corral et al. 2011; De Rosa et al. 2012) or is hidden among the various mass, distance, and inclination effects, although steeper Γ values for brighter sources have often been noticed in AGN samples (Sobolewska & Papadakis 2009; Mateos et al. 2010; Gibson & Brandt 2012; Serafinelli et al. 2017; Zappacosta et al. 2018), provided they lie in the radiatively efficient regime (Gu & Cao 2009; Connolly et al. 2016; Peretz & Behar 2018).

Assuming there is indeed not only a phenomenological but also a physical connection between radiatively efficient (not jet-dominated) AGN and XRBs, we can exploit the high-cadence monitoring on single XRBs to obtain a less-biased and more comprehensive analysis of the possible co-evolution of the disk–corona spectral components. However, our results then imply that

the physical scatter of the $\log L_{disk} - \log L_{cor}$ cannot be $\lessapprox 0.19 - 0.20$ dex (Lusso & Risaliti 2016; Chiaraluce et al. 2018). Indeed, this estimate might be contaminated by the adopted Γ distribution, which is likely biased narrow in flux-limited AGN samples. A common procedure in AGN samples is indeed to cut the extreme Γ values as a selection criterion for more robust sources. Alternatively, a standard photon index of $\sim 1.8 - 1.9$ is typically attributed to faint spectra that do not allow its constraint, with the obvious consequence of an artificial narrowing of the observed Γ distribution. Including all these extreme Γ values would result in a larger scatter of the $\log L_{disk} - \log L_{cor}$ and possibly an increased fraction of X-ray weak sources (e.g. Nardini et al. 2019). Hence, assuming a priori that extreme Γ values come from unreliable spectral fits, and then looking for physical correlations involving that parameter itself, is circular and might be misleading. Here, we simply selected spectra above a ratio of ~ 1.3 between source-plus-background and background-only $10 - 25$ keV count rates (see Section 4.4 and Section 4.3.2.1). This approach was purely observational and resulted in a slight narrowing in the Γ distribution (see colour-coding in Fig.4.12) only as a secondary consequence. This being said, we want to highlight that increasing the observed scatter of the $\log L_{disk} - \log L_{cor}$ relation in AGN was shown with detailed simulations to imprint a minor effect on the cosmology, only slightly enlarging the uncertainty in the slope and, consequently, on the cosmological contours (D. Coffey, PhD thesis and private communication).

Finally, still working under the assumption that a unified prescription of radiatively efficient XRBs and AGN is present, it is of interest to find out what the AGN counterparts of the excluded background-contaminated XRB states (i.e. with a very weak, hard component) would look like. Some AGN counterparts could be the optically bright X-ray weak quasars found at $z \sim 3.0 - 3.3$ by Nardini et al. (2019; see also Martocchia et al. 2017) showing unusually flat slopes, which would be in accordance with the softer-when-brighter trend we discussed above. This could be indeed an interesting science case for the extended ROentgen Survey with an Imaging Telescope Array (eROSITA; Predehl et al. 2020).

4.7 Conclusions

Throughout the last two decades, several attempts have been made to connect accretion in AGN and XRBs in a BH mass scale-invariant fashion (e.g. Merloni et al. 2003; Maccarone et al. 2003; Falcke et al. 2004; Uttley & McHardy 2005; McHardy et al. 2006; Körding et al. 2006; Sobolewska et al. 2009, 2011; Svoboda et al. 2017; Ruan et al. 2019a, and references therein). Besides the more or less understood differences in the composition of their matter reservoir (i.e. density, temperature, ionisation, and consequently pressure support) and their environmental surroundings (a single star with respect to the centre of a galaxy) their timing and spectral phenomenology have always been found to be comparable. The simplistic but commonly accepted picture that has emerged from decades of multi-wavelength efforts connects strong radio-emitting low-luminosity AGN to hard-state XRBs, both showing a prominent jet component and a radiatively inefficient accretion flow (e.g. Merloni et al. 2003; Falcke et al. 2004), strong radio-emitting high-luminosity AGN to hard-intermediate states in XRBs, both showing an efficient accretion flow in coexistence with a jet (e.g. Körding et al. 2006; Svoboda et al. 2017),

and (very) weak radio-emitting moderately- to highly accreting AGN (both combined spanning $\lambda_{edd} = L/L_{edd} \simeq 0.0x - 1$) to XRBs in the soft states and soft-intermediate states (e.g. Maccarone et al. 2003; Körding et al. 2006; Sobolewska et al. 2009).

Here, we attempt to improve on this AGN–XRB connection in the radiatively efficient (and non- or weakly-jetted) end of accretion mode. Motivated by the tight relationship observed between the disk and coronal luminosities in AGN (e.g. Lusso & Risaliti 2016, and references therein), we analysed 458 RXTE-PCA archival observations of the XRB GX 339-4, using this object as a test case for XRB properties in general (Section 4.2). We focused on soft and soft-intermediate states, which have been suggested to be analogous to radiatively efficient (and non- or weakly jetted) AGN (e.g. Maccarone 2003; Körding et al. 2006; Sobolewska et al. 2009), modelling the emission with a thermal accretion disk and a Comptonising corona (Section 4.3). We then populated the $\log L_{disk} - \log L_{cor}$ plane with a quantitative focus on the physics hidden in the scatter, which represents the diversity of X-ray corona emission given a narrow range in accretion disks (Section 4.4).

The observed scatter in the $\log L_{disk} - \log L_{cor}$ plane of XRBs is high (~ 0.43 dex) and significantly larger than in our control sample of radiatively efficient (non- or weakly jetted) broad-line AGN (~ 0.30 dex). This would appear contrary to the hypothesis that the systems simply scale with mass. However, we also find that our AGN and XRB samples appear to have very different observed $\dot{m}$ and Γ distributions. In particular, while we are not able to exclude that the intrinsic $\dot{m}$ distributions are compatible, Γ is arguably a more robust estimate and appears to be directly linked to the observed scatter (Fig. 4.12). Even after accounting for the measured uncertainties, the XRB Γ distribution was estimated to be broader (dispersion of ~ 0.16 with respect to ~ 0.08) and shifted to softer slopes (mean value of ~ 2.20 with respect to ~ 2.07).

It is nonetheless remarkable that once similarly broad Γ and $\dot{m}$ distributions were selected (i.e. compatible σ_Γ and $\sigma_{\dot{m}}$, regardless of $<\Gamma>$ and $<\dot{m}>$), AGN and XRBs overlapped quite nicely in the mass-normalised $\log L_{disk} - \log L_{cor}$ plane, both showing an observed scatter of $\sim 0.30 - 0.33$ dex (Section 4.5). This indicates that a mass-scaling between the properties of the two might indeed hold, with our results being consistent with the disk–corona systems in AGN and XRBs exhibiting the same physical processes, albeit under different conditions, for instance in terms of temperature, optical depth, electron energy distribution in the corona, heating–cooling balance, coronal geometry, and/or black hole spin (see Section 4.6.3).

The amplitude of this common scatter ($\sim 0.30 - 0.33$ dex) is still significantly higher than $\lessapprox 0.19-0.20$ dex, which is what was claimed to be the physical intrinsic (i.e. not due to variability and non-simultaneity) scatter in the $L_X - L_{UV}$ (or $\alpha_{OX} - L_{UV}$) relation in AGN (e.g. Vagnetti et al. 2013; Lusso & Risaliti 2016; Chiaraluce et al. 2018). On the other hand, it is worth stressing that when a single XRB is used, as in our case, any possible issue arising from non-simultaneity of the data probing the two components is avoided and there is no additional scatter coming from a mixed bag of masses, distances, and inclinations, which is instead typical of AGN. Hence, under the assumption of a mass-scaling paradigm, one would expect the scatter in XRBs to be lower. We conclude that, as the results of the past few decades and in this work suggest, since the two systems are similar, both in their phenomenology and physical processes, the physical scatter of the disk-corona emission in AGN is likely not as low as we think, with important implications for both accretion physics and quasar cosmology.

Chapter 5

X-ray Quasi-Periodic Eruptions

In Chapter 3 we studied the emission of persistent X-ray and optically bright AGN. In Chapter 4 we showed that there are strong similarities between radiatively-efficient broad-line AGN and even XRBs in terms of both spectral and timing variability. Not all accreting SMBHs behave in this well-controlled way, however. Newly discovered, Quasi-Periodic Eruptions (QPEs) are extreme high-amplitude bursts of X-ray radiation of unknown nature recurring every few hours and originating near the central supermassive black holes in galactic nuclei. Before this Thesis work, only two examples were known, found either serendipitously or in archival X-ray data. Both have emission lines in their optical spectra classifying their nuclei as hosting an actively accreting supermassive black hole. In this Chapter we present the detection of QPEs in two further galaxies, obtained with a blind and systematic search over half of the X-ray sky with eROSITA. The optical spectra of these galaxies show no signature of black hole activity, indicating that a pre-existing accretion flow typical of active nuclei is not required to trigger these remarkable events. Indeed, the period, amplitudes and profiles of the newly discovered QPEs are inconsistent with current models that invoke radiation-pressure driven accretion disk instabilities. Instead, QPEs might be driven by an orbiting compact object. Furthermore, their observed properties require the mass of the secondary object to be much smaller than the main body. Future X-ray observations may constrain possible changes in the period due to orbital evolution. This scenario could make QPEs a viable candidate for the electromagnetic counterparts of the so-called extreme mass ratio inspirals, with considerable implications for multi-messenger astrophysics and cosmology.

This Chapter is based on the article published as Arcodia et al. (2021) in *Nature*, Volume 592, Issue 7856, p. 704-707.

5.1 What we know about QPEs

QPEs were very recently discovered and consist of extreme high-amplitude bursts of X-ray radiation characterised by a count rate increase of more than one order of magnitude over a quiescent plateau. They were first associated to the nuclei of low-z galaxies, namely GSN 069 (Miniutti et al. 2019) at $z = 0.018$ and RX J1301.9+2747 (Giustini et al. 2020) at $z = 0.024$. The X-ray spectral properties are remarkably consistent between these two objects, as the spectrum varies

between a cold ($\sim 50\,\mathrm{eV}$) phase in the low-counts regime and a warm ($\sim 100 - 300\,\mathrm{eV}$) phase at the peak of the eruptions. In the cold phase, the almost featureless thermal spectra may be revealing the tail of an accretion disk spectrum in a low-mass super-massive black-hole (e.g. $\approx 10^5 - 10^7\,M_\odot$), which would allow us to estimate its mass and to probe the inner accretion disk physics. QPEs in GSN 069 were observed only after the source went through a X-ray bright and decaying (and QPE-free throughout; Shu et al. 2018) phase and were observed since their discovery for $\gtrsim 1.5 - 2$ years (Miniutti et al. 2019). QPEs in RX J1301.9+2747 were instead detected almost ~ 19 years apart (Giustini et al. 2020) and this source too seemed to have a decaying phase from the first ROSAT detection (Dewangan et al. 2000) to the first XMM-Newton observation, which showed $\sim 1 - 2$ eruptions (Giustini et al. 2020). However, while GSN 069 showed ~ 1 hr-long eruptions separated by a quasi-period of ~ 9 hr, in RX J1301.9+2747 a much less regular recurrence time, with an alternating separation of ∼20 and ∼13.5 ks, was observed (Giustini et al. 2020).

Their optical spectra show no evidence of canonic AGN broad emission lines (see e.g. Section 1.3.1), however the relative strength of narrow emission lines indicates unambiguous AGN-driven ionisation (Miniutti et al. 2013; Sun et al. 2013). Moreover, infrared photometry does not indicate the presence of hot dust (the so-called torus; Netzer 2015) and radio and UV observations of GSN 069, performed quasi-simultaneously with X-rays, did not show any evidence of analogous variability (Miniutti et al. 2019). Therefore, what we know to date is that QPEs are events that can likely be detected only in the soft X-rays. However, it is currently unknown what triggers these events, how long they last and how they are connected to the physical properties of the inner accretion flows. A few scenarios to explain the QPEs have been suggested (Miniutti et al. 2019; King 2020; Sniegowska et al. 2020; Raj & Nixon 2021), some based on the presumed active nature of the QPEs' host black holes. These include so-called limit-cycle radiation-pressure accretion instabilities (Janiuk et al. 2002; Janiuk & Czerny 2011; Merloni & Nayakshin 2006; Grzędzielski et al. 2017b; Sniegowska et al. 2020), proposed for GSN 069 (Miniutti et al. 2019) based on the similarities between its observed properties and two extremely variable stellar-mass black holes, namely GRS 1915+105 (Taam et al. 1997; Belloni et al. 2000; Neilsen et al. 2011) and IGR J17091-3624 (Altamirano et al. 2011). Alternatively, extreme or sinusoidal quasi-periodic variability as seen in QPEs is also typically associated with compact objects binaries (e.g. De Rosa et al. 2019, and references therein). For instance, in GSN069 the average luminosity in a QPE cycle can be reproduced by a periodic mass-inflow rate from a white dwarf orbiting the black hole with a highly eccentric orbit (King 2020). Regardless of their origin, the QPEs seen so far seem to be found in relatively low-mass super-massive black-holes ($\approx 10^5 - 10^7\,M_\odot$) and finding more will help us to understand how black holes are activated in low-mass galaxies, a poorly explored mass range so far in their co-evolution history (Kelly & Merloni 2012; Heckman & Best 2014), which is however crucial for synergies with future LISA gravitational waves signals (Amaro-Seoane et al. 2017).

5.2 Blind search for QPEs with eROSITA

Currently, the only way of systematically finding new QPEs as they happen is provided by the extended ROentgen Survey with an Imaging Telescope Array (eROSITA; Predehl et al. 2020), which is the main instrument aboard the Spectrum-Roentgen-Gamma (SRG) mission (Sunyaev et al. 2021). On December 13 2019, eROSITA started the first of eight deep All-Sky Surveys (eRASS1-8), one every six months, in the 0.2 − 10 keV band. In each scan, every point of the sky is observed a few times (depending on its position and ∼ 6 on the Ecliptic plane) for ∼ 40 s each time and every ∼ 4 hr. Our search for QPE candidates starts with a systematic screening of all eROSITA light curves, produced for each detected source on a weekly basis by the eROSITA Science Analysis Software (eSASS; Brunner et al., in preparation). Light curves are binned to yield one data point for each 4-hour revolution (called an 'eROday'). A light curve generated by the eSASS pipeline will trigger a 'QPE alert' if it shows two or more high-count states with (at least) one low-count state in between (see Fig. 5.1 and 5.4 as examples) in any of its standard energy bands (0.2-0.6, 0.6-2.3, 2.3-5.0 keV). A factor of 5 (including uncertainties in the X-ray count rates) between the bright and faint eROday is adopted in case the faint one is a detection, otherwise a factor 3. Since neither the survey scans nor QPEs are strictly periodic, every eRASS can be treated as an independent sky to find new candidates. This search produces a census of X-ray sources varying on hours timescales for each eRASS, albeit only for the specific intermittent pattern described above. Unsurprisingly, most of the automatically generated alerts are produced by Galactic sources (mainly flaring coronally active stars), but we can filter them out by finding the multi-wavelength counterpart associated to every X-ray source (Salvato et al., in preparation). Good QPE candidates are then selected screening the alerts with a secure or possible extra-galactic counterpart. Thanks to this process, we identified the two best eROSITA QPE candidates which were worth immediate follow-up, promptly obtained with XMM-Newton and, in one case, NICER. Given the success of our initial search over the first nine months of the survey, we are confident that we can detect up to ~2-3 good eROSITA QPE candidates every year. Therefore, by the end of the last eROSITA all-sky survey in December 2023 this search may provide a sample of up to ~10 new QPEs.

5.3 Data reduction

Here we report details of the processing of the complete data-sets used throughout this Chapter. We show a summary of the observations in Table 5.1.

5.3.1 eROSITA

Members of the German eROSITA consortium (eROSITA-DE) have full and immediate access to survey data at Galactic longitudes 180 $<l<$360. These data were processed using eSASS v946 (H. Brunner et al. in preparation). For eRO-QPE1 (eRO-QPE2), photons were extracted choosing a circular aperture of radius 80" (67"), while background counts were extracted from an annulus (off-centered circle) of inner and outer radii 178" (382") and 996", respectively, excluding all the

Table 5.1: Summary of the observations performed.

Source	Instrument	Obs. ID	Start date
eRO-QPE1	eROSITA	–	16 January 2020
	XMM-Newton	0861910201	27 July 2020
	XMM-Newton	0861910301	4 August 2020
	NICER	3201730103	19 August 2020
	SALT	–	24 September 2020
eRO-QPE2	eROSITA	–	23 June 2020
	XMM-Newton	0872390101	6 August 2020
	SALT	–	8 September 2020

other sources detected within the area. eRO-QPE1 was detected with a detection likelihood of 440 and a total number of 119 counts in the 0.2-5.0 keV band. eRO-QPE2 was detected with a detection likelihood of 125 and a total number of 48 counts in the 0.2-5.0 keV band.

5.3.2 XMM-Newton

XMM-Newton data from EPIC MOS1-2 (Turner et al. 2001) and EPIC-PN (Strüder et al. 2001) cameras and the Optical Monitor (OM Mason et al. 2001) were processed using standard tools (SAS v. 18.0.0 and HEAsoft v. 6.25) and procedures. Event files from EPIC cameras were filtered for flaring particle background. Source (background) regions were extracted within a circle of 38" and 34" in eRO-QPE1 and eRO-QPE2, respectively, centered on the source (in a source-free region). eRO-QPE1 was consecutively observed three times with the U filter, then seven times with UVW1 and nine (eight) times with the UVM2 in the first (second) XMM-Newton observation, each exposure ~4400 s long. The source was detected only in the U and UVW1 with mean magnitudes ~19.9 and ~20.3 in both XMM-Newton observations (OM light curves in Fig. 5.2). eRO-QPE2 was consecutively observed twice with the U filter, then ten times with UVW1, six with UVM2 and three with UVW2 with all exposures beding 4400s. It was almost always detected in all filters with mean magnitudes of ~17.4, ~17.5, ~18.0, and ~18.1, for U, UVW1, UVM2 and UVW2 filter, respectively (OM light curves in Fig. 5.5). eRO-QPE2 was flagged as extended in the U, UVW1 and UVM2 filters, therefore the reported absolute magnitudes include at least some contamination from the host galaxy.

5.3.3 NICER

NICER's X-ray Timing Instrument (XTI Gendreau et al. 2012; Arzoumanian et al. 2014) onboard the ISS observed eRO-QPE1 between 17 August 2020 and 31 August 2020. Beginning late on 19 August, high-cadence observations were performed during almost every ISS orbit, which is roughly 93 minutes. All the data were processed using the standard NICER Data Analysis Software (NICERDAS) task 'nicerl2'. Good time intervals (GTIs) were chosen with standard

defaults, yielding ~186 ks of exposure time. We further divided the GTIs into intervals of 128 s, and on this basis we extracted the spectra and applied the '3C50' model (R.R. et al., submitted) to determine the background spectra. The light curve for eRO-QPE1 in soft X-rays (Fig. 5.2) was determined by integrating the background-subtracted spectrum for each 128-s GTI over the range 0.3-1.0 keV.

5.3.4 SALT

Optical spectra of eRO-QPE1 and eRO-QPE2 were obtained using the Robert Stobie Spectrograph (RSS; Burgh et al. 2003) on SALT (Buckley et al. 2006) on the nights of 2020 September 24 and 8, respectively. The PG900 VPH grating was used to obtain pairs of exposures (900 s and 500 s, respectively) at different grating angles, allowing for a total wavelength coverage of 3500-7400Å. The spectra were reduced using the PySALT package, a PyRAF-based software package for SALT data reductions (Crawford et al. 2012), which includes gain and amplifier cross-talk corrections, bias subtraction, amplifier mosaicing, and cosmetic corrections. The individual spectra were then extracted using standard IRAF procedures, wavelength calibration (with a calibration lamp exposure taken immediately after the science spectra), background subtraction and extraction of 1D spectra. We could only obtain relative flux calibrations, from observing spectrophotometric standards in twilight, due to the SALT design, which has a time-varying, asymmetric and underfilled entrance pupil (Buckley et al. 2018).

5.4 The two discoveries

5.4.1 eRO-QPE1

The first QPE, here named eRO-QPE1, is eRASSU J023147.2-102010 located at the astrometrically corrected X-ray position of RA_{J2000}, DEC_{J2000}=(02:31:47.26, -10:20:10.31), with a total 1σ positional uncertainty of ~2.1". It was observed ten times between 16 and 18 January 2020 during eRASS1 with 339 s of total exposure. It showed a strong X-ray signal in two eROSITA survey scans which were preceded, separated and followed by scans showing it to be much fainter (left panel of Fig. 5.1). Like the two previously known QPE sources, GSN 069 and RX J1301.9+2747 (Miniutti et al. 2019; Giustini et al. 2020), the X-ray spectrum is very soft with most of the counts originating from below ~1.5-2 keV and consistent with a thermal black-body emission. As with the light curve, the spectrum shows oscillations from a faint to a bright phase (right panel of Fig. 5.1).

Using the Bayesian cross-matching algorithm NWAY (Salvato et al. 2018) we associated eRO-QPE1 with the galaxy 2MASS 02314715-1020112 at RA_{J2000}, DEC_{J2000}=(02:31:47.15, -10:20:11.22). It is in the DESI Legacy Imaging Surveys (Dey et al. 2019) DR8 footprint and the XMM-Newton position is consistent with the nucleus[1] (Fig. 5.3). We took an optical spec-

[1]X-ray XMM-Newton positions were corrected with the 'eposcorr' task cross-correlating the sources in the X-ray image with external optical and infrared catalogs. The counterparts of the QPE itself was excluded from the cross-correlation to obtain a more unbiased estimate of the possible offset from the nucleus.

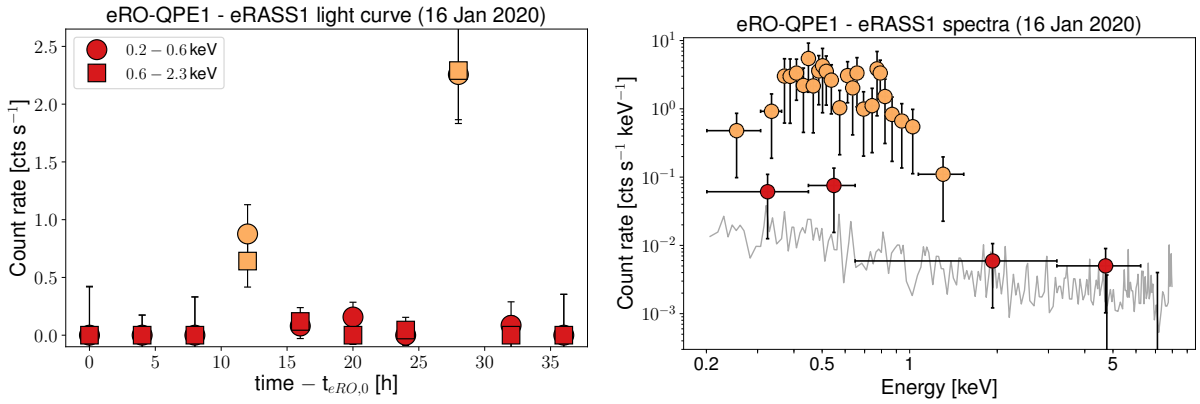

Figure 5.1: *Left:* eROSITA light curve in the 0.2-0.6 keV and 0.6-2.3 keV energy bands (circles and squares, respectively), with red and orange highlighting faint and bright observations, respectively. The start of the light curve is $t_{eRO,0}$ is MJD~58864.843. *Right:* eROSITA X-ray spectra of the bright and faint states in orange and red as in the left panel.

trum with the Southern African Large Telescope (SALT; Buckley et al. 2006) and measured spectroscopic redshift of 0.0505 (Fig. 5.3). This allowed us to compute eROSITA quiescence (1σ upper limit) and peak intrinsic 0.5-2 keV luminosities, which are $<2.1\text{x}10^{41}$and ~$9.4\text{x}10^{42}$ erg s^{-1}, respectively, if the X-ray spectra are modeled with a standard accretion disk model (see Section 5.5).

Two follow-up observations triggered with XMM-Newton confirmed the remarkable bursting nature of the source (Fig. 5.2). The first observation (hereafter eRO-QPE1-XMM1) found the source in a faint state for ~30 ks, followed by a sequence of three consecutive asymmetric bursts, possibly partially overlapping (Fig. 1c), behaviour which has not been observed before in QPEs (Miniutti et al. 2019; Giustini et al. 2020). In terms of intrinsic 0.5-2 keV luminosity, after an initial quiescent phase at ~$2.3\text{x}10^{40}$erg s^{-1} the first burst was characterised by a fast rise and slower decay lasting ~30 ks and peaking at ~$3.3\text{x}10^{42}$erg s^{-1}; it was then followed by a second fainter burst (peak at ~$7.9\text{x}10^{41}$erg s^{-1}) and by a third, which was the brightest (peak at ~$2.0\text{x}10^{43}$erg s^{-1}) but was only caught during its rise. The second XMM-Newton observation (hereafter eRO-QPE1-XMM2) showed an eruption very similar to the first seen in eRO-QPE1-XMM1 in terms of amplitude and luminosity, although lasting for >40 ks, namely for almost as much as the three in eRO-QPE1-XMM1 combined (Fig. 1c). There is no evidence of simultaneous optical/UV variability (see Fig. 1c), in agreement with the behaviour of GSN 069 (Miniutti et al. 2019). To better characterise the physics and to determine the duty cycle of these eruptions, we started an intense monitoring campaign with the NICER X-ray instrument aboard the International Space Station (ISS), which revealed 15 eruptions in about 11 days (Fig. 5.2).

eRO-QPE1 has not previously been detected in X-rays, although upper limits can be obtained from the XMM-Newton upper limits server for ROSAT (Truemper 1982), both from the survey and a pointed observation (taken in 1991 and 1992, with ~270 and ~5300 seconds, respectively), and the XMM-Newton Slew Survey (Saxton et al. 2008) taken in 2004, 2007, 2008 and 2017, all between ~3-8 seconds of exposure. The ROSAT pointed observation puts a stringent upper limit

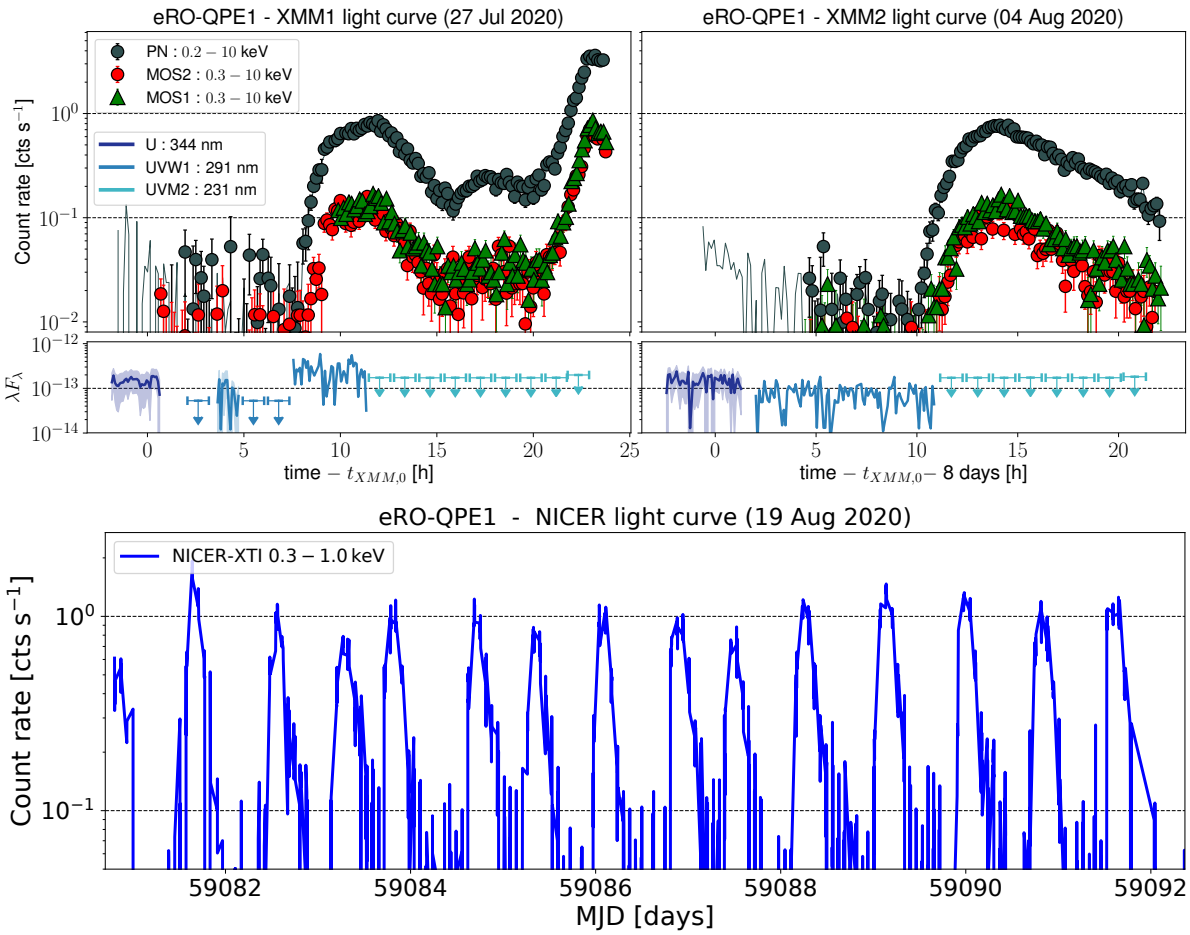

Figure 5.2: *Top:* background subtracted XMM-Newton X-ray light curves with 500 s bins for EPIC PN (dark gray), MOS1 (green) and MOS2 (red) in the energy band shown in the legend. The beginning of both observations was contaminated by flares in the background and excluded; the dark grey solid line and contours show the underlying $\lesssim$1 keV EPIC-PN light curve to give a zeroth-order extrapolation of the rate, excluding the presence of obvious soft X-ray eruptions. $t_{XMM,0}$ corresponds to the start of the cleaned MOS2 exposure in the first observation, namely MJD~59057.805. XMM-Newton optical and UV fluxes are shown in the lower sub-panels (units of erg cm^{-2} s^{-1}), with non-detections shown as upper limits. *Bottom:*, background subtracted NICER-XTI light curve. The mean (and dispersion on) rise-to-decay duration is ~7.6 hours (~1.0 hours) and the peak-to-peak separation is ~18.5 hours (~2.7 hours). In all panels 1σ uncertainties are shown, as error bars or shaded regions.

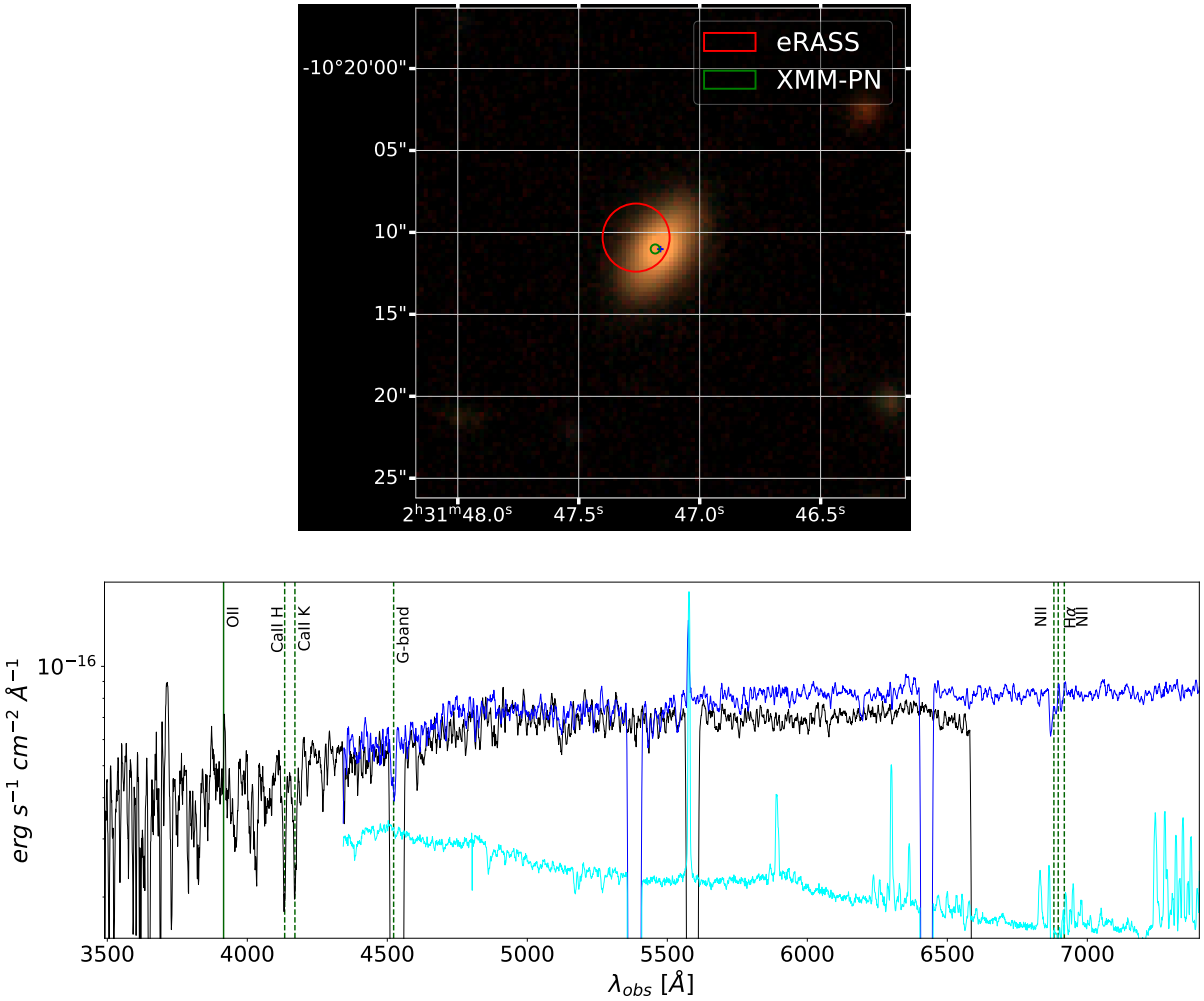

Figure 5.3: *Top:* Legacy DR8 image cut-out around the optical counterpart of eRO-QPE1. Red and green circles represent the astrometry-corrected eROSITA and XMM-PN positions, respectively, with 1σ positional uncertainties. The EPIC-PN position was corrected excluding the target (blue cross) to ensure an unbiased estimate of the possible positional offset. *Bottom:* SALT spectra of eRO-QPE1 shown in black and blue with related 1σ errors as shaded regions. The cyan spectrum represents a re-normalized sky spectrum to guide the eye for the residual sky feature around 5577Å.

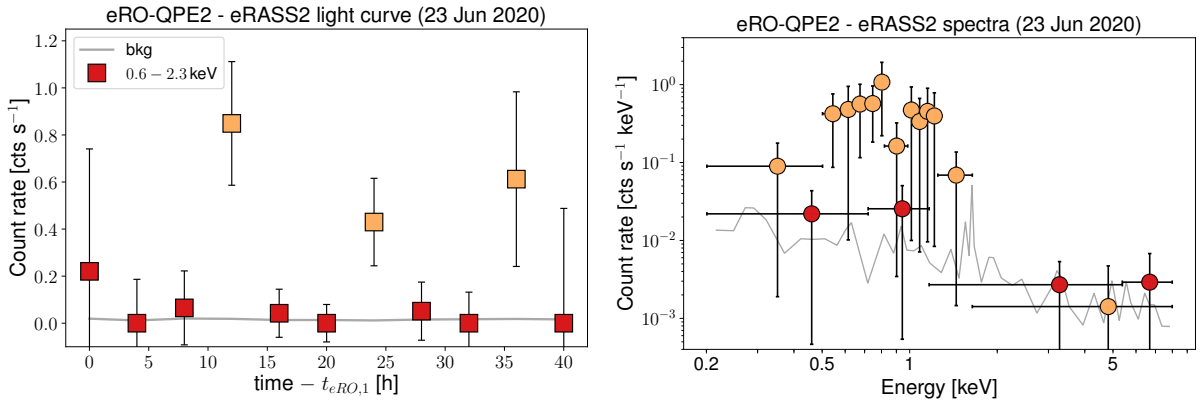

Figure 5.4: Same as Fig. 5.1 but for eRO-QPE2. The start of the eROSITA light curve is MJD~59023.191.

at $\lesssim$3.8x10^{-14} cgs in the 0.2-2.0 keV band. However, given the very short exposures compared with the timescales of eRO-QPE1, we can not rule out that QPEs were already ongoing and that all previous missions caught eRO-QPE1 in a faint state.

5.4.2 eRO-QPE2

The second QPE, here named eRO-QPE2, is eRASSU J023448.9-441931 located at the astrometrically corrected X-ray position of RA$_{J2000}$, DEC$_{J2000}$=(02:34:48.97, -44:19:31.65), with a total positional uncertainty of ~3.2". It was observed 11 times between 23 and 24 June 2020 during eRASS2, showing similar variability patterns and X-ray spectra as eRO-QPE1 during the X-ray all-sky survey (Fig. 5.4). It was associated via the same method (Salvato et al. 2018) with 2MASX J02344872-4419325, a galaxy at RA$_{J2000}$, DEC$_{J2000}$=(02:34:48.69, -44:19:32.72). Similarly to eRO-QPE1, the host galaxy is in the DESI Legacy Imaging Surveys (Dey et al. 2019) DR8 footprint and the X-ray position is consistent with the nucleus (Fig. 5.6). An optical spectra taken with SALT allowed us to measure $z \sim 0.0175$ (Fig. 5.6). The intrinsic 0.5-2 keV luminosity of the quiescent (1σ upper limit) and peak phase is <4.0x10^{40}erg s^{-1} and ~1.0x10^{42}erg s^{-1}, respectively. A follow-up observation with XMM-Newton revealed 9 eruptions in a single day, oscillating between ~1.2x10^{41}erg s^{-1} and ~1.2x10^{42}erg s^{-1}in the 0.5-2 keV band (Fig. 5.5). As in eRO-QPE1 no simultaneous optical/UV variability was observed (see Fig. 5.5).

Like eRO-QPE1, eRO-QPE2 has not been previously detected in X-rays. Upper limits were again computed for ROSAT (taken in 1990, ~480 seconds of exposure) and the XMM-Newton Slew survey (taken in 2004, 2008, 2012 and 2013, all between ~4-8 seconds). The most stringent upper limit, at $\lesssim$8.8x10^{-14} cgs in the 0.2-2.0 keV band, comes from ROSAT. It is slightly below the flux observed by XMM-Newton in quiescence in the same band (Fig. 5.8), perhaps indicating that the QPE behaviour only started more recently.

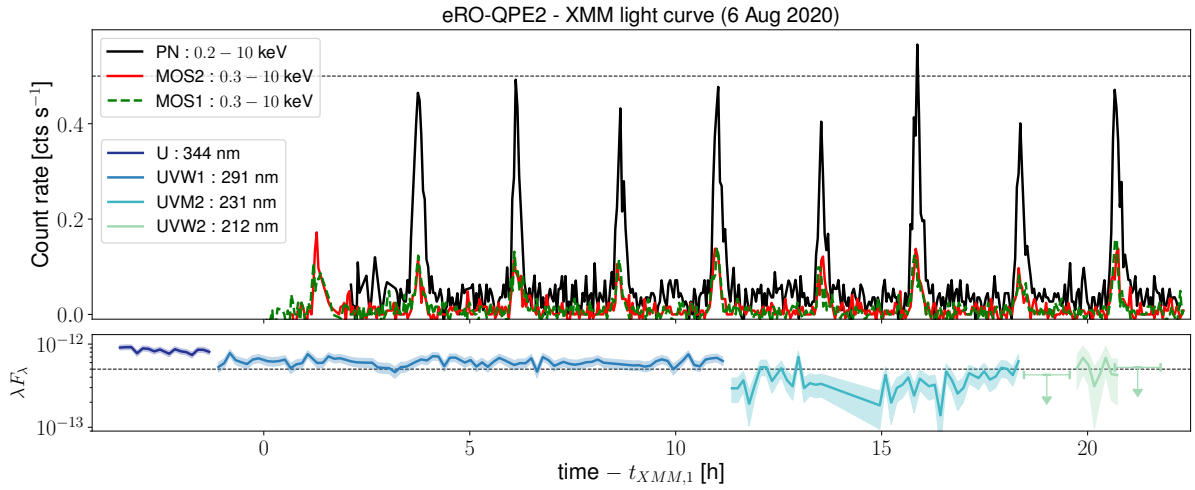

Figure 5.5: Same as the Fig. 5.2 but for the XMM-Newton observation of eRO-QPE2. $t_{XMM,1}$ corresponds to the start of the cleaned MOS1 exposure, namely MJD~59067.846. The mean (and related dispersion) of the rise-to-decay duration is ~27 minutes (~3 minutes), with a peak-to-peak separation of ~2.4 hours (~5 minutes). In all panels 1σ uncertainties are shown, as error bars or shaded regions.

5.5 X-ray spectral analysis

In this work, X-ray spectral analysis was performed using v3.4.2 of the BXA (Buchner et al. 2014) with the nested sampling Monte Carlo algorithm MLFriends (Buchner 2014, 2019) using UltraNest[2] and XSPEC v12.10.1 (Arnaud 1996) as fitting environment, with its Python oriented interface pyXSPEC. eROSITA source plus background spectra were fit including a model component for the background, which was determined via a principal component analysis (PCA) from a large sample of eROSITA background spectra (Simmonds et al. 2018, Buchner et al. in prep.). XMM-Newton EPIC-PN spectra were instead fit using wstat, namely XSPEC implementation of the Cash statistic (Cash 1979), given the good counts statistics in both source and background spectra. We quote, unless otherwise states, median values with the related 16th and 84th percentiles and upper limits at 1σ. Results are also reported in Table 5.2 and 5.3.

For eRO-QPE1 both eROSITA and XMM-Newton EPIC-PN spectra were fit with a simple absorbed black-body or accretion disk, using the models tbabs, zbbody or diskbb (Mitsuda et al. 1984). Galactic absorption was frozen at the column density of N_H~2.23x10^{20}cm^{-2}, as reported by the HI4PI Collaboration (HI4PI Collaboration et al. 2016). For eROSITA, we jointly extracted and analysed spectra of the faint states (red points in Fig 1a) and, separately, of the two bright states observed in eRASS1 (orange points in Fig 1a). In the eROSITA bright states the temperature, in terms of k_BT in eV, is 138^{146}_{131} eV and 180^{195}_{168} eV, using zbbody and diskbb as source model, respectively. The related unabsorbed rest-frame 0.5-2.0 keV fluxes are $1.6^{1.8}_{1.4}$x10^{-12} cgs and $1.5^{1.7}_{1.4}$x10^{-12} cgs, respectively. The eROSITA spectrum of the faint states combined is con-

[2] https://johannesbuchner.github.io/UltraNest/

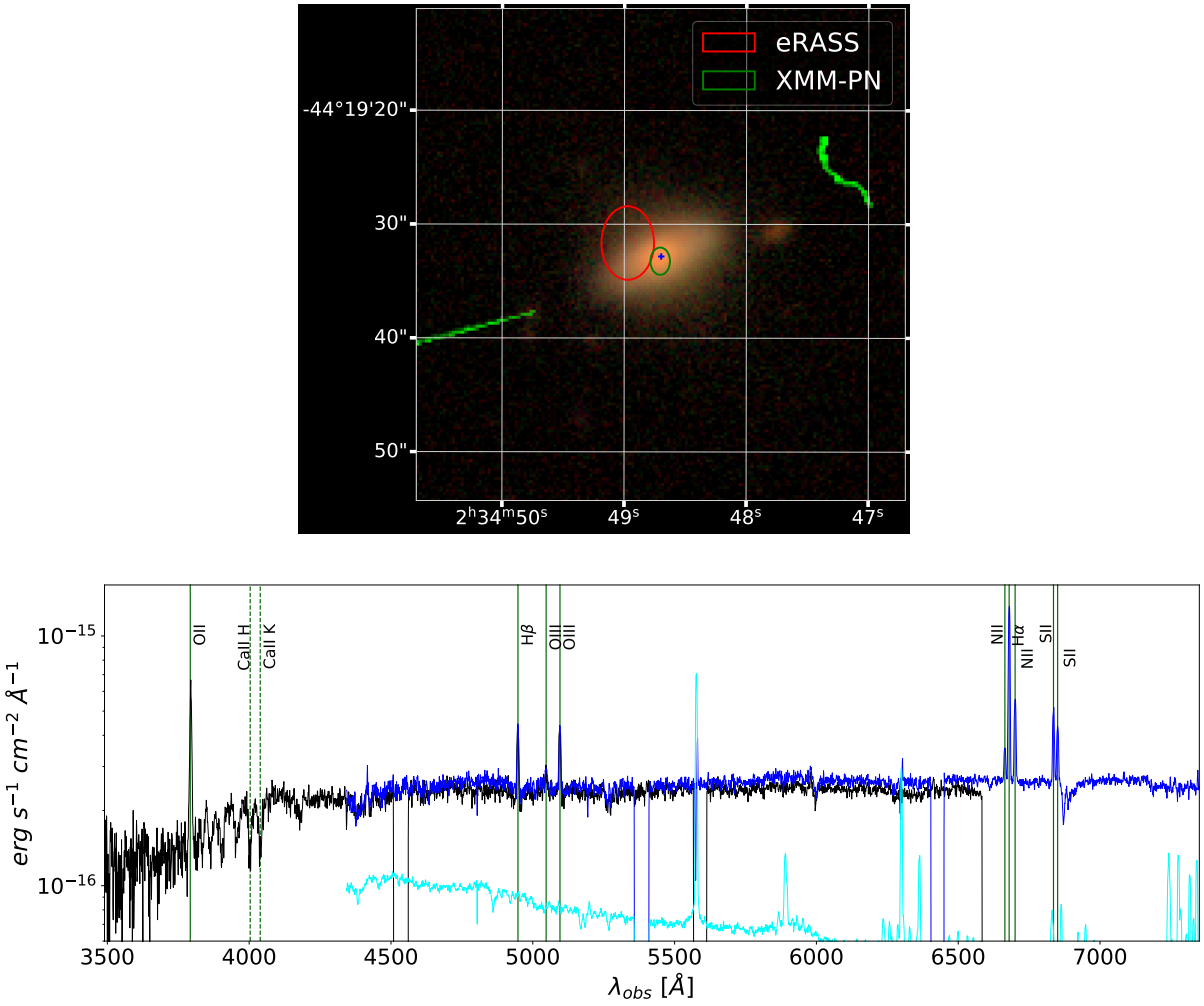

Figure 5.6: Same as in Fig. 5.3, but for eRO-QPE2.

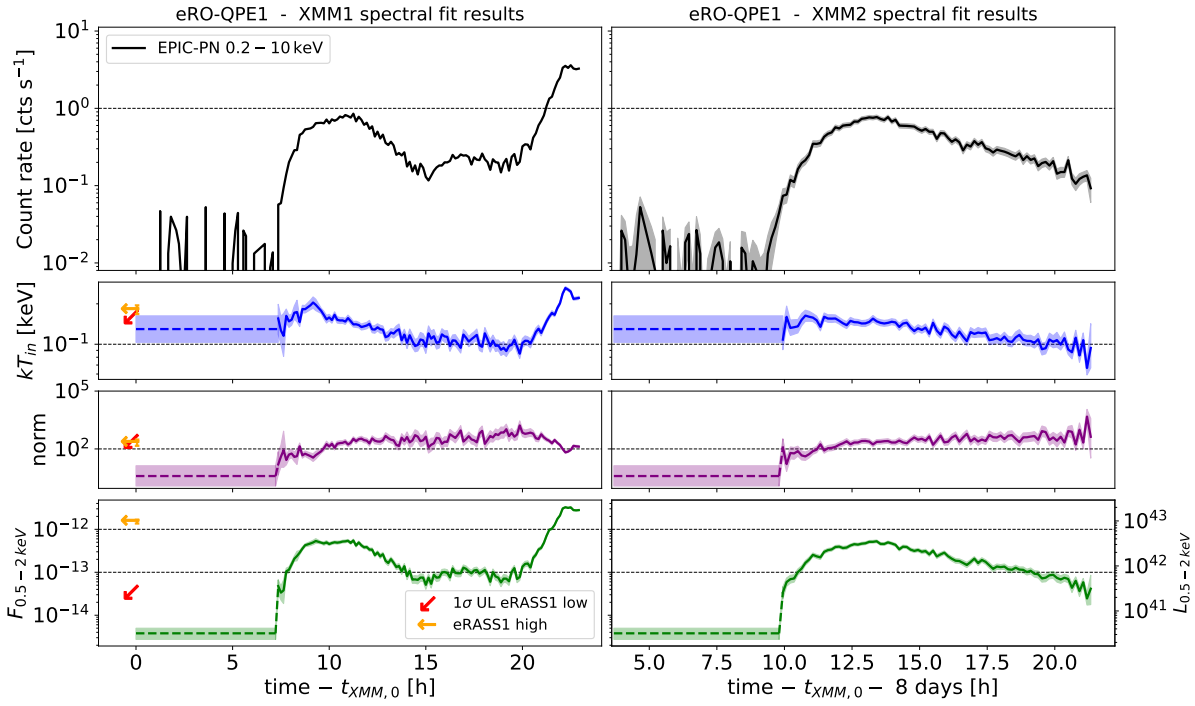

Figure 5.7: XMM-Newton PN light-curve (top panel) and time-resolved spectroscopy fit results for spectra extracted in the 500 s time bins (bottom panels) of the two XMM-Newton observations of eRO-QPE1 using an accretion disk model (diskbb): in particular, the evolution of the peak accretion disk temperature and the normalization, which is proportional to the inner radius once distance and inclination are known. The quiescence level is fit combining the first part of both XMM-Newton observations. It is shown with a dashed line because due to low counts the fit is more uncertain (see top panel of Fig. 5.9). Median fit values and fluxes of the high and low eROSITA states are reported with orange and red arrows pointing left (upper limits are denoted with diagonal arrows). 1σ uncertainties on the fit results are shown with shaded regions around the median.

sistent with background, with the temperature and unabsorbed rest-frame 0.5-2.0 keV flux constrained to be $\lesssim$124 eV ($\lesssim$160 eV) and $\lesssim$3.5x10^{-14}cgs ($\lesssim$3.4x10^{-14}cgs) for zbbody (diskbb). We also analysed the observations of eRO-QPE1 obtained six months later during eRASS2, which triggered our QPE search again: two bright states were observed separated by several faint ones, with fluxes consistent with eRASS1. We performed time-resolved X-ray spectral analysis on XMM-Newton data, extracting a spectrum in each 500s time bin of the EPIC-PN light curve, with the exception of the quiescence spectrum, which was extracted and analysed combining all the related time bins of both observations (i.e. before t$\sim$ 26500 s in eRO-QPE1-XMM1 and before t$\sim$ 35788 s in eRO-QPE1-XMM2, with times as defined in Fig. 5.2). Fit results obtained using XMM-Newton EPIC-PN spectra with diskbb as the source model component are shown in Fig. 5.7. Furthermore, we show for visualization three EPIC-PN spectra and related best-fit models (Fig. 5.9) corresponding to the quiescence phase and the peak of both XMM-Newton

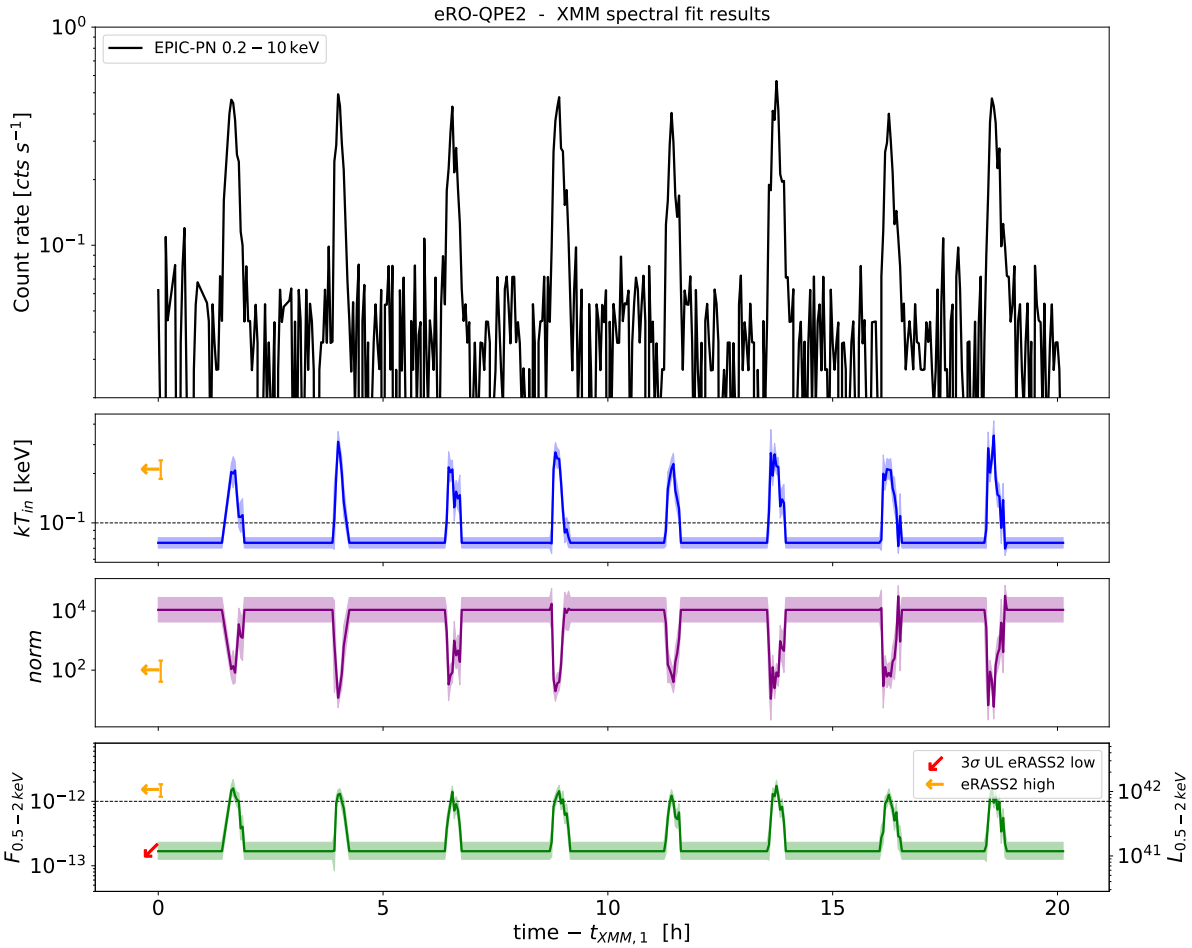

Figure 5.8: Same as Fig. 5.7, but for eRO-QPE2.

observations.

For eRO-QPE2 eROSITA's faint and bright phases were also separately combined and analysed (Fig. 5.4). The faint state as observed by eROSITA is consistent with background. The temperature and normalization of the source can not be constrained, thus we only quote an upper limit for the unabsorbed rest-frame 0.5-2.0 keV flux of $\lesssim$1.9x10^{-14}cgs ($\lesssim$5.7x10^{-14}cgs) using zbbody (diskbb). The spectrum of the eROSITA bright states constrains the temperature to 164^{182}_{149} eV and at 209^{241}_{185} eV, using zbbody and diskbb as source model, respectively. The related unabsorbed rest-frame 0.5-2.0 keV fluxes are $1.4^{1.8}_{1.2}$x10^{-12}cgs and $1.5^{1.8}_{1.2}$x10^{-12}cgs, respectively. The triggering eROSITA observation was obtained during eRASS2, although a single bright state (thus not satisfying our trigger criterion) was also detected in eRASS1 with the same flux level. For eRO-QPE2, in addition to the Galactic column density N_H~1.66x10^{20} cm^{-2} (HI4PI Collaboration et al. 2016) we included an absorption component at the redshift of the host galaxy (i.e. with the models tbabs, ztbabs, and zbbody or diskbb). This excess absorption was inferred to be present based on the XMM-Newton spectrum (see below). For XMM-Newton, we performed time-resolved X-ray spectral analysis for each 150 s time bin of the EPIC-PN light curve. The

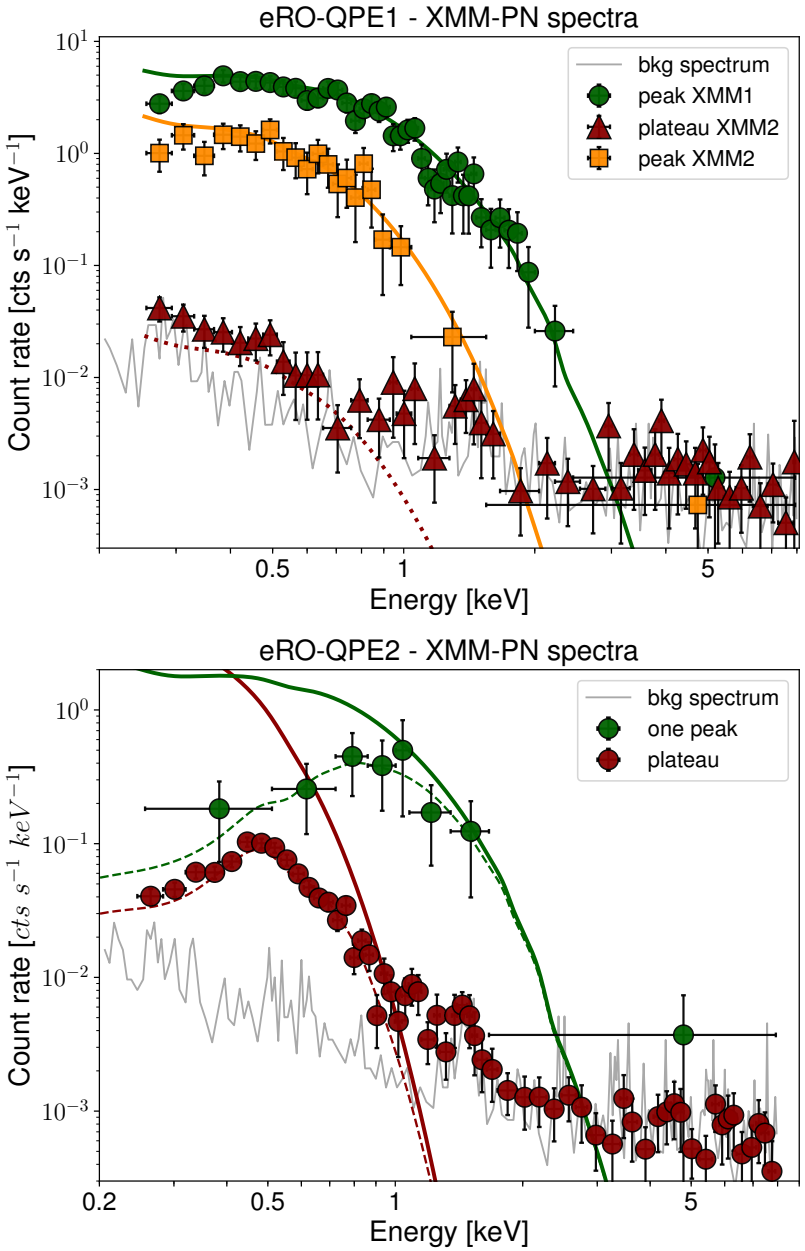

Figure 5.9: *Top:* XMM-Newton EPIC-PN source plus background spectra for eRO-QPE1. Red, orange and green data correspond to quiescence and to the peak of the second and first XMM-Newton observation, respectively, with error bars showing 1σ uncertainties. The related solid lines show the unabsorbed source model obtained with diskbb, just for visualization. The grey line represents the background spectrum alone. The plateau is shown with a dotted line because due to low counts the fit is more uncertain. *Bottom:* same but for eRO-QPE2. Here green data represent one of the peaks and the additional dashed lines indicate the absorbed source model.

Table 5.2: Summary of spectral fit results for eRO-QPE1. The median value and related 16$^{\text{th}}$ and 84$^{\text{th}}$ percentile values are reported for every quantity; for unconstrained values 1σ upper limits are quoted using the 84$^{\text{th}}$ percentile value of the parameter posterior distribution and are denoted with $\downarrow$. Reported results are obtained with the model `tbabs x diskbb`, with Galactic N_H frozen at $2.23\text{x}10^{20}\text{cm}^{-2}$, as reported by the HI4PI Collaboration (HI4PI Collaboration et al. 2016). Fluxes and luminosities are unabsorbed and rest-frame. The two eROSITA states are shown in Fig. 5.1, whilst the three XMM-Newton observations in the table correspond to the three spectra in Fig. 5.9. F_{disk} is computed within 0.001 and 100 keV (e.g. Dunn et al. 2010).

Observation	k_bT [eV]	$F_{0.5-2.0\,keV}$ [cgs]	F_{disk} [cgs]	$L_{0.5-2.0\,keV}$ [cgs]
eROSITA low	$\downarrow 160$	$\downarrow 3.4\times10^{-14}$	$\downarrow 2.4\times10^{-13}$	$\downarrow 2.1\times10^{41}$
eROSITA high	180^{195}_{168}	$1.5^{1.7}_{1.4}\times10^{-12}$	$4.2^{4.6}_{3.7}\times10^{-12}$	$0.9^{1.0}_{0.8}\times10^{43}$
XMM quiescence	130^{163}_{103}	$3.8^{5.0}_{2.7}\times10^{-15}$	$1.9^{2.5}_{1.5}\times10^{-14}$	$2.3^{3.1}_{1.7}\times10^{40}$
XMM1 peak	262^{269}_{256}	$3.3^{3.4}_{3.2}\times10^{-12}$	$6.4^{6.6}_{6.2}\times10^{-12}$	$2.0^{2.1}_{1.9}\times10^{43}$
XMM2 peak	148^{156}_{141}	$5.3^{5.6}_{4.9}\times10^{-13}$	$2.0^{2.1}_{1.8}\times10^{-12}$	$3.2^{3.5}_{3.0}\times10^{42}$

absorption in addition to the Galactic value was first fitted in the XMM-Newton quiescence spectrum, which was extracted combining all the low states in the XMM-Newton light curve (Fig. 5.5 and Fig. 5.8). The fit yielded a $N_H=0.35^{0.40}_{0.30}\text{x}10^{22}$ cm^{-2}. In all other observations, including all eROSITA spectra and the rises, peaks and decays in the XMM-Newton light curve, the additional N_H was left free to vary between the 10th and 90th percentile of the fitted posterior distribution of the quiescent spectrum. Under the assumption that absorption did not vary throughout the observation, this ensures that no spurious effects is imprinted on the fit temperature and normalisations due to degeneracies with N_H; at the same time, in this way parameters are marginalised over a reasonable range in N_H. Freezing the value instead would artificially narrow the uncertainties on the temperature and normalisations. Fit results obtained with diskbb as the source model are shown in Fig. 5.8. Furthermore, we show for visualization the EPIC-PN spectra and best-fit models of the quiescence and peak phases (Fig. 5.9). Similar results are obtained using zbbody as the source model.

5.6 Timing properties

In Fig. 5.10 we show the median (with related 16$^{\text{th}}$ and 84$^{\text{th}}$ percentile contours) light curve profiles obtained by folding the light curve at the eruptions peaks (e.g. see Neilsen et al. 2011). First, a random representative burst is selected and cross-correlated with the whole light curve. The peaks of this cross-correlation identify the times when the phase is zero. Data are then folded at these phase zero times to obtain a template median profile, which is then used to repeat

Table 5.3: Summary of spectral fit results for eRO-QPE2. Same as Table 5.2, but for eRO-QPE2. Reported results are obtained with the model `tbabs x ztbabs x diskbb`, with Galactic N_H frozen at 1.66 x10^{20}cm^{-2}, as reported by the HI4PI Collaboration (HI4PI Collaboration et al. 2016); absorption in excess was estimated from 'XMM quiescence' and was allowed to vary within its 10th and 90th percentiles for all the other observations. The two eROSITA states are shown in Fig. 5.4 and model parameters in the low state are unconstrained; the two XMM-Newton observations in the table correspond to the spectra in Fig. 5.9.

Observation	$N_H(z)$ [cm^{-2}]	k_bT [eV]	$F_{0.5-2.0\,keV}$ [cgs]	F_{disk} [cgs]	$L_{0.5-2.0\,keV}$ [cgs]
eROSITA low	$0.32^{0.38}_{0.28} \times 10^{22}$	–	$\downarrow 5.7 \times 10^{-14}$	$\downarrow 3.4 \times 10^{-13}$	$\downarrow 4.0 \times 10^{40}$
eROSITA high	$0.32^{0.37}_{0.28} \times 10^{22}$	209^{241}_{185}	$1.5^{1.8}_{1.2} \times 10^{-12}$	$3.3^{4.5}_{2.4} \times 10^{-12}$	$1.0^{1.3}_{0.8} \times 10^{42}$
XMM quiescence	$0.35^{0.40}_{0.30} \times 10^{22}$	76^{81}_{70}	$1.7^{2.3}_{1.3} \times 10^{-13}$	$8.0^{14.0}_{4.5} \times 10^{-13}$	$1.2^{1.6}_{0.9} \times 10^{41}$
XMM peak	$0.33^{0.39}_{0.30} \times 10^{22}$	222^{249}_{199}	$1.7^{2.1}_{1.5} \times 10^{-12}$	$9.1^{14.5}_{4.3} \times 10^{-12}$	$1.2^{1.5}_{1.0} \times 10^{42}$

the same operation and yield Fig. 5.10. A phase bin of ~0.1 corresponds to ~6600s and ~820s for eRO-QPE1 and eRO-QPE2, respectively. Moreover, XMM-Newton and NICER light curve profiles were fit with UltraNest (see Fig. 5.11). Motivated by the strong asymmetry in eRO-QPE1 (Fig. 5.2 and Fig 3a), we adopted a model with Gaussian rise and an exponential decay, a generic model often adopted for transients (van Velzen et al. 2019). eRO-QPE2, on the other hand, can be fit with a simple Gaussian profile (Fig. 5.10 and 5.11), possibly due to the much shorter timescales. The main purpose of this analysis is to infer basic bursts properties (peaks, widths and separations) to test theoretical models (e.g. Section 5.7.2 and 5.7.3). A more thorough characterisation of the time evolution of the eruptions is deferred to future work.

eRO-QPE1 shows a range of QPE rise-to-decay duration with a mean (dispersion) of ~7.6 hours (~1.0 hours) and peak-to-peak separations of ~18.5 hours (~2.7 hours), as derived from the NICER light curve (Fig. 5.2). The duty-cycle (mean duration over mean separation) is ~41%. Conversely, eRO-QPE2 shows much narrower and more frequent eruptions (see Fig. 5.5): the mean (dispersion) of the rise-to-decay duration is ~27 minutes (~3 minutes), with a peak-to-peak separation of ~2.4 hours (~5 minutes) and a duty-cycle of ~19%. Interestingly, compared to the two previously known QPEs (Miniutti et al. 2019; Giustini et al. 2020), eRO-QPE1 and eRO-QPE2 extend the parameter space of QPE widths and recurrence times towards longer and shorter timescales, respectively.

5.7 Discussion

5.7.1 The host galaxies of QPEs

Very little was known on both galaxies from published multi-wavelength catalogs, except for WISE infrared monitoring indicating a quite stable W1~W2 emission, typical of inactive galac-

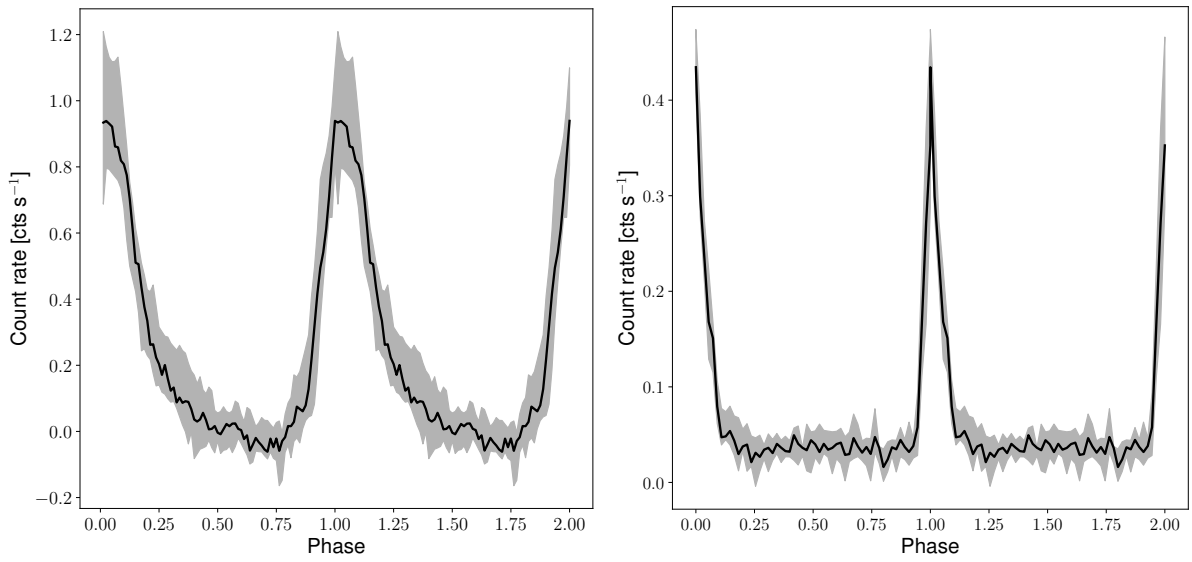

Figure 5.10: Median light curve profile (with related 16th and 84th percentile contours) for eRO-QPE1 (*left*) and eRO-QPE2 (*right*), folded at the eruptions peaks.

tic nuclei, for the last few years. Most of our knowledge is based on optical spectra taken with SALT after the X-ray discovery. The optical counterpart of eRO-QPE1 is classified as a passive galaxy from the absence of any significant emission line (Fig. 5.3), whereas eRO-QPE2 shows very strong and narrow [O_{II}], Hβ, [O_{III}], Hα, [N_{II}] and [S_{II}] in emission (Fig. 5.6). The high [O_{II}]/[O_{III}] ratio and Hβ being as strong and [O_{III}] are already strongly indicative that star forming processes are the dominant ionization mechanism (Silverman et al. 2009). We computed the flux ratios log([O_{III}]/Hβ)=-0.05, log([O_{II}]/Hβ)=0.44 and log([N_{II}]/Hα)=-0.68, as well as logEW_{OII}=2.56 and D_n(4000)=1.26, where D_n(4000) is the ratio of the continuum level after and before the 4000Å break (Zabludoff et al. 1996). Using standard line diagnostics plots (Comparat et al. 2013) we can confirm that indeed eRO-QPE2 can be classified as star forming. Spectroscopic classification of future QPEs will be crucial to confirm whether their host galaxies are indeed preferentially inactive, as our pilot study suggests, or not. A first census in a statistically significant sample may bring new insights as has been the case for other transients, such as TDEs (Arcavi et al. 2014; French et al. 2016; Law-Smith et al. 2017; van Velzen et al. 2021).

A preliminary analysis of the properties of QPEs' host galaxies was performed by fitting the optical spectra (Fig. 5.3 and 5.6) with Firefly (Wilkinson et al. 2017; Maraston et al. 2020). We first re-normalized the flux of the optical spectra using the most recent g-band and r-band archival magnitudes, since SALT spectra are not calibrated to absolute values Buckley et al. (2018). For eRO-QPE1, gri-band photometry (g=18.7±0.06, r=18.0±0.05, i=17.8±0.05 mag) was taken on July 30th 2020 with the Rapid Response Robotic Telescope at Fan Mountain Observatory, indicating that the source did not change significantly with respect to archival photometry (Abbott et al. 2018). The total stellar masses inferred with Firefly from the optical spectra are M_*~$3.8^{+0.4}_{-1.9}$x10^9 $M_\odot$ and ~$1.01^{+0.01}_{-0.50}$x10^9 $M_\odot$ for eRO-QPE1 and eRO-QPE2, respectively. Systematic errors and degeneracy due to the use of different stellar population models (Maraston & Strömbäck 2011)

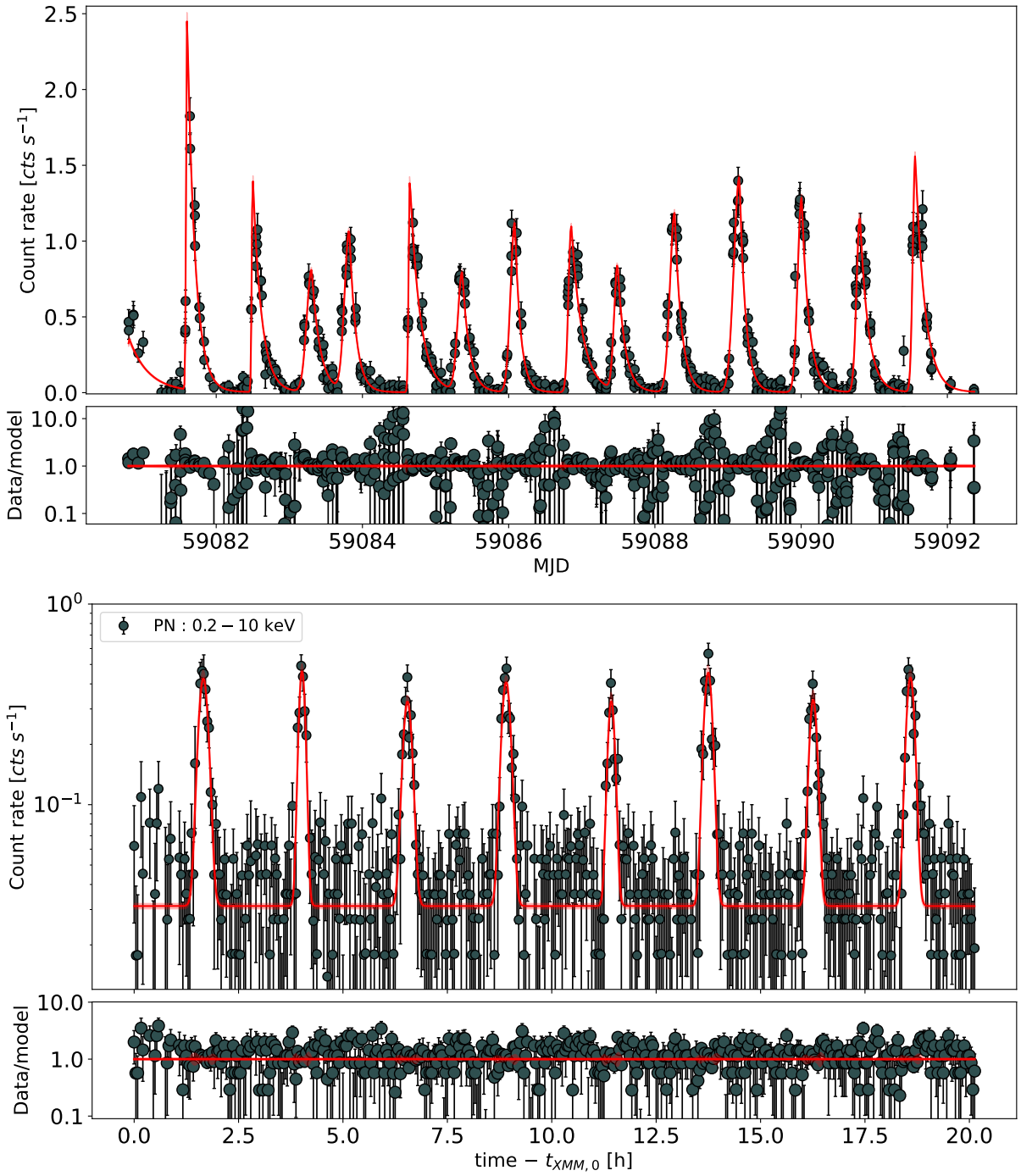

Figure 5.11: Light curve fit of eRO-QPE1 (*top*, asymmetric profile) and eRO-QPE2 (*bottom*, symmetric profile). The median model (with related 16$^{\text{th}}$ and 84$^{\text{th}}$ percentile shaded contours) is shown in red.

would push M_* to higher values for eRO-QPE1 (~4.8x10^9 $M_\odot$) and lower values for eRO-QPE2 (~0.6x10^9 $M_\odot$), enhancing their relative difference. Firefly also yields an estimate of the age of the stellar population and the SFR, although for medium and low signal-to-noise ratios these estimates are more prone to biases (Wilkinson et al. 2017). For eRO-QPE2, the mean signal-to-noise ratio (~23) is high enough to yield a fairly reliable SFR~$0.078^{+0.001}_{-0.066}M_\odot$/yr, which is also consistent within uncertainties with the SFR that can be estimated from the [O_{II}] and Hα luminosities (Kennicutt 1998; Kewley et al. 2004). For eRO-QPE1 the mean signal-to-noise ratio (~8) is lower and no reliable estimate of the SFR was obtained. We therefore inferred an upper limit of ~$0.01M_\odot$/yr from the absence of significant narrow emission lines (Kennicutt 1998; Kewley et al. 2004). We report in Fig. 5.12 the M_*-SFR plane with our two newly discovered QPEs, together with normal galaxies, and hosts of known TDEs (Law-Smith et al. 2017) and CLAGN (Dodd et al. 2021), all taken below z<0.1 and within the Sloan Digital Sky Survey MPA-JHU DR7 catalog (Brinchmann et al. 2004). Evidence is mounting that both TDEs (Law-Smith et al. 2017; Hammerstein et al. 2021) and CLAGN (Dodd et al. 2021) might be over represented in galaxies in the so-called 'green valley', perhaps indicating that they are activated in specific periods of galaxy co-evolution with their central black holes. For QPEs, a statistically meaningful sample still needs to be built before reaching any conclusion.

We have estimated that the host galaxy of eRO-QPE1 is more massive than that of eRO-QPE2. We here refrain from quoting absolute values for black hole masses using their scaling relations with the host galaxies properties, since our stellar masses are lower than the ones used to calibrate them (Reines & Volonteri 2015). However, it is worth mentioning that the relative ratio of ~4-8 in stellar masses, between eRO-QPE1 and eRO-QPE2, would propagate to a black hole mass ratio of the order of ≈10 (Reines & Volonteri 2015). This is in line with the X-ray timing properties in eRO-QPE1 and eRO-QPE2, since their peak-to-peak separation and rise-to-decay duration scale roughly by the same amount. Finally, X-ray emission from eRO-QPE1 and eRO-QPE2 was observed to be positionally consistent with the galaxy nucleus for both objects (Fig. 5.3 and 5.6; Section 5.4). If a future QPE is found in a more nearby galaxy we can aim to constrain more precisely the X-ray position with respect to the galactic nucleus. This will allow us to determine conclusively whether or not these phenomena are nuclear.

5.7.2 On accretion flow instabilities

As introduced with more details in Section 2.2.2 of this Thesis, accretion disks (Shakura & Sunyaev 1973) with an accretion rate such that radiation-pressure dominates in the inner flow are thought to be subject to thermal-viscous instabilities (Lightman & Eardley 1974). The net result of these instabilities is that the luminosity is predicted to oscillate (Janiuk et al. 2002; Janiuk & Czerny 2011; Merloni & Nayakshin 2006; Grzędzielski et al. 2017b) with timescales and amplitude proportional to the black-hole mass and bolometric luminosity (Czerny et al. 2009; Wu et al. 2016). The predicted light curves profiles show first a stable and slow rise in luminosity, as both temperature and surface density increase while matter is slowly accumulated. Thereafter a sharp luminosity burst is produced by a runaway increase (decrease) in temperature (surface density) propagating outwards within the unstable region. Finally, the inner flow, devoid of the matter supply, cools down rapidly and cycles back to the initial stable state with low temperature

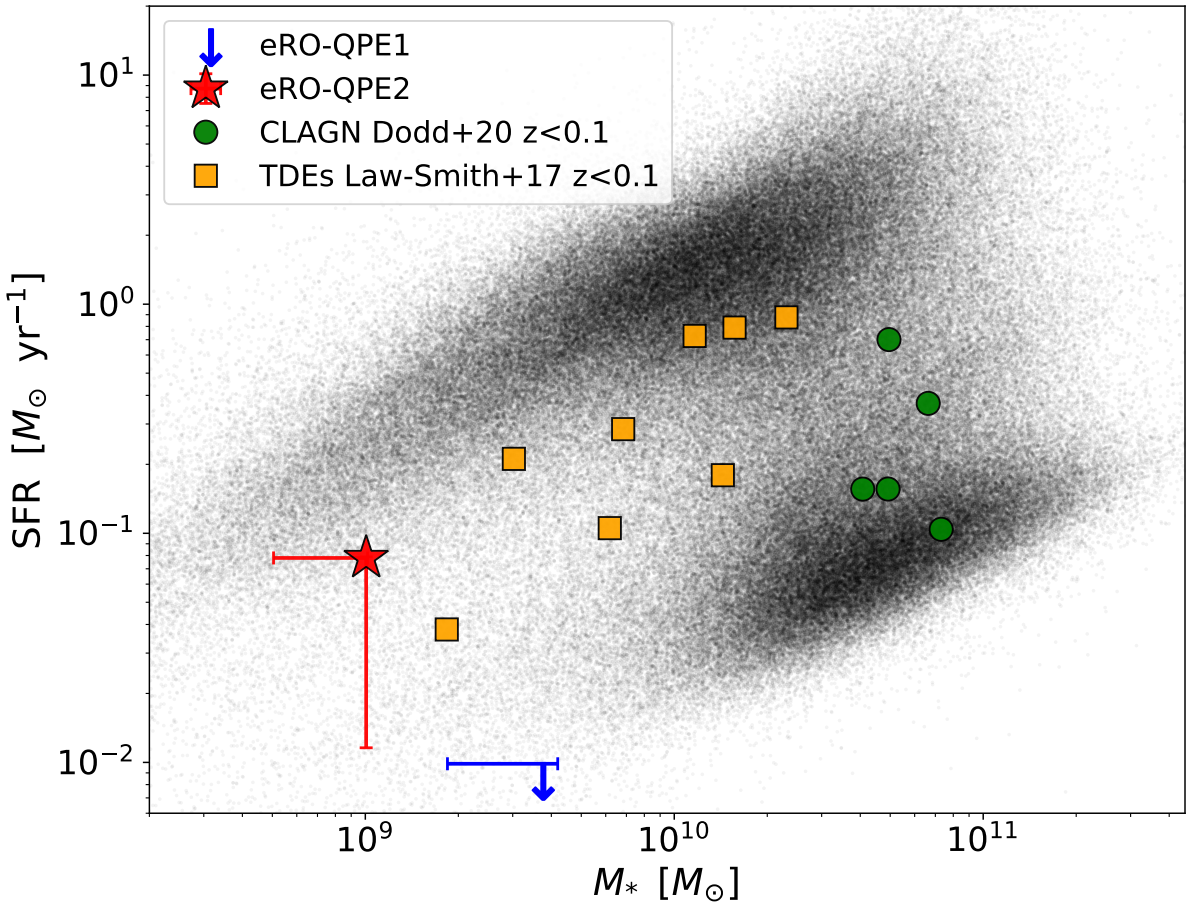

Figure 5.12: Stellar mass M_* and star formation rate (SFR) for eRO-QPE1 (blue) and eRO-QPE2 (red), with related 1σ uncertainties; for eRO-QPE1 SFR is largely unconstrained (see Section 5.7.1). For a comparison, normal galaxies (Brinchmann et al. 2004), TDEs (Law-Smith et al. 2017) and CLAGN (Dodd et al. 2021), all below z<0.1, are also shown.

and density. Both heating and cooling fronts propagate following thermal timescales (Janiuk & Czerny 2011), where $\tau_{th} \sim \alpha^{-1}\ (GM_{BH}/R^3)^{-1/2}$. These so-called limit-cycle or heartbeat instabilities have been successfully applied to a few accreting sources across all mass scales, for instance to the stellar-mass black holes GRS 1915+105 (Taam et al. 1997; Belloni et al. 2000; Neilsen et al. 2011), IGR J17091-3624 (Altamirano et al. 2011) and 4XMM J111816.0-324910 (Motta et al. 2020) and to super-massive black holes in a statistical fashion (Czerny et al. 2009; Wu et al. 2016). The similarity of their timing properties with QPEs in GSN069 is tantalizing and naturally led to the proposed connection with limit-cycle instabilities for that object. In particular, the symmetry of the eruptions in GSN069 was compared to the fast heating and cooling phases of the instability (Miniutti et al. 2019), both following similar τ_{th} under the assumption of invariant α across the two phases (Janiuk et al. 2004). The lack of a slow rise before the eruptions in QPEs, predicted by the instability models, could be due to our limited coverage of the full disk temperature profile in the soft X-ray band.

With the two newly discovered QPEs we can now argue against at least this type of accretion disk instability as the origin of QPEs. Specifically, the strong asymmetric nature of the eruptions in eRO-QPE1, which show a faster rise and a much slower decay (Fig. 5.10 and 5.11), argues against this interpretation. Qualitatively, our data would suggest that QPEs are not related to τ_{th}, since α is not expected to change between the hot and cold phases in AGN (Janiuk et al. 2004). Moreover, if instead it is the front propagation timescales, following $\tau_{front} \sim (H/R)^{-1}\ \tau_{th}$, or viscous timescales, following $\tau_{visc} \sim (H/R)^{-2}\ \tau_{th}$, that regulates the rise (decay) in the cold (hot) phase, it would imply a thicker flow in the cold and stable phase than in the hot and unstable phase. This runs contrary to the theoretical expectation that unstable flows should be thicker (Janiuk & Czerny 2011). The limit-cycle oscillation theory further predicts that once the period, duty cycle and luminosity amplitude are known and a viscosity prescription for the accretion flow is adopted, there are only specific values of M_{BH} and α that unstable sources are allowed to follow (Grzędzielski et al. 2017b). Here we adopt for eRO-QPE1 (eRO-QPE2) a peak-to-peak period T_{pp}=18.5 h (2.4 h), an amplitude A~294 (~11) and a duty-cycle D=41% (19%). The amplitude A is the ratio of the disk luminosity (computed within the 0.001-100 keV range) for peak and quiescence, taken as proxy of the maximum and minimum bolometric luminosity, while D is here defined as the ratio of the flare duration (rise-to-decay T_{rd}) and the period T_{pp}. We begin by adopting a standard viscosity prescription, with the average stress between the annuli proportional to the gas plus radiation pressure P_{tot} (Shakura & Sunyaev 1973). The allowed M_{BH} and α values for eRO-QPE1 (eRO-QPE2) are $M_{BH} \sim 4\text{x}10^6\ M_\odot$ and $\alpha \sim 5$ ($M_{BH} \sim 3\text{x}10^6\ M_\odot$ and $\alpha \sim 3$), therefore an unphysically high viscosity parameter would be required. Considering alternative viscosity prescriptions (Merloni & Nayakshin 2006; Grzędzielski et al. 2017b), for eRO-QPE1 (eRO-QPE2) a more reasonable $\alpha \sim 0.1$ or ~ 0.01 would correspond to allowed $M_{BH} \sim 2.4\text{x}10^3\ M_\odot$ or $M_{BH} \sim 60\ M_\odot$ ($M_{BH} \sim 4.3\text{x}10^3\ M_\odot$or $M_{BH} \sim 30\ M_\odot$), respectively. The above combinations are either unphysical or very unlikely. Adopting $\alpha \sim 0.2$ and alternative viscosity prescriptions eRO-QPE1 (eRO-QPE2) would yield an intermediate-mass black hole (IMBH) at $M_{BH} \sim 0.9\text{x}10^4\ M_\odot$ ($M_{BH} \sim 1.6\text{x}10^4\ M_\odot$) accreting at ~0.1 (~0.3) Eddington in quiescence and at ~30 (~3) Eddington at the peak. However, this IMBH scenario would not account for the opposite asymmetry shown by eRO-QPE1 compared to the theoretical predictions, nor would the resulting thermal timescales be self-consistent for either of the two: for eRO-QPE1 (eRO-

QPE2) τ_{th}~ 20s (35s) at 20 r_g adopting M_{BH}~ 0.9x10^4 $M_\odot$ (M_{BH}~ 1.6x10^4 $M_\odot$), which is orders of magnitude smaller than the observed QPE durations, and the rise-to-peak times would be only reconciled with τ_{th} at ~ 780 r_g (~ 250 r_g). Analogous results can be obtained using the observed properties of RX J1301.9+2747 (Giustini et al. 2020), adopting T_{pp}~20 ks (or the second period T_{pp}~13 ks), D=6% (9%) and A~9.4, the latter obtained taking the ratio of the quoted quiescence and peak 0.3-2.0 keV flux as proxy for a bolometric luminosity ratio: adopting from Giustini et al. (2020) α ~ 0.15 the allowed black hole mass is ~ 2.2x10^4 $M_\odot$ (~ 1.5x10^4 $M_\odot$), much lower than the quoted ~ 0.8-2.8x10^6 $M_\odot$ (Giustini et al. 2020; Shu et al. 2017).

When a given source is in a 'sweet-spot' regime in mass accretion rate , some more recent modified accretion disks viscosity prescriptions predict the presence of a narrow unstable zone placed within an inner inefficient advection-dominated flow and an outer standard geometrically-thin and stable flow (Sniegowska et al. 2020). This model would reduce the propagation timescales by a factor ~dR/R, where dR is the radial extent of the unstable zone at a distance R from the black hole, which may help reconcile the model with the dramatic and fast variability observed in CLAGN (MacLeod et al. 2016). This would not, however, change the inconsistency with the asymmetric shape of the newly observed QPEs, nor was it successful in modeling all the observables in GSN 069 (Sniegowska et al. 2020). In summary, our data for both our newly-detected QPEs are inconsistent with published models for radiation pressure instability (Janiuk et al. 2002; Janiuk & Czerny 2011; Merloni & Nayakshin 2006; Grzędzielski et al. 2017b). The role of more complex, or exotic phenomenology (Sniegowska et al. 2020) should be further explored.

We also note that a fast-rise exponential-decay profile, like the one in eRO-QPE1, can be naturally produced by ionization instability models which are used for some bursting stellar-mass accreting compact objects (Hameury 2020). To our knowledge there is no evidence so far of such instabilities taking place in AGN (Hameury et al. 2009). In addition, the predicted timescales are many orders of magnitude longer than QPEs for both AGN (Hameury et al. 2009; Lin & Shields 1986; Yan & Xie 2018) and IMBH masses (Lasota et al. 2011).

Finally, we discuss disk warping and tearing induced by Lense-Thirring precession (Nixon et al. 2012; Raj et al. 2021), which has been recently qualitatively compared also to QPE sources (Raj & Nixon 2021). In this work we presented new evidence of QPEs being observed in previously inactive galaxies, therefore the accretion flow in these systems should be young. Moreover, a key element of disk warping and tearing due to Lense-Thirring precession is that mass needs to flow in from large inclination with respect to the black hole spin. Both conditions are satisfied if the accretion flow is formed, for instance, by a fully-stripped TDE. However, in this case the warped inner flow would be damped quite fast (Franchini et al. 2016), which would be in contrast with QPEs lasting at least months or even years (Figure 1 and 2; Miniutti et al. 2019; Giustini et al. 2020). A more quantitative comparison is beyond the reach of this work and of current disk warping and tearing simulations, but this is a promising scenario worth exploring in the future.

5.7.3 On the presence of an orbiting body

Periodic variability is also often associated to binary systems of compact objects (De Rosa et al. 2019) and the connection with the quasi-periodic nuclear emission observed in QPEs is tempting.

We here assume the main body to be a super-massive black hole ranging between ~10^4-10^7 $M_\odot$ and we first consider the presence of a second orbiting super-massive black hole with a similar mass. There are several reasons which, when combined, disfavor such a scenario. Firstly, simulations show that the accretion flow of such objects is composed by a circum-binary disk with two inner small mini-disks (Farris et al. 2014; Bowen et al. 2018; Tang et al. 2018), which are thought to produce a quasi-sinusoidal modulated emission (Farris et al. 2015; D'Orazio et al. 2015). This signature can be detected in transient surveys (Graham et al. 2015a; Charisi et al. 2016) or in single sources (Graham et al. 2015b), with a well-known extreme case being OJ 287 (Sillanpaa et al. 1988; Valtonen et al. 2008). However, so far there is no evidence of such variability in optical and UV data (Miniutti et al. 2019) of QPEs (Fig. 5.2 and 5.5), in particular in eRO-QPE1, which was covered in g- and r-band by the Zwicky Transient Facility DR3 (Graham et al. 2019) until the end of 2019. Nor can this prediction be reconciled with the dramatic non-sinusoidal eruptions observed in X-rays, even in the case of binary self lensing (D'Orazio & Di Stefano 2018) which can produce sharper bursts, albeit achromatic therefore in contrast with the energy dependence of QPEs (Miniutti et al. 2019; Giustini et al. 2020). Moreover, we do not observe peculiar single- or double-peaked emission lines (Wang et al. 2009; Smith et al. 2010; Eracleous et al. 2012) and this can not be reconciled by enhanced obscuration (Pfeifle et al. 2019), since infrared photometry in QPEs is not AGN-like (WISE observed W1~W2 for the past 6-7 years) and X-rays do not indicate the presence of strong absorption. Secondly, super-massive black hole binaries are expected to form mostly via galactic mergers (Khan et al. 2016; Kelley et al. 2017), but the host galaxies of the two newly discovered QPEs look unperturbed (Fig. 5.3 and 5.6). Perhaps most importantly, a binary of super-massive black holes observed with a periodicity of the order of hours, such as the four observed QPEs, would show a large period derivative, due to gravitational wave emission, and would be relatively close to merger. To have (at least) four such objects very close to merger within z~0.02-0.05 is very unlikely (Payne et al. 2020) and would imply that they are much more common in the local Universe than observations suggest (Graham et al. 2015a; Charisi et al. 2016).

Under the simplified assumption that the orbital evolution is dominated by gravitational waves emission, Fig. 5.13 shows the allowed parameter space in terms of $\dot{P}$ and M_2 for a range of $M_{BH,1}$~10^4-10^7 $M_\odot$ and zero or high orbit eccentricity (e_O~0.9), given the rest-frame period of both eRO-QPE1 and eRO-QPE2. We have additionally imposed $M_2 \leq M_{BH,1}$. For both sources we can draw a tentative line at the minimum period derivative that, if present, we would have measured already within the available observations: quite conservatively, we adopt a period decrease of one cycle over the 15 observed by NICER for eRO-QPE1 and the 9 observed by XMM-Newton for eRO-QPE2 (Fig. 5.2 and 5.5). Our constraint on $\dot{P}$ is not very stringent for eRO-QPE1 and only high M_2 and eccentricities are disfavored; instead, for eRO-QPE2 only an orbiting IMBH, or smaller, is allowed for zero eccentricity, while only a stellar-mass compact object is allowed for high eccentricity (e_O~0.9). Future observations of eRO-QPE1 and eRO-QPE2 in the next months may lead to tighter constraints on the mass and eccentricity of the putative orbiting body.

The preliminary conclusion of our analysis is that, if QPEs are driven by the presence of an orbiting body around a central black hole, it is more likely that this is a compact object with a mass significantly smaller than the ~10^4-10^7 $M_\odot$ assumed for the main body. This scenario could make QPEs a viable candidate for EMRI (Amaro-Seoane et al. 2007; Babak et al. 2017; Wang

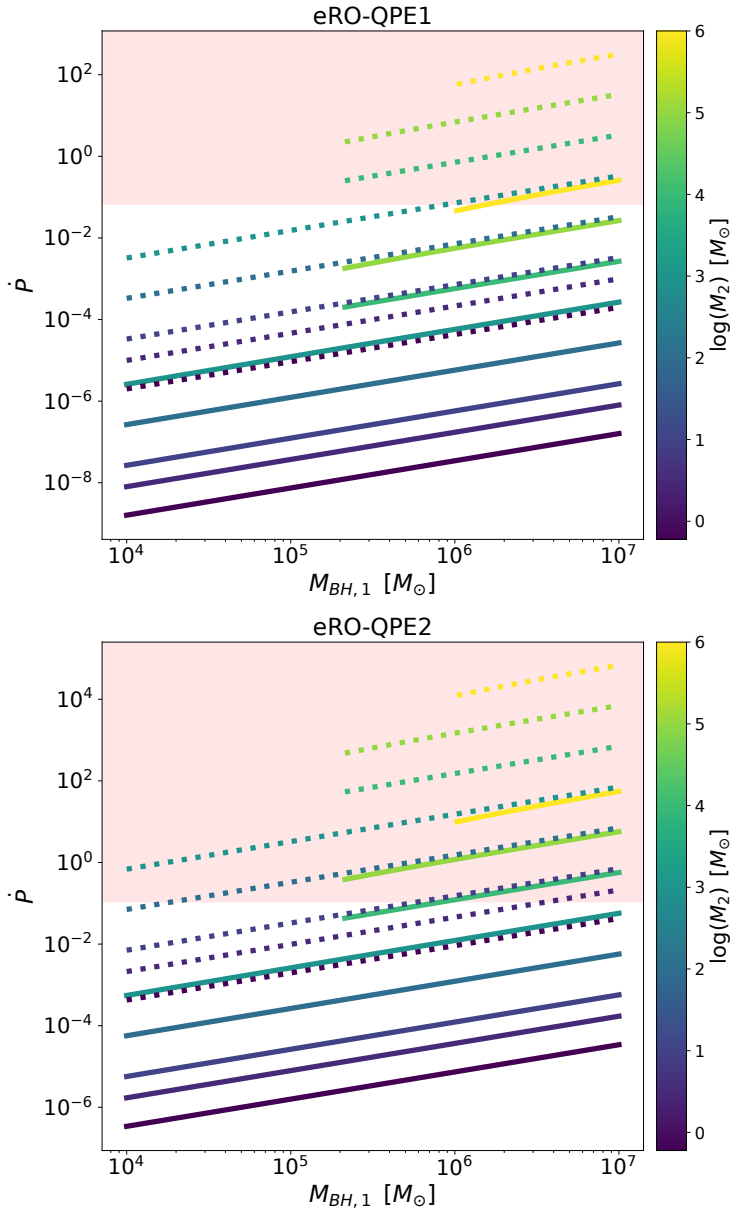

Figure 5.13: *Top:* allowed parameter space in terms of period derivative and secondary mass M_2 for a range of primary mass $M_{BH,1}$~10^4-10^7 $M_\odot$ and zero (solid lines) or high orbit eccentricity (e_O~0.9, dotted lines), in which can reproduce the rest-frame period of eRO-QPE1. We have additionally imposed $M_2 \leq M_{BH,1}$. We have drawn an approximate threshold at the minimum period derivative that, if present, we would have measured already within the available observations, corresponding to a period decrease of one QPE cycle over the 15 observed by NICER (Fig. 5.2). The excluded region is shaded in red. *Bottom:* same as the top panel but for eRO-QPE2 and adopting as tentative minimum $\dot{P}$ a period decrease of one cycle over the 9 observed with XMM-Newton (Fig. 5.5).

et al. 2019b), with considerable implications for multi-messenger astrophysics and cosmology (Bloom et al. 2009; Tamanini 2017). Interestingly, it has been recently suggested for GSN 069 that a stellar-mass compact object orbiting around a super-massive black hole could be the origin of QPEs: a white dwarf of ~0.2$M_\odot$ on a highly eccentric orbit (e_O~0.94) could reproduce the mass inflow rate needed to produce the observed X-ray luminosity averaged over a QPE cycle (King 2020). This is reminiscent of a suggested, albeit still observationally elusive, EMRI formation channel (Sesana et al. 2008; Zalamea et al. 2010; Wang et al. 2019b; Eracleous et al. 2019). For GSN 069, a possible explanation of the QPE-free X-ray bright and decaying phase could be given by an accretion flow expanding and intercepting the body at a later time (Miniutti et al. 2019); or if the orbiting body was originally a massive star and the stripped envelope produced the TDE-like behavior of the past decade (Miniutti et al. 2019) while the remaining core started interacting with the newly born or expanded accretion flow only at a later stage, which would also explain the relatively small mass required by the white dwarf calculations (King 2020). For the other QPEs which did not show evidence of a past X-ray bright and decaying phase, this scenario is not necessary and the interaction with a second stellar-mass (or more massive) compact object could qualitatively reproduce the periodic behavior (Fig. 5.13). Future X-ray observations of the known QPEs would help in further constraining the possible orbital evolution. It should be pointed out that these calculations so far only matched the average observed QPE luminosity with the mass inflow rate required to produce it (King 2020), but details on the exact physical mechanism that would produce these X-ray bursts are still elusive (see Section 5.7.2).

Finally, we address the lack of UV and optical variability in the scenario of an orbiting body. The X-ray plateau at minimum shows an almost featureless accretion disk thermal spectrum (Fig. 5.9; Miniutti et al. 2019; Giustini et al. 2020), which could have been built up during the first orbiting cycles. This accretion flow should be unusually small due to the lack of a broad line region (Miniutti et al. 2013; Sun et al. 2013), which would respond in light-days and that, if present, should have been observed in the SALT spectra taken months after the X-ray QPEs (Fig. 5.3 and 5.6). The lack of strong UV and optical variability might be then due to the fact that the accretion disk is not large enough to even emit strong enough UV-optical radiation to emerge above the galaxy emission, which we can assume to be most of the observed L~4.0x10^{41} erg s^{-1}(L~4.3x10^{41} erg s^{-1}) in the OM-UVW1 filter at 2910Å for eRO-QPE1 (eRO-QPE2). Using a simplified but physically motivated accretion disk model (Arcodia et al. 2019) for a spin zero black hole accreting at ~0.1 Eddington, we computed the distance at which the bulk of 2910Å radiation would be emitted, namely ~1100 and ~500 r_g for a black hole mass of 10^5 and 10^6 $M_\odot$, respectively. This would shift to even larger radii for increasing accretion rate (e.g. ~1850 and ~860 r_g at ~0.5 Eddington), while even for high spinning sources (spin ~0.9) the peak of OM-UVW1 flux would still come from ~775 and ~360 r_g. Furthermore, the predicted OM-UVW1 disk luminosity would be at least one or two orders of magnitude lower than the observed L~4.0x10^{41} erg s^{-1} in the most luminous scenario. Therefore, even an UV-optical eruption 100 times brighter than the plateau would be barely detectable above the galaxy component.

5.7.4 Predicted numbers and future study of QPEs

Detailed self-consistent calculations of the real intrinsic QPE rates and how they compare, for instance, to predicted rate of EMRI events, are beyond the scope of this Thesis. Instead, we provide here a rough model-independent estimate of the expected number of *observed* eROSITA QPEs, regardless of their origin. The only assumption for this calculation is that these sources are low-mass SMBHs and their quiescent phase is given by a thermal emission from an accretion disk (i.e. a function of mass, accretion rate and distance). For the former assumption, observations currently find QPEs in low-mass galaxies likely hosting a low-mass SMBHs. We do not know whether this is merely an observational bias, but for the sake of computing *observed* eROSITA QPE rates in a single eRASS, we also assume that if QPEs existed in more massive SMBHs they would evolve over longer timescales than the typical eRASS exposure and would be therefore missed. QPE patterns can in principle be identified in light curves even if the quiescent flux is consistent with background, provided the bright phase flux can be significantly detected above it. To make predictions for eROSITA, we convolved a black hole mass function (Merloni & Heinz 2008) between ~$10^{4.5}$-$10^{6.5}$$M_\odot$ up to z~0.03 with the eROSITA sensitivity, namely we computed the number of black holes which are accreting highly enough (e.g., Aird et al. 2012) that eROSITA would detect (or marginally non-detect) their quiescent phase. This yields N≈100, which is then reduced with some educated guesses on a number of unknowns: during what fraction of their X-ray bright phase such sources undergo QPE behavior (the biggest unknown; e.g. >20% for GSN 069); how many such sources are obscured and missed (≈2/3); how many times we detect ongoing QPEs given the eROSITA sampling (depends on the period and the burst duration; e.g. ≈20% for GSN 069). This results in a (extremely uncertain) number of order unity per eRASS scan in the eROSITA-DE hemisphere, which is remarkably in agreement with our pilot study of the first few months of eROSITA operations. Thus, the low observed numbers do not necessarily imply that these events are a rare phenomenon intrinsically and they can actually be a fairly common product of the black holes co-evolution with their host galaxies (Heckman & Best 2014). With a statistically meaningful sample of QPEs, inverting this calculation may allow us to constrain the black hole mass function in a poorly known mass regime (Kelly & Merloni 2012).

Since neither eROSITA's observing cadence nor QPEs are exactly periodic, every eRASS can be treaed as an independent sampling of the sky. Therefore if ≈ 1 QPE source per eRASS is reasonably expected, about ~ 5 – 10 QPEs may be observed during the survey. Moving forward, an option could be to follow-up with eROSITA itself, in pointing mode after the end of the all-sky surveys, the second-tier and less secure candidates found during the survey. Moreover, other planned or incoming X-ray facilities can be used to improve on our knowledge of QPEs. One example is the Einstein Probe[3] (EP), led by the Chinese Academy of Sciences and expected to launch in late 2022 or early 2023 (Z. Liu, priv. comm.). It is composed by two complementary X-ray instruments: the Wide-field X-ray Telescope (WXT), which boasts a large field of view (~ 3600 deg^2) and a moderate spatial resolution (~ 5 arcmin), and the Follow-up X-ray Telescope (FXT), which is more sensitive but with a smaller field of view compared to WXT. FXT is effectively based on eROSITA-like optics and CCDs and it is therefore comparable to 1/7 of

[3] http://ep.nao.cas.cn/

eROSITA (Predehl et al. 2020). The EP is intended to be put on a low orbit of ∼ 97minutes, during which it will observe the night-side sky (i.e. opposite to the Sun) with three pointings of ∼ 20 min each. After three orbits most of the night-sky will be covered, therefore every point in the night-sky will be covered a few times per day and for several days minimum, until Earth's revolution around the Sun 'moves' the night-sky over different positions. The whole sky will be observed at least once within the first six-months. The goal of EP is to discover and monitor variable objects in the soft X-rays. It is therefore suitable to perform an all-sky QPEs search in parallel to, and in continuation of, eROSITA's.

Athena (Advanced Telescope for High Energy Astrophysic) is the next-generation X-ray observatory selected by the European Space Agency, planned to launch in the early 2030s. The main scientific goal is to study the 'hot and energetic Universe', namely observations of large-scale structures and the study of black holes growth and co-evolution with their host galaxies (Nandra et al. 2013). A single mirror assembly with silicon pore optics technology will have in its focus alternatively the wide-field imager (WFI) and the X-ray integral field unit (X-IFU). WFI will boast large imaging power in the $\sim 0.2 - 15.0$ keV energy range via its $40' \times 40'$ field of view, as well as higher time resolution and photons rates capabilities compared to current-generation Silicon detectors used in X-ray astronomy (Meidinger et al. 2020). X-IFU instead uses micro-calorimetry sensors and it is designed for much higher spectral resolution imaging (∼ 2.5 eV below 7 keV) but within a much smaller field of view, with diameter ∼ $5'$ (Barret et al. 2013). For the science case of QPEs it is of interest the planned nominal fast response to transients ($\lesssim$ 4 hours) and the overlap with LISA, particular in the QPE-EMRI scenario.

5.8 Summary and Conclusions

In this Chapter we presented the detection of QPEs in two galaxies, obtained with a blind and systematic search over half of the X-ray sky with eROSITA. Compared to the only two previously known QPEs (Miniutti et al. 2019; Giustini et al. 2020), the two new ones, named eRO-QPE1 and eRO-QPE2, extend the parameter space of QPE widths and recurrence times towards longer and shorter timescales, respectively. We also note that eRO-QPE1 is the most luminous ($L_{0.5-2.0\,keV} \sim 2. \times 10^{43}$ erg s^{-1} at the peak) and the most distant (z∼ 0.0505) QPE source discovered to date, and the most extreme in terms of timescales (mean peak-to-peak separation of ∼18.5 hours). The outbursts duration and recurrence times in eRO-QPE1 are approximately an order of magnitude longer than in eRO-QPE2 (mean peak-to-peak separation of ∼2.4 hours). This could simply be an effect of the timescales scaling with black hole mass (McHardy et al. 2006). We estimated the total stellar mass of the two host galaxies, which is 4-8 times higher in eRO-QPE1 compared to eRO-QPE2. Assuming a standard scaling of the black hole mass with stellar mass (Reines & Volonteri 2015), this is broadly in agreement with their different X-ray timing properties (see Section 5.6) Furthermore, peak soft X-ray luminosities of ∼ 2x10^{43}erg s^{-1} and ∼10^{42}erg s^{-1}, for eRO-QPE1 and eRO-QPE2 respectively, exclude a stellar-mass black hole origin and their X-ray positions, within uncertainties, suggest a nuclear origin within their galaxies (Fig. 5.3 and 5.6).

The optical counterparts of eRO-QPE1 and eRO-QPE2 are local low-mass galaxies with no canonical AGN-like broad emission lines in the optical nor any infrared photometric excess indi-

cating the presence of hot dust. In this sense they are similar to GSN 069 and RX J1301.9+2747, whose optical spectra, however, show narrow emission lines with clear AGN-driven ionisation (Miniutti et al. 2013; Sun et al. 2013). Instead, the optical counterpart of eRO-QPE1 is easily classified as a passive galaxy from the absence of any significant emission line (Fig. 5.3) and in eRO-QPE2 the strong narrow emission lines observed classify it as a star forming galaxy (Fig. 5.6 and Section 5.7.1). This in turns suggests that the two newly discovered galaxies have not been active for at least the last $\approx 10^3$-10^4 years, assuming narrow-line region light-travel timescales (Chen et al. 2019). While the number of known QPEs is too low to reach firm statistical conclusions, our blind search with eROSITA is inherently designed to sample the QPEs' host galaxies population without bias, as opposed to serendipitous or archival discoveries which relied on the source being previously active and known (Miniutti et al. 2019; Giustini et al. 2020). These results hint that perhaps the parent population of QPE hosts consists more of passive, than active galaxies. The QPEs X-ray spectra in quiescence are consistent with an almost featureless accretion disk model (see Section 5.5; Miniutti et al. 2019; Giustini et al. 2020), although the inactive nature of the host galaxies of our sources argues against a *pre-existing* AGN-like accretion system. Moreover, the observed properties of our newly discovered QPEs, as well as those of RX J1301.9+2747[2], are inconsistent with the theoretical predictions of so-called limit-cycle radiation-pressure accretion instabilities (Section 5.7.2; Janiuk et al. 2002; Janiuk & Czerny 2011; Merloni et al. 2006; Grzędzielski et al. 2017b).

Extreme or sinusoidal quasi-periodic variability as seen in QPEs is also typically associated with compact objects binaries, a scenario which would not require the galactic nuclei to be previously active, as our new evidence suggests. Drawing a simplistic scenario, we assume the mass of the main body to be in the range $\sim 10^4$-10^7 $M_\odot$ for both eRO-QPE1 and eRO-QPE2 and computed the expected period decrease of a compact binary due to emission of gravitational waves. We inferred that an orbiting body with a similar mass, namely a supermassive black-hole binary with a mass ratio of order unity (De Rosa et al. 2019), is unlikely given the properties of the observed optical, UV, infrared and X-ray emission in QPEs and the lack of evident periodicity and/or strong period decrease therein. If QPEs are triggered by the presence of a secondary orbiting body, our data suggest its mass (M_2) to be much smaller than the main body. This is in agreement with at least one proposed scenario for the origin of GSN069, for which the average luminosity in a QPE cycle can be reproduced by a periodic mass-inflow rate from a white dwarf orbiting the black hole with a highly eccentric orbit (King 2020). This scenario could make QPEs a viable candidate for the electromagnetic counterparts of the so-called extreme mass ratio inspirals (Amaro-Seoane et al. 2007; Sesana et al. 2008; Zalamea et al. 2010; Babak et al. 2017; Wang et al. 2019b), with considerable implications for multi-messenger astrophysics and cosmology (Bloom et al. 2009; Tamanini 2017). Future X-ray observations on longer temporal baselines (months or years) will help to constrain or rule out this scenario and to monitor the possible orbital evolution of the system.

Chapter 6

Summary, Conclusions and Outlook

Many of the most luminous persistent and transient phenomena we know in the Universe are related to accretion of matter onto black holes of various masses. Over the last few decades, both theoretical and observational fronts within this field have advanced considerably. While an in-depth understanding of all the related observed properties is far from being reached, the many open questions in this field may be tackled from the following different angles. Firstly, the physical origin of the most common observational properties of each class of accreting black holes needs to be overall understood; only then we can improve our understanding expanding to more and more complex scenarios. Secondly, different source classes (defined in terms of black hole mass) have different observational advantages and disadvantages: if (even some of) the physical processes are in common between them, we can improve our understanding on a given class of accreting sources benefiting from the knowledge obtained from another. Thirdly, the study of rare outliers showing extreme observational properties can shed new light onto an otherwise potentially stagnating research field. The aim of this Thesis was indeed to improve on our knowledge of accretion onto black holes across the mass scale, by following all the three above-mentioned approaches.

Firstly, we attempted to understand the physical driver of one of the most important observed relation in bright active galactic nuclei: a correlation between optical/UV and X-ray luminosities, which represents the energetic interplay between the inner parts of accretion flows, namely the accretion disk in the optical/UV and the X-ray corona. While the observed correlation is well established and used in the literature since half a century ago, a solid and conclusive theoretical explanation is still lacking. In this Thesis, I used a self-consistently coupled disk-corona model, adapted and improved from the literature, to identify the possible physical driver of the most crucial observed characteristic: the observed slope of the scaling relation between UV and X-ray luminosities is smaller than one in log-space, namely the X-ray emission increases less, relative to the disk emission, going from fainter to brighter sources. In the latter, our model predicts that radiation pressure dominates in a much larger region compared to fainter sources. This pressure regime notoriously damps the otherwise efficient energy transfer to the X-ray corona, which therefore dissipates a lower fraction of accretion power, relative to the disk, compared to fainter sources. However, our model is not able to simultaneously recover this behavior and the overall luminosity of the X-ray coronae, unless the observed black hole population is predominantly

highly spinning. While this is not a far fetched scenario, our model is arguably incomplete in recovering all the many faces of black hole accretion beyond this simple observed relationship. This is due to the many simplifications by which analytic models have to abide, and this is a bar that is hard to raise within a given theoretical framework. Moving further, a self-consistent physical environment can be obtained with global 3D radiation-MHD accretion disk simulations, which have been put forward in the last few years. However, currently there is a large gap between simulations and observations, that needs to be bridged if we want to solely rely on the former to understand the latter.

Secondly, this Thesis also studied and compared the observational properties of stellar-mass and supermassive black holes. There is an intriguing and long-standing question as to whether the accretion flow around black holes is similar among masses that are orders of magnitude apart, and to what extent this analogy holds. For instance, this question can be answered by benefiting from the many observational advantages of accreting stellar-mass black holes: they evolve (even several times) over 'human' timescales, therefore we can study a more or less complete accretion cycle spanning different states in a single object, namely with one given mass, spin and inclination. Moreover, matter around them is hotter and denser with respect to their super-massive relatives, therefore spectroscopy studies and accretion disk modelling suffer from less complications. In this Thesis, I compared the observational properties of disk-corona systems in both stellar-mass and supermassive black holes in their radiatively-efficient phases. I find that they show different observed accretion rate and X-ray spectral index distributions. Once this difference is controlled for, however, the disk-corona systems in the two black holes classes compare quite nicely. This indicates that a mass-scaling of properties might indeed hold, with my results being consistent with disk-corona systems exhibiting the same physical processes, albeit under different conditions: for instance in terms of temperature, optical depth and/or electron energy distribution in the corona, heating-cooling balance, coronal geometry and/or black hole spin; contributions which are degenerate and very hard to constrain. Moving forward, it is likely that most of these unknowns will remain such in the near future. For instance the degeneracy between the temperature and optical depth of the corona, which together determine the X-ray spectral index, can be broken by observing the possible high-energy cutoff of the Comptonization spectrum. However, at least in the soft state of both source classes this is beyond the reach of any hard X-ray instrument of the current and next generation. Furthermore, the geometry of the corona cannot be directly resolved; even if the EHT - the current state of the art - probed such spatial scales around the black hole at the centre of our Milky Way or M87, these sources are not in the same accretion regime as the ones studied here. Regarding the spin, there are several techniques which are able to yield an estimate, but only for a few of the best-observed sources. Future multi-messenger observations of binary systems, including gravitational waves detections, of a statistically sufficient sample of sources might help in providing the typical spin distribution of a population of black holes. This work can be improved upon by adding to the disk-corona plane the ejection dimension, which is provided by radio data. In the accretion regime studied here, it is expected to find sources in a radio-quiet state. However, a complete and sensitive set of radio observations might unveil a finer structure to this otherwise well-known dichotomy between radio-loud and -quiet sources.

Finally, black hole accretion can also be a transient phenomenon and for a few to a few

tens of sources we have evidence of previously inactive galaxies suddenly lighting up and being brought to our attention. These events usually fade in a few days to a few years, much more slowly than they appeared, and are triggered by a star venturing too close to a black hole and being torn apart by its gravitational pull. However, very recently a new possible channel to activate the nuclei of previously quiescent low-mass galaxies has been found. High-amplitude X-ray bursts from galactic nuclei, repeating in a quasi-periodic fashion, were recently discovered and named Quasi-Periodic Eruptions (QPEs). Another important new contribution of this Thesis is the discovery of QPEs in two further galaxies (doubling the total sample of known QPEs!). We have found them with a blind and systematic search over half of the X-ray sky with the newly-launched eROSITA X-ray telescope. The main novelty brought by our discovery is that, contrary to the two previously known QPEs, the host galaxies' optical spectra of the two new QPE sources show no signature of black hole activity. This might indicate that a pre-existing accretion flow typical of active nuclei is not required to trigger these events. Indeed, the periods, amplitudes and profiles of the newly discovered QPEs are inconsistent with current models that invoke radiation-pressure driven accretion disk instabilities, which were previously suggested. Instead, QPEs might be driven by an orbiting compact object. Their observed properties require the mass of the secondary object to be smaller than the main body and future X-ray observations may constrain possible changes in the period due to orbital evolution. This newly-born science case will continue with eROSITA during its ongoing and future all-sky surveys, and with future generations of X-ray missions as well. These include the up-coming Einstein Probe, and the next revolutionary X-ray space mission Athena, for which we can also exploit the multi-messenger synergies with LISA, in case the current leading scenario for the QPEs' origin will be confirmed. In any case, X-ray eyes can now continue to study this new and exotic manifestation of black hole accretion.

Bibliography

Abbott, B. P., Abbott, R., Abbott, T. D., et al. 2016a, Phys. Rev. Lett., 116, 061102

Abbott, B. P., Abbott, R., Abbott, T. D., et al. 2016b, Phys. Rev. Lett., 116, 241103

Abbott, B. P., Abbott, R., Abbott, T. D., et al. 2019, Phys. Rev. X, 9, 031040

Abbott, B. P., Abbott, R., Abbott, T. D., et al. 2017, ApJ, 851, L35

Abbott, B. P., Abbott, R., Abbott, T. D., et al. 2017a, Phys. Rev. Lett., 119, 141101

Abbott, B. P., Abbott, R., Abbott, T. D., et al. 2017b, Phys. Rev. Lett., 118, 221101

Abbott, R., Abbott, T. D., Abraham, S., et al. 2020, arXiv e-prints, arXiv:2010.14527

Abbott, R., Abbott, T. D., Abraham, S., et al. 2020, Phys. Rev. Lett., 125, 101102

Abbott, T. M. C., Abdalla, F. B., Allam, S., et al. 2018, ApJS, 239, 18

Abdo, A. A., Ackermann, M., Agudo, I., et al. 2010, ApJ, 716, 30

Abe, Y., Fukazawa, Y., Kubota, A., Kasama, D., & Makishima, K. 2005, PASJ, 57, 629

Abramowicz, M. A., Czerny, B., Lasota, J. P., & Szuszkiewicz, E. 1988, ApJ, 332, 646

Agol, E. & Krolik, J. H. 2000, ApJ, 528, 161

Ahumada, R., Prieto, C. A., Almeida, A., et al. 2020, ApJS, 249, 3

Ai, Y. L., Yuan, W., Zhou, H. Y., Wang, T. G., & Zhang, S. H. 2011, ApJ, 727, 31

Aird, J., Coil, A. L., & Georgakakis, A. 2017, MNRAS, 465, 3390

Aird, J., Coil, A. L., Georgakakis, A., et al. 2015, MNRAS, 451, 1892

Aird, J., Coil, A. L., Moustakas, J., et al. 2012, ApJ, 746, 90

Alexander, K. D., van Velzen, S., Horesh, A., & Zauderer, B. A. 2020, Space Sci. Rev., 216, 81

Alston, W. N., Fabian, A. C., Kara, E., et al. 2020, Nature Astronomy, 2

Altamirano, D., Belloni, T., Linares, M., et al. 2011, ApJ, 742, L17

Amaro-Seoane, P., Audley, H., Babak, S., et al. 2017, arXiv e-prints, arXiv:1702.00786

Amaro-Seoane, P., Gair, J. R., Freitag, M., et al. 2007, Classical and Quantum Gravity, 24, R113

Ananna, T. T., Treister, E., Urry, C. M., et al. 2020, ApJ, 889, 17

Aneesha, U., Mandal, S., & Sreehari, H. 2019, MNRAS, 486, 2705

Antonucci, R. 1993, ARA&A, 31, 473

Antonucci, R. 2015, ArXiv e-prints [arXiv:1501.02001]

Antonucci, R. R. J. & Cohen, R. D. 1983, ApJ, 271, 564

Antonucci, R. R. J. & Miller, J. S. 1985, ApJ, 297, 621

Arcavi, I., Gal-Yam, A., Sullivan, M., et al. 2014, ApJ, 793, 38

Arcodia, R., Campana, S., Salvaterra, R., & Ghisellini, G. 2018, A&A, 616, A170

Arcodia, R., Merloni, A., Nandra, K., et al. 2021, Nature, 592, 704

Arcodia, R., Merloni, A., Nandra, K., & Ponti, G. 2019, A&A, 628, A135

Arcodia, R., Ponti, G., Merloni, A., & Nandra, K. 2020, A&A, 638, A100

Arnaud, K. A. 1996, in Astronomical Society of the Pacific Conference Series, Vol. 101, Astronomical Data Analysis Software and Systems V, ed. G. H. Jacoby & J. Barnes, 17

Arzoumanian, Z., Gendreau, K. C., Baker, C. L., et al. 2014, in Society of Photo-Optical Instrumentation Engineers (SPIE) Conference Series, Vol. 9144, Space Telescopes and Instrumentation 2014: Ultraviolet to Gamma Ray, ed. T. Takahashi, J.-W. A. den Herder, & M. Bautz, 914420

Bañados, E., Venemans, B. P., Mazzucchelli, C., et al. 2018, Nature, 553, 473

Baade, W. & Minkowski, R. 1954, ApJ, 119, 215

Babak, S., Gair, J., Sesana, A., et al. 2017, Phys. Rev. D, 95, 103012

Bai, X.-N. & Stone, J. M. 2013, ApJ, 767, 30

Balbus, S. A. & Hawley, J. F. 1991, ApJ, 376, 214

Balbus, S. A. & Hawley, J. F. 1992, ApJ, 400, 610

Baronchelli, L., Nandra, K., & Buchner, J. 2018, MNRAS, 480, 2377

Barret, D., den Herder, J. W., Piro, L., et al. 2013, arXiv e-prints, arXiv:1308.6784

Barth, A. J., Ho, L. C., Rutledge, R. E., & Sargent, W. L. W. 2004, ApJ, 607, 90

Barvainis, R. 1987, ApJ, 320, 537

Baskin, A. & Laor, A. 2018, MNRAS, 474, 1970

Becker, R. H., White, R. L., & Helfand, D. J. 1995, ApJ, 450, 559

Beckmann, V., Soldi, S., Ricci, C., et al. 2009, A&A, 505, 417

Begelman, M. C. & Silk, J. 2017, MNRAS, 464, 2311

Belloni, T., Homan, J., Casella, P., et al. 2005, A&A, 440, 207

Belloni, T., Klein-Wolt, M., Méndez, M., van der Klis, M., & van Paradijs, J. 2000, A&A, 355, 271

Belloni, T., Parolin, I., Del Santo, M., et al. 2006, MNRAS, 367, 1113

Belloni, T. M. 2010, States and Transitions in Black Hole Binaries, ed. T. Belloni, Vol. 794, 53

Belloni, T. M. & Motta, S. E. 2016, Astrophysics and Space Science Library, Vol. 440, Transient Black Hole Binaries, ed. C. Bambi, 61

Beloborodov, A. M. 1999, in Astronomical Society of the Pacific Conference Series, Vol. 161, High Energy Processes in Accreting Black Holes, ed. J. Poutanen & R. Svensson, 295

Beloborodov, A. M. 2017, ApJ, 850, 141

Blackburne, J. A., Pooley, D., Rappaport, S., & Schechter, P. L. 2011, ApJ, 729, 34

Blackman, E. G. & Pessah, M. E. 2009, ApJ, 704, L113

Blaes, O. 2007, in Astronomical Society of the Pacific Conference Series, Vol. 373, The Central Engine of Active Galactic Nuclei, ed. L. C. Ho & J.-W. Wang, 75

Blaes, O. 2014, Space Sci. Rev., 183, 21

Blaes, O. & Socrates, A. 2001, ApJ, 553, 987

Blandford, R., Meier, D., & Readhead, A. 2019, ARA&A, 57, 467

Blandford, R. D. & McKee, C. F. 1982, ApJ, 255, 419

Bloom, J. S., Holz, D. E., Hughes, S. A., et al. 2009, arXiv e-prints, arXiv:0902.1527

Boissay, R., Ricci, C., & Paltani, S. 2016, A&A, 588, A70

Boksenberg, A. & Netzer, H. 1977, ApJ, 212, 37

Boller, T., Brandt, W. N., & Fink, H. 1996, A&A, 305, 53

Bondi, H. 1952, MNRAS, 112, 195

Bongiorno, A., Merloni, A., Brusa, M., et al. 2012, MNRAS, 427, 3103

Bongiorno, A., Schulze, A., Merloni, A., et al. 2016, A&A, 588, A78

Bowen, D. B., Mewes, V., Campanelli, M., et al. 2018, ApJ, 853, L17

Brenneman, L. W., Reynolds, C. S., Nowak, M. A., et al. 2011, ApJ, 736, 103

Brinchmann, J., Charlot, S., White, S. D. M., et al. 2004, MNRAS, 351, 1151

Buchner, J. 2014, arXiv e-prints, arXiv:1407.5459

Buchner, J. 2019, PASP, 131, 108005

Buchner, J. & Bauer, F. E. 2017, MNRAS, 465, 4348

Buchner, J., Brightman, M., Nandra, K., Nikutta, R., & Bauer, F. E. 2019, A&A, 629, A16

Buchner, J., Georgakakis, A., Nandra, K., et al. 2014, A&A, 564, A125

Buckley, D. A. H., Andreoni, I., Barway, S., et al. 2018, MNRAS, 474, L71

Buckley, D. A. H., Swart, G. P., & Meiring, J. G. 2006, in Society of Photo-Optical Instrumentation Engineers (SPIE) Conference Series, Vol. 6267, Society of Photo-Optical Instrumentation Engineers (SPIE) Conference Series, ed. L. M. Stepp, 62670Z

Burgh, E. B., Nordsieck, K. H., Kobulnicky, H. A., et al. 2003, in Society of Photo-Optical Instrumentation Engineers (SPIE) Conference Series, Vol. 4841, Instrument Design and Performance for Optical/Infrared Ground-based Telescopes, ed. M. Iye & A. F. M. Moorwood, 1463–1471

Burm, H. 1985, A&A, 143, 389

Buxton, M. M., Bailyn, C. D., Capelo, H. L., et al. 2012, AJ, 143, 130

Caballero-García, M. D., Miller, J. M., Trigo, M. D., et al. 2009, ApJ, 692, 1339

Caccianiga, A., Severgnini, P., Braito, V., et al. 2004, A&A, 416, 901

Cackett, E. M., Chiang, C.-Y., McHardy, I., et al. 2018, ApJ, 857, 53

Cadolle Bel, M., Rodriguez, J., D'Avanzo, P., et al. 2011, A&A, 534, A119

Calderone, G., Ghisellini, G., Colpi, M., & Dotti, M. 2013, MNRAS, 431, 210

Cao, X. 2009, MNRAS, 394, 207

Capellupo, D. M., Netzer, H., Lira, P., Trakhtenbrot, B., & Mejía-Restrepo, J. 2015, MNRAS, 446, 3427

Capellupo, D. M., Netzer, H., Lira, P., Trakhtenbrot, B., & Mejía-Restrepo, J. 2016, MNRAS, 460, 212

Capetti, A., Axon, D. J., Macchetto, F., Sparks, W. B., & Boksenberg, A. 1996, ApJ, 469, 554

Casares, J., Jonker, P. G., & Israelian, G. 2017, X-Ray Binaries, 1499

Cash, W. 1979, ApJ, 228, 939

Chandrasekhar, S. 1960, Proceedings of the National Academy of Science, 46, 253

Charisi, M., Bartos, I., Haiman, Z., et al. 2016, MNRAS, 463, 2145

Chen, J., Shi, Y., Dempsey, R., et al. 2019, MNRAS, 489, 855

Cherepashchuk, A. M. & Lyutyi, V. M. 1973, Astrophys. Lett., 13, 165

Chiaraluce, E., Vagnetti, F., Tombesi, F., & Paolillo, M. 2018, A&A, 619, A95

Comparat, J., Kneib, J.-P., Escoffier, S., et al. 2013, MNRAS, 428, 1498

Connolly, S. D., McHardy, I. M., Skipper, C. J., & Emmanoulopoulos, D. 2016, MNRAS, 459, 3963

Connors, R. M. T., García, J. A., Dauser, T., et al. 2020, ApJ, 892, 47

Coppi, P. S. 1999, Astronomical Society of the Pacific Conference Series, Vol. 161, The Physics of Hybrid Thermal/Non-Thermal Plasmas, ed. J. Poutanen & R. Svensson, 375

Corbel, S., Coriat, M., Brocksopp, C., et al. 2013, MNRAS, 428, 2500

Coriat, M., Corbel, S., Buxton, M. M., et al. 2009, MNRAS, 400, 123

Coriat, M., Fender, R. P., & Dubus, G. 2012, MNRAS, 424, 1991

Corral, A., Della Ceca, R., Caccianiga, A., et al. 2011, A&A, 530, A42

Crawford, S. M., Still, M., Schellart, P., et al. 2012, PySALT: SALT science pipeline

Crummy, J., Fabian, A. C., Gallo, L., & Ross, R. R. 2006, MNRAS, 365, 1067

Curtis, H. D. 1918, Publications of Lick Observatory, 13, 55

Czerny, B. 2019, Open Astronomy, 28, 200

Czerny, B., Du, P., Wang, J.-M., & Karas, V. 2016, ApJ, 832, 15

Czerny, B., Siemiginowska, A., Janiuk, A., Nikiel-Wroczyński, B., & Stawarz, Ł. 2009, ApJ, 698, 840

D'Agostini, G. 2003, Bayesian reasoning in data analysis: A critical introduction

D'Agostini, G. 2005, ArXiv Physics e-prints [physics/0511182]

Davidson, K. 1972, ApJ, 171, 213

Davidson, K. & Netzer, H. 1979, Reviews of Modern Physics, 51, 715

Davis, S. W. & El-Abd, S. 2019, ApJ, 874, 23

Davis, S. W. & Hubeny, I. 2006, ApJS, 164, 530

Davis, S. W. & Laor, A. 2011, ApJ, 728, 98

De Marco, B., Ponti, G., Cappi, M., et al. 2013, MNRAS, 431, 2441

De Rosa, A., Panessa, F., Bassani, L., et al. 2012, MNRAS, 420, 2087

De Rosa, A., Vignali, C., Bogdanović, T., et al. 2019, New A Rev., 86, 101525

Debnath, D., Chakrabarti, S. K., & Nandi, A. 2010, A&A, 520, A98

Della Ceca, R., Caccianiga, A., Severgnini, P., et al. 2008, A&A, 487, 119

Delvecchio, I., Gruppioni, C., Pozzi, F., et al. 2014, MNRAS, 439, 2736

Dermer, C. D. 1995, ApJ, 446, L63

Desroches, L.-B. & Ho, L. C. 2009, ApJ, 690, 267

Dewangan, G. C., Singh, K. P., Mayya, Y. D., & Anupama, G. C. 2000, MNRAS, 318, 309

Dexter, J. & Begelman, M. C. 2019, MNRAS, 483, L17

Dey, A., Schlegel, D. J., Lang, D., et al. 2019, AJ, 157, 168

Dezen, T. & Flores, B. 2018, ApJ, 861, 18

Di Matteo, T. 1998, MNRAS, 299, L15

Dinçer, T., Kalemci, E., Buxton, M. M., et al. 2012, ApJ, 753, 55

Dodd, S. A., Law-Smith, J. A. P., Auchettl, K., Ramirez-Ruiz, E., & Foley, R. J. 2021, ApJ, 907, L21

Doe, S., Nguyen, D., Stawarz, C., et al. 2007, in Astronomical Society of the Pacific Conference Series, Vol. 376, Astronomical Data Analysis Software and Systems XVI, ed. R. A. Shaw, F. Hill, & D. J. Bell, 543

Done, C. & Davis, S. W. 2008, ApJ, 683, 389

Done, C., Davis, S. W., Jin, C., Blaes, O., & Ward, M. 2012, MNRAS, 420, 1848

Done, C., Gierliński, M., & Kubota, A. 2007, A&A Rev., 15, 1

D'Orazio, D. J. & Di Stefano, R. 2018, MNRAS, 474, 2975

D'Orazio, D. J., Haiman, Z., & Schiminovich, D. 2015, Nature, 525, 351

Dubus, G., Hameury, J. M., & Lasota, J. P. 2001, A&A, 373, 251

Dunn, R. J. H., Fender, R. P., Körding, E. G., Belloni, T., & Cabanac, C. 2010, MNRAS, 403, 61

Dunn, R. J. H., Fender, R. P., Körding, E. G., Belloni, T., & Merloni, A. 2011, MNRAS, 411, 337

Dunn, R. J. H., Fender, R. P., Körding, E. G., Cabanac, C., & Belloni, T. 2008, MNRAS, 387, 545

Edelson, R., Gelbord, J., Cackett, E., et al. 2019, ApJ, 870, 123

Edelson, R., Gelbord, J. M., Horne, K., et al. 2015, ApJ, 806, 129

Eilek, J. A., Auman, J. R., Ulrych, T. J., Walker, G. A. H., & Kuhi, L. V. 1973, ApJ, 182, 363

Elitzur, M. & Ho, L. C. 2009, ApJ, 701, L91

Elvis, M., Maccacaro, T., Wilson, A. S., et al. 1978, MNRAS, 183, 129

Eracleous, M., Boroson, T. A., Halpern, J. P., & Liu, J. 2012, ApJS, 201, 23

Eracleous, M., Gezari, S., Sesana, A., et al. 2019, Bull. Am. Astron. Soc., 51, 10

Eracleous, M. & Halpern, J. P. 1994, ApJS, 90, 1

Esin, A. A., McClintock, J. E., & Narayan, R. 1997, ApJ, 489, 865

Event Horizon Telescope Collaboration, Akiyama, K., Alberdi, A., et al. 2019, ApJ, 875, L1

Fabian, A. C., Alston, W. N., Cackett, E. M., et al. 2017, Astronomische Nachrichten, 338, 269

Fabian, A. C., Zoghbi, A., Ross, R. R., et al. 2009, Nature, 459, 540

Falcke, H., Körding, E., & Markoff, S. 2004, A&A, 414, 895

Farris, B. D., Duffell, P., MacFadyen, A. I., & Haiman, Z. 2014, ApJ, 783, 134

Farris, B. D., Duffell, P., MacFadyen, A. I., & Haiman, Z. 2015, MNRAS, 446, L36

Fausnaugh, M. M., Denney, K. D., Barth, A. J., et al. 2016, ApJ, 821, 56

Fausnaugh, M. M., Starkey, D. A., Horne, K., et al. 2018, ApJ, 854, 107

Fender, R., Corbel, S., Tzioumis, T., et al. 1999, ApJ, 519, L165

Fender, R. & Gallo, E. 2014, Space Sci. Rev., 183, 323

Fender, R. P. 2001, MNRAS, 322, 31

Fender, R. P., Belloni, T. M., & Gallo, E. 2004, MNRAS, 355, 1105

Feroz, F., Hobson, M. P., & Bridges, M. 2009, MNRAS, 398, 1601

Filippenko, A. V. & Ho, L. C. 2003, ApJ, 588, L13

Foreman-Mackey, D., Hogg, D. W., Lang, D., & Goodman, J. 2013, PASP, 125, 306

Fossati, G., Maraschi, L., Celotti, A., Comastri, A., & Ghisellini, G. 1998, MNRAS, 299, 433

Franchini, A., Lodato, G., & Facchini, S. 2016, MNRAS, 455, 1946

Frank, J., King, A., & Raine, D. J. 2002, Accretion Power in Astrophysics: Third Edition

Freeman, P., Doe, S., & Siemiginowska, A. 2001, in Proc. SPIE, Vol. 4477, Astronomical Data Analysis, ed. J.-L. Starck & F. D. Murtagh, 76–87

French, K. D., Arcavi, I., & Zabludoff, A. 2016, ApJ, 818, L21

Galeev, A. A., Rosner, R., & Vaiana, G. S. 1979, ApJ, 229, 318

Gallo, E. & Sesana, A. 2019, ApJ, 883, L18

Gammie, C. F. 1999, ApJ, 522, L57

García, J. A., Kara, E., Walton, D., et al. 2019, ApJ, 871, 88

García, J. A., Steiner, J. F., McClintock, J. E., et al. 2015, ApJ, 813, 84

García-Burillo, S., Combes, F., Ramos Almeida, C., et al. 2016, ApJ, 823, L12

Gendreau, K. C., Arzoumanian, Z., & Okajima, T. 2012, in Society of Photo-Optical Instrumentation Engineers (SPIE) Conference Series, Vol. 8443, Space Telescopes and Instrumentation 2012: Ultraviolet to Gamma Ray, ed. T. Takahashi, S. S. Murray, & J.-W. A. den Herder, 844313

Genzel, R., Eckart, A., Ott, T., & Eisenhauer, F. 1997, MNRAS, 291, 219

Georgakakis, A., Aird, J., Schulze, A., et al. 2017, MNRAS, 471, 1976

Ghez, A. M., Klein, B. L., Morris, M., & Becklin, E. E. 1998, ApJ, 509, 678

Ghisellini, G., Righi, C., Costamante, L., & Tavecchio, F. 2017, MNRAS, 469, 255

Ghisellini, G., Tavecchio, F., Foschini, L., et al. 2010, MNRAS, 402, 497

Gibson, R. R. & Brandt, W. N. 2012, ApJ, 746, 54

Gierliński, M., Middleton, M., Ward, M., & Done, C. 2008, Nature, 455, 369

Gierliński, M., Zdziarski, A. A., Poutanen, J., et al. 1999, MNRAS, 309, 496

Gilfanov, M. 2010, X-Ray Emission from Black-Hole Binaries, ed. T. Belloni, Vol. 794, 17

Gilfanov, M. & Merloni, A. 2014, Space Sci. Rev., 183, 121

Gilli, R., Comastri, A., & Hasinger, G. 2007, A&A, 463, 79

Giustini, M., Miniutti, G., & Saxton, R. D. 2020, A&A, 636, L2

Graham, M. J., Djorgovski, S. G., Stern, D., et al. 2015a, MNRAS, 453, 1562

Graham, M. J., Djorgovski, S. G., Stern, D., et al. 2015b, Nature, 518, 74

Graham, M. J., Kulkarni, S. R., Bellm, E. C., et al. 2019, Publications of the Astronomical Society of the Pacific, 131, 078001

Gravity Collaboration, Abuter, R., Accardo, M., et al. 2017, A&A, 602, A94

GRAVITY Collaboration, Amorim, A., Bauböck, M., et al. 2021, arXiv e-prints, arXiv:2102.00068

Gravity Collaboration, Amorim, A., Bauböck, M., et al. 2020a, A&A, 643, A154

Gravity Collaboration, Dexter, J., Shangguan, J., et al. 2020b, A&A, 635, A92

Gravity Collaboration, Pfuhl, O., Davies, R., et al. 2020c, A&A, 634, A1

Gravity Collaboration, Sturm, E., Dexter, J., et al. 2018, Nature, 563, 657

Greene, J. E. & Ho, L. C. 2007, ApJ, 670, 92

Greene, J. E., Strader, J., & Ho, L. C. 2020, ARA&A, 58, 257

Greenstein, J. L. 1963, Nature, 197, 1041

Greenstein, J. L. & Matthews, T. A. 1963, AJ, 68, 279

Grier, C. J., Peterson, B. M., Pogge, R. W., et al. 2012, ApJ, 755, 60

Grimm, H. J., Gilfanov, M., & Sunyaev, R. 2003, MNRAS, 339, 793

Grove, J. E., Johnson, W. N., Kroeger, R. A., et al. 1998, ApJ, 500, 899

Grupe, D., Komossa, S., Leighly, K. M., & Page, K. L. 2010, ApJS, 187, 64

Grzędzielski, M., Janiuk, A., & Czerny, B. 2017a, ApJ, 845, 20

Grzędzielski, M., Janiuk, A., Czerny, B., & Wu, Q. 2017b, A&A, 603, A110

Gu, M. & Cao, X. 2009, MNRAS, 399, 349

Guillochon, J., Ramirez-Ruiz, E., Rosswog, S., & Kasen, D. 2009, ApJ, 705, 844

Haardt, F. & Maraschi, L. 1991, ApJ, 380, L51

Haardt, F. & Maraschi, L. 1993, ApJ, 413, 507

Haardt, F., Maraschi, L., & Ghisellini, G. 1994, ApJ, 432, L95

Hameury, J. M. 2020, Advances in Space Research, 66, 1004

Hameury, J. M., Viallet, M., & Lasota, J. P. 2009, A&A, 496, 413

Hammerstein, E., Gezari, S., van Velzen, S., et al. 2021, ApJ, 908, L20

Hao, H., Sargent, M. T., Elvis, M., et al. 2014, arXiv e-prints, arXiv:1408.1090

Harrison, C. 2014, PhD thesis, Durham University

Harry, G. M., Fritschel, P., Shaddock, D. A., Folkner, W., & Phinney, E. S. 2006, Classical and Quantum Gravity, 23, 4887

Hawley, J. F. & Balbus, S. A. 1991, ApJ, 376, 223

Hawley, J. F. & Balbus, S. A. 1992, ApJ, 400, 595

Hawley, J. F., Gammie, C. F., & Balbus, S. A. 1995, ApJ, 440, 742

Hazard, C., Mackey, M. B., & Shimmins, A. J. 1963, Nature, 197, 1037

Heckman, T. M. & Best, P. N. 2014, ARA&A, 52, 589

Heger, A., Fryer, C. L., Woosley, S. E., Langer, N., & Hartmann, D. H. 2003, ApJ, 591, 288

Heida, M., Jonker, P. G., Torres, M. A. P., & Chiavassa, A. 2017, ApJ, 846, 132

Heinz, S. & Sunyaev, R. A. 2003, MNRAS, 343, L59

HI4PI Collaboration, Ben Bekhti, N., Flöer, L., et al. 2016, A&A, 594, A116

Hickox, R. C. & Alexander, D. M. 2018, ARA&A, 56, 625

Hills, J. G. 1975, Nature, 254, 295

Hjalmarsdotter, L., Axelsson, M., & Done, C. 2016, MNRAS, 456, 4354

Ho, L. C. 2002, ApJ, 564, 120

Ho, L. C. 2009, ApJ, 699, 638

Ho, L. C. & Kim, M. 2016, ApJ, 821, 48

Homan, J., Buxton, M., Markoff, S., et al. 2005, ApJ, 624, 295

Homayouni, Y., Trump, J. R., Grier, C. J., et al. 2019, ApJ, 880, 126

Hopkins, P. F., Richards, G. T., & Hernquist, L. 2007, ApJ, 654, 731

Hoshi, R. 1985, in Galactic and Extra-Galactic Compact X-ray Sources, ed. Y. Tabaka & W. H. G. Lewin, 143

Hubeny, I., Agol, E., Blaes, O., & Krolik, J. H. 2000, ApJ, 533, 710

Hubeny, I., Blaes, O., Krolik, J. H., & Agol, E. 2001, ApJ, 559, 680

Hynes, R. I., Steeghs, D., Casares, J., Charles, P. A., & O'Brien, K. 2003, ApJ, 583, L95

Hynes, R. I., Steeghs, D., Casares, J., Charles, P. A., & O'Brien, K. 2004, ApJ, 609, 317

Ichimaru, S. 1977, ApJ, 214, 840

Jahoda, K., Swank, J. H., Giles, A. B., et al. 1996, in EUV, X-Ray, and Gamma-Ray Instrumentation for Astronomy VII, ed. O. H. W. Siegmund & M. A. Gummin, Vol. 2808, International Society for Optics and Photonics (SPIE), 59 – 70

Janiuk, A. & Czerny, B. 2011, MNRAS, 414, 2186

Janiuk, A., Czerny, B., & Siemiginowska, A. 2002, ApJ, 576, 908

Janiuk, A., Czerny, B., Siemiginowska, A., & Szczerba, R. 2004, ApJ, 602, 595

Janiuk, A., Czerny, B., & Życki, P. T. 2000, MNRAS, 318, 180

Jansen, F., Lumb, D., Altieri, B., et al. 2001, A&A, 365, L1

Jarvis, M. J. & McLure, R. J. 2006, MNRAS, 369, 182

Jiang, Y.-F., Blaes, O., Stone, J. M., & Davis, S. W. 2019a, ApJ, 885, 144

Jiang, Y.-F., Davis, S. W., & Stone, J. M. 2016, ApJ, 827, 10

Jiang, Y.-F., Green, P. J., Greene, J. E., et al. 2017, ApJ, 836, 186

Jiang, Y.-F., Stone, J. M., & Davis, S. W. 2014, ApJ, 784, 169

Jiang, Y.-F., Stone, J. M., & Davis, S. W. 2019b, ApJ, 880, 67

Jiménez-Vicente, J., Mediavilla, E., Muñoz, J. A., & Kochanek, C. S. 2012, ApJ, 751, 106

Jin, C., Ward, M., & Done, C. 2012, MNRAS, 422, 3268

Kadowaki, L. H. S., De Gouveia Dal Pino, E. M., & Stone, J. M. 2018, ApJ, 864, 52

Kalogera, V. & Baym, G. 1996, ApJ, 470, L61

Kamizasa, N., Terashima, Y., & Awaki, H. 2012, ApJ, 751, 39

Kara, E., Steiner, J. F., Fabian, A. C., et al. 2019, Nature, 565, 198

Kawano, T., Done, C., Yamada, S., et al. 2017, PASJ, 69, 36

Kellermann, K. I., Sramek, R., Schmidt, M., Shaffer, D. B., & Green, R. 1989, AJ, 98, 1195

Kelley, L. Z., Blecha, L., & Hernquist, L. 2017, MNRAS, 464, 3131

Kelly, B. C., Bechtold, J., Trump, J. R., Vestergaard, M., & Siemiginowska, A. 2008, ApJS, 176, 355

Kelly, B. C. & Merloni, A. 2012, Advances in Astronomy, 2012, 970858

Kennicutt, Robert C., J. 1998, ARA&A, 36, 189

Kewley, L. J., Geller, M. J., & Jansen, R. A. 2004, AJ, 127, 2002

Khabibullin, I. & Sazonov, S. 2014, MNRAS, 444, 1041

Khadka, N. & Ratra, B. 2020, MNRAS, 492, 4456

Khan, F. M., Fiacconi, D., Mayer, L., Berczik, P., & Just, A. 2016, ApJ, 828, 73

Kilerci Eser, E. & Vestergaard, M. 2018, MNRAS, 474, 1590

King, A. 2020, MNRAS, 493, L120

Kishimoto, M., Antonucci, R., Blaes, O., et al. 2008, Nature, 454, 492

Klindt, L., Alexander, D. M., Rosario, D. J., Lusso, E., & Fotopoulou, S. 2019, MNRAS, 488, 3109

Kobayashi, S., Laguna, P., Phinney, E. S., & Mészáros, P. 2004, ApJ, 615, 855

Kokubo, M. 2018, PASJ, 70, 97

Kolehmainen, M. & Done, C. 2010, MNRAS, 406, 2206

Komossa, S. 2015, Journal of High Energy Astrophysics, 7, 148

Koratkar, A. & Blaes, O. 1999, PASP, 111, 1

Körding, E. G., Jester, S., & Fender, R. 2006, MNRAS, 372, 1366

Kormendy, J. & Richstone, D. 1995, ARA&A, 33, 581

Krawczyk, C. M., Richards, G. T., Mehta, S. S., et al. 2013, ApJS, 206, 4

Kubota, A. & Done, C. 2004, MNRAS, 353, 980

Kubota, A. & Done, C. 2016, MNRAS, 458, 4238

Kubota, A. & Done, C. 2018, MNRAS, 480, 1247

Kubota, A. & Makishima, K. 2004, ApJ, 601, 428

Kubota, A., Makishima, K., & Ebisawa, K. 2001, ApJ, 560, L147

Kubota, A., Tanaka, Y., Makishima, K., et al. 1998, PASJ, 50, 667

Kylafis, N. D. & Belloni, T. M. 2015, A&A, 574, A133

LaMassa, S. M., Cales, S., Moran, E. C., et al. 2015, ApJ, 800, 144

Laor, A. 1991, ApJ, 376, 90

Lasota, J.-P. 2001, New A Rev., 45, 449

Lasota, J. P., Alexander, T., Dubus, G., et al. 2011, ApJ, 735, 89

Law-Smith, J., Ramirez-Ruiz, E., Ellison, S. L., & Foley, R. J. 2017, ApJ, 850, 22

Lawrence, A. 2012, MNRAS, 423, 451

Lawrence, A., Watson, M. G., Pounds, K. A., & Elvis, M. 1985, MNRAS, 217, 685

Liang, E. P. T. & Price, R. H. 1977, ApJ, 218, 247

Lightman, A. P. & Eardley, D. M. 1974, ApJ, 187, L1

Lightman, A. P. & White, T. R. 1988, ApJ, 335, 57

Lin, D. N. C. & Shields, G. A. 1986, ApJ, 305, 28

Liu, B. F., Mineshige, S., & Shibata, K. 2002, ApJ, 572, L173

Liu, H.-Y., Yuan, W., Dong, X.-B., Zhou, H., & Liu, W.-J. 2018a, ApJS, 235, 40

Liu, J.-Y. & Liu, B.-F. 2009, Research in Astronomy and Astrophysics, 9, 966

Liu, J. Y., Liu, B. F., Qiao, E. L., & Mineshige, S. 2012, ApJ, 754, 81

Liu, J. Y., Qiao, E. L., & Liu, B. F. 2016a, ApJ, 833, 35

Liu, T., Merloni, A., Wang, J.-X., et al. 2018b, MNRAS, 479, 5022

Liu, Z., Merloni, A., Georgakakis, A., et al. 2016b, MNRAS, 459, 1602

Loredo, T. J. 1992, in Statistical Challenges in Modern Astronomy, 275–297

Ludlam, R. M., Miller, J. M., & Cackett, E. M. 2015, ApJ, 806, 262

Luo, J., Chen, L.-S., Duan, H.-Z., et al. 2016, Classical and Quantum Gravity, 33, 035010

Lusso, E. 2019a, Astronomische Nachrichten, 340, 267

Lusso, E. 2019b, Astronomische Nachrichten, 340, 267

Lusso, E., Comastri, A., Simmons, B. D., et al. 2012, MNRAS, 425, 623

Lusso, E., Comastri, A., Vignali, C., et al. 2010, A&A, 512, A34

Lusso, E., Piedipalumbo, E., Risaliti, G., et al. 2019, A&A, 628, L4

Lusso, E. & Risaliti, G. 2016, ApJ, 819, 154

Lusso, E. & Risaliti, G. 2017, A&A, 602, A79

Lynden-Bell, D. 1969, Nature, 223, 690

Maccacaro, T., Gioia, I. M., Wolter, A., Zamorani, G., & Stocke, J. T. 1988, ApJ, 326, 680

Maccarone, T. J. 2003, A&A, 409, 697

Maccarone, T. J., Gallo, E., & Fender, R. 2003, MNRAS, 345, L19

MacLeod, C. L., Ross, N. P., Lawrence, A., et al. 2016, MNRAS, 457, 389

Madau, P. & Dickinson, M. 2014, ARA&A, 52, 415

Makishima, K., Maejima, Y., Mitsuda, K., et al. 1986, ApJ, 308, 635

Malzac, J., Beloborodov, A. M., & Poutanen, J. 2001, MNRAS, 326, 417

Maraston, C., Hill, L., Thomas, D., et al. 2020, MNRAS, 496, 2962

Maraston, C. & Strömbäck, G. 2011, MNRAS, 418, 2785

Marchesini, D., Celotti, A., & Ferrarese, L. 2004, MNRAS, 351, 733

Marconi, A., Axon, D. J., Maiolino, R., et al. 2008, ApJ, 678, 693

Marconi, A., Risaliti, G., Gilli, R., et al. 2004, MNRAS, 351, 169

Marecki, A. & Swoboda, B. 2011, A&A, 525, A6

Markert, T. H., Canizares, C. R., Clark, G. W., et al. 1973, ApJ, 184, L67

Markoff, S., Nowak, M. A., & Wilms, J. 2005, ApJ, 635, 1203

Martocchia, S., Piconcelli, E., Zappacosta, L., et al. 2017, A&A, 608, A51

Mason, K. O., Breeveld, A., Much, R., et al. 2001, A&A, 365, L36

Mateos, S., Carrera, F. J., Page, M. J., et al. 2010, A&A, 510, A35

Matthews, T. A. & Sandage, A. R. 1963, ApJ, 138, 30

McHardy, I. M. 1989, in ESA Special Publication, Vol. 296, Two Topics in X-Ray Astronomy, Volume 1: X Ray Binaries. Volume 2: AGN and the X Ray Background, ed. J. Hunt & B. Battrick

McHardy, I. M., Connolly, S. D., Horne, K., et al. 2018, MNRAS, 480, 2881

McHardy, I. M., Connolly, S. D., Peterson, B. M., et al. 2016, Astronomische Nachrichten, 337, 500

McHardy, I. M., Koerding, E., Knigge, C., Uttley, P., & Fender, R. P. 2006, Nature, 444, 730

McHardy, I. M., Papadakis, I. E., Uttley, P., Page, M. J., & Mason, K. O. 2004, MNRAS, 348, 783

Meidinger, N., Albrecht, S., Beitler, C., et al. 2020, in Society of Photo-Optical Instrumentation Engineers (SPIE) Conference Series, Vol. 11444, Society of Photo-Optical Instrumentation Engineers (SPIE) Conference Series, 114440T

Melia, F. 2019, MNRAS, 489, 517

Menzel, M.-L., Merloni, A., Georgakakis, A., et al. 2016, MNRAS, 457, 110

Merloni, A. 2003, MNRAS, 341, 1051

Merloni, A., Bongiorno, A., Brusa, M., et al. 2014, MNRAS, 437, 3550

Merloni, A., Dwelly, T., Salvato, M., et al. 2015, MNRAS, 452, 69

Merloni, A. & Fabian, A. C. 2002, MNRAS, 332, 165

Merloni, A. & Fabian, A. C. 2003, MNRAS, 342, 951

Merloni, A., Fabian, A. C., & Ross, R. R. 2000, MNRAS, 313, 193

Merloni, A. & Heinz, S. 2008, MNRAS, 388, 1011

Merloni, A., Heinz, S., & di Matteo, T. 2003, MNRAS, 345, 1057

Merloni, A., Malzac, J., Fabian, A. C., & Ross, R. R. 2006, MNRAS, 370, 1699

Merloni, A. & Nayakshin, S. 2006, MNRAS, 372, 728

Meyer, F. & Meyer-Hofmeister, E. 1982, A&A, 106, 34

Middei, R., Bianchi, S., Petrucci, P. O., et al. 2019, MNRAS, 483, 4695

Miller, K. A. & Stone, J. M. 2000, ApJ, 534, 398

Miniutti, G., Saxton, R. D., Giustini, M., et al. 2019, Nature, 573, 381

Miniutti, G., Saxton, R. D., Rodríguez-Pascual, P. M., et al. 2013, MNRAS, 433, 1764

Minoshima, T., Hirose, S., & Sano, T. 2015, ApJ, 808, 54

Mirabel, I. F. & Rodríguez, L. F. 1994, Nature, 371, 46

Mirabel, I. F. & Rodríguez, L. F. 1999, ARA&A, 37, 409

Mitsuda, K., Inoue, H., Koyama, K., et al. 1984, PASJ, 36, 741

Miyaji, T., Hasinger, G., Salvato, M., et al. 2015, ApJ, 804, 104

Miyamoto, S., Kitamoto, S., Hayashida, K., & Egoshi, W. 1995, ApJ, 442, L13

Moreno, J., Vogeley, M. S., Richards, G. T., & Yu, W. 2019, PASP, 131, 063001

Morgan, C. W., Kochanek, C. S., Morgan, N. D., & Falco, E. E. 2010, ApJ, 712, 1129

Mosquera, A. M., Kochanek, C. S., Chen, B., et al. 2013, ApJ, 769, 53

Motta, S., Belloni, T., & Homan, J. 2009, MNRAS, 400, 1603

Motta, S. E., Marelli, M., Pintore, F., et al. 2020, ApJ, 898, 174

Muñoz-Darias, T., Casares, J., & Martínez-Pais, I. G. 2008, MNRAS, 385, 2205

Mudd, D., Martini, P., Zu, Y., et al. 2018, ApJ, 862, 123

Naddaf, M.-H., Czerny, B., & Szczerba, R. 2021, arXiv e-prints, arXiv:2102.00336

Nandi, A., Debnath, D., Mandal, S., & Chakrabarti, S. K. 2012, A&A, 542, A56

Nandra, K., Barret, D., Barcons, X., et al. 2013, arXiv e-prints, arXiv:1306.2307

Nandra, K., O'Neill, P. M., George, I. M., & Reeves, J. N. 2007, MNRAS, 382, 194

Nandra, K., Pounds, K. A., Stewart, G. C., et al. 1991, MNRAS, 248, 760

Nanni, R., Vignali, C., Gilli, R., Moretti, A., & Brand t, W. N. 2017, A&A, 603, A128

Narayan, R. & McClintock, J. E. 2008, New A Rev., 51, 733

Narayan, R. & Yi, I. 1994, ApJ, 428, L13

Narayan, R. & Yi, I. 1995, ApJ, 452, 710

Nardini, E., Lusso, E., Risaliti, G., et al. 2019, A&A, 632, A109

Neilsen, J., Remillard, R. A., & Lee, J. C. 2011, ApJ, 737, 69

Nenkova, M., Sirocky, M. M., Nikutta, R., Ivezić, Ž., & Elitzur, M. 2008, ApJ, 685, 160

Netzer, H. 2015, ARA&A, 53, 365

Niedźwiecki, A., Szanecki, M., & Zdziarski, A. A. 2019, MNRAS, 485, 2942

Nixon, C., King, A., Price, D., & Frank, J. 2012, ApJ, 757, L24

Noda, H. & Done, C. 2018, MNRAS, 480, 3898

Nomura, M., Ohsuga, K., & Done, C. 2020, MNRAS, 494, 3616

Novikov, I. D. & Thorne, K. S. 1973, in Black Holes (Les Astres Occlus), 343–450

Oda, S., Shidatsu, M., Nakahira, S., et al. 2019, PASJ, 71, 108

Oke, J. B. 1963, Nature, 197, 1040

Osterbrock, D. E., Koski, A. T., & Phillips, M. M. 1976, ApJ, 206, 898

Özel, F., Psaltis, D., Narayan, R., & McClintock, J. E. 2010, ApJ, 725, 1918

Padovani, P. 2011, MNRAS, 411, 1547

Padovani, P., Alexander, D. M., Assef, R. J., et al. 2017, A&A Rev., 25, 2

Papaloizou, J. C. B. & Lin, D. N. C. 1995, ARA&A, 33, 505

Pâris, I., Petitjean, P., Ross, N. P., et al. 2017, A&A, 597, A79

Parker, M. L., Tomsick, J. A., Kennea, J. A., et al. 2016, ApJ, 821, L6

Payne, A. V., Shappee, B. J., Hinkle, J. T., et al. 2020, arXiv e-prints, arXiv:2009.03321

Peretz, U. & Behar, E. 2018, MNRAS, 481, 3563

Petrucci, P.-O., Ursini, F., De Rosa, A., et al. 2018, A&A, 611, A59

Pfeifle, R. W., Satyapal, S., Secrest, N. J., et al. 2019, ApJ, 875, 117

Pfister, H., Toscani, M., Wong, T. H. T., et al. 2021, arXiv e-prints, arXiv:2103.05883

Piconcelli, E., Jimenez-Bailón, E., Guainazzi, M., et al. 2005, A&A, 432, 15

Pier, E. A. & Krolik, J. H. 1992, ApJ, 401, 99

Pierre, M., Pacaud, F., Adami, C., et al. 2016, A&A, 592, A1

Plant, D. S., Fender, R. P., Ponti, G., Muñoz-Darias, T., & Coriat, M. 2014, MNRAS, 442, 1767

Ponti, G., Fender, R. P., Begelman, M. C., et al. 2012, MNRAS, 422, L11

Pounds, K. 2014, Space Sci. Rev., 183, 5

Pounds, K. A., Done, C., & Osborne, J. P. 1995, MNRAS, 277, L5

Pounds, K. A., Nandra, K., Stewart, G. C., George, I. M., & Fabian, A. C. 1990, Nature, 344, 132

Poutanen, J. & Svensson, R. 1996, ApJ, 470, 249

Pozdnyakov, L. A., Sobol, I. M., & Syunyaev, R. A. 1983, Astrophys. Space Phys. Res., 2, 189

Predehl, P., Andritschke, R., Arefiev, V., et al. 2020, arXiv e-prints, arXiv:2010.03477

Pringle, J. E. 1976, MNRAS, 177, 65

Pringle, J. E. 1981, ARA&A, 19, 137

Pringle, J. E. & Rees, M. J. 1972, A&A, 21, 1

Pringle, J. E., Rees, M. J., & Pacholczyk, A. G. 1973, A&A, 29, 179

Raj, A. & Nixon, C. 2021, arXiv e-prints, arXiv:2101.05825

Raj, A., Nixon, C., & Dogan, S. 2021, arXiv e-prints, arXiv:2101.05824

Ramos Almeida, C. & Ricci, C. 2017, Nature Astronomy, 1, 679

Rees, M. J. 1988, Nature, 333, 523

Reines, A. E. & Volonteri, M. 2015, ApJ, 813, 82

Reis, R. C. & Miller, J. M. 2013, ApJ, 769, L7

Remillard, R. A. & McClintock, J. E. 2006, Annual Review of Astronomy and Astrophysics, 44, 49

Reynolds, C. S. 2013, Classical and Quantum Gravity, 30, 244004

Reynolds, C. S. 2019, Nature Astronomy, 3, 41

Ricci, C., Trakhtenbrot, B., Koss, M. J., et al. 2017, ApJS, 233, 17

Richards, G. T., Lacy, M., Storrie-Lombardi, L. J., et al. 2006, ApJS, 166, 470

Ripperda, B., Porth, O., Sironi, L., & Keppens, R. 2019, MNRAS, 485, 299

Risaliti, G. & Lusso, E. 2015, ApJ, 815, 33

Risaliti, G. & Lusso, E. 2019, Nature Astronomy, 3, 272

Ross, J., Latter, H. N., & Guilet, J. 2016, MNRAS, 455, 526

Rothschild, R. E., Blanco, P. R., Gruber, D. E., et al. 1998, ApJ, 496, 538

Ruan, J. J., Anderson, S. F., Eracleous, M., et al. 2019a, ApJ, 883, 76

Ruan, J. J., Anderson, S. F., Eracleous, M., et al. 2019b, arXiv e-prints, arXiv:1909.04676

Ruffini, R. & Wheeler, J. A. 1971, Physics Today, 24, 30

Runnoe, J. C., Brotherton, M. S., & Shang, Z. 2012, MNRAS, 422, 478

Sakimoto, P. J. & Coroniti, F. V. 1981, ApJ, 247, 19

Salpeter, E. E. 1964, ApJ, 140, 796

Salvato, M., Buchner, J., Budavári, T., et al. 2018, MNRAS, 473, 4937

Salvesen, G., Simon, J. B., Armitage, P. J., & Begelman, M. C. 2016, MNRAS, 457, 857

Salvestrini, F., Risaliti, G., Bisogni, S., Lusso, E., & Vignali, C. 2019, A&A, 631, A120

Sana, H., de Mink, S. E., de Koter, A., et al. 2012, Science, 337, 444

Sandage, A. 1965, ApJ, 141, 1560

Sano, T., Inutsuka, S.-i., Turner, N. J., & Stone, J. M. 2004, ApJ, 605, 321

Sato, S., Kawamura, S., Ando, M., et al. 2009, Journal of Physics: Conference Series, 154, 012040

Saxton, R., Komossa, S., Auchettl, K., & Jonker, P. G. 2020, Space Sci. Rev., 216, 85

Saxton, R. D., Read, A. M., Esquej, P., et al. 2008, A&A, 480, 611

Sbarrato, T., Ghisellini, G., Tagliaferri, G., et al. 2015, MNRAS, 446, 2483

Sądowski, A. 2016, MNRAS, 459, 4397

Schartmann, M., Meisenheimer, K., Camenzind, M., et al. 2008, A&A, 482, 67

Schmidt, M. 1962, ApJ, 136, 684

Schmidt, M. 1963, Nature, 197, 1040

Schmidt, M. 1968, ApJ, 151, 393

Schmidt, M. 1978, Phys. Scr, 17, 135

Schnittman, J. D., Krolik, J. H., & Noble, S. C. 2013, ApJ, 769, 156

Schödel, R., Ott, T., Genzel, R., et al. 2002, Nature, 419, 694

Seaton, M. J. 1995, The opacity project

Seaton, M. J., Yan, Y., Mihalas, D., & Pradhan, A. K. 1994, MNRAS, 266, 805

Serafinelli, R., Vagnetti, F., & Middei, R. 2017, A&A, 600, A101

Sesana, A., Vecchio, A., Eracleous, M., & Sigurdsson, S. 2008, MNRAS, 391, 718

Seyfert, C. K. 1943, ApJ, 97, 28

Shadmehri, M., Khajenabi, F., Dib, S., & Inutsuka, S.-i. 2018, MNRAS, 481, 5170

Shakura, N. I. & Sunyaev, R. A. 1973, A&A, 24, 337

Shakura, N. I. & Sunyaev, R. A. 1976, Monthly Notices of the Royal Astronomical Society, 175, 613

Shang, Z., Brotherton, M. S., Green, R. F., et al. 2005, ApJ, 619, 41

Shankar, F., Weinberg, D. H., & Miralda-Escudé, J. 2009, ApJ, 690, 20

Shapiro, S. L. 2005, ApJ, 620, 59

She, R., Ho, L. C., & Feng, H. 2017a, ApJ, 842, 131

She, R., Ho, L. C., & Feng, H. 2017b, ApJ, 835, 223

Shen, Y. 2013, Bulletin of the Astronomical Society of India, 41, 61

Shen, Y., Greene, J. E., Strauss, M. A., Richards, G. T., & Schneider, D. P. 2008, ApJ, 680, 169

Shen, Y., Hall, P. B., Horne, K., et al. 2019, ApJS, 241, 34

Shen, Y. & Liu, X. 2012, ApJ, 753, 125

Shu, X. W., Wang, S. S., Dou, L. M., et al. 2018, ApJ, 857, L16

Shu, X. W., Wang, T. G., Jiang, N., et al. 2017, ApJ, 837, 3

Sikora, M., Stawarz, Ł., & Lasota, J.-P. 2007, ApJ, 658, 815

Sillanpaa, A., Haarala, S., Valtonen, M. J., Sundelius, B., & Byrd, G. G. 1988, ApJ, 325, 628

Silverman, J. D., Lamareille, F., Maier, C., et al. 2009, ApJ, 696, 396

Simmonds, C., Buchner, J., Salvato, M., Hsu, L. T., & Bauer, F. E. 2018, A&A, 618, A66

Sądowski, A. 2009, ApJS, 183, 171

Slone, O. & Netzer, H. 2012, MNRAS, 426, 656

Smith, K. L., Shields, G. A., Bonning, E. W., et al. 2010, ApJ, 716, 866

Sniegowska, M., Czerny, B., Bon, E., & Bon, N. 2020, A&A, 641, A167

Sobolewska, M. A., Gierliński, M., & Siemiginowska, A. 2009, MNRAS, 394, 1640

Sobolewska, M. A. & Papadakis, I. E. 2009, MNRAS, 399, 1597

Sobolewska, M. A., Siemiginowska, A., & Gierliński, M. 2011, MNRAS, 413, 2259

Soltan, A. 1982, MNRAS, 200, 115

Sridhar, N., García, J. A., Steiner, J. F., et al. 2020, ApJ, 890, 53

Steffen, A. T., Strateva, I., Brandt, W. N., et al. 2006, AJ, 131, 2826

Stella, L. & Rosner, R. 1984, ApJ, 277, 312

Stern, B. E., Poutanen, J., Svensson, R., Sikora, M., & Begelman, M. C. 1995, ApJ, 449, L13

Strateva, I. V., Brandt, W. N., Schneider, D. P., Vanden Berk, D. G., & Vignali, C. 2005, AJ, 130, 387

Strüder, L., Briel, U., Dennerl, K., et al. 2001, A&A, 365, L18

Sun, L., Shu, X., & Wang, T. 2013, ApJ, 768, 167

Sunyaev, R., Arefiev, V., Babyshkin, V., et al. 2021, arXiv e-prints, arXiv:2104.13267

Svensson, R. & Zdziarski, A. A. 1994, ApJ, 436, 599

Svoboda, J., Guainazzi, M., & Merloni, A. 2017, A&A, 603, A127

Szuszkiewicz, E. 1990, MNRAS, 244, 377

Taam, R. E., Chen, X., & Swank, J. H. 1997, ApJ, 485, L83

Taam, R. E. & Lin, D. N. C. 1984, ApJ, 287, 761

Tamanini, N. 2017, in Journal of Physics Conference Series, Vol. 840, Journal of Physics Conference Series, 012029

Tanaka, Y., Nandra, K., Fabian, A. C., et al. 1995, Nature, 375, 659

Tananbaum, H., Avni, Y., Branduardi, G., et al. 1979, ApJ, 234, L9

Tang, Y., Haiman, Z., & MacFadyen, A. 2018, MNRAS, 476, 2249

Thorne, K. S. 1974, ApJ, 191, 507

Tohline, J. E. & Osterbrock, D. E. 1976, ApJ, 210, L117

Toscani, M., Rossi, E. M., & Lodato, G. 2020, MNRAS, 498, 507

Trakhtenbrot, B., Arcavi, I., MacLeod, C. L., et al. 2019, ApJ, 883, 94

Truemper, J. 1982, Advances in Space Research, 2, 241

Turner, M. J. L., Abbey, A., Arnaud, M., et al. 2001, A&A, 365, L27

Turner, N. J., Stone, J. M., & Sano, T. 2002, ApJ, 566, 148

Turner, T. J. & Pounds, K. A. 1989, MNRAS, 240, 833

Ueda, Y., Akiyama, M., Ohta, K., & Miyaji, T. 2003, ApJ, 598, 886

Uttley, P., Cackett, E. M., Fabian, A. C., Kara, E., & Wilkins, D. R. 2014, A&A Rev., 22, 72

Uttley, P. & McHardy, I. M. 2005, MNRAS, 363, 586

Uttley, P., McHardy, I. M., & Papadakis, I. E. 2002, MNRAS, 332, 231

Uzdensky, D. A. 2013, ApJ, 775, 103

Uzdensky, D. A. 2016, in Astrophysics and Space Science Library, Vol. 427, Magnetic Reconnection: Concepts and Applications, ed. W. Gonzalez & E. Parker, 473

Uzdensky, D. A. & Goodman, J. 2008, ApJ, 682, 608

Vagnetti, F., Antonucci, M., & Trevese, D. 2013, A&A, 550, A71

Vahdat Motlagh, A., Kalemci, E., & Maccarone, T. J. 2019, MNRAS, 485, 2744

Valtonen, M. J., Lehto, H. J., Nilsson, K., et al. 2008, Nature, 452, 851

van Dyk, D. A., Connors, A., Kashyap, V. L., & Siemiginowska, A. 2001, ApJ, 548, 224

van Paradijs, J. 1996, ApJ, 464, L139

van Velzen, S. 2018, ApJ, 852, 72

van Velzen, S. & Farrar, G. R. 2014, ApJ, 792, 53

van Velzen, S., Gezari, S., Cenko, S. B., et al. 2019, ApJ, 872, 198

van Velzen, S., Gezari, S., Hammerstein, E., et al. 2021, ApJ, 908, 4

van Velzen, S., Holoien, T. W. S., Onori, F., Hung, T., & Arcavi, I. 2020, Space Sci. Rev., 216, 124

Vasudevan, R. V. & Fabian, A. C. 2007, MNRAS, 381, 1235

Vasudevan, R. V. & Fabian, A. C. 2009, MNRAS, 392, 1124

Vasudevan, R. V., Fabian, A. C., Reynolds, C. S., et al. 2016, MNRAS, 458, 2012

Velten, H. & Gomes, S. 2020, Phys. Rev. D, 101, 043502

Vestergaard, M., Wilkes, B. J., & Barthel, P. D. 2000, ApJ, 538, L103

Vignali, C., Brandt, W. N., & Schneider, D. P. 2003, AJ, 125, 433

Vincentelli, F. M., Casella, P., Maccarone, T. J., et al. 2018, MNRAS, 477, 4524

Vio, R. & Andreani, P. 2018, arXiv e-prints [arXiv:1812.03995]

Vito, F., Brandt, W. N., Bauer, F. E., et al. 2019, A&A, 630, A118

Volonteri, M. 2010, A&A Rev., 18, 279

Wang, C., Yu, L.-M., Bian, W.-H., & Zhao, B.-X. 2019a, MNRAS, 487, 2463

Wang, J.-M., Chen, Y.-M., Hu, C., et al. 2009, ApJ, 705, L76

Wang, J.-M., Watarai, K.-Y., & Mineshige, S. 2004, ApJ, 607, L107

Wang, Y. Y., Wang, F. Y., Zou, Y. C., & Dai, Z. G. 2019b, ApJ, 886, L22

Werner, G. R., Philippov, A. A., & Uzdensky, D. A. 2019, MNRAS, 482, L60

Wevers, T. 2020, MNRAS, 497, L1

Wevers, T., Pasham, D. R., van Velzen, S., et al. 2021, arXiv e-prints, arXiv:2101.04692

Wevers, T., van Velzen, S., Jonker, P. G., et al. 2017, MNRAS, 471, 1694

White, N. E., Fabian, A. C., & Mushotzky, R. F. 1984, A&A, 133, L9

Wilkins, D. R., Cackett, E. M., Fabian, A. C., & Reynolds, C. S. 2016, MNRAS, 458, 200

Wilkinson, D. M., Maraston, C., Goddard, D., Thomas, D., & Parikh, T. 2017, MNRAS, 472, 4297

Williams, O. R., Turner, M. J. L., Stewart, G. C., et al. 1992, ApJ, 389, 157

Willingale, R., Starling, R. L. C., Beardmore, A. P., Tanvir, N. R., & O'Brien, P. T. 2013, MNRAS, 431, 394

Wills, B. J. & Browne, I. W. A. 1986, ApJ, 302, 56

Woosley, S. E. & Weaver, T. A. 1995, ApJS, 101, 181

Wu, Q., Czerny, B., Grzedzielski, M., et al. 2016, ApJ, 833, 79

Yamada, S., Makishima, K., Done, C., et al. 2013, PASJ, 65, 80

Yan, Z. & Xie, F.-G. 2018, MNRAS, 475, 1190

Yang, T., Banerjee, A., & Ó Colgáin, E. 2020, Phys. Rev. D, 102, 123532

You, B., Cao, X., & Yuan, Y.-F. 2012, ApJ, 761, 109

Young, M., Elvis, M., & Risaliti, G. 2009, ApJS, 183, 17

Young, M., Elvis, M., & Risaliti, G. 2010, ApJ, 708, 1388

Yu, Z., Martini, P., Davis, T. M., et al. 2020, ApJS, 246, 16

Zabludoff, A. I., Zaritsky, D., Lin, H., et al. 1996, ApJ, 466, 104

Zalamea, I., Menou, K., & Beloborodov, A. M. 2010, MNRAS, 409, L25

Zappacosta, L., Comastri, A., Civano, F., et al. 2018, ApJ, 854, 33

Zdziarski, A. A. & Gierliński, M. 2004, Progress of Theoretical Physics Supplement, 155, 99

Zdziarski, A. A., Gierliński, M., Mikołajewska, J., et al. 2004, MNRAS, 351, 791

Zdziarski, A. A., Johnson, W. N., & Magdziarz, P. 1996, MNRAS, 283, 193

Zdziarski, A. A., Poutanen, J., & Johnson, W. N. 2000, ApJ, 542, 703

Zdziarski, A. A., Poutanen, J., Mikolajewska, J., et al. 1998, MNRAS, 301, 435

Zdziarski, A. A., Ziółkowski, J., & Mikołajewska, J. 2019, MNRAS, 488, 1026

Zel'dovich, Y. B. 1964, Soviet Physics Doklady, 9, 195

Zhang, W., Dovčiak, M., & Bursa, M. 2019, ApJ, 875, 148

Zheng, X., Liao, K., Biesiada, M., et al. 2020, ApJ, 892, 103

Życki, P. T., Done, C., & Smith, D. A. 1999, MNRAS, 309, 561

Acknowledgements

Here we are, at the end of this fantastic journey. Going back, I would do it all again! Thumbs down for the pandemic, obviously, but to be fair now we know that things like this can happen. Hopefully we have learned what's important: so let's work less and enjoy our life more [*throws away papers*]! Kidding.. I need to publish [*picks up papers*].

I have to thank many people for these four years!

To Dr. Andrea Merloni, for being an amazing supervisor and day by day the wisest, calmest, kindest guide to be around.

To Prof. Paul Nandra, for always finding time to help me improve our projects and research.

To Dr. Gabriele Ponti, for always being there to give great scientific and personal advice.

To Dr. Mara Salvato, for all the help and support and for defending the well-being of any student to the death.

To Dr. Johannes Buchner, for patiently listening many times and patiently explaining many more.

To the high-energy group at MPE, for being a great working environment.

To Felix, Sebo, Jacob and Adam (ordered from the oldest to youngest, roughly 25 years apart), for our chaotic lunch breaks, our unpredictable nights out, our last-minute trips (Pack 3.0 loading..), our friendship.

To Jacob and Damien, for the nicest office environment possible (I've missed our chats so much in home office time!).

To Julien (can't write your fav nickname here unfortunately..), for the beers and walks over at Little Berlin. To Linda, Yru and all the other friends students, for the fun lunch breaks and crazy parties.

To them Queens, aka Jacob, Sebo, Fruzsi, Oxi (sorry, I don't see orders) for helping me in keeping my mental (in)sanity during the pandemic (5 real you know..) and for the crazy inside jokes (don't forget to bring your towel!). You guys have been like a second family in these dire times (and I knew it)!

To my MIL-Basket teammates, because it was important for me not to quit playing my favourite sport and you let me do it in the chillest environment.

I also want to thank again Felix for translating my abstract auf Deutsch (ich bin thank you mate!), and Adam for proofreading my veri gud inglish (I can see you [*handwaving with an open hand facing the chest and moving the wrist in circles, whilst the mouth bends downward in appreciation and humming 'Mamma mia che roba'*]).

Vorrei ovviamente ringraziare la mia famiglia: a Mamma e Papa', per avermi sempre dato

supporto, per avermi viziato come un "Principe" ad ogni rimpatrio, per le chiamate Skype deliranti; a Franci, perche' anche se siamo lontani sei sempre la mia migliore amica (tranne quando mi fai decidere le cose per te.. ma che ne so? Non so neanche dov'e' io..).

A Toska, per essere "anche tu quii.. in casa?" (*suono di stecche fatto male*), partner di Brezn Production ("Lockdown bleibt gleich" diventera' un banger cult), ma prima di tutto un fratello. Did you understand dear Toska?

A Laura (il concetto di Fistalloni di t-rex, elefantino o panda rosso), a cui va accreditato molto del mio benessere durante l'inizio di questa nuova avventura.

Agli amici a casa (gang Okeechobee), per non cambiare mai e per essere la mia valvola di sfogo (ogni volta che torno abbiamo tutti di nuovo solo 20 anni).

Ai Podcaster With Attitude, per aver condiviso con me un gran bel progetto in amicizia, rabbia (occasionalmente), ma soprattutto "caciara" ("Stare fro re bore na we he!").

To the random unknown reader from the future who got here by chance, feel free to drop me an email (or whatever neuro/cyber/video-call crazy sci-fi stuff is up at that time) to say hi.

To my future-self reading this, I hope you are still cool and healthy, but most importantly it is imperative that you remember to finish what y